Designing Functional Materials Driven by the Lattice Degree of Freedom

TECHNISCHE
UNIVERSITÄT
DARMSTADT

Materials and Earth
Sciences Department
Institute of Materials
Science
Theory of Magnetic
Materials

Designing Functional Materials Driven by the Lattice Degree of Freedom

Accepted doctoral thesis by Chen Shen

Date of submission: 10.11.2022
Date of thesis defense: 21.12.2022

Darmstadt, Technische Universität Darmstadt

This thesis is dedicated to my beloved parents.
老爸，老妈，你们辛苦了！

Erklärungen laut Promotionsordnung

§ 8 Abs. 1 lit. c PromO

Ich versichere hiermit, dass die elektronische Version meiner Dissertation mit der schriftlichen Version übereinstimmt.

§ 8 Abs. 1 lit. d PromO

Ich versichere hiermit, dass zu einem vorherigen Zeitpunkt noch keine Promotion versucht wurde. In diesem Fall sind nähere Angaben über Zeitpunkt, Hochschule, Dissertationsthema und Ergebnis dieses Versuchs mitzuteilen.

§ 9 Abs. 1 PromO

Ich versichere hiermit, dass die vorliegende Dissertation selbstständig und nur unter Verwendung der angegebenen Quellen verfasst wurde.

§ 9 Abs. 2 PromO

Die Arbeit hat bisher noch nicht zu Prüfungszwecken gedient.

Darmstadt, 10.11.2022

_____

Chen Shen

Contents

Acknowledgements

Abstract

Advanced functional materials play a vital role in modern industry and human society. Therefore, accelerating the discovery and exploration of novel functional materials is critical for us as a society to tackle the energy issues and further developments. In this regard, computational materials science based on quantum mechanics is now well established as a crucial pillar in condensed matter physics, chemistry, and materials science research, in addition to experiments and phenomenological theories. In this thesis, the strategy of designing new functional materials driven by the lattice degree of freedom is explored, where "lattice" refers to (1) the ground state crystal structures, (2) elementary excitations as represented by phonons, (3) coupling within themselves (*i.e.*, anharmonicity) and the other degrees of freedom (*i.e.*, electron-phonon interaction). We systematically studied several classes of physical phenomena and the resulting properties, such as magneto-structural coupling and magnetocalorics, anharmonicity and thermal conductivity, electron-phonon interaction and superconductivity. Additionally, an integrated computational paradigm that combines the high-throughput (HTP) calculations, phonon theory, and CALPHAD methods is established and applied to design metastable functional materials, extending the applicability of DFT beyond 0 K.

Considering lattice as crystal structures, we selected MAB phases with nanolaminated crystal structure as a test case, and performed an HTP screening for stable magnetic MAB compounds and predicted potential candidate magnets for permanent magnets and magnetocaloric applications. After a comprehensive validation, 21 novel compounds are predicted to be stable based on the systematic evaluation of thermodynamic, mechanical, and dynamical stabilities, and the number of stable compounds is increased to 434 taking the tolerance of convex hull being 100 meV/atom. The detailed evaluation of the magnetocrystalline anisotropy energy (MAE) and the magnetic deformations ($\sum_M$) leads to 23 compounds with significant uniaxial anisotropy (MAE > 0.4 MJ/m^3) and 99 systems with reasonable magnetic deformation ($\sum_M > 1.5\%$). For those compounds containing no expensive, toxic, or critical elements, it is observed that $Fe_3Zn_2B_2$ is a reasonable candidate as gap permanent magnet, and Fe_4AlB_4, Fe_3AlB_4, Fe_3ZnB_4, and Fe_5B_2 as potential magnetocaloric materials. This work paves the way for designing novel

magnetic materials for energy applications based on the combinatorial sampling of the chemical space with specific crystal structure prototypes.

Moreover, considering the elementary excitations of lattice vibrations, *i.e.*, phonons, the anharmonicity caused by phonon-phonon interaction leads to many intriguing properties such as the lattice thermal conductivity. We performed DFT calculations to evaluate the thermal transport properties of novel 2D $MoSi_2N_4$ and WSi_2N_4, and found their thermal conductivities being 162 $Wm^{-1}K^{-1}$ and 88 $Wm^{-1}K^{-1}$ at room temperature, respectively, which are 7 and 4 times the one for monolayer MoS_2, 16 and 9 times the one for silicene. These results show that, $MoSi_2N_4$ and WSi_2N_4 have promising potential being thermal management materials. Additionally, to gain insight into the low thermal conductivity of 2D materials, we investigated the mechanism of anharmonicity from the fundamental phonon mode and electronic structure level for GaX (X= N, P, As). The thermal conductivity of GaP is calculated to be 1.52 $Wm^{-1}K^{-1}$, which is unexpectedly ultra-low and in sharp contrast to GaN and GaAs. The reason for the low thermal conductivity of the GaP can be attributed to the fact that the FA phonon dominates the thermal conductivity of GaN but contributes less to that of GaP, which is due to the symmetry-based selection rule and difference of atomic structure. The phonon anharmonicity quantified by the Grüneisen parameter is further analyzed to understand the phonon–phonon scattering, indicating the strong phonon-phonon scattering of GaP and the strongest phonon anharmonicity of GaP. The buckling structure has strong influence on the anharmonicity, leading to the low thermal conductivity. The non-bonding lone pair electrons of P and As atoms are stronger, which induces nonlinear electrostatic forces upon thermal agitation, leading to increased phonon anharmonicity in the lattice and thus reducing the thermal conductivity. Furthermore, high order phonon anharmonicity could have significant effect on the thermal transport properties in materials within strong anharmonicity. Hence, we calculated the thermal conductivity of pristine $EuTiO_3$. And the role of the quartic anharmonicity in the lattice dynamics and thermal transport of the cubic $EuTiO_3$ was elucidated by combining *ab initio* self-consistent phonon theory with compressive sensing techniques. The anti-ferromagnetic G-type magnetic structure is used to mimic the para-magnetic $EuTiO_3$. We find that the strong quartic anharmonicity of oxygen atoms plays an important role in the phonon quasiparticles without imaginary frequencies and causes the hardening of the vibrational frequencies of soft modes.

Furthermore, in terms of electron-phonon interaction, we derived from DFT calculations the formation energies of a newly synthesized orthorhombic compound $GeNCr_3$, which is a metastable phase. In accordance with the experimentally discovered superconductivity in antiperovskite $MgCNi_3$, we performed calculations to evaluate the electron-phonon interaction and the resulting superconducting critical temperature of $GeNCr_3$. It is observed that its superconducting temperature is about 8.2 K driven by the electron phonon interaction. Correspondingly, it is suspected that the superconductivity may

exist in the other MAX, MAB, and APV compounds, which will be investigated in the future based on the established workflow to evaluate the electron phonon coupling. Such a workflow allows us to obtain the T-dependence of electric conductivities and also the lattice thermal conductivities.

Last but not least, considering the thermodynamic properties where the lattice free energy plays a dominant role at the finite temperatures, we combined DFT calculations and CALPHAD modeling to optimize the phase diagrams, which can be validated with experiments and be bridged to phase field simulations to map out the processing-microstructure-property relationships. For instance, the thermodynamic properties of the Fe-Sn system are studied. First-principles phonon calculations with the quasi-harmonic approximation (QHA) approach were performed to compute the thermodynamic properties at finite temperatures. Thermodynamic properties, phonon dispersions of pure elements, and intermetallics were predicted to make up for the shortage of experimental data. A set of self-consistent thermodynamic parameters of Fe-Sn system are obtained by the CALPHAD approach. Thermodynamic modeling of the Fe-Sn phase diagram has been re-established. The metastable phase Fe_3Sn was first introduced into the current metastable phase diagram and corrected phase locations of Fe_5Sn_3 and Fe_3Sn_2 under the newly measured corrected temperature ranges.

In summary, in my thesis, a systematic computational paradigm has been established based on DFT to tackle both the thermodynamic and non-equilibrium transport properties associated with the lattice degree of freedom. Such a paradigm allows us to design and optimize functional materials with physical properties driven by magneto-structural coupling, phonon-phonon coupling, and electron-phonon interaction, and also to bridge to large-scale simulations.

Zusammenfassung

Fortschrittliche Funktionswerkstoffe spielen in der modernen Industrie und der menschlichen Gesellschaft eine entscheidende Rolle. Daher ist die Beschleunigung der Entdeckung und Erforschung neuartiger Funktionsmaterialien für uns als Gesellschaft von entscheidender Bedeutung, um die Energieprobleme und weitere Entwicklungen anzugehen. In diesem Zusammenhang hat sich die auf der Quantenmechanik basierende rechnergestützte Materialwissenschaft neben Experimenten und phänomenologischen Theorien als wichtige Säule der Physik der kondensierten Materie, der Chemie und der materialwissenschaftlichen Forschung etabliert. In dieser Arbeit wird die Strategie des Entwurfs neuer funktioneller Materialien untersucht, die durch den Freiheitsgrad des Gitters angetrieben werden, wobei sich "Gitter" auf (1) die Grundzustands-Kristallstrukturen, (2) elementare Anregungen, wie sie durch Phononen dargestellt werden, (3) die Kopplung in sich selbst (d. h. Anharmonizität) und die anderen Freiheitsgrade (d. h. Elektron-Phonon-Wechselwirkung) bezieht. Wir haben systematisch mehrere Klassen physikalischer Phänomene und die daraus resultierenden Eigenschaften untersucht, wie z. B. magnetisch-strukturelle Kopplung und Magnetokalorik, Anharmonizität und Wärmeleitfähigkeit, Elektron-Phonon-Wechselwirkung und Supraleitung. Darüber hinaus wurde ein integriertes Berechnungsparadigma entwickelt, das Berechnungen mit hohem Durchsatz (HTP), Phononentheorie und CALPHAD-Methoden kombiniert und zur Entwicklung metastabiler funktioneller Materialien eingesetzt wird, wodurch die Anwendbarkeit von DFT über 0 K hinaus erweitert wird.

Unter Berücksichtigung des Gitters als Kristallstruktur haben wir MAB-Phasen mit nanolaminierter Kristallstruktur als Testfall ausgewählt und ein HTP-Screening nach stabilen magnetischen MAB-Verbindungen durchgeführt und potenzielle Magnetkandidaten für Permanentmagnete und magnetokalorische Anwendungen vorhergesagt. Nach einer umfassenden Validierung wurden 21 neue Verbindungen auf der Grundlage der systematischen Bewertung der thermodynamischen, mechanischen und dynamischen Stabilität als stabil eingestuft, und die Anzahl der stabilen Verbindungen wurde auf 434 erhöht, wobei die Toleranz der konvexen Hülle 100 meV/Atom beträgt. Die detaillierte Auswertung der magnetokristallinen Anisotropieenergie (MAE)

und der magnetischen Verformungen ($\sum_M$) führt zu 23 Verbindungen mit signifikanter uniaxialer Anisotropie (MAE > 0.4 MJ/m^3) und 99 Systemen mit angemessener magnetischer Verformung ($\sum_M > 1.5\%$). Bei den Verbindungen, die keine teuren, giftigen oder kritischen Elemente enthalten, ist Fe$_3$Zn$_2$B$_2$ ein geeigneter Kandidat für einen Lückenmagneten. Fe$_4$AlB$_4$, Fe$_3$AlB$_4$, Fe$_3$ZnB$_4$ und Fe$_5$B$_2$ können potenzielle magnetokalorische Materialien sein. Diese Arbeit ebnet den Weg für die Entwicklung neuartiger magnetischer Materialien für Energieanwendungen auf der Grundlage der kombinatorischen Abtastung des chemischen Raums mit spezifischen Kristallstruktur-prototypen.

Betrachtet man darüber hinaus die elementaren Anregungen der Gitterschwingungen, d. h. die Phononen, so führt die Anharmonizität, die durch die Phonon-Phonon-Wechselwirkung verursacht wird, zu vielen faszinierenden Eigenschaften wie zum Beispiel die Wärmeleitfähigkeit des Gitters. Wir haben DFT-Berechnungen zur Bewertung die thermischen Transporteigenschaften von neuartigem 2D MoSi$_2$N$_4$ und WSi$_2$N$_4$ durchgeführt und fanden deren Wärmeleitfähigkeiten bei 162 Wm^{-1}K^{-1} und 88 Wm^{-1}K^{-1} bei Raumtemperatur, was 7- bzw. 4-fach höher ist als die Wärmeleitfähigkeit von einlagigem MoS$_2$ und 16- bzw. 9-fach höher ist als die Wärmefähigkeit für Silicen. Diese Ergebnisse zeigen, dass MoSi$_2$N$_4$ und WSi$_2$N$_4$ ein vielversprechendes Potenzial als Thermomanagementmaterialien haben. Um einen Einblick in die niedrige Wärmeleitfähigkeit von 2D-Materialien zu erhalten, haben wir den Mechanismus der Anharmonizität anhand des fundamentalen Phononenmodus und des elektronischen Strukturniveaus für GaX (X= N, P, As) untersucht. Die Wärmeleitfähigkeit von GaP wird berechnet bei 1,52 Wm^{-1}K^{-1}, das ist unerwartet niedrig und steht in scharfem Kontrast zu GaN und GaAs. Der Grund für die niedrige Wärmeleitfähigkeit von GaP kann darauf zurückgeführt werden, dass das FA-Phonon die Wärmeleitfähigkeit von GaN dominiert, aber weniger zur Wärmeleitfähigkeit von GaP beiträgt, was auf die symmetriebasierte Selektionsregel und die unterschiedliche atomare Struktur zurückzuführen ist. Die Phonon Anharmonizität, quantifiziert durch den Grüneisen-Parameter, wird weiter analysiert, um die die Phonon-Phonon-Streuung zu verstehen, was auf die starke Phonon-Phonon-Streuung von GaP und die stärkste Phonon-Anharmonizität von GaP deutet. Die Knickstruktur hat einen starken Einfluss auf die Anharmonizität, was zu einer niedrigen Wärmeleitfähigkeit führt. Die nicht-bindenden einsamen Elektronenpaare von P- und As-Atomen sind stärker, was bei thermischer Bewegung nichtlineare elektrostatische Kräfte bei thermischer Bewegung induzieren, was zu einer erhöhten Phononenharmonizität im Gitter führt und damit zu einer Verringerung der Wärmeleitfähigkeit. Außerdem könnte die hohe Ordnung Phononenanharmonizität erhebliche Auswirkungen auf die thermischen Transporteigenschaften in Materialien mit starker Anharmonizität haben. Daher haben wir die Wärmeleitfähigkeit von unbehandeltem EuTiO$_3$ berechnet. Und die Rolle der quartischen Anharmonizität für die Gitterdynamik und des Wärmetransports von kubischem EuTiO$_3$ wurde durch die Kombination von ab initio selbst konsistenten Phononentheorie mit Techniken der

Drucksensorik aufgeklärt. Die anti-ferromagnetische G-Typ-Magnetstruktur wird zur Nachahmung des paramagnetischen $EuTiO_3$ verwendet. Wir finden, dass die starke quartische Anharmonizität der Sauerstoffatome eine wichtige Rolle bei den Phononen Quasiteilchen ohne imaginäre Frequenzen spielt und die Verhärtung der vibrationellen Frequenzen der weichen Moden verursacht.

Darüber hinaus haben wir anhand von DFT-Berechnungen die Bildungsenergien einer neu synthetisierten orthorhombischen Verbindung $GeNCr_3$ ermittelt, die eine metastabile Phase ist. In Übereinstimmung mit der experimentell entdeckten Supraleitfähigkeit im Antiperowskit $MgCNi_3$ haben wir Berechnungen durchgeführt, um die Elektron-Phonon-Wechselwirkung und die daraus resultierende kritische Temperatur für die Supraleitung von $GeNCr_3$ zu bestimmen. Es wurde festgestellt, dass die supraleitende Temperatur bei etwa 8.2 K liegt, was auf die Elektron-Phonon-Wechselwirkung zurückzuführen ist. Dementsprechend wird vermutet, dass die Supraleitung auch in den anderen MAX-, MAB- und APV-Verbindungen existieren könnte, die in Zukunft auf der Grundlage des etablierten Arbeitsablaufs zur Bewertung der Elektron-Phonon-Kopplung untersucht werden sollen. Ein solcher Arbeitsablauf ermöglicht es uns, die T-Abhängigkeit der elektrischen Leitfähigkeiten und auch die thermischen Leitfähigkeiten des Gitters zu erhalten.

Nicht zuletzt unter Berücksichtigung der thermodynamischen Eigenschaften, bei denen die freie Gitterenergie bei endlichen Temperaturen eine dominante Rolle spielt, haben wir DFT-Berechnungen und CALPHAD-Modellierung kombiniert, um die Phasendiagramme zu optimieren, die mit Experimenten validiert und mit Phasenfeldsimulationen verknüpft werden können, um die Beziehungen zwischen Verarbeitung und Mikrostruktur und Eigenschaften zu ermitteln. So werden beispielsweise die thermodynamischen Eigenschaften des Fe-Sn-Systems untersucht. Zur Berechnung der thermodynamischen Eigenschaften bei endlichen Temperaturen wurden First-Principles-Phonon-Berechnungen mit dem Ansatz der quasi-harmonischen Annäherung (QHA) durchgeführt. Die thermodynamischen Eigenschaften und die Phononendispersionen der reinen Elemente und der intermetallischen Verbindungen wurden vorhergesagt, um den Mangel an experimentellen Daten auszugleichen. Eine Reihe von selbstkonsistenten thermodynamischen Parametern des Fe-Sn-Systems wurde mit Hilfe des CALPHAD-Ansatzes ermittelt. Die thermodynamische Modellierung des Fe-Sn-Phasendiagramms wurde wiederhergestellt. Die metastabile Phase Fe_3Sn wurde zunächst in das aktuelle metastabile Phasendiagramm eingeführt und die Phasenlagen von Fe_5Sn_3 und Fe_3Sn_2 unter den neu gemessenen korrigierten Temperaturbereichen korrigiert.

Zusammenfassend lässt sich sagen, dass in meiner Dissertation ein systematisches Berechnungsparadigma entwickelt wurde auf der Grundlage von DFT, um sowohl die thermodynamischen als auch die Nicht-Gleichgewichts-Transporteigenschaften im Zusammenhang mit dem Gitterfreiheitsgrad zu untersuchen. Ein solches Paradigma

ermöglicht es uns, funktionelle Materialien mit physikalischen Eigenschaften zu entwerfen und zu optimieren, die durch magnetisch-strukturelle Kopplung, Phonon-Phonon-Kopplung und Elektron-Phonon-Wechselwirkung bestimmt werden, und auch eine Brücke zu groß angelegten Simulationen zu schlagen.

List of Figures

List of Tables

1. Introduction

1.1. Computational Design of Functional Materials

Advanced functional materials play an essential role in modern industries and humankind society. In fact, every stage in the human history has been accompanied by the development of materials science. From the Stone Age to the Silicon Age, various novel functional materials have introduced, with tremendous improvements in technology and industry, benefiting humankind's welfare. Nowadays, as energy becomes an apparent constraint to the whole human society, accelerated discovery and exploration of novel functional materials are critical for global competitiveness. The conventional way of developing materials is mainly based on try-and-error or empirical structure-property relationships, which is time- and resource-costly. Fortunately, the computational modeling of materials has grown dramatically in the past few decades with new innovative methods and applications, which, together with enhancing the capability of computer hardware, have established it as an essential pillar of study for materials understanding and discovery. Early in 2011, the Materials Genome Initiative (MGI) [1] was launched by the US government to accelerate the discovery, design, development, and deployment of new materials, at a fraction of the cost, by harnessing the power of data and computational tools in concert with experiment. Later, in 2015, the Chinese government announced Materials Genome Engineering (MGE) program [2], aiming to revolutionize the research and development mode of new materials, significantly improving the research efficiency, shortening the research time, and reducing the cost. In 2019, the European Materials Modeling Council (EMMC) program was created to integrate materials modeling and digitization critical for more agile and sustainable product development in Europe.

A multi-scale modeling framework (as shown in Figure 1.1) is established and embraced in the above programs, leading to the integrated computational materials engineering (ICME) approach [3]. From Figure 1.1, various computational methodologies are usually positively interconnected, stimulating the vitality of interdisciplinary computational materials design. Note that the many-body Hamiltonian builds the foundation. According to it, the electron quantum ground state can be described as a functional of
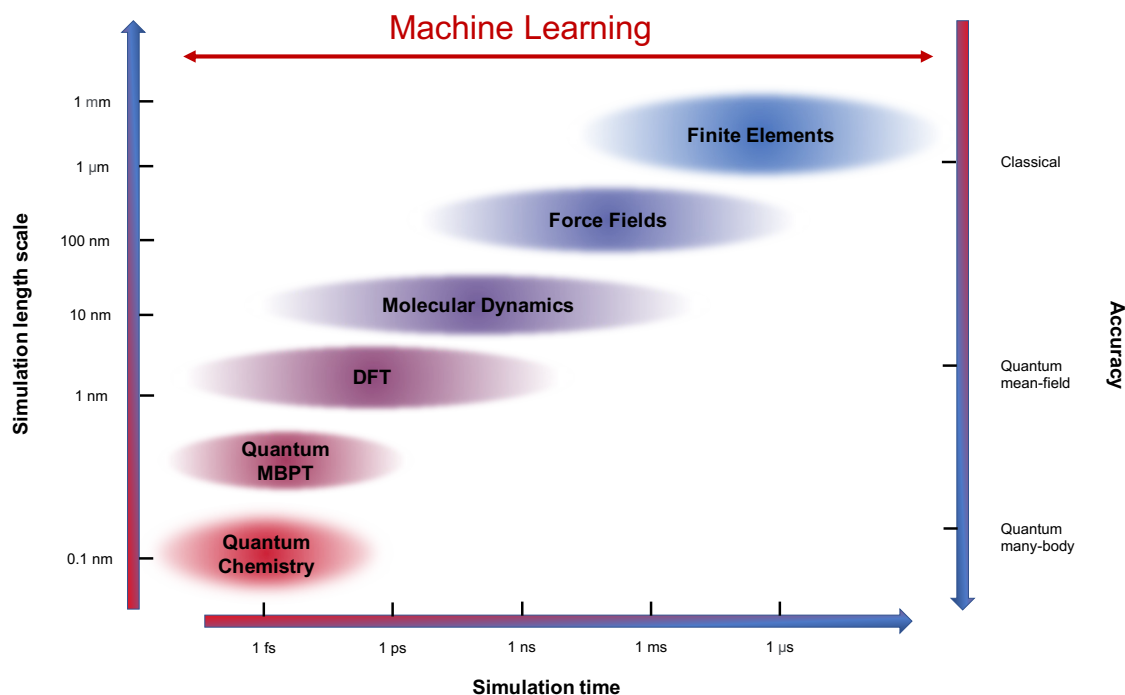
Figure 1.1.: A multi-scale modeling framework of computational materials science. Contemporary quantum and classical computational methodologies address systems spanning from microscopic length scales (∼0.1 nm) to macroscopic length scales (∼1 mm).

the electronic charge density within density functional theory (DFT). The excited states demand the introduction of the concepts of elementary excitations such as quasiparticles excited from the ground state (most current *ab initio* quasiparticle calculations of weakly to moderately correlated materials use the GW approach based on quantum many-body perturbation theory (MBPT)). For larger-scale systems, quantum mechanical descriptions of local effects may be fed into more coarse-grained models that describe atom and molecule dynamics and their collective motions. So far, the unification of these methods into multi-scale models has primarily been driven by the insights of scientists. Furthermore, machine learning techniques can identify new correlations in complex systems and between different scales, accelerating the simulation speed and saving costs.

Over the past few decades, DFT (more fundamentals in Chapter 2) has been arguably the most predominant and flourishing technique for the *ab initio* computational study of ground-state properties of the materials due to its power to calculate the accurate electronic structure. This can help us to obtain a clear understanding of the physical

properties of the materials. Moreover, DFT can be applied to evaluate the needed parameters for large-scale quantitative simulations. Only DFT can predict novel materials, not any other large-scale simulation tools. Furthermore, the more substantial power of DFT-based computational materials science has now become apparent owing to the wide range of properties and spectroscopies that can be studied for systems of increasing complexity [4, 5]. In a review paper from Marzari *et al.*, they sketched the very rich phenomena that can be addressed nowadays, providing pointers to the models, theories, and electronic-structure toolbox that can be used to make these predictions [5]. They also summarized some milestone approaches that are now widely used. Nowadays, the maturity of DFT-based methods and the fast blossoming of high-performance computing (HPC) resources have created new opportunities for high-throughput (HTP) calculations and designing novel materials with desired properties.

1.2. HTP Design of Functional Materials

Thanks to the accuracy and efficiency of first-principles calculations and the exponential availability of computational power, not only has the range of calculated materials properties expanded dramatically but also the use of these methods to design and discover novel materials has become an extremely active and growing research area. Here the emphasis transforms from computing the property of interest of one system at a time to calculating it at scale for many systems. In the extreme, people can even attempt to calculate properties for all known or predicted compounds. HTP calculations aim to perform the first-principles calculations under the automated workflow. Robust rates of automation for these calculations have little or no manual intervention. In addition, owing to the applicability of first-principles methods to most or all elements of the periodic table, HTP DFT calculations can be implemented in various complex systems. Till now, HTP DFT calculations have been applied to design various functional materials, such as electro-catalysts [6], advanced magnets [7], thermoelectrics [8], photovoltaics [9], high entropy alloys [10], solar cell [11], and so on. Correspondingly, large open databases of materials structures and properties, such as Materials Project [12], AFLOW [13], NOMAD [14], and he Open Quantum Materials Database (OQMD) [15], have been build, with integrated platforms like AiiDA [16] and Atomate [17] available. Each of these databases is based on DFT-calculated properties of experimentally synthesized and of novel, predicted compounds. On the one hand, they can obtain properties from standard ground-state energy calculations, such as total energy, the density of states, electronic structure, and magnetic moments. On the other hand, these databases have been increasingly used to curate additional datasets for more complex properties, for example, elastic and piezoelectric tensors, thermoelectric properties, surface energies, phonon dispersions, and x-ray absorption near-edge

spectroscopy spectra.

Hence, the HTP DFT screening changes the way of performing calculations from a few compounds to thousands of compounds. This technical innovation needs people to think and employ an efficient screening strategy for treating large datasets. One starts with a large pool of candidate compounds and applies more and more stringent criteria to downselect the most promising compounds. Efficiency and cost should be considered the most important factors. Selection criteria prioritize relatively straightforward ad inexpensive quantities to calculate, and only later introduce more computationally complex, and hence expensive, quantities for further refinement. A very common criterion is thermodynamical stability, which is identified through the formation of energy and a convex hull approach. Such a screening strategy is illustrated in Section 3.1, but the literature offers many examples that have been summarized in several reviews [18, 19, 20].

1.3. Designing Functional Materials Driven by the Lattice Degree of Freedom

Among all the physical properties which can be tackled based on DFT calculations, those driven by the lattice degree of freedom are very interesting. Due to the motion of the nuclei, the corresponding elementary excitation, *i.e.*, phonons, is introduced, leading further to phonon-phonon interactions and electron-phonon interactions. These couplings between electrons and nuclei going beyond the Born–Oppenheimer approximation are central to many important physical properties, such as thermodynamical properties, thermal transport properties, and superconductivity.

Firstly, after considering the lattice dynamics, the phonon dispersion relations and materials' thermodynamic properties can be computed. Generally, the lattice free energy makes the most contributions to the total Gibbs free energy. Lattice free energy can be obtained based on the quasi-harmonic approximation (QHA) with volume-dependent harmonic phonons as part of the anharmonic effect. Hence, the DFT calculations can be bridged to the thermodynamic properties of systems, to the atomistic modeling at a larger length scales while maintaining accuracy, and to experiments with mutual validation. In this way, the limitation of DFT calculations can be overcome, namely, valid only at 0 K with a substantial size limit. Additionally, the calculated Gibbs free energies can be fed into the CALPHAD method [21] as initial input values. The CALPHAD method models the thermodynamic properties of compounds and obtains global minimization of the Gibbs free energies of all the competing phases out of one system, leading to multi-component phase diagrams. Such phase diagrams offer a roadmap for experimental synthesis.

Secondly, the phonon-phonon scattering governed by phonon anharmonicity is the critical factor limiting the heat transfer. Indeed, thermal conductivity is a crucial physical property of materials, which is important for many applications, such as heat dissipation in ever-smallest integrated circuits, energy conversion in thermoelectrics, thermal insulation in high-power engines, and information processing based on novel thermal transistors. Based on the single mode relaxation time approximation (RTA) of the phonon Boltzmann transport equation (BTE), thermal conductivity in a system is governed by the phonon dispersion relations, which determine heat capacity, group velocity, and phonon lifetime (due to phonon anharmonicity). In principle, all these components are determined by the nature of the interatomic potentials, which can be feasibly modulated by changing either the structure topography or the relative position of atoms. In principle, atomistic models with DFT accuracy can be constructed by developing interatomic potentials combining HTP calculations and machine learning. Recently, machine learning interatomic potentials (MLIP) have been developed and implemented for both molecular and solid [22]. In the multi-scale modeling framework, molecular dynamics is effective in modeling the microstructure properties and can be further bridged to macroscopic modeling. And the interatomic potentials lie at the core of MD. However, MD is mostly implemented based on the empirical interatomic potentials of analytical functional forms, which is challenging to obtain for multi-component systems due to the many-body nature of potential energy surface (PES). In this regard, MLIP can aid MD in treating more complex systems within DFT accuracy.

Besides the phonon-phonon interactions, the interaction between electrons and phonons also plays an essential role in materials properties [23], such as the transition temperature of conventional superconductors [24], the carrier mobility in semiconductors [25], the temperature dependence of optical spectra in direct and indirect-gap semiconductors [26], the nonadiabatic corrections to phonon dispersion relations [23], and so on. Among that, the prediction of superconductiviting transition temperature attracts more attention in this thesis. In conventional superconductors below the transition temperature electron pairing results from a subtle interplay between the repulsive Coulomb interaction and the attractive electron-phonon interaction [24]. Starting from the seminal work of Bardeen, Cooper, and Schrieffer (BCS) [27], several techniques for the computation of the superconducting properties have been proposed, ranging from semi-empirical methods such as the McMillan-Allen-Dynes formula [28] to first-principles Green's-function methods such as the Migdal-Eliashberg (ME) formalism [29, 30], and more recently also approaches based on the DFT concept, such as the density-functional theory for superconductors (SCDFT) [31, 32]. Furthermore, the output from electron-phonon interactions calculations, such as electron-phonon relaxation times, can be used as inputs for nonadiabatic molecular dynamics (NAMD) simulations [33], which is particularly suitable for simulating large molecular systems.

Therefore, **going beyond the currently intensively studied designing of materials by performing HTP DFT evaluation of the ground state electronic structure, I aim at exploring and developing further how HTP DFT calculations can be performed to tackle the physical properties driven by the lattice degree of freedom.** All aspects covered are summarized in Figure 1.2.
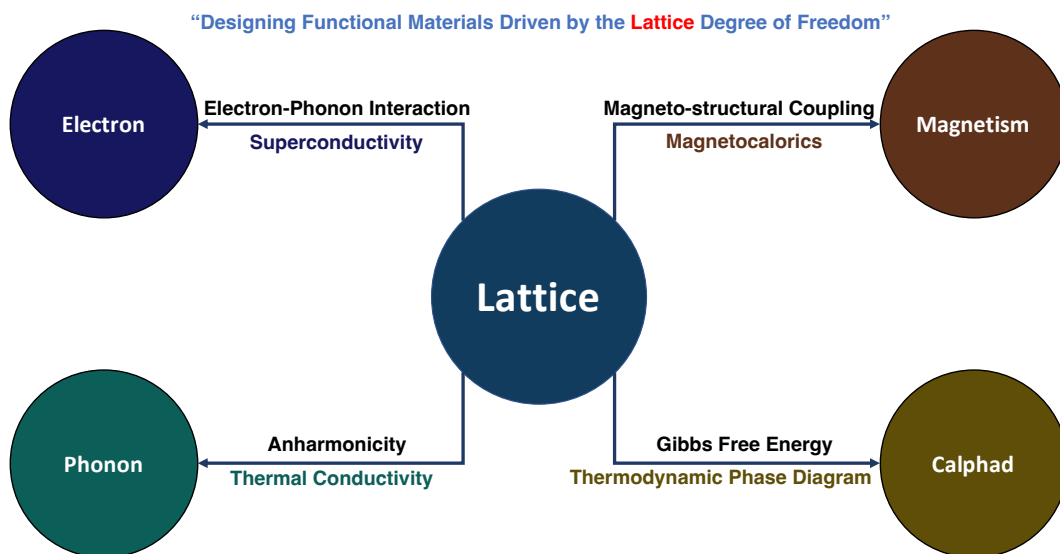
Figure 1.2.: Designing functional materials driven by the lattice degree of freedom.

1.4. Machine Learning Accelerates Materials Design

The rapid growth of data-driven machine learning approaches and algorithms in recent years has altered our anticipations of what computational simulations can achieve [4, 5, 34]. The speed of designing new materials can be accelerated faster by aiding Data-driven machine learning approaches [35]. Materials informatics methods are commonly based on three distinct elements: materials databases, a representation to quantitatively describe each material, and machine learning algorithms to discover patterns within the data or to predict the properties of new materials [36]. The combination of high-throughput calculation with machine learning approaches holds promise for unprecedented speed-up in the discovery of new functional materials [37]. The use of HTP DFT calculations for data collection has the great benefit of improving systematically and exponentially the size of the database, which is queried and fed into machine learning models to predict new materials with targeted properties [38].

Turning to the main topic of this thesis, namely "Designing Functional Materials Driven by Lattice Degree of Freedom", machine learning also can significantly aid us. Firstly, to consider the higher-order anharmonicity for phonon thermal transport, the calculations of finite displacement methods or density functional perturbation theory (DFPT) are cumbersome and time-consuming. Recently, people have used compressive sensing (CS) [39], a technique developed in the field of information science for recovering sparse solutions from incomplete data, to simultaneously determine which anharmonic terms are essential and to find their values [40, 41]. Hence, compressive sensing lattice dynamics (CSLD) can handle large, complex unit cells and strong anharmonicity, including materials with harmonically unstable phonon modes. Additionally, machine learning can be used to create interatomic potentials, which represent remarkable progress toward large length scale and long-time atomistic simulations beyond the reach of direct *ab initio* calculations. For instance, the machine learning interatomic potentials (MLIP) fitted from DFT calculations significantly improve the accuracy of potential functions used in MD simulations for calculating thermal transport for large and complex systems. Furthermore, the error associated with the so-obtained interatomic potential is within the chemical accuracy (1 kcal/mol), MLIP can hence be applied to study the phase transition in Zr [42], phase diagram optimization [43], and high entropy alloys [44]. The literature offers many examples that have been summarized in several reviews [34, 35] Last but not least, machine learning models of materials properties have seen a large number of applications targeted at the discovery of novel materials with promising properties. Recent studies have shown how machine-learned models can be aided to HTP studies to predict novel superconductors [45, 46, 47], and machine learning method can constructs CALPHAD database and optimize phase diagram automatically [48]. In summary, combining DFT calculations with interpretable machine learning is a very efficient methodology for studying and systematizing whole classes of materials and is easily extendable to other families of compounds or physical properties.

1.5. Organization of the Thesis

As introduced above, focusing on the materials design driven by the lattice degree of freedom, the rest parts of the thesis are organized as follows: The theoretical background will be documented in Chapter 2, with detailed discussion on the fundamental aspects for the methods used for the researches in this thesis. In Chapter 3, the workflows and selection of options and parameters involved in the numerical computations are discussed. The reason to do so is that a practical workflow is critical for calculating target properties efficiently and economically. In Chapter 4, we investigate how to design functional magnets for permanent magnet and magnetocaloric applications

based on HTP DFT. In Chapter 5, after considering phonon-phonon interactions, the thermal transport properties are calculated based on the Boltzmann transport equation (BTE) coupled, enabling us to design novel 2D materials for thermal management. In Chapter 6, a microscopic picture is established from the fundamental level of electronic structure, which explains the mechanism underlying the phonon anharmonicity in Ga-based 2D materials based on the buckled structures and lone-pair electrons. In Chapter 7, we investigate the role of the quartic anharmonicity in the lattice dynamics and thermal transport of the cubic $EuTiO_3$ by combining ab initio self-consistent phonon theory with compressive sensing techniques. In Chapter 8, after considering electron-phonon interactions, we design a new electron-phonon driven superconductor $GeNCr_3$. Finally, in Chapter 9, beyond 0 K, the finite temperature-dependent free energy of Fe-Sn is investigated, which is more realistic and practical for designing materials in the lab. Summary and outlook are placed at the end of the thesis as Chapter 10.

2. Theoretical Background

In this chapter, the fundamental aspects of the underlying theories for the applied methods will be thoroughly elucidated, in order to provide a physically sound basis for all the calculations done to understand and design novel materials with intriguing physical properties.

2.1. Quantum Many-body Problem

Solids generally consist of 10^{22} or more ions and 10^{23} or more electrons, with Coulomb interaction between each other. Hence, studying solid state materials is to solve quantum many-body problems. Correspondingly, the total non-relativistic Hamiltonian describing the behaviour of the constitute particles (*i.e.*, nuclei and electrons), from a quantum mechanics point of view, can be written as:

$$
\begin{aligned}
\hat{H}_{tot} &= \hat{T}_e + \hat{V}_{e-e} + \hat{V}_{ext} + \hat{T}_n + \hat{V}_{n-n} \\
&= -\sum_{i=1}^{N} \frac{\hbar^2}{2m_e} \nabla_i^2 + \frac{1}{2} \sum_{i \neq j} \frac{e^2}{|r_i - r_j|} - \sum_i^N \sum_I^M \frac{Z_n e^2}{|r_i - R_I|} - \sum_{I=1}^{M} \frac{\hbar^2}{2m_n} \nabla_I^2 \\
&\quad + \frac{1}{2} \sum_{I \neq J} \frac{Z_I Z_J e^2}{|R_i - R_j|},
\end{aligned}
\tag{2.1}
$$

where $m_{e(n)}$, $r(R)$, and ∇ denote the mass, position, and momentum operator of electrons (nuclei), respectively, Z stands for the atomic number, M and N denote the total number of ions and electrons, respectively; $\hat{T}_{e(n)}$ is the kinetic energy operator for electrons (nuclei), $\hat{V}_{e-e\ (n-n)}$ is the electron-electron (nuclei-nuclei) interaction, $\hat{V}_{ext}$ is the Coulomb interaction between the electrons and nuclei. Note that relativistic effect and spin-orbit coupling are not considered.

In principle, the ground state of the system can be found by solving the time-independent Schrödinger equation using this interacting Hamiltonian:

$$\hat{H}_{tot}(\boldsymbol{r}, \boldsymbol{R})\Psi(\boldsymbol{r}, \boldsymbol{R}) = E\Psi(\boldsymbol{r}, \boldsymbol{R}), \tag{2.2}$$

where $\Psi(\boldsymbol{r}, \boldsymbol{R})$ is the total wave function, which depends on both the positions of all electrons and the positions of all nuclei. Based on this fact, the many-body system is generally a superposition of combinations of single-particle states. Taking CO_2 as an example, the full wave function depends on $22 \times 3 = 66$ coordinates. As a result of the calculation, the wave function needs to be stored. Using a very poor grid of 10 points per coordinate, the storage would require 10^{66} memory units, which is an astronomically large number. There is no plausible way to store it in usable form. Hence, it is impossible to obtain the analytical solutions for these many-body problems directly. Reasonable approximations have been proposed in order to develop physically meaningful solutions for such complicated entangled quantum many-body problems.

2.1.1. Born-Oppenheimer Approximation

Considering that the mass ratio between an atomic nucleus and an electron is quite large, which is of the magnitude of 10^3. This means, generally speaking, the motion velocity of the nuclei is far less than the velocity of the electrons. When electrons move, the nuclei can be assumed as stationary. As a result, the motion of electrons and the motion of the nucleus can be considered as dynamically decoupled that do not affect each other, *i.e.*, the two subsystems can be regarded as moving adiabatically, namely, electrons follow adiabatically the motion of ions while ions move in an effective potential due to electrons. The separation of the nuclei and electrons into two individual mathematical problems is the Born-Oppenheimer approximation (adiabatic approximation). Then the electronic component of the Hamiltonian in the Schrödinger equation of system can be written as:

$$\hat{H}_{el} = -\sum_{i=1}^{N} \frac{\hbar^2}{2m_e}\nabla_i^2 + \frac{1}{2}\sum_{i \neq j} \frac{e^2}{|\boldsymbol{r}_i - \boldsymbol{r}_j|} - \sum_i^N \sum_I^M \frac{Z_n e^2}{|\boldsymbol{r}_i - \boldsymbol{R}_I|}. \tag{2.3}$$

Under the Born-Oppenheimer approximation, the Schrödinger equation of the electronic part of the Hamiltonian is:

$$\hat{H}_{el}(\boldsymbol{r}, \boldsymbol{R})\psi_i(\boldsymbol{r}, \boldsymbol{R}) = U_i(\boldsymbol{R})\psi_i(\boldsymbol{r}, \boldsymbol{R}), \tag{2.4}$$

where U_i are the electronic energy eigenvalues for the fixed nuclei, with $i = 0$ referring to the electronic ground state. Repeating this calculation for different $\boldsymbol{R}$, we obtain the form of the effective or mean-field potential for the electronic states on which the nuclei can move. These effective potentials are known as Born–Oppenheimer (adiabatic) potential-energy surfaces (PES).

For the nuclear degree of freedom, a Hamiltonian for the ith electronic PES is defined as

$$\hat{H}_{nuc,i} = -\sum_{I=1}^{M} \frac{\hbar^2}{2m_n} \nabla_I^2 + U_i(\boldsymbol{R}), \tag{2.5}$$

Note that the PES can be expanded according to:

$$U(\boldsymbol{R}) = U(\boldsymbol{R}_0) + \frac{\partial^2 U}{\partial \delta_1 \delta_2}, \tag{2.6}$$

where δ is a small displacement giving rise to the interatomic force constant giving rise to phonons.

After considering this approximation, is the situation better? The answer is *No*. The Schrödinger equation Eq. 2.3 is still a many-body problem, due to the electron-electron interaction.

2.1.2. Hartree-Fock Approximation

Hartree Equation: To solve the eigenvalue equations of Hamiltonian in Eq. 2.3, the Coulomb interactions among the electrons should be simplified. Similar to a strategy for approximating the interaction between electrons and nuclei, the interaction between electrons might also be approximated (there is no interaction between electrons). We then can transform the problem into a more straightforward problem of solving a single electron motion in a given potential field. In 1928, Hartree implemented a mean-field theory (MFT) method to transfer electron-electron interactions problem into a single electron motion equation problem [49]. The well-known Hartree wave function (Hartree product) is the product of the one-electron wave function, in which each single-electron wave function is only dependent on its spatial coordinate position,

$$\Psi(\boldsymbol{r}) = \psi_1(\boldsymbol{r}_1)\psi_2(\boldsymbol{r}_2)...\psi_i(\boldsymbol{r}_i)...\psi_N(\boldsymbol{r}_N). \tag{2.7}$$

Based on the Hartree approximation, Hartree equation can be obtained, namely, the Schrödinger equation for the single-electron wave function,

$$H_i \psi_i(\boldsymbol{r}) = E_i \psi_i(\boldsymbol{r}), \tag{2.8}$$

where the Hamiltonian for one electron can be written as:

$$H_i = -\frac{\hbar^2}{2m}\nabla^2 + \sum_{i'(\neq i)} \int dr' \frac{|\psi_{i'}(r')|^2}{|r_i - r_i'|} - \sum_j V_{e-n}(R_j). \tag{2.9}$$

The effective potential $\sum_{i'(\neq i)} \int dr' \frac{|\psi_{i'}(r')|^2}{|r_i - r_i'|}$ is originated from the interaction of one electron with the other electrons, formulated based on the charge density of the other electrons as an effective mean field potential. The second potential $\sum_j V_{e-n}(R_j)$ represents the motion of one electron in the potential field from the nuclei in lattice. Hence, the significant contribution of the Hartree equation is that the original N-electrons system, in which electrons interact with each other, is transformed into N independent sub-systems each with an effective mean-field potential averaged over the motion of other electrons. And each independent sub-system can be expressed by the same Schrödinger equation.

Hartree-Fock Equation: It is well known, that electrons are Fermions thus the corresponding many-body wave function should be antisymmetric with respect to the exchange of two particles. Apparently, such a requirement is not fulfilled by the ansatz wave function Eq. 2.7 in the Hartree approximation. The antisymmetry principle indicates that the wave function must alternate signs if two electrons exchange not only position but also spin, *i.e.*, any degree of freedom. However, the sign of the Hartree term in Eq. 2.9 does not change when exchanging two electrons. In 1929, Slater proposed the famous Slater determinant to overcome this serious drawback. To obtain a more reasonable approximation to the many-body wave function of a many-fermion system, N orthogonal normalized one-electron wave functions is applied to construct the N-electron wave function (including the spin of electrons σ) with the following determinant:

$$\Psi(\boldsymbol{r}_1\sigma_1, \boldsymbol{r}_2\sigma_2, ..., \boldsymbol{r}_n\sigma_n) = \frac{1}{\sqrt{N!}} \begin{vmatrix} \psi_1(\boldsymbol{r}_1, \sigma_1) & \psi_1(\boldsymbol{r}_2, \sigma_2) & \cdots & \psi_1(\boldsymbol{r}_N, \sigma_N) \\ \psi_2(\boldsymbol{r}_1, \sigma_1) & \psi_2(\boldsymbol{r}_2, \sigma_2) & \cdots & \psi_2(\boldsymbol{r}_N, \sigma_N) \\ \vdots & \vdots & \ddots & \vdots \\ \psi_N(\boldsymbol{r}_1, \sigma_1) & \psi_N(\boldsymbol{r}_2, \sigma_2) & \cdots & \psi_N(\boldsymbol{r}_N, \sigma_N) \end{vmatrix} \tag{2.10}$$

The Slater determinant implicitly builds in a physical description of electron exchange, which satisfies the Pauli exclusion principle. When two different electrons have the same one-electron wave function or same coordinates, the determinant equals zero, which means the total wave function $\Psi(\boldsymbol{r})$ is zero.

Correspondingly, the total Hamiltonian of the electrons system is:

$$
\begin{aligned}
E &= \langle \Psi | H | \Psi \rangle \\
&= \sum_{i,\sigma} \int dr \psi_i^{\sigma*}(\boldsymbol{r}) H_i \psi_i^\sigma(\boldsymbol{r}) + \frac{1}{2} \sum_{i,i'(\neq i),\sigma_i,\sigma_{i'}} \int dr dr' \frac{|\psi_i^{\sigma_i}(\boldsymbol{r})|^2 |\psi_{i'}^{\sigma_{i'}}(\boldsymbol{r}')|^2}{|\boldsymbol{r}-\boldsymbol{r}'|} \\
&\quad - \frac{1}{2} \sum_{i,i'(\neq i),\sigma_i,\sigma_{i'}} \int dr dr' \frac{\psi_i^{\sigma_i}(\boldsymbol{r}) \psi_i^{\sigma_i*}(\boldsymbol{r}') \psi_{i'}^{\sigma_{i'}}(\boldsymbol{r}') \psi_{i'}^{\sigma_{i'}*}(\boldsymbol{r})}{|\boldsymbol{r}-\boldsymbol{r}'|},
\end{aligned}
\tag{2.11}
$$

where the first term is the one body expectation values, the second term represents the direct (Hartree) interactions between electrons, the last term is the effective exchanging (Fock) interaction. Through the method of the Lagrange undetermined multipliers to do the variation on the Lagrangian and find the minimum of the functional concerning the system energy, we can get the following one electron Schrödinger equation which is the Hartree-Fock equation:

$$
\begin{aligned}
&\left[-\frac{\hbar^2}{2m} \nabla^2 - V_{e-n}(\boldsymbol{r}) + \sum_{i'(\neq i),\sigma} \int dr' \frac{|\psi_{i'}^\sigma(\boldsymbol{r}')|^2}{|\boldsymbol{r}-\boldsymbol{r}'|} \right. \\
&\left. - \sum_{i'(\neq i)} dr' \frac{\psi_{i'}^{\sigma_i*}(\boldsymbol{r}') \psi_i^\sigma(\boldsymbol{r}')}{|\boldsymbol{r}-\boldsymbol{r}'|} \right] \psi_i^\sigma(\boldsymbol{r}) = E_i^\sigma \psi_i^\sigma(\boldsymbol{r}).
\end{aligned}
\tag{2.12}
$$

Due to the presence of the exchange term, the equation needs to be solved using a nonlinear method, namely, the self-consistent field method. Hence, a Hartree-Fock calculation is an iterative procedure: 1. make an initial density; 2. construct a potential; 3. solve the Hartree-Fock equations and obtain a new density. 4. estimate whether the new density is converged with respect to the one in the previous iteration. If no, put new density into step 2. The process is repeated until the charge density and associated quantities are converged. In fact, at last, the limitation of the Hartree–Fock approximation should be mentioned. The energy calculated from the Hartree–Fock method is not the same as the energy for the true electron wave function. The reason is that the Hartree–Fock approximation does not consider the electron correlation.

2.2. Density Functional Theory

Compared with the Hartree-Fock approximation, the central tenet of DFT is to apply electron density instead of the wave function as the primary variable. This change can greatly reduce the degrees of the freedom for the N-electron system from $3N$ to 3. More clearly, the wave function of the N-electron system has $3N$ variables (each electron has three spatial variables), and the electron density is only a function of 3 variables. Therefore, dealing with functional dependent on the electron DFT holds both practically and conceptually advantages simultaneously, which is a more effective computational tool for calculating the ground state energy, electronic structures, and other physical properties of molecules and solids. The development of DFT has experienced the ongoing exploration and collision of the wisdom of several generations of scientists. In 1927, the Thomas-Fermi model was developed, statistical physics was used to describe the atomic charge distribution approximately, and system energy can be expressed as the functional of the electron density. However, this brilliant idea didn't raise much attention. In 1964, Hohenberg and Kohn published the milestone theoretical work on DFT. More and more scientists worked in this field. The remarkable achievements of local density approximation (LDA) and generalized-gradient approximation (GGA) functionals within the Kohn-Sham formalism have raised widespread attention.

2.2.1. Hohenberg-Kohn Theorems

In the Hohenberg and Kohn's milestone paper [50], it is argued that the total energy of the ground state of inhomogeneous electron gas could be obtained by introducing a generic functional (independent of the external potential $V(\boldsymbol{r})$) of electron density $n(\boldsymbol{r})$. The Hohenberg-Kohn theorems include two parts, which established the theoretical basis for the DFT.

Theorem I: The external potential $V(\boldsymbol{r})$ is uniquely determined by the functional of the ground state charge density $n(\boldsymbol{r})$.

Proof of Theorem I

Now, we suppose that there are two different external potentials $V_{ext}^{(1)}$ and $V_{ext}^{(2)}$, which differ by more than a constant, leading to the same ground state density $n(\boldsymbol{r})$. Obviously, the two external potentials belong to distinct Hamiltonians, $\hat{H}^{(1)}$ and $\hat{H}^{(2)}$. Hence, different Hamiltonians have different ground state wave functions $\Psi^{(1)}$ and $\Psi^{(2)}$. Since $\Psi^{(1)} \neq \Psi^{(2)}$, $\Psi^{(2)}$ is not the ground state wave function of $\hat{H}^{(1)}$, it follows that

$$E^{(1)} = \left\langle \Psi^{(1)} | H^{(1)} | \Psi^{(1)} \right\rangle < \left\langle \Psi^{(2)} | H^{(1)} | \Psi^{(2)} \right\rangle. \tag{2.13}$$

Here we can assume the ground state is not degenerated, the last term in Eq. 2.13 can be rewritten as:

$$\begin{aligned}
\left\langle \Psi^{(2)} | H^{(1)} | \Psi^{(2)} \right\rangle &= \left\langle \Psi^{(2)} | H^{(2)} | \Psi^{(2)} \right\rangle + \left\langle \Psi^{(2)} | H^{(1)} - H^{(2)} | \Psi^{(2)} \right\rangle \\
&= E^{(2)} + \int d^3 r [V_{ext}^{(1)}(\boldsymbol{r}) - V_{ext}^{(2)}(\boldsymbol{r})] n_0(\boldsymbol{r}).
\end{aligned} \tag{2.14}$$

Combining Eq. 2.13 and Eq. 2.14, we obtain

$$E^{(1)} < E^{(2)} + \int d^3 r [V_{ext}^{(1)}(\boldsymbol{r}) - V_{ext}^{(2)}(\boldsymbol{r})] n_0(\boldsymbol{r}) \tag{2.15}$$

On the other hand, we can get $E^{(2)}$ similarly:

$$E^{(2)} < E^{(1)} + \int d^3 r [V_{ext}^{(2)}(\boldsymbol{r}) - V_{ext}^{(1)}(\boldsymbol{r})] n_0(\boldsymbol{r}) \tag{2.16}$$

After that, adding together Eq. 2.15 and Eq. 2.16, we approach at the contradictory inequality

$$E^{(1)} + E^{(2)} < E^{(1)} + E^{(2)}. \tag{2.17}$$

Therefore, there cannot be two different external potentials differing by more than a constant which give rise to the same non-degenerate ground state charge density. That is, there is a one-to-one mapping between the ground state charge density and external potential.

Theorem II: The total energy $E[n]$ in terms of the density $n(\boldsymbol{r})$ can be obtained variationally by defining a universal functional $F_{HK}[n]$, valid for any external potential $V_{ext}(\boldsymbol{r})$. For any particular $V_{ext}(\boldsymbol{r})$, the exact ground state energy of the system is the global minimum value of this functional, and the density $n(\boldsymbol{r})$ that minimizes the functional is the exact ground state density $n_0(\boldsymbol{r})$.

Proof of Theorem II Since all properties of a multi-electron system can be uniquely determined if $n(\boldsymbol{r})$ is specified, the total energy functional can be regarded as a functional of $n(\boldsymbol{r})$

$$E_{HK}[n] = T[n] + E_{int}[n] + \int d^3 r V_{ext}(\boldsymbol{r})n(\boldsymbol{r}) + E_{II}$$

$$\equiv F_{HK}[n] + \int d^3 r V_{ext}(\boldsymbol{r})n(\boldsymbol{r}) + E_{II}, \tag{2.18}$$

where E_{II} represents the interaction energy of the nuclei. In Eq. 2.18, the functional $F_{HK}[n] = T[n] + E_{int}[n]$ consist of all internal energies, kinetic and potential, of the multi-electron system.

Now we consider a system with the ground state density $n^{(1)}(\boldsymbol{r})$, which corresponds to external potential $V_{ext}^{(1)}(\boldsymbol{r})$ and wave function $\Psi^{(1)}$. The energy can be then written as:

$$E^{(1)} = E_{HK}[n^{(1)}] = \left\langle \Psi^{(1)} | H^{(1)} | \Psi^{(1)} \right\rangle. \tag{2.19}$$

After that, a different density $n^{(2)}(\boldsymbol{r})$ corresponding to a different wave function $\Psi^{(2)}$ is assumed. Then the energy $E^{(2)}$ is greater than $E^{(1)}$, since

$$E^{(1)} = \left\langle \Psi^{(1)} | H^{(1)} | \Psi^{(1)} \right\rangle < \left\langle \Psi^{(2)} | H^{(1)} | \Psi^{(2)} \right\rangle = E^{(2)}. \tag{2.20}$$

Thus the energy from Eq. 2.18 in term of the Hohenberg-Kohn functional evaluated for the correct ground state density $n_0(\boldsymbol{r})$ is the lowest one with respect to any other density $n(\boldsymbol{r})$. That is, there is a one-to-one mapping between the charge density and the ground state energy.

2.2.2. Kohn-Sham Equations

Following the discussion above, the Hohenberg-Kohn theorems provide the feasibility of implementing the electron density as a basic variable to calculate the ground-state properties. However, the explicit form of the ground state energy functional has not been specified thus the Hohenberg-Kohn theorems alone cannot be implemented to perform calculations, thought it is physically exact. In 1965, Kohn and Sham proposed [51]: *to replace the original many-body problem by an auxiliary independent-particle problem.* That means, in principle, we can use independent-particle methods to solve for the exact calculations of properties of many-body systems. Namely, interacting systems can be projected to the non-interacting systems with the same densities, which provides a operational formulation of the missing Hohenberg-Kohn functional which can be then solved based on the variational principles.

For non-interacting systems, only the kinetic energy $T[n(\boldsymbol{r})]$ contributes to the universal F-functional: $F^0[n(\boldsymbol{r})] = T[n(\boldsymbol{r})]$ (the superscript zero is for non-interacting systems). Hence, the F-functional of the interacting systems is decomposed by using the formal Kohn-Sham logic as:

$$F[n(\boldsymbol{r})] = T[n(\boldsymbol{r})] + U_H[n(\boldsymbol{r})] + E_{XC}[n(\boldsymbol{r})], \qquad (2.21)$$

in which $U_H[n(\boldsymbol{r})]$ denotes the electrostatic interaction, which is well defined for all densities as:

$$U_H[n(\boldsymbol{r})] = \frac{1}{2} \int \int \frac{n(\boldsymbol{r})n(\boldsymbol{r}')}{|\boldsymbol{r} - \boldsymbol{r}'|} dr dr'. \qquad (2.22)$$

The kinetic energy in Eq. 2.21 is taken to be that of the non-interacting homogeneous systems which have the same charge density as the interacting non-homogeneous systems. The true kinetic energy difference between interacting and non-interacting systems with same densities will be incorporated together with the other interactions beyond the electrostatic one in the term $E_{XC}[n(\boldsymbol{r})]$.

Furthermore, the charge density can be formulated using the non-interacting wave function ansatz as

$$n(\boldsymbol{r}) = \sum_i n_i |\phi_i(\boldsymbol{r})|^2, \qquad (2.23)$$

$$\langle \phi_i | \phi_j \rangle = \delta_{ij}, \qquad (2.24)$$

the kinetic energy $T[n(\boldsymbol{r})]$ can be defined explicitly as:

$$T[n] = \min_{n_i, \phi_i} \left\{ \sum_i \left\langle \phi_i \left| -\frac{\partial^2}{\partial \boldsymbol{r}^2} \right| \phi_i \right\rangle \right\}, n(\boldsymbol{r}) = \sum_i n_i(\boldsymbol{r}) |\phi_i(\boldsymbol{r})|^2, \langle \phi_i | \phi_j \rangle = \delta_{ij}. \qquad (2.25)$$

Therefore, the ground state energy can be evaluated by

$$E[v_{ext}, n] = \min_{n_i, \phi_i} \left\{ T[\sum_i n_i |\phi_i|^2] + U_H[\sum_i n_i |\phi_i|^2] + E_{XC}[\sum_i n_i |\phi_i|^2] - \langle n | V_{ext} \rangle \right\},$$
$$n(\boldsymbol{r}) = \sum_i n_i(\boldsymbol{r}) |\phi_i(\boldsymbol{r})|^2, \langle \phi_i | \phi_j \rangle = \delta_{ij}. \qquad (2.26)$$

The exchange-correlation term $E_{XC}[n(\mathbf{r})]$ collect all many-body effects of exchange and including also the difference of the kinetic energies. Performing the variational principle, the single-particle-like Schrödinger equation can be obtained

$$[-\frac{1}{2}\boldsymbol{\nabla}^2 + V_{KS}(\mathbf{r})]\phi_j(\mathbf{r}) = \varepsilon_j\phi_j(\mathbf{r}), \tag{2.27}$$

where $\phi_j(\mathbf{r})$ represents the Kohn-Sham orbital, namely one-electron wave function of the fictitious Kohn-Sham non-interacting system. And ε_j is the corresponding Kohn-Sham eigenvalue. In Eq. 2.27, $V_{KS}(\mathbf{r})$ can be expressed as

$$V_{KS}(\mathbf{r}) = v_{ext}(\mathbf{r}) + V_H(\mathbf{r}) + V_{XC}(\mathbf{r}), \tag{2.28}$$

which means the electron moves in the effective Kohn-Sham potential. $v_{ext}(\mathbf{r})$ is for the external potential, $V_H(\mathbf{r})$ is the Hartree potential, expressed as:

$$V_H(\mathbf{r}) = \frac{\partial U[n]}{\partial n(\mathbf{r})} = \int \frac{n(\mathbf{r}')}{|\mathbf{r} - \mathbf{r}'|}d\mathbf{r}'. \tag{2.29}$$

As well, the exchange-correlation potential is

$$V_{XC}(\mathbf{r}) = \frac{\partial E_{XC}[n]}{\partial n(\mathbf{r})}. \tag{2.30}$$

After the discussion above, we get the famous Kohn-Sham equation. The importance of this equation is that it can simplify the many-body interacting problem into a non-interacting problem of a single electron. Since the exchange-correlation functional is generally orbital-dependent, we can solve the Kohn-Sham equation self-consistently, as shown in Figure 2.1. From the solution, we can obtain the charge density constructed by the single electron wave function, which is the ground state charge density of the interaction systems. Notably, the only difference between the Kohn-Sham equation and the Hartree equation is that the effective potential in the single-electron equation includes an extra exchange-correlation potential, which is yet unknown. Till now, combining the Hohenberg-Kohn theorems and Kohn-Sham equation, an exact formalism of DFT can be obtained, which provides an operational computational framework to solve the many-body problem of interacting electrons. The only pending issue is that the exact form of the exchange correlation functional is not available, leading to many different flavors of approximations as detailed below.
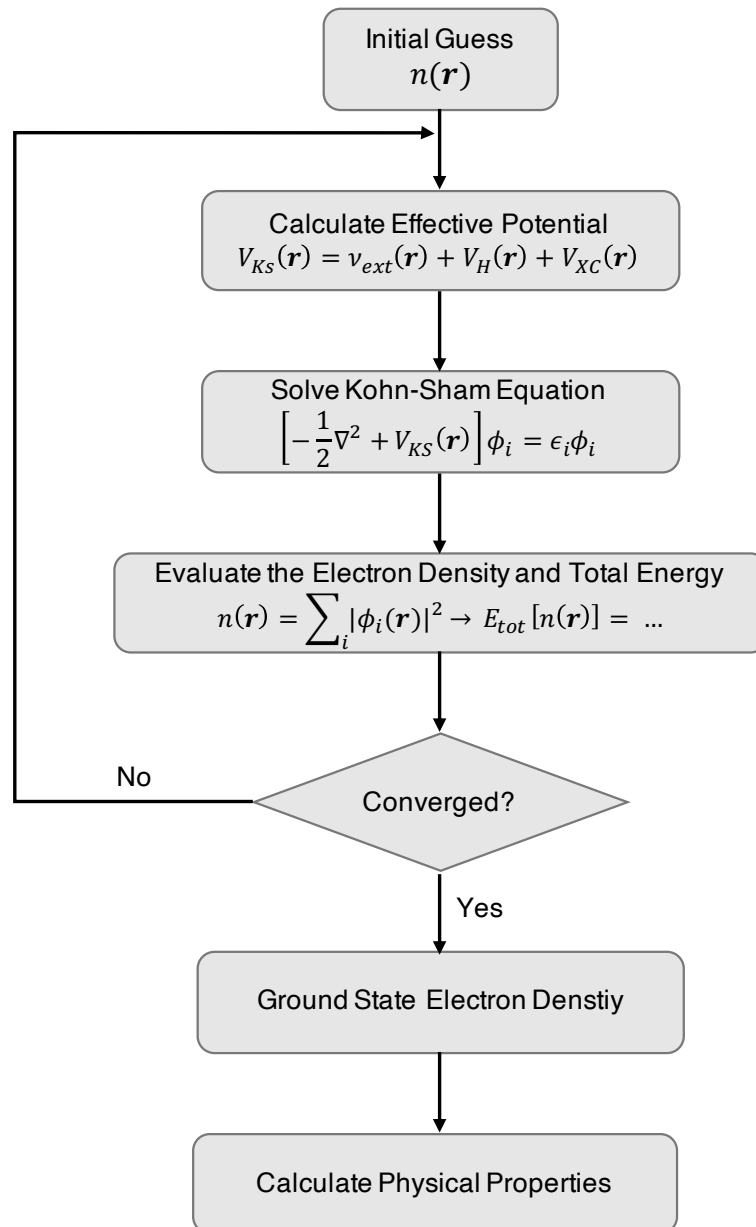
Figure 2.1.: A flow chart of the self-consistent method to procedure Kohn-Sham equations for normal DFT calculations.

2.2.3. Exchange Correlation Functional

Turning now to the exchange correlation energy, it is the crucial quantity in the Kohn-Sham equation, which is expressed as a functional of the density $E_{XC}[n]$ in Eq. 2.26. The choice of the proper exchange-correlation functional is critical, which determines the accuracy of the results calculated from DFT. In principle, the exchange-correlation functional including all the unknown quantum mechanical effects can be decomposed in two parts, namely the exchange part and the correlation part:

$$E_{XC}[n] = E_X[n] + E_C[n]. \tag{2.31}$$

In fact, the true form of the exchange-correlation functional is impossible to obtain. Hence, some further approximations are used to approach the exchange-correlation functional, such as a local, semi-local, or non-local functional of the density. Among that, the local density approximation (LDA) and the generalized gradient approximation (GGA) are widely used.

Local Density Approximation: At the time, in Kohn and Sham's seminal paper [51], they indicated that solids can be treated as close to the limit of the homogeneous electron gas. Meanwhile, a multi-electron system can be separated into many smaller subsystems, and the each local subsystem can be considered as a homogeneous system. Based on these ideas, hence, they proposed the concept of LDA, and more generally the local spin density approximation (LSDA) when spin-polarization is considered. L(S)DA assumes that an inhomogeneous electrons system can be divided into many small enough volume element $\mathrm{d}r$, treated as the non-interacting homogeneous electron gas, hence the exchange correlation energy is simply an integral over all space with the exchange correlation energy density at each element. Now, the exchange-correlation functional can be approximated as:

$$\begin{aligned} E_{XC}[n] &\approx E_{XC}^{LSDA}[n] \\ &= \int \mathrm{d}^3 r\, n(\boldsymbol{r}) \varepsilon_{XC}^{hom}(n(\boldsymbol{r}), \zeta(\boldsymbol{r})), \end{aligned} \tag{2.32}$$

where $\varepsilon_{XC}^{hom}(n(\boldsymbol{r}), \zeta(\boldsymbol{r}))$ is for the the exchange-correlation energy per electron in homogeneous electron gas. $\zeta(\boldsymbol{r})$ denotes the degree of spin-polarization. So introducing spin densities (spin-up density $n(+)$, spin-down density $n(-)$, and total electron density n), the $\zeta(\boldsymbol{r})$ is expressed as

$$\zeta(\boldsymbol{r}) = \frac{n(+) - n(-)}{n}. \tag{2.33}$$

The corresponding exchange-correlation effective potential can also be obtained by functional derivation:

$$V_{XC}^{LSDA}(\boldsymbol{r},\pm) = \frac{\delta E_{XC}^{LSDA}}{\delta n(\boldsymbol{r},\pm)} = \frac{\partial}{\partial n_\pm}[n\varepsilon_{XC}(n,\zeta)]. \qquad (2.34)$$

When the system is non-polarized, $\zeta = 0$. In summary, the L(S)DA can give good results in metallic systems because the homogeneous electron gas show the metallic system behaviour. However, L(S)DA tends to underestimate the exchange energy and overestimate the binding energies, resulting in too short bond lengths. Despite these deficiencies, several L(S)DA exchange correlation functionals, such as VWN [52], PZ81 [53], CP [54], PW92 [55], are widely applied in modern DFT calculations.

Generalized Gradient Approximation: To get more close to the real system and reduce the error caused by the inhomogeneous charge density distribution in space, next step is to go beyond the LDA based on the homogeneous electron gas model, to consider the electron density gradient in the energy density functional. Such an approximation is the so called GGA, in which the exchange-correlation functional is made by a functional of both the electron density $n(\boldsymbol{r})$ and the corresponding gradient $\nabla n(\boldsymbol{r})$. Therefore, GGA is mainly used for reflecting the inhomogeneity of the electron gas of real system, which yields

$$E_{XC}^{GGA}[n] = \int d^3r\, n(\boldsymbol{r})\varepsilon_{XC}^{hom}[n(\boldsymbol{r})]F_{XC}[n(\boldsymbol{r}),\nabla n(\boldsymbol{r})]. \qquad (2.35)$$

$F_{XC}[n(\boldsymbol{r}),\nabla n(\boldsymbol{r})]$ represents the enhancement factor that modifies the LDA exchange correlation potentials, and is dimensionless. Because of the enhancement factor is not a unique function of the electron density, there are various existing methods to the GGA exchange correlation functional. For instance, people fitted the experimental data to obtain the functional with empirical parameters, like B88 [56], FT98 [57]. Or directly obtaining from first principles calculations, the functional is without any empirical parameters, such as B86 [58], PBE [59]. At present, the most widely used GGA form is PBE(Perdew-Burke-Ernzerhof) [59], which can be written as:

$$\begin{aligned}
E_{XC}^{PBE}[n] &= \int d^3r\, n(\boldsymbol{r})\varepsilon_{XC}^{hom}[n(\boldsymbol{r})]F_{XC}[n(\boldsymbol{r}),\nabla n(\boldsymbol{r})] \\
&= E_X^{PBE}[n] + E_C^{PBE}[n],
\end{aligned} \qquad (2.36)$$

where the exchange term is

$$E_X^{PBE}[n] = \int d^3 rn(\boldsymbol{r}) \varepsilon_X^{hom}[n(\boldsymbol{r})] F_X^{PBE}(s)$$

$$F_X^{PBE}(s) = [1 + k - \frac{k}{1 + \beta \pi^2 s(\boldsymbol{r})^2 / 3k}]$$

$$s(\boldsymbol{r}) = \frac{|\nabla n(\boldsymbol{r})|}{2n(\boldsymbol{r})k_F(\boldsymbol{r})}$$

$$k = 0.804$$

$$\beta = 0.066725$$

(2.37)

and the correlation term is

$$E_C^{PBE}[n] = \int d^3 rn(\boldsymbol{r})[\varepsilon_C^{hom}[n(\boldsymbol{r})] + H^{PBE}(r_s, t)]$$

$$H_X^{PBE}(r_s, t) = \frac{\beta^2}{2\alpha} ln(1 + \frac{2\alpha}{\beta} \frac{t^2 + At^4}{1 + At^2 + A^2 t^4})$$

$$A = \frac{2\alpha}{\beta e^{\frac{-2\alpha \varepsilon_C^{hom}(n)}{\beta^2}} - 1}$$

$$t = \frac{|\nabla n(\boldsymbol{r})|}{2k_s n}$$

$$k_s = \sqrt{4k_F / \pi}$$

$$\alpha = 0.0716$$

$$\beta = 0.066725$$

(2.38)

At last, LDA and GGA successfully describe the electrons of s and p orbitals. However, s and p orbitals are non-localized, and there are significant deviations in describing the strongly correlated electrons in partially occupied d and f orbitals with LDA and GGA. One problem in practical calculations is that both LDA and GGA will underestimate the band gap of semiconductors. This is because the band gap is a property of the excited states, marginally related to the d/f correlation problem. Thus, it is necessary to modify LDA and GGA in calculating d and f electrons. One correcting method is to introduce a strong interaction in the energy expression, and the interaction origins from the inner electron shell of an atom. Correspondingly, we can describe the $d - d$ electron Coulomb interaction more precisely, similar to the Hubbard model's form. This correcting method is also known as LDA(GGA)+U.

2.2.4. Spin-polarized Density Functional Theory

The above discussion about DFT mainly focuses on how to perform calculations on non-magnetic systems. However, magnetism in solids is a fascinating topic in physics and materials science. To get insight into magnetic materials, the current DFT should be extended in the spin-polarized systems [60, 61, 62]. In this regard, the functional is formulated with respect to the spin density matrix ρ, which can be written

$$\rho_{\alpha\beta} = n(\boldsymbol{r})\delta\alpha\beta + \boldsymbol{m}(\boldsymbol{r}) \cdot \boldsymbol{\sigma}_{\alpha\beta}, \tag{2.39}$$

where $n(\boldsymbol{r})$ is the electron density, $\boldsymbol{m}(\boldsymbol{r})$ is the magnetization density originating from the spin polarization, σ is the Pauli matrices, and α and β are corresponding to the spin directions. Now, we expand the spin density formula by using $\boldsymbol{m}(\boldsymbol{r}) \cdot \boldsymbol{\sigma} = m_x \sigma_x + m_y \sigma_y + m_z \sigma_z$, the charge density then can be written in a matrix form as:

$$\rho(\boldsymbol{r}) = \begin{bmatrix} n(\boldsymbol{r}) + m_z(\boldsymbol{r}) & m_x(\boldsymbol{r}) - im_y(\boldsymbol{r}) \\ m_x(\boldsymbol{r}) + im_y(\boldsymbol{r}) & n(\boldsymbol{r}) - m_z(\boldsymbol{r}) \end{bmatrix} \tag{2.40}$$

In the spin-polarized framework, the orbitals are spinors given by:

$$\Psi_i(\boldsymbol{r}) = \begin{bmatrix} \psi_{i\alpha}(\boldsymbol{r}) \\ \psi_{i\beta}(\boldsymbol{r}) \end{bmatrix} \tag{2.41}$$

Hence, the charge density or spin-polarized charge density in terms of the spinors is given by:

$$\rho(\boldsymbol{r}) = \begin{bmatrix} \psi_{i\alpha}(\boldsymbol{r})\psi_{i\alpha}^*(\boldsymbol{r}) & \psi_{i\alpha}(\boldsymbol{r})\psi_{i\beta}^*(\boldsymbol{r}) \\ \psi_{i\beta}(\boldsymbol{r})\psi_{i\alpha}^*(\boldsymbol{r}) & \psi_{i\beta}(\boldsymbol{r})\psi_{i\beta}^*(\boldsymbol{r}) \end{bmatrix} \tag{2.42}$$

The magnetic ground state is determined by the spin orientation. Specifically, if there is a common spin quantization axis, the material exhibits a collinear nature, whereas, in its absence, it is non-collinear.

For a collinear magnetic material, note that the non-diagonal terms of the spin density matrix of Eq. 2.40 disappear, hence the charge and magnetization density read:

$$n(\boldsymbol{r}) = \sum_i \Psi_i^\dagger(\boldsymbol{r}) \boldsymbol{I} \Psi_i(\boldsymbol{r})$$

$$\boldsymbol{m}(\boldsymbol{r}) = \mu_B \sum_i \Psi_i^\dagger(\boldsymbol{r}) \boldsymbol{\sigma} \Psi_i(\boldsymbol{r}), \tag{2.43}$$

in which $\boldsymbol{I}$ is the identity matrix. Same as obtaining the energy functional in the non-spin-polarized system, the spin-polarized energy functional is defined as:

$$\begin{aligned} E_{KS}[\boldsymbol{\rho}] &= T[\boldsymbol{\rho}] + E_H[\boldsymbol{\rho}] + E_{ext}[\boldsymbol{\rho}] + E_{XC}[\boldsymbol{\rho}] \\ &= T[\boldsymbol{\rho}] + \int d\boldsymbol{r} d\boldsymbol{r}' \frac{\rho(\boldsymbol{r})\rho(\boldsymbol{r}')}{|\boldsymbol{r}-\boldsymbol{r}'|} + \sum_{\alpha\beta} \int d\boldsymbol{r} V_{ext}^{\alpha\beta}(\boldsymbol{r}) \rho_{\alpha\beta}(\boldsymbol{r}) + E_{XC}[\boldsymbol{\rho}] \end{aligned} \tag{2.44}$$

and then the spin-dependent Kohn-Sham equations is

$$\sum_\beta [-\delta_{\alpha\beta} \frac{1}{2} \nabla^2 + V_{ext}^{\alpha\beta}(\boldsymbol{r}) + \delta_{\alpha\beta} \int \frac{\rho(\boldsymbol{r}')}{|\boldsymbol{r}-\boldsymbol{r}'|} d\boldsymbol{r}' + V_{XC}^{\alpha\beta}(\boldsymbol{r})] \psi_{i\beta}(\boldsymbol{r}) = \delta_{\alpha\beta} \psi_{i\beta}(\boldsymbol{r}), \tag{2.45}$$

and

$$V_{XC}^{\alpha\beta}(\boldsymbol{r}) = \frac{\delta E_{XC}[\boldsymbol{\rho}]}{\delta \rho_{\alpha\beta}(\boldsymbol{r})}. \tag{2.46}$$

Further, the non-collinear magnetic DFT calculations can be realized by substituting a 3D charge density matrix into the spin-polarized calculations scheme, more details can be found in Ref. [63].

2.2.5. Relativistic Effect

One important effect due to the full relativistic expansion is spin-orbit coupling (SOC) [64]. It is directly related to several interesting spintronics effects such as the magnetocrystalline anisotropy and the spin Hall effect. The well-known four-component formulated Dirac equation generalizes the Schödinger equation in a relativistically covariant form

$$i\hbar \frac{\partial}{\partial t} \Psi = (c\boldsymbol{\alpha} \cdot \boldsymbol{p} + \beta mc^2) \psi = H^D \Psi, \tag{2.47}$$

where Ψ represents a four-component single-particle wave function. $p = -i\hbar\nabla$ is the momentum operator. And the (4×4) matrices α_i and β is expressed in terms of the Pauli matrices

$$\alpha_i = \begin{pmatrix} 0 & \sigma_i \\ \sigma_i & 0 \end{pmatrix}, \quad \beta = \begin{pmatrix} 1 & 0 \\ 0 & -1 \end{pmatrix}, \tag{2.48}$$

where σ_i are the (2×2) Pauli spin matrices

$$\sigma_1 = \begin{pmatrix} 0 & 1 \\ 1 & 0 \end{pmatrix}, \quad \sigma_2 = \begin{pmatrix} 0 & -i \\ i & 0 \end{pmatrix}, \quad \sigma_3 = \begin{pmatrix} 1 & 0 \\ 0 & -1 \end{pmatrix}, \tag{2.49}$$

and the unit entries of β are (2×2) unit matrices.

Assuming the electronmagnetimetic field is described by the scalar potential φ and the vector potential $\boldsymbol{A}$, the momentum can be obtained by minimal substitution $p^\mu \rightarrow \boldsymbol{p} - q\boldsymbol{A}$.

Firstly, considering only the effect of time-independent vector potential $q\boldsymbol{A}$, the stationary Dirac equation for one electron can be described as

$$H\Psi = E\Psi = [c\boldsymbol{\alpha} \cdot (\boldsymbol{p} + e\boldsymbol{A}) + \beta mc^2]\Psi \tag{2.50}$$

It is convenient to write the solution in the form

$$\Psi = \begin{bmatrix} \phi \\ \chi \end{bmatrix} \tag{2.51}$$

where ϕ and χ are time-independent two-component spinors describing the spatial and spin-$\frac{1}{2}$ degree of freedom. And for electrons, ϕ is the large component and χ is the small component. Then, the Dirac equation transforms a set of coupled equations for ϕ and χ

$$c\boldsymbol{\sigma} \cdot (\boldsymbol{p} + e\boldsymbol{A})\chi + mc^2\phi = E\phi, \tag{2.52}$$

$$c\boldsymbol{\sigma} \cdot (\boldsymbol{p} + e\boldsymbol{A})\phi - mc^2\chi = E\chi, \tag{2.53}$$

Define $W = E - mc^2$, is the energy shifting over the rest mass energy. In the non-relativistic limit, $W \ll mc^2$.

Then,

$$\chi = \frac{c\boldsymbol{\sigma} \cdot (\boldsymbol{p} + e\boldsymbol{A})}{2mc^2 + W}\phi \approx \frac{c\boldsymbol{\sigma} \cdot (\boldsymbol{p} - e\boldsymbol{A})}{2mc^2}\phi, \tag{2.54}$$

next,

$$[\frac{1}{2m}(\boldsymbol{p} + e\boldsymbol{A}))^2 - \frac{e\hbar}{2m}\boldsymbol{\sigma} \cdot (\boldsymbol{\nabla} \times \boldsymbol{A})]\phi = W\phi. \tag{2.55}$$

AS one known, $\boldsymbol{\nabla} \times \boldsymbol{A} = \boldsymbol{B}$, so $\frac{e\hbar}{2m}\boldsymbol{\sigma} \cdot (\boldsymbol{\nabla} \times \boldsymbol{A})$ is the Zeeman splitting induced by the magnetic field.

Now, for the time-independent scalar potential $V = -e\varphi$. The stationary Dirac equation is written as

$$H\Psi = E\Psi = [c\boldsymbol{\sigma} \cdot \boldsymbol{p} + \beta mc^2 + V]\Psi. \tag{2.56}$$

Then,

$$c\boldsymbol{\sigma} \cdot \boldsymbol{p}\chi + (V + mc^2)\phi = E\phi, \tag{2.57}$$

$$c\boldsymbol{\sigma} \cdot \boldsymbol{p}\phi + (V - mc^2)\chi = E\chi, \tag{2.58}$$

so we get

$$\chi = \frac{c\boldsymbol{\sigma} \cdot \boldsymbol{p}}{E - V + mc^2}\phi. \tag{2.59}$$

Same as vector potential case, we define $W = E - mc^2$, then

$$\begin{aligned}
\frac{1}{E - V + mc^2} &= \frac{1}{E - V + 2mc^2} \\
&= \frac{1}{2mc^2}(1 + \frac{W - V}{2mc^2})^{-1} \\
&\approx \frac{1}{2mc^2}(1 - \frac{W - V}{2mc^2}).
\end{aligned} \tag{2.60}$$

Combining Eq. 2.59 and Eq. 2.60, we get

$$\chi = c\boldsymbol{\sigma}\cdot\boldsymbol{p}\frac{1}{2mc^2}(1-\frac{W-V}{2mc^2})\phi. \tag{2.61}$$

Therefore,

$$(\frac{\boldsymbol{p}^2}{2m}+V-\frac{\boldsymbol{p}^4}{8m^3c^2}-\frac{i\boldsymbol{\sigma}\cdot\boldsymbol{p}\times[\boldsymbol{p},V]}{4m^2c^2}-\frac{\boldsymbol{p}\times[\boldsymbol{p},V]}{4m^2c^2})\phi = W\phi, \tag{2.62}$$

where,

$$[\boldsymbol{p},V(\boldsymbol{r})]\phi = -i\hbar(\boldsymbol{\nabla}V(\boldsymbol{r}))\phi. \tag{2.63}$$

If we consider the relativistic effect as perturbation, we can decompose the Dirac Hamiltonian into two independent parts as

$$H^D\Psi = W\Psi + H_{SOC} = \Psi = E\Psi, \tag{2.64}$$

where W represents non-relativistic term and H_{SOC} denotes the relativistic or spin-orbit coupling effect part. Then, spin-orbit coupling term is expressed as

$$\begin{aligned} H_{SOC} &= -\frac{i\boldsymbol{\sigma}\cdot\boldsymbol{p}\times[\boldsymbol{p},V]}{4m^2c^2} \\ &= -\frac{\hbar\boldsymbol{\nabla}V}{4m^2c^2}\boldsymbol{\sigma}\cdot\boldsymbol{p}\times\boldsymbol{r} \\ &\approx \xi(r)\boldsymbol{\sigma}\cdot\boldsymbol{l}, \end{aligned} \tag{2.65}$$

where $\boldsymbol{\nabla}V(\boldsymbol{r})$ represents the electrostatic potential induced by the electron. The electrostatic potential always has strong effect in the core regions. Thus SOC term can be regarded as the summation of the local contribution $\xi(r)\boldsymbol{\sigma}\cdot\boldsymbol{l}$. The SOC constant ξ denotes a radial function as:

$$\xi(r) = \frac{-Ze\hbar^2}{2m^2c^2}\frac{1}{r}\frac{d\phi}{dr}. \tag{2.66}$$

Using the Dirac theory, the magnetism or spin can be explained for electrons physically [65]. First of all, the magnetization connects spin with the Maxwell equation. Then, the spin-orbit interaction is the origin of the magnetocrystalline anisotropy. The former concept is to construct the modern spin-density-functional theory.

2.3. Phonon Theory

When people achieve a lot of developments in the computational electronic structure, the atomic motions are meanwhile explored by using first-principles methods. The fundamental question concerning nuclei dynamics is: how does the system respond to forces induced by atomic displacements? Before answering this question, we will discuss the phonon theory in this section. Phonons are bosons, propagating as lattice vibrational waves through crystalline solids, as shown in Table 2.5, which are collective excitations of all atoms. In other words, the phonons are the quantum mechanical description of elementary vibrational motions in which atoms uniformly oscillate at a single frequency [66]. In classical mechanics, this means a normal mode of vibration. While normal modes are wave-like phenomena in classical mechanics, phonons show particle-like properties, treated as quasi-particle in quantum mechanics. Lattice (phonon) conduction driven heat transfer in solids is proportional to the lattice (phonon) thermal conductivity tensor $\boldsymbol{K}_p$, namely $\boldsymbol{q}_k = \boldsymbol{K}_p \cdot \nabla T$. And the vibrational (phonon) specific heat capacity determines the sensible heat storage, as well the vibrational free energy makes a dominant contribution to the total free energy in most cases. Hence, the phonon theory is one of the crucial concepts in condensed matter physics. In this section, we will briefly discuss the fundamental concepts in the phonon theory, including harmonic approximation and lattice specific heat capacity.

2.3.1. Normal Modes

A normal mode is a pattern of motion in which all parts of the system move sinusoidally with the fixed frequency and with a fixed phase relation. Normal modes are essential because any arbitrary lattice vibration can be considered as a superposition of these elementary vibration modes. Firstly, assume a system within n point-mass-like particles interconnected by harmonic springs. It induces *3n* equations of motions and *3n* degrees of freedom. These 3n degrees of freedom consist of *3* translational and *3n-3* vibrational degrees of freedom. The system is, in principle, ultimately solvable, albeit excessively challenging to tackle directly when the number of particles becomes large. In practice, we can transform such a problem with many coupled variables into many individual problems, and each resulting problem has only one variable. This method is widely used for mechanical systems and is commonly done by diagonalizing the dynamical matrix from the equations of motion [67]. Now, for a *n*-particle system, it has *3n-3* normal modes (except for some geometric arrangements), the general motions of the system are superpositions of all normal modes. The normal modes are uncoupled, which means that in a harmonic system, excitation of one mode will never induce the motion of a different mode, *i.e.*, there is no energy transfer between these (harmonic) normal modes.

In solids with periodic lattices, these harmonic normal modes' evenly spaced energy levels are precisely the phonons. Assume the unit cell of solid has more than one type of atom, there are correspondingly the solid has two types of phonons, namely acoustic phonons and optical phonons. Some of characteristics of acoustic and optical phonons are summarized in Table 2.1.

Table 2.1.: Characteristics of lattice-vibrational acoustic and optical phonons [68].

Characteristic	Acoustic Phonon	Optical Phonon
Group velocity	sound waves, constant for wave number $k \to 0$	smaller than acoustic mode
Displacement of adjacent atoms	in-phase	out-of-phase
Largest frequency	at the edge of Brillouin zone	higher than acoustic polarization
Density of states (per unit volume, per dω	Debye model $D_{p,D,\alpha} = \frac{\omega^2}{2\pi^2 u_{p,g,\alpha}^3}$	Debye-Gaussian Model $D_{p,DG} = \mathrm{d}\omega^2 exp[-(\frac{\omega-\omega_c}{\Delta\omega})^2]$
Phonon number density	$n_{p,A} = \int f_p D_{p,A}(\omega)\mathrm{d}\omega$	$n_{p,O} = \int f_p D_{p,O}(\omega)\mathrm{d}\omega$
Acoustic mode number density	3n n is the atomic number density	(3N_0-3)n N_0 is the number of atoms per primitive cell
Number of polazrizations	two transverse and one longitudinal (per unit-cell lattice)	3N_0-3
f or ω vs. λ or $1/\lambda = k$ (dispersion relation)	longer-wavelength modes have smaller frequency, and for $\lambda \to \infty (k \to 0), \omega \to 0$	even long-wavelength modes have a finite frequency

Acoustic phonons are in-phase movements of atoms out of their equilibrium positions and are named after their close relation to sound waves. Acoustic phonons are long-wavelength modes having smaller frequency. They can be both longitudinal (LA, in the direction of propagation) or transverse (TA, perpendicular to the propagation

direction). Acoustic phonons mostly have a linear dispersion relationship between frequency and phonon wavevector, in which the frequency goes to zero in the limit of longer-wavelength.

Optical phonons are short-wavelength, out-of-phase movements of the atoms in the lattice and only occur if the lattice basis consists of two or more atoms. They are named optical because in some ionic crystals, they can be excited by electromagnetic radiation (light) through infrared absorption or Raman scattering. Optical phonons are even long-wavelength modes having a finite frequency. They have a non-zero frequency at the Brillouin zone center and because of the symmetry, they show no dispersion near that long-wavelength limit. This is because they correspond to a mode of vibration where positive and negative ions at adjacent lattice sites swing against each other, creating a time-varying electrical dipole moment. Similar to acoustic phonons, optical phonons are also abbreviated as LO and TO phonons, for the longitudinal and transverse modes respectively; the splitting between LO and TO frequencies is often described accurately by the Lyddane–Sachs–Teller relation [69].

2.3.2. Symmetry Analysis

With group theory, finding the vibrational states of different phonon modes is possible.

Basic concepts of group theory
The mathematical definition of a group is a collection of elements A, B, C, ..., which are interrelated according to certain rules:

- The product of any two elements in the group must be an element in the group; If $A, B \in G$ then $AB = C \in G$.

- The associative law is valid, i.e., $(AB)C = A(BC)$.

- There exists an identity element E, then $AE = EA = A$.

- For every element A there exists an inverse element A^{-1} such that $AA^{-1} = A^{-1}A = E$.

In general, the elements of a group will not commute, i.e., $AB \neq BA$. But if all elements of a group commute, the group is then called an Abelian group.

Here, we list a simple example of a group, the permutation group for three numbers, $P(3)$.

$$E = \begin{pmatrix} 1 & 2 & 3 \\ 1 & 2 & 3 \end{pmatrix} \quad A = \begin{pmatrix} 1 & 2 & 3 \\ 1 & 3 & 2 \end{pmatrix} \quad B = \begin{pmatrix} 1 & 2 & 3 \\ 3 & 2 & 1 \end{pmatrix}$$
$$C = \begin{pmatrix} 1 & 2 & 3 \\ 2 & 1 & 3 \end{pmatrix} \quad D = \begin{pmatrix} 1 & 2 & 3 \\ 3 & 1 & 2 \end{pmatrix} \quad F = \begin{pmatrix} 1 & 2 & 3 \\ 2 & 3 & 1 \end{pmatrix} . \tag{2.67}$$

Eq. 2.67 shows the $3! = 6$ possible permutations that can be accomplished. The top and bottom rows represent the initial and final arrangement of the three numbers, respectively. Each permutation is an element of $P(3)$. Now, we use three points in an equilateral triangle (see Figure 2.2) to present the elements in Eq. 2.67. For example, in symmetry operation F, 1 goes to position 3, and 2 goes to position 1, while 3 goes to position 2, which shows a counterclockwise rotation of $2\pi/3$. As the effect of the six distinct symmetry operations that can be performed on these points, we can call each symmetry operation an element of the group.
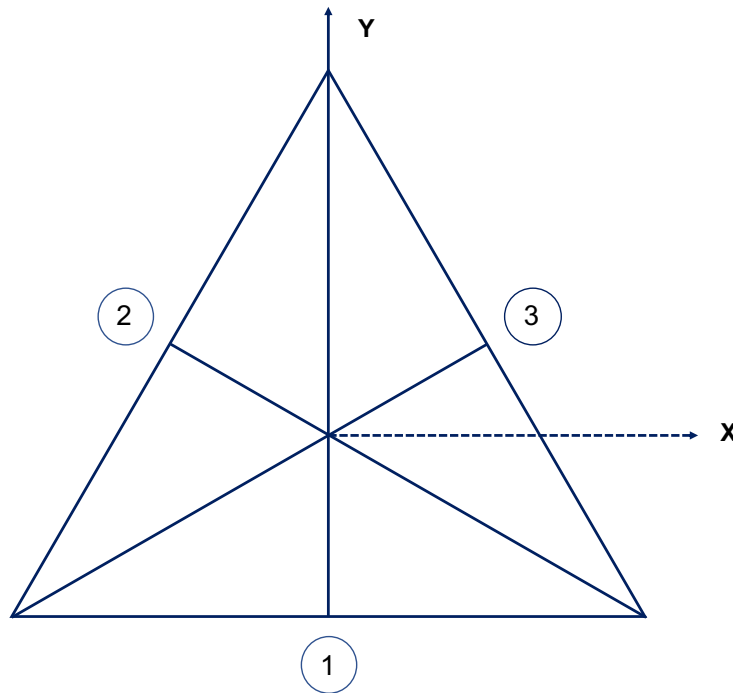
Figure 2.2.: The symmetry operations on an equilateral triangle are the rotations by $\pm 2\pi/3$ about the origin and the rotations by π about the three twofold axes. Here the axes or points of the equilateral triangle are denoted by numbers in circles.

The multiplication Table 2.3.2 presents the product of group elements. As one can see, the symmetry operations satisfy the four rules of a group. Each element of $P(3)$ has

a one-to-one correspondence to the symmetry operations of an equilateral triangle. Hence, these two groups are isomorphic to each other.

Table 2.2.: Multiplication table for the point symmetry operations of an equilateral triangle.

	E	A	B	C	D	F
E	E	A	B	C	D	F
A	A	E	D	F	B	C
B	B	F	E	D	C	A
C	C	D	F	E	A	B
D	D	C	A	B	F	E
F	F	B	C	A	E	D

Group theory is helpful for some physical problems, especially symmetry operations in a crystal. If we can associate each element with a matrix that obeys the same multiplication table as the elements themselves, that is, if the elements obey $AB = D$, then the matrices representing the elements must obey

$$M(A)M(B) = M(D). \tag{2.68}$$

If this relation is satisfied, then we perform all geometrical operations analytically in terms of arithmetic operations on matrices, which are usually easier to perform. The one-to-one identification of a generalized symmetry operation with a matrix is the basic idea of a representation and why group theory plays such an essential role in solving practical problems.

Here, we list a set of matrices that satisfy the Table 2.3.2 for $P(3)$ as

$$E = \begin{pmatrix} 1 & 0 \\ 0 & 1 \end{pmatrix} \qquad A = \begin{pmatrix} -1 & 0 \\ 0 & 1 \end{pmatrix} \qquad B = \begin{pmatrix} 1/2 & -\sqrt{3}/2 \\ -\sqrt{3}/2 & -1/2 \end{pmatrix}$$
$$C = \begin{pmatrix} 1/2 & \sqrt{3}/2 \\ \sqrt{3}/2 & -1/2 \end{pmatrix} \quad D = \begin{pmatrix} -1/2 & \sqrt{3}/2 \\ -\sqrt{3}/2 & -1/2 \end{pmatrix} \quad F = \begin{pmatrix} -1/2 & -\sqrt{3}/2 \\ \sqrt{3}/2 & -1/2 \end{pmatrix}. \tag{2.69}$$

Note that the matrix corresponding to the identity operator E is always a unit matrix. The matrix in Eq. 2.69 constitute a matrix representation of the group that is isomorphic to $P(3)$ and to the symmetry operations on an equilateral triangle. The A, B, and C matrix show a rotation by $\pm\pi$ about the Y-axis, 2-axis, and 3-axis, respectively. D and F show rotation of $-2\pi/3$ and $2\pi/3$ around the center of the triangle.

Besides these essential rules of the group theory, there are also some crucial concepts in the group theory [70],

- The order of the group is defined as the number of elements in the group. Then groups have finite order and infinite order. We will be mainly concerned with finite groups.

- A subgroup is the smaller groups, whose elements are taken from the larger group.

- The order of an element is the smallest value of n in the relation $X^n = E$.

- A, B and X are elements of a group, if $B = X^{-1}AX$, we say B is conjugate with A.

- A class is a complete set of elements which are conjugate to on another.

- The elements of the same class are of the same order, because if $B = XAX^{-1}$ and $A^n = E$, then $B^n = (XAX^{-1}) = XAX^{-1} \ldots XAX^{-1} = E$.

- The factor group is constructed with respect to a self-conjugate subgroup as the collection of cosets of the self-conjugate subgroup, each coset being considered an element of the factor group.

Representation theory

Representation theory is necessary for developing the group theoretical framework that is used for the applications of group theory to solid state physics. Representations of groups are a set of matrices, each corresponding to a single operation in the group, that can be combined among themselves in a manner parallel to how the group elements combine. The assigned matrices follow the multiplication relation of the original abstract group. We assign a matrix $D(A)$ to each element A of the abstract group such that $D(AB) = D(A)D(B)$. Then, the dimensionality of a representation equals the dimensionality of each of its matrices, which is, in turn, equivalent to the number of rows or columns of the matrix. These representations are not unique. For instance, by executing a similarity transformation $UD(A)U^{-1}$, we generate a new set of matrices that provides an equally good representation. A simple physical example of this transformation is the rotation of reference axes, such as (x, y, z) to (x', y', z'). Hence, people can generate a new representation by taking one or more representations and combining them according to

$$\begin{pmatrix} D(A) & \mathscr{O} \\ \mathscr{O} & D'(A) \end{pmatrix}, \tag{2.70}$$

where $\mathscr{O} = (m \times n)$ matrix of zeros, not necessarily a square zero matrix. The matrices $D(A)$ and $D'(A)$ can be identical or not. This is a reducible representation because the matrix corresponding to each and every element of the group is in the same block form. To overcome the difficulty of the ambiguity of representations in general, irreducible representations (irrep) are introduced. The definition of irrep is that, if by one and the same equivalence transformation, all the matrices in the representation of a group can

be made to acquire the same block form, then the representation is said to be reducible; otherwise, it is irreducible. Thus, an irreducible representation cannot be expressed in terms of representations of lower dimensionality.

Here, there are three irreps for the $P(3)$:

$$
\begin{array}{cccc}
& E & A & B \\
\Gamma_1: & (1) & (1) & (1) \\
\Gamma_{1'}: & (1) & (-1) & (-1) \\
\Gamma_2: & \begin{pmatrix} 1 & 0 \\ 0 & 1 \end{pmatrix} & \begin{pmatrix} -1 & 0 \\ 0 & 1 \end{pmatrix} & \begin{pmatrix} 1/2 & -\sqrt{3}/2 \\ -\sqrt{3}/2 & -1/2 \end{pmatrix} \\
& C & D & F \\
\Gamma_1: & (1) & (1) & (1) \\
\Gamma_{1'}: & (-1) & (1) & (1) \\
\Gamma_2: & \begin{pmatrix} 1/2 & \sqrt{3}/2 \\ \sqrt{3}/2 & -1/2 \end{pmatrix} & \begin{pmatrix} -1/2 & \sqrt{3}/2 \\ -\sqrt{3}/2 & -1/2 \end{pmatrix} & \begin{pmatrix} -1/2 & -\sqrt{3}/2 \\ \sqrt{3}/2 & -1/2 \end{pmatrix}
\end{array}
\tag{2.71}
$$

A reducible representation having these three irreps is

$$
\begin{array}{cccc}
& E & A & B \\
\Gamma_R & \begin{pmatrix} 1 & 0 & 0 & 0 \\ 0 & 1 & 0 & 0 \\ 0 & 0 & 1 & 0 \\ 0 & 0 & 0 & 1 \end{pmatrix} & \begin{pmatrix} 1 & 0 & 0 & 0 \\ 0 & -1 & 0 & 0 \\ 0 & 0 & -1 & 0 \\ 0 & 0 & 0 & 1 \end{pmatrix} & \begin{pmatrix} 1 & 0 & 0 & 0 \\ 0 & 1 & 0 & 0 \\ 0 & 0 & \frac{1}{2} & \frac{\sqrt{3}}{2} \\ 0 & 0 & -\frac{\sqrt{3}}{2} & -\frac{1}{2} \end{pmatrix} & \cdots
\end{array}
\tag{2.72}
$$

where Γ_R is of the form

$$
\begin{pmatrix} \Gamma_1 & 0 & \mathcal{O} \\ 0 & \Gamma_{1'} & \mathcal{O} \\ \mathcal{O} & \mathcal{O} & \Gamma_2 \end{pmatrix}.
\tag{2.73}
$$

Γ_R can be denoted as

$$
\Gamma_R = \Gamma_1 + \Gamma_{1'} + \Gamma_2.
\tag{2.74}
$$

Representation theory is useful for treating physical problems because of a particular orthogonality theorem, also called the "Wonderful Orthogonality Theorem," which we will present. Before that, the unitarity of representations should be mentioned; that is, every representation with matrices having nonvanishing determinants can be brought

into unitary form by an equivalence (similarity) transformation. The orthonormality relation is defined as

$$\sum_R D_{\mu\nu}^{(\Gamma_j)}(R) D_{\mu'\nu'}^{(\Gamma_{j'})}(R^{-1}) = \frac{h}{l_j} \delta_{\Gamma_j,\Gamma_{j'}} \delta_{\mu\mu'} \delta_{\nu\nu'}, \tag{2.75}$$

which is obeyed for all the inequivalent irreps of a group, where the summation is over all h group elements A_1, A_2, ..., A_h. l_j and $l_{j'}$ are the dimensionalities of representations Γ_j and $\Gamma_{j'}$, respectively. If the representations are unitary, the orthonormality relation becomes

$$\sum_R D_{\mu\nu}^{(\Gamma_j)}(R) [D_{\mu'\nu'}^{(\Gamma_{j'})}(R)]^* = \frac{h}{l_j} \delta_{\Gamma_j,\Gamma_{j'}} \delta_{\mu\mu'} \delta_{\nu\nu'}, \tag{2.76}$$

More details of proof can be found in Ref. [70].

Character of a representation

To get around the arbitrariness of a representation with regard to similarity or equivalence transformations, we now present the use of the character of a matrix representation which remains invariant under a similarity transformation. The character of the matrix representation $\chi^{\Gamma_j}(R)$ for a symmetry operation R in a representation $D^{(\Gamma_j)}(R)$ is the sum over diagonal matrix elements of the matrix of the representation:

$$\chi^{\Gamma_j}(R) = \text{trace} D^{(\Gamma_j)}(R) = \sum_{\mu=1}^{l_j} D^{(\Gamma_j)}(R)_{\mu\mu}. \tag{2.77}$$

From the definition, it follows that Γ_j will have h characters, one for each element in the group. Since the trace of a matrix is invariant under a similarity transformation, the character is invariant under such a transformation. Furthermore, the character for each element in a class is the same. This theorem is called "the great beauty of character" by van Vleck. If two elements of a group are in the same class, this means that they correspond to similar symmetry operations. Here, considering the permutation group $P(3)$ as an example, we summarize the information on the characters of this group in the well-known character table (see Table 2.3.2).

The wonderful orthogonality theorem and the second orthogonality theorem for character give the fundamental orthogonality relations used to set up character tables. The wonderful orthogonality theorem is

$$\sum_R \chi^{(\Gamma_j)}(R)\chi^{(\Gamma_{j'})}(R^{-1}) = h\delta_{\Gamma_j}\delta_{\Gamma_{j'}}, \tag{2.78}$$

and for the unitary representations is

$$\sum_R \chi^{(\Gamma_j)}(R)\chi^{(\Gamma_{j'})}(R^*) = h\delta_{\Gamma_j}\delta_{\Gamma_{j'}}, \tag{2.79}$$

those describe that the primitive characters of an irreducible representation obey the orthogonality relation; in other words, unless the representations are identical or equivalent, the characters are orthogonal in h-dimensional space, where h is the order of the group.

Moreover, a second orthogonality theorem for characters sums over the irreps and is quite practical for constructing character tables.

$$\sum_{\Gamma_j} \chi^{(\Gamma_j)}(C_k)[\chi^{(\Gamma_j)}(C_{k'})]N_k = h\delta_{kk'}, \tag{2.80}$$

where N_k denotes the number of elements in class k. Thus, the wonderful orthogonality theorem for character yields an orthogonality relation between rows in the character table while the second orthogonality theorem gives a similar relation between the columns of the character table.

Basis functions
Basic functions associated with each irrep are used to generate the matrices that represent the symmetry elements of a particular irrep. Having a group G with symmetry elements R and symmetry operators $\hat{P}_R$, we can represent the irrep by Γ_n (n labels the representation). Then a set of basis vector $|\Gamma_n j \Gamma_n j\rangle$ is defined, and each vector $|\Gamma_n j\rangle$ of Γ_n is called a component (j labels the component of the representation). All components collectively generate the matrix representation denoted by $D^{(\Gamma_n)}(R)$. The relation between $\hat{P}_R$ and $D^{(\Gamma_n)}(R)$ is expressed as

Table 2.3.: Character table for the permutation group $P(3)$.

class→	C_1	$3C_2$	$2C_3$
Irrep ↓	$\chi(E)$	$\chi(A,B,C)$	$\chi(D,F)$
Γ_1	1	1	1
$\Gamma_{1'}$	1	-1	1
Γ_2	2	0	-1

$$\hat{P}_R|\Gamma_n\alpha\rangle = \sum_j D^{(\Gamma_n)}(R))j\alpha|\Gamma_n j\rangle. \tag{2.81}$$

The basis vectors also follow orthogonality relations

$$\langle\Gamma_n j|\Gamma_{n'} j'\rangle = \delta_{nn'}\delta_{jj'}. \tag{2.82}$$

According to the above expression, we have a relation between each matrix element of $D^{(\Gamma_n)}(R)_{j\alpha}$ and the effect of the symmetry operation on the basis function [70]:

$$D^{(\Gamma_n)}(R)_{j\alpha} = \langle\Gamma_{n'} j'|\hat{P}_R|\Gamma_n\alpha\rangle. \tag{2.83}$$

Therefore, taking matrix elements of a symmetry operator $\hat{P}_R$ between all possible components of an irrep, the matrix representation $D^{(\Gamma_n)}(R)_{j\alpha}$ can be generated. This is the easiest way to practically obtain these matrix representations for the symmetry elements.

Now, the projection operation $\hat{P}_{kl}^{(\Gamma_n)}$ is defined as transforming one basis vector $|\Gamma_n l\rangle$ into another basis vector $|\Gamma_n k\rangle$ of the same irrep Γ_n:

$$\hat{P}_{kl}^{(\Gamma_n)}|\Gamma_n l\rangle \equiv |\Gamma_n k\rangle. \tag{2.84}$$

The utility of projection operators is mainly to project out basis functions for a given component of a given irrep from an arbitrary function.

Group theory for lattice modes

Group theoretical techniques are important for lattice dynamics in formulating the normal mode secular determinant in block diagonal form, and symmetry is also important in determining the selection rules for optical processes involving lattice modes such as infrared and Raman activity.

The general outline for procedures that operate group theory to solve for the lattice modes in solids is as follows [70]:

1. Find the symmetry operations for the group of the wave vector $k = 0$, the appropriate character table and irreducible representations.

2. Find the irreducible representations using $\Gamma_{\text{lattice modes}} = \Gamma^{\text{equivalence}} \otimes \Gamma_{\text{vector}}$.

3. Find the irreducible representations of $\Gamma_{\text{lattice modes}}$. The characters for the lattice mode representation express the symmetry types and degeneracies of the lattice modes.

4. Find the normal mode patterns.

5. Repeat items 1–4 for other points in the Brillouin zone and find the lattice for $\boldsymbol{k} \neq 0$.

6. Using the compatibility relations, connect up the lattice modes at neighboring $\boldsymbol{k}$ points to form a phonon branch.

2.3.3. Harmonic Approximation

Now we have a crystal consisting of N unit cells each containing n atoms, where the atoms are in their equilibrium positions. The instantaneous position $\mathbf{R}_l^k(t)$ of the kth atom in the lth unit cell at time t with displacement $\mathbf{u}_{lk}(t)$ can be written as

$$\mathbf{R}_l^k(t) = \mathbf{R}_l + \tau^k, \tag{2.85}$$

where the lattice vector $\mathbf{R}_l$ represents the position vector of the lth unit cell. And the τ^k is the position vector of atom k with respect to the origin of the unit cell. If the atoms vibrate about their equilibrium positions by a displacement vector $\mathbf{u}^k(\mathbf{R})$, the kinetic energy of the lattice is written as

$$T = \frac{1}{2} \sum_{k\alpha\mathbf{R}} M_k \dot{u}_\alpha^k(\mathbf{R}), \tag{2.86}$$

where $\alpha = x, y, z$ is Cartesian indices and M is the atomic mass. The equation of motion for k^{th} atom in the lth unit cell can be expressed as

$$M_k \ddot{u}_\alpha^k(\mathbf{R}_l) = -\frac{\partial \Phi}{\partial u_\alpha^k(\mathbf{R}_l)}, \tag{2.87}$$

where the Φ is the lattice potential energy. For lattice dynamics, the Hamiltonian for nucleus motions in a crystal is given as [71, 72]

$$H_n = \sum_{l,k} \frac{\mathbf{P}_{lk}^2}{2M_k} + \Phi, \tag{2.88}$$

where $\mathbf{P}$ is the momentum of the kth atom in the lth unit cell. And the lattice potential energy (potential energy surface) is Φ. The Φ can then be expanded into a Taylor series in powers of the $\mathbf{u}^k(\mathbf{R}_l)$, about their equilibrium positions

$$\Phi = \Phi_0 + \sum_{k\alpha\mathbf{R}} \Phi_\alpha^k(\mathbf{R}) u_\alpha^k(\mathbf{R})$$

$$+ \frac{1}{2!} \sum_{k_1\alpha_1\mathbf{R}_1} \sum_{k_2\alpha_2\mathbf{R}_2} \Phi_{\alpha_1\alpha_2}^{k_1 k_2}(\mathbf{R}_1\mathbf{R}_2) u_{\alpha_1}^{k_1}(\mathbf{R}_1) u_{\alpha_2}^{k_2}(\mathbf{R}_2) \qquad (2.89)$$

$$+ \frac{1}{3!} \sum_{k_1\alpha_1\mathbf{R}_1} \sum_{k_2\alpha_2\mathbf{R}_2} \sum_{k_3\alpha_3\mathbf{R}_3} \Phi_{\alpha_1\alpha_2\alpha_3}^{k_1 k_2 k_3}(\mathbf{R}_1\mathbf{R}_2\mathbf{R}_3) u_{\alpha_1}^{k_1}(\mathbf{R}_1) u_{\alpha_2}^{k_2}(\mathbf{R}_2) u_{\alpha_3}^{k_3}(\mathbf{R}_3)$$

$$+ \cdots$$

The Φ_0 is the equilibrium value of the lattice potential energy. The second term vanishes since the atoms are in equilibrium and have no forces acting upon them. The quadratic term is the harmonic lattice potential energy. In the harmonic approximation, the series expansion is cut at this term so as not to include the higher order terms.

The Harmonic Equations of Motion is

$$M_k \ddot{u}_\alpha^k(\mathbf{R}) = - \sum_{k'\mathbf{R}'} \frac{\partial^2 \Phi}{\partial u_\alpha^k(\mathbf{R}) \partial u_{\alpha'}^{k'}(\mathbf{R}')} u_{\alpha'}^{k'}(\mathbf{R}'). \qquad (2.90)$$

Assuming that the **u** is time dependent, the time derivatives in the equations of motion can be evaluated

$$M_k \omega^2 u_\alpha^k(\mathbf{R}) = \sum_{k'\mathbf{R}'} \Phi_{\alpha\alpha'}^{kk'}(\mathbf{R},\mathbf{R}') u_{\alpha'}^{k'}(\mathbf{R}'). \qquad (2.91)$$

This eigenvalue problem can be diagonalized to yield the phonon frequencies, atomic displacement patterns, and dynamical matrices.

2.3.4. Phonon Density of States

The density of states (DOS) of phonons is employed to determine the total number of phonons N_p and the phonon-related properties. The phonon DOS $D_p(\omega)$ is the total number of modes in the frequency range ω to $\omega + d\omega$, divided by volume V. First, we use $\nabla_k \omega_\alpha$ relate dk and $d\omega_\alpha$, where α is for acoustic and optical branches, the density of normal modes for three-dimensional cubic lattice with lattice constant L is written as

$$D_p(\omega) = \frac{1}{L^3} \left(\frac{L}{2\pi}\right)^3 \sum_\alpha \frac{1}{|\nabla_k \omega_\alpha|} = \left(\frac{1}{2\pi}\right)^3 \sum_\alpha 4\pi k^2 \frac{dk}{d\omega_\alpha}. \qquad (2.92)$$

For any quantity ϕ related to the modes, we have

$$\sum_\alpha \sum_k \phi[\omega_\alpha(k)] = \sum_\alpha \int_k \frac{1}{(2\pi)^3} \phi[\omega_\alpha(k)] \mathrm{d}k$$
$$\equiv \sum_\alpha \int_{\omega_\alpha} D_p(\omega_\alpha) \phi(\omega_\alpha) \mathrm{d}\omega_\alpha. \tag{2.93}$$

We also can use the Dirac delta function δ_D to represent the total DOS for normal modes. Then, $D_p(\omega)$ is given as

$$D_p(\omega) = \sum_\alpha \int_{k'} \frac{dk'}{(2\pi)^3} \delta_D[\omega - \omega_{\alpha(k')}], \ \ \mathrm{d}k' = 4\pi k'^2 \mathrm{d}k'. \tag{2.94}$$

Therefore, the phonon frequency density of states $D_p(\omega)$ converts the number of phonons of wave number k to those of frequency ω, using the dispersion relations.

For acoustic phonons, as listed in Table 2.1, there is a linear dispersion at zone center $k \to 0$, leading to a constant group velocity. In this regard, the Debye model (parabolic DOS, proportional to E_p^2, $E_p = \hbar\omega = \hbar u_{p,g} k$) is used to describe the acoustic modes (two TA and one LA). From Eq. 2.92 for a 3D k-space, the Debye DOS model is

$$D_{p,D,\alpha}(\omega) = \frac{4\pi k^2}{(2\pi)^3} \frac{1}{u_{p,g,\alpha}} = \frac{1}{2\pi^2} \frac{\omega^2}{u_{p,g,\alpha}^3}, \ \ \frac{\mathrm{d}\omega}{\mathrm{d}k} = u_{p,g,\alpha} = \frac{\omega}{k} = u_{p,p,\alpha}$$
$$= \frac{1}{2\pi^2} \frac{E_p^2}{\hbar^2 u_{p,g,\alpha}^3}. \tag{2.95}$$

If we assume two TA and one LA modes are the same, we obtain a simple Debye DOS model, which is

$$D_{p,D}(\omega) = \frac{3}{2\pi^2} \frac{\omega^2}{u_{p,A}^3}, \tag{2.96}$$

where $u_{p,A}^3$ is average modal acoustic-phonon velocity. Then, we can define two quantities from the Debye model,

The Debye polarization temperature:

$$T_{D,\alpha} = \frac{\hbar\omega_{D,\alpha}}{k_B} = \frac{\hbar}{k_B} u_{p,g,\alpha} (6\pi^2 n)^{1/3}, \tag{2.97}$$

where n is the atomic number density.

The Debye cut-off frequency:

$$\omega_D = (6\pi^2 n u_{p,A}^3)^{1/3} = (6\pi^2 n)^{1/3} u_{p,A} \tag{2.98}$$

The physical meaning of ω_D is the maximum frequency of atomic vibrations. When $\omega > \omega_D$, the $D_{p,D}(\omega) = 0$.

For optical phonons, the Debye–Gaussian model can be used to describe the density of states, i.e.,

$$D_p(E_p) = CE_p^2 \exp[-(\frac{E_p - E_{p,c}}{\Delta E_p})^2], \ D_p(E_p) = D_p(\omega)\frac{\partial \omega}{\partial E_p}, \tag{2.99}$$

where C is a normalization constant, $E_{p,c}$ represents the energy at the center of the DOS, ΔE_p is the width of the distribution. At low phonon energies, the Debye–Gaussian model behaves similarly to the Debye model, and near the center behaves similarly to a Gaussian distribution. This also avoids the appearance of a cut-off frequency.

2.3.5. Thermodynamics of Phonons

After obtaining the phonon dispersion and the phonon DOS, many phonon-related properties can be determined, such as phonon specific heat capacity, which is an essential quantity in the thermodynamic properties of solids. At a finite temperature, the lattice will vibrate following the finite temperature dependence of phonon modes inducing energy fluctuations, which can be regarded as a gas of phonon. Meanwhile, a phonon mode can be created and dismissed with random energy fluctuations. As listed in Table 2.5, phonons are bosons that obey the Bose-Einstein statistics. In other words, there is no limit to how many phonons can present in each normal mode. Hence, in thermal equilibrium and within the harmonic regime, the phonon occupancy $f(\omega, T)$ with a given angular frequency ω at temperature T is:

$$f(\omega, T) = \frac{1}{\exp(\frac{\hbar\omega}{k_B T}) - 1}. \tag{2.100}$$

And the total energy of phonons, in a volume V, is

$$E_p = \sum_p \int_0^\infty \hbar\omega \frac{1}{\exp(\frac{\hbar\omega}{k_B T}) - 1} D_p(\omega)\mathrm{d}\omega. \tag{2.101}$$

Now, the lattice (phonon) specific heat capacity of a solid at constant volume is defined as:

$$C_{V,p} = \frac{\partial E_p}{\partial T}|_V = \sum_p \int_0^\infty \hbar\omega \frac{\partial}{\partial T}[\exp(\frac{\hbar\omega}{k_B T}) - 1]^{-1} D_p(\omega)\mathrm{d}\omega. \qquad (2.102)$$

The differentiation on the right-side can be simplified as

$$\frac{\partial}{\partial T}[\exp(\frac{\hbar\omega}{k_B T}) - 1]^{-1} = \frac{\hbar\omega}{k_B T^2}\frac{e^x}{(e^x - 1)^2}, \; x = \frac{\hbar\omega}{k_B T}. \qquad (2.103)$$

Finally, we get

$$C_{V,p} = k_B \sum_p \int \frac{x^2 e^x}{(e^x - 1)^2} D_p(\omega)\mathrm{d}\omega. \qquad (2.104)$$

According to the Debye DOS model in last subsection, the lattice specific heat capacity can be approximately obtained as

$$C_{V,p} = 9Nk_B(\frac{T}{T_D})^3 \int_0^{T_D/T} \frac{x^4 e^x}{(e^x - 1)^2}\mathrm{d}x. \qquad (2.105)$$

Eq. 2.105 is known as the Debye T^3 law. $T_D = \hbar\omega_D/k_B$ is the Debye temperature. The high-temperature and low-temperature expansions of the lattice specific heat capacity are

$$C_V(T) \sim 3Nk_B[1 - \frac{1}{20}(\frac{T_D}{T})^2], \;\; T \gg T_D, \qquad (2.106)$$

$$C_V(T) \sim \frac{12\pi^4}{5}Nk_B(\frac{T}{T_D})^3 = 234Nk_B(\frac{T}{T_D})^3, \;\; T \ll T_D. \qquad (2.107)$$

In addition, before the Debye model, the earliest quantum theories of lattice specific heat capacity was put forth by Einstein in 1907, namely the Einstein phonon model. In which, the atomic vibrations are represented by the Einstein approximation, which is described by a fixed frequency ν that does not depend on k. Hence, the equilibrium total energy of phonons is

$$E_{p,E} = 3N[\frac{1}{2}h\nu + \frac{h\nu}{e^{h\nu/k_B T} - 1}]. \qquad (2.108)$$

Thus, the molar specific heat capacity of phonon gas or atomic vibrations are

$$C_{mole}(T) = 3Nk_B(\frac{T_E}{T})^2 \frac{e^{T_E/T}}{(e^{T_E/T}-1)^2}, \qquad (2.109)$$

where $T_E = h\nu/k_B$ is the Einstein temperature. In the Einstein model, the high-temperature and low-temperature expansions of the lattice specific heat capacity are

$$C_{mole}(T) \simeq 3R[1 - \frac{1}{12}(\frac{T_E}{T})^2], \quad T \gg T_E, \qquad (2.110)$$

$$C_{mole}(T) \simeq 3R(\frac{T_E}{T})^2 e^{-T_E/T}, \quad T \ll T_E. \qquad (2.111)$$

Therefore, the high-temperature expansion in Einstein model matches well with experimental values, tending to the Dulong-Petit law $C_{mole} = 3R$. The Einstein model is often used to approximate the optical phonon part of the phonon spectrum. At low temperature, the Debye T^3 law agrees better with experiments.

2.4. Finite-temperature Thermodynamics in DFT

Till now, phonon theory provides a connection between DFT calculations at zero temperature and thermodynamic properties at finite temperature. Hence, DFT calculations can be bridged to the thermodynamic properties at finite temperatures and the experiments with mutual validation. To access the thermodynamic properties and phase transitions of functional materials, the Gibbs free energies should be calculated instead of the total energies for the ground states at 0 K. At finite temperature, in addition to the lattice free energy due to phonons, there are also electronic and magnetic contributions to the total Gibbs free energy. The most fundamental quantity is the Gibbs free energy, which can be formulated as a function of temperature T, pressure P, and magnetization direction M. Following the Legendre transformation, the Gibbs free energy $G(T,P,M)$ can be reformulated into the sum of Helmholtz free energy $H(T,V,M)$ and the PV term which can be obtained explicitly fitting of the equation of states. The Helmholtz free energy has four contributions [73], as shown in Figure 2.3.

2.4.1. Helmholtz Energy

In Figure 2.3, $E(V,P,M)$ is the static total energy, which is the total energy of the system at zero Kelvin without the zero-point energy contribution, which was determined by fitting the energies concerning the volume data using the Birch-Murnaghan equation of state (EOS) [74].

$$E = a + bV^{-2/3} + cV^{-4/3} + dV^{-2} + eV^{-8/3} \qquad (2.112)$$

Vibrational Contributions

Under the harmonic/quasi-harmonic approximation, lattice dynamics or phonon theory is currently the most established method, which has been discussed in the previous sections. Hence, the $F_{vib}(V,T)$ in Figure 2.3 represents the lattice vibrational contribution to the Helmholtz energy, which can be derived from the phonon density of states (PhDOS), $g(\omega,V)$, by using the following equation [75]:

$$F_{vib}(V,T) = k_B T \int_0^\infty \ln\left[2\sinh\frac{\hbar\omega}{2k_B T}\right] g(\omega,V) d\omega, \qquad (2.113)$$

where k_B is the Boltzmann constant, and ω denotes the phonon frequency for a given wave vector q. The PhDOS $g(\omega,V)$ can be obtained by integrating the phonon dispersion in the Brillouin zone. It is recommended that $g(\omega,V)$ is calculated at the same volume set at which the static total static energies are calculated.

Electronic Contributions

The third term F_{el} in Figure 2.3 expresses the electronic contribution to the Helmholtz free energy, obtained by [76]:

$$F_{el}(V,T) = E_{el}(V,T) - T \cdot S_{el}(V,T) \qquad (2.114)$$
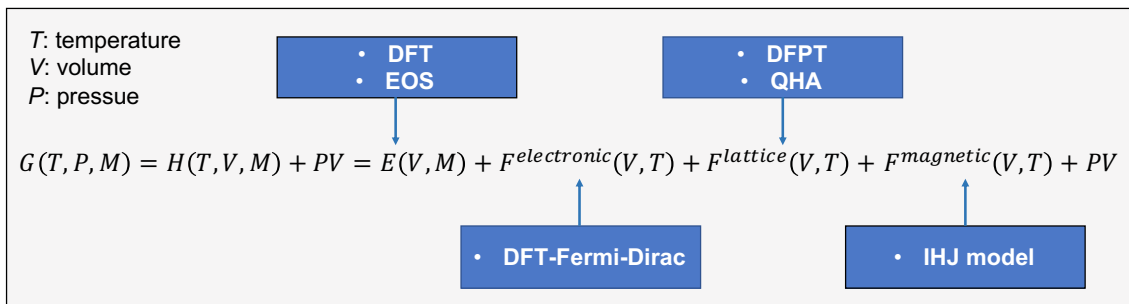
Figure 2.3.: Different contributions to the total Gibbs free energy.

where $E_{el}(V,T)$ and $S_{el}(V,T)$ indicate the thermal electronic energy and bare electronic entropy, respectively. With the electronic *DOS*, both terms can be formulated as [76]:

$$E_{el}(V,T) = \int n(\varepsilon) f \varepsilon d\varepsilon - \int_{-\infty}^{\varepsilon_F} n(\varepsilon,V) d\varepsilon, \qquad (2.115)$$

$$S_{el}(V,T) = -k_B \int n\varepsilon [f ln f + (1-f) ln(1-f)] d\varepsilon, \qquad (2.116)$$

where $n(\varepsilon)$ is the electronic *DOS*, f represents the Fermi-Dirac distribution function and ε_F is the Fermi energy.

Magnetic Contributions

Finally, based on the original Inden–Hillert–Jarl (IHJ) model [77, 78] and further improved expression by Xiong [79], the magnetic Gibbs energy can be formulated as:

$$G_{magn} = RT ln(\beta^* + 1) f(\tau), \qquad (2.117)$$

where τ is T/T^*, T^* is the critical temperature (the Cutie temperature T_C for ferromagnetic materials or the Neel temperature T_N for antiferromagnetic materials). β^* is the effective magnetic moment per atom, which can be expressed as $\beta^* = \prod_i (\beta_i + 1)^{x_i} - 1$. [79]. And $g(\tau)$ is given by:

$$g(\tau) = 1 - [\frac{0.38438376\tau^{-1}}{p} + 0.63570895(\frac{1}{p} - 1)$$
$$\times (\frac{\tau^3}{6} + \frac{\tau^9}{135} + \frac{t^{15}}{600} + \frac{t^{21}}{1617})]/D, \quad 0 < \tau \le 1 \qquad (2.118)$$
$$g(\tau) = -[\frac{\tau^{-7}}{21} + \frac{\tau^{-21}}{630} + \frac{\tau^{-45}}{2975} + \frac{\tau^{-49}}{8232}]/D, \quad \tau > 1$$

where $D = 0.33471979 + 0.49649686(\frac{1}{p} - 1)$.

In addition, magnetic free energy can be evaluated by integrating the specific heat obtained by Monte Carlo simulation of the Heisenberg model $H_{mag} = \sum_{ij} J_{ij} \mathbf{S}_i \cdot \mathbf{S}_j$, where the exchange parameters J_{ij} can be calculated using DFT calculations [80].

2.4.2. Thermodynamic Properties

After calculating the free energy of a system, we can quickly obtain the thermodynamic properties of the system, such as entropy, enthalpy, and heat capacity. The equilibrium

voluem $V_{eq}(P,T)$ at given T and P can be calculated by finding the root of the following equation

$$-(\frac{\partial F(V,T)}{\partial V})_T = P \tag{2.119}$$

The entropy $S(V,T)$ can be obtained through free energy of system by

$$S(V,T) = -(\frac{\partial F(V,T)}{\partial T})_V \tag{2.120}$$

Based on free energy and entropy, the enthalpy at given P and T is defined as

$$H(V,T) = F(V,T) + TS(V,T) + PV \tag{2.121}$$

After getting the equilibrium volume $V_{eq}(P,T)$, the volume thermal expansion coefficient can be obtained as

$$\beta_P(P,T) = \frac{1}{V_{eq}}(\frac{\partial V_{eq}(P,T)}{\partial T})_P \tag{2.122}$$

The heat capacity at constant volume can be calculated from

$$C_V(V,T) = (\frac{\partial U(V,T)}{\partial T})_V, \tag{2.123}$$

where the internal energy is $U(V,T) = F(V,T) + TS(V,T)$.

Then the heat capacity at constant pressure is defined as

$$C_P(P,T) = C_V(V,T) + VTB_T(V,T)(\beta(P,T))^2. \tag{2.124}$$

It can be seen that thermal expansion makes the difference between the heat capacity at constant volume and the heat capacity at constant pressure. And in the equation, $B_T(V,T)$ is the isothermal bulk modulus. The bulk modulus of a solid represents the substance's resistance to uniform compression. Depending on how the temperature varies during compression, a distinction should be made between the isothermal bulk modulus (constant temperature) and the adiabatic bulk modulus (constant entropy or no heat transfer). Now, the $B_T(V,T)$ can be obtained as

$$B_T(V,T) = V \left(\frac{\partial F^2(V,T)}{\partial V^2} \right)_T,$$ (2.125)

and the adiabatic bulk modulus can be then calculated

$$B_S(V,T) = (C_P/C_V)B_T(V,T).$$ (2.126)

2.5. CALPHAD Modeling

The calculated thermodynamic properties can be fed into the CALculation of PHAse Diagram (CALPHAD) method [81] as initial input values. The CALPHAD method models the thermodynamic properties of compounds and obtains global minimization of Gibbs free energy of the system, leading to multi-component phase diagrams. Such phase diagrams offer a roadmap for experimental synthesis. Traditionally only the experimental measurements are used in the thermodynamic assessment. However, even extensive experiments cannot provide all the parameters needed, whereas DFT can give reasonable values for the thermodynamic quantities of the reference phases. Hence, the CALPHAD method can be a bridge between theoretical predictions and experimental validations. Here we briefly discussed the thermodynamic description in the CALPHAD method of a binary system.

Pure elements

The Gibbs free energies for pure element i were taken from the Scientific Group Thermodata Europe (SGTE) pure element database [82], which was described by:

$$\begin{aligned}
^\circ G_i^\phi(T) &= G_i^\phi(T) - H_{i,SER}(298.15\ K) \\
&= a + bT + cT\ln(T) + dT^2 + eT^3 + fT^{-1} + gT^7 + hT^{-9},
\end{aligned}$$ (2.127)

where $H_{i,SER}(298.15\ K)$ is the molar enthalpy of element i at 298.15 K and 1 bar in its standard element reference (SER) state, and a to h are known coefficients.

Solution Phases

The solution phases are normally described using the substitutional solution model, with the corresponding molar Gibbs free energy formulated as:

$$G_m^\varphi = x_A G_A^\varphi(T) + x_B G_B^\varphi(T) + RT(x_A \ln x_A + x_B \ln x_B) + G^{ex} + G^{magn},$$ (2.128)

where x_A and x_B are the mole fraction of elements A and B in the solution, respectively. Taken from SGTE [82], G_i^φ denotes the molar Gibbs free energy of pure A and B in the structure φ at the given temperature. G^{ex} denotes the excess Gibbs energy of mixing, which measures the deviation of the actual solution from the ideal solution behaviour, modelled using a Redlich-Kister polynomial [83]:

$$G^{ex} = x_A x_B \sum_{j=0}^{n} {}^{(j)} L_{A,B}^\varphi (x_A - x_B)^j . \tag{2.129}$$

The $j-th$ interaction parameter between A and B is described by ${}^{(j)} L_{A,B}^\varphi$, which is modelled in terms of a*+b*T.

Stoichiometric intermetallic compounds

$A_x B_y$ is considered as stoichiometric phases. The Gibbs free energies per mole atom of these phases were thus expressed as follows:

$$G_m^{A_x B_y} = \frac{x}{x+y} G_{A,SER} + \frac{y}{x+y} G_{B,SER} + \Delta G_f^{A_x B_y}(T) , \tag{2.130}$$

where $\Delta G_f^{A_x B_y}(T)$ is the Gibbs free energy of formation of the stoichiometric compound $A_x B_y$ which can be expressed as:

$$\Delta G_f^{A_x B_y}(T) = \zeta + \vartheta T , \tag{2.131}$$

where the coefficients ζ, ϑ are the parameters to be optimized. Generally, the calculated enthalpies of formation for these phases from DFT calculations can be treated as initial values of the coefficient ζ in Eq. 2.131 in the present optimization.

2.6. Boltzmann Transport Equation

Till now, we have been focusing on the equilibrium properties of the solids, *i.e.*, for electrons based on DFT. Transport properties belong to the non-equilibrium properties, *i.e.*, how electrons/phonon behave with stimuli. Based on classical Hamiltonian statistical mechanics, the Boltzmann equation or Boltzmann transport equation (BTE) is to describe the steady state of a particle by its position x and momentum p and relates their time derivatives appearing in the equation of motion to their derivatives of the Hamiltonian, through $\frac{\partial x}{\partial t} = \frac{\partial H}{\partial p}$, $\frac{\partial p}{\partial t} = -\frac{\partial H}{\partial x}$ [84]. In addition, BTE also recognizes the particle and its energy according to its position and momentum (x, p), and also allows

for the determination of a non-equilibrium probability distribution of particles f_i under an applied field and also the return to equilibrium, after an initial non-equilibrium state. These distributions are used in determining transport coefficients under the influence of driving forces in cases of non-equilibria. BTE can be further for electrons, phonons, and photons based on their corresponding probability distribution function f_e, f_p, and f_{pt}.

A Simple Derivation of BTE

BTE is the equation governing the evolution of the distribution function based on non-equilibrium in time and space. We can start with being the fraction of particles whose positions and momenta are x and p at time t derive it. Under the external driving forces, if no collision happens, after a short time Δt, the particle would move from x to $x + u\Delta t$, where u is the velocity of the particle. And the particle momentum would change from p to $p + F\Delta t$, where F is the sum of the external forces on the particle at time t. Furthermore, if there are any difference between $f(x, p, t)$ and $f(x + u\Delta t, p + F\Delta t, t + \Delta t)$, the reason is the collision. Thus, the collision term is defined in term of a collision rate $\partial f/\partial t|_s$, including particles of positions x' and momenta p' over the time interval Δt entering (x, p). Note that, this term represents a change, not a formal derivative.

As shown in Figure 2.4, we generated a presentation of balance on f in the $x - p_x$ space. Then, we obtain

$$[f(x + u\Delta t,\ p + F\Delta t,\ t + \Delta t) - f(x, p, t)]\mathrm{d}x\mathrm{d}p = \frac{\partial f}{\partial t}|_s \mathrm{d}x'\mathrm{d}p'\Delta t \qquad (2.132)$$

where $\frac{\partial f}{\partial t}|_s$ is the time rate of change of f due to collisions. Here, neither a new particle is created nor an old particle is removed, it only changes particles momentum.

Then, using the Taylor expansion the first term on the left is defined as

$$
\begin{aligned}
f(x + u\Delta t, p + F\Delta t, t + \Delta t) &= f(x, p, t) + \left(\frac{\partial f}{\partial x_j}u_j + \frac{\partial f}{\partial p_j}F_j + \frac{\partial f}{\partial t}\right)\Delta t \\
&= f(x, p, t) + [(\nabla_x f) \cdot u + (\nabla_p f) \cdot F + \frac{\partial f}{\partial t}]\Delta t.
\end{aligned}
\qquad (2.133)
$$

Now, considering the limit as $\Delta t \to 0$, and introducing a sink/source term $\dot{s}_f$, we obtain

$$\frac{\partial f}{\partial t} + u_j \frac{\partial f}{\partial x_j} + F_j \frac{\partial f}{\partial p_j} = \frac{\partial f}{\partial t}\Big|_s + \dot{s}_f$$

$$\frac{\partial f}{\partial t} + \boldsymbol{u} \cdot (\nabla_x f) + \boldsymbol{F} \cdot (\nabla_p f) = \frac{\partial f}{\partial t}\Big|_s + \dot{s}_f. \tag{2.134}$$

This is the Boltzmann transport equation (BTE), and the velocity term in the equation represent the speed of propagation of the energy of the carrier, namely the group velocity. The the carrier i can be considered as phonons, electrons, and photons, we hence listed a Table 2.4 for carrier i.

In summary, the critical characteristic of BTE is the return from non-equilibrium distribution f to the equilibrium distribution f^0, through scattering $\frac{\partial f}{\partial t}\Big|_s$.

Using the BTE, studying phonon and electron transport properties is our goal. Firstly, thermal equilibrium particle (energy occupancy) distribution (statistical) function f_i^0
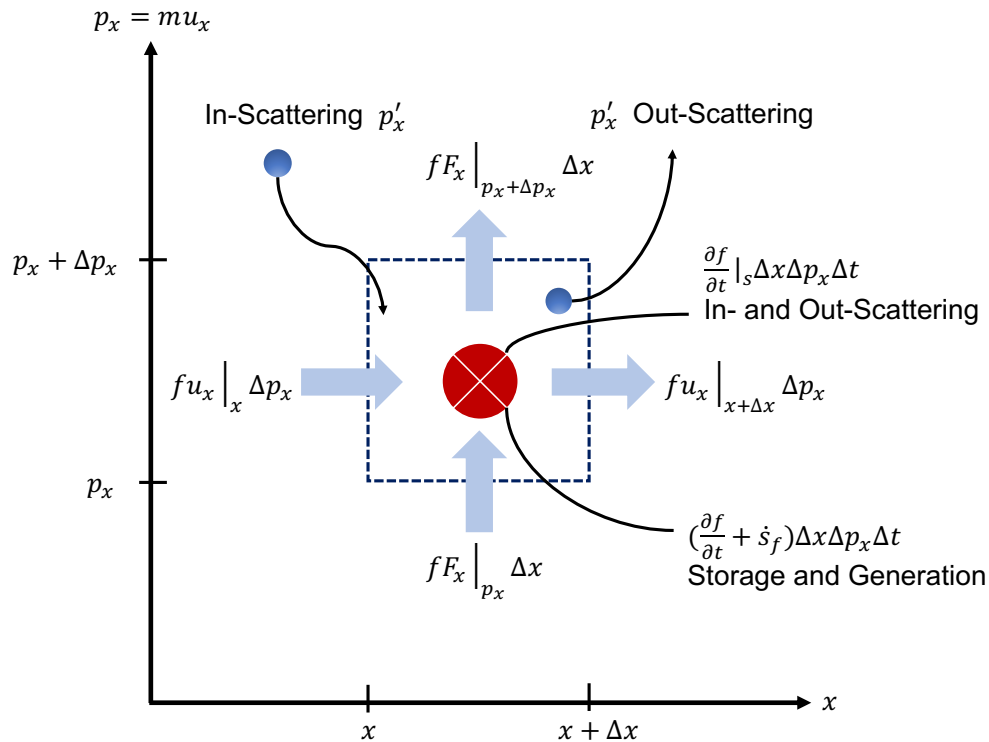
Figure 2.4.: Simple, infinitesimal $(\Delta x \to 0,\ \Delta p_x \to 0)$ balance on conserved property f, in single-space x and single-momentum p_x coordinates. The storage, scattering, and source terms are also shown.

Table 2.4.: The Boltzmann transport equation (BTE) for particle i [85].

$$\frac{\partial f_i}{\partial t} + \boldsymbol{u_i} \cdot (\nabla_x f_i) + \boldsymbol{F_i} \cdot (\nabla_p f_i) = \frac{\partial f_i}{\partial t}|_s + \dot{s}_{f,i}, \quad i = p, \ e, \ ph$$

$\boldsymbol{F_i}$	external force
f_i	probability distribution function of particle i
$\dot{s}_f$	i carrier source rate, 1/s
∇_x	spatial gradient, 1/m
∇_p	momentum gradient, 1/N-s

is listed in Table 2.5. Hence, the derivatives in Eq. 2.134, such as $\partial f/\partial t$, $\partial f/\partial x_j$, $F_j \partial f/\partial p_j$, respond to scattering events (and source/sink or generation $\dot{s}_{f,i}$) in return to the equilibrium population. Clearly, the transport properties are related to the process of scattering from f to f^0, which means the slower the rate of scattering the more effective is the transport.

2.6.1. Scattering Effects

The probability distribution function in BTE has their positions and momenta changed after collisions (scattering) with each other or with other particles. At time t_0, only the momentum of the scattered particle change, but the instantaneous position keeps. A scheme of particle scattering is plotted in Figure 2.5.

For no collision $\frac{\partial f}{\partial t}|_s = 0$, the particles keep the original path (dashed curve) moving, then the f_i^0 keeps original also. We have

$$\begin{aligned} f_i^0(\boldsymbol{x} - \boldsymbol{u}\Delta t, \boldsymbol{p} - \boldsymbol{F}\Delta t, t - \Delta t) &= f_i^0(\boldsymbol{x}, \boldsymbol{p}, t) \\ &= f_i^0(\boldsymbol{x} + \boldsymbol{u}\Delta t, \boldsymbol{p} + \boldsymbol{F}\Delta t, t + \Delta t), \end{aligned} \tag{2.135}$$
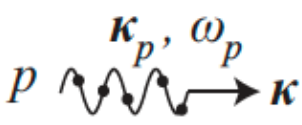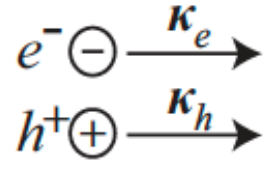
or called **equilibrium distribution**, which means the status of energy state does not change anymore (*i.e.*, occupied state is still occupied.), then having

$$\frac{Df_i^0}{Dt} = (\frac{\partial}{\partial t} + \boldsymbol{u} \cdot \nabla_x + \boldsymbol{F} \cdot \nabla_p) f_i^0 = 0. \tag{2.136}$$

For collision (scattering) cases, on the one hand, a particle moves from state $(\boldsymbol{x}, \boldsymbol{p})$ into another state $(\boldsymbol{x}, \boldsymbol{p}')$ (like particle **B** in Figure 2.5). This is defined as out-scattering,

which decreases the probability of occupation of this state. On the another hand, after scattering, a particle $(\boldsymbol{x}, \boldsymbol{p'})$ enter a state $(\boldsymbol{x}, \boldsymbol{p})$ (like particle **C** in Figure 2.5). This is called in-scattering.

Table 2.5.: Thermal equilibrium particle (energy occupancy) distribution (statistical) function $f_i^0 = (E_i)$, i = p (phonon) and e (electron) and its temperature dependence for principal energy carriers.

Attributes	Phonon	Electron and Hole
Iconic presentation		
Energy presentation	wave vector $\boldsymbol{k}_p$, dispersion $\boldsymbol{k}_p(\omega_p)$, and polarization in reciprocal lattice space $\boldsymbol{g}$	wave vector $\boldsymbol{k}_e$ band structure, and spins
Particle type	Bose-Einstein (boson)	Fermi-Dirac (fermion)
Nature of particle	particles are indistinguishable, integer spin (angular momentum), and any number of particles may occupy a given eigenstate	particles are indistinguishable, odd, half-integer spin (angular momentum) and obey the Pauli exclusion principle
Equilibrium distribution function	$\dfrac{1}{exp(\frac{E_p}{k_B T})-1}$	$\dfrac{1}{exp(\frac{E_e-\mu}{k_B T})+1}$
Energy	$E_p = E_{p,potential} + E_{p,kinetic}$	$E_p = E_{e,potential} + E_{e,kinetic}$

$\mu = E_F[1 = \frac{1}{3}(\frac{\pi k_B T}{2E_F})^2]$ is the chemical potential.

A general relation can be used for all particles as $f_i^0 = \dfrac{1}{exp(\frac{E_i-\mu}{k_B T})+\gamma}$,

where $\gamma = 1$ for fermion, $\gamma = -1$ for boson.
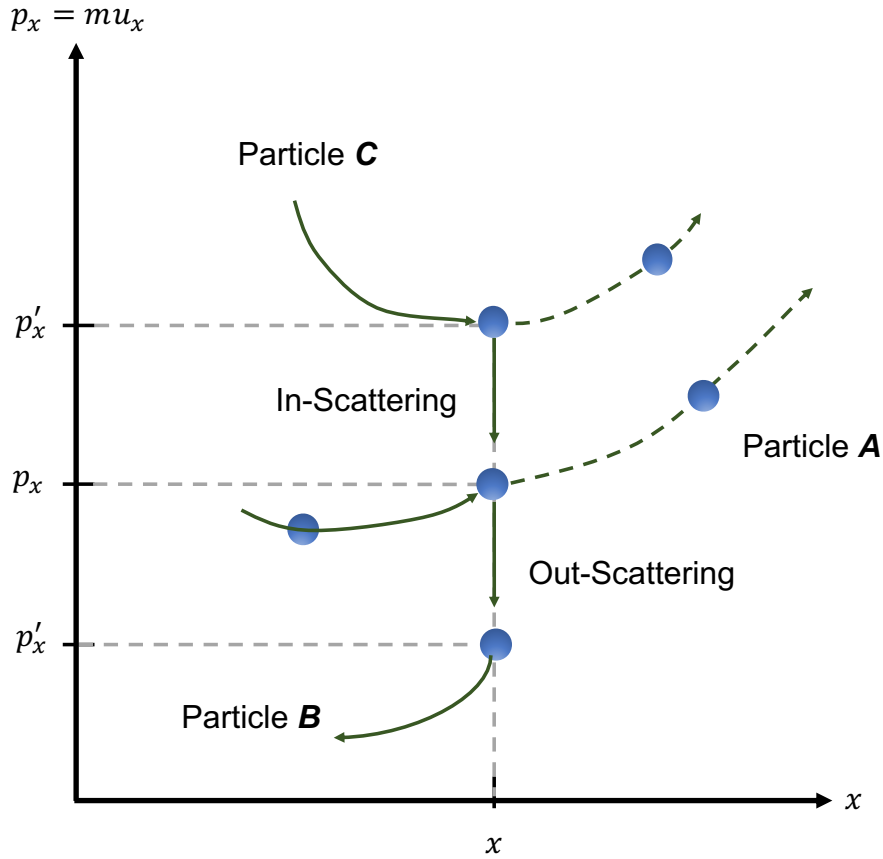
Figure 2.5.: Two-dimensional (x, p_x) rendering of particle scattering that results in a change in the particle momentum. In-scattering adds particles to state (x, p_x), whereas out-scattering removes particles from it.

Hence, for **nonequilibrium distribution**, we have

$$\frac{Df_i}{Dt} = \frac{\partial f_i}{\partial t}\big|_s + \dot{s}_{f,i},$$

(2.137)

where $\dot{s}_{f,i}$ would collect for any other source/sink not incorporated in $\frac{\partial f_i}{\partial t}\big|_s$.

Now, we sum over all possible scattering processes ($\boldsymbol{p'}$ to $\boldsymbol{p}$ and $\boldsymbol{p}$ to $\boldsymbol{p'}$), so $\frac{\partial f_i}{\partial t}\big|_s$ is

$$\frac{\partial f_i}{\partial t}\big|_s = \sum_{\boldsymbol{p'}} f_i(\boldsymbol{p'})[1 - f_i(\boldsymbol{p})]\dot{\gamma}_i(\boldsymbol{p'}, \boldsymbol{p}) - \sum_{\boldsymbol{p'}} f_i(\boldsymbol{p})[1 - f_i(\boldsymbol{p'})]\dot{\gamma}_i(\boldsymbol{p}, \boldsymbol{p'}),$$

(2.138)

where $\dot{\gamma}_i(\boldsymbol{p}', \boldsymbol{p})$ is the transition-probability rate, particle at state $\boldsymbol{p}'$ scatters to state $\boldsymbol{p}$. Eq. 2.138 relies on the sum of in- and out-scattering. The first term represents in-scattering, $f_i(\boldsymbol{p}')$ shows the probability that $\boldsymbol{p}'$ is occupied, and $[1 - f_i(\boldsymbol{p})]$ shows the probability, which can be occupied by $\boldsymbol{p}$. The second term represents out-scattering. $f_i(\boldsymbol{p})$ and $[1 - f_i(\boldsymbol{p}')]$ are the probabilities that $\boldsymbol{p}$ is occupied and $\boldsymbol{p}'$ is empty, respectively.

The sum of the collisions presented in $\frac{\partial f_i}{\partial t}|_s$ does not create or destroy carriers (particles), leading to

$$\sum_p \frac{\partial f_i}{\partial t}|_s = 0 \quad \textit{overall balance equation.} \tag{2.139}$$

This indicates that in-scattering originates from out-scattering of another state, and when adding all exchanges, the net rate of change of f_i is zero. And this is a steady state, not the equilibrium state.

2.6.2. Relaxation-Time Approximation of Scattering

As discussed above, the collision or scattering term represents particles' elastic- (where the energy of principal carrier groups is conserved) or inelastic- (energy change between principal carriers) scattering rate in BTE. Such collisions could involve phonons, electrons, fluid particles, and photons [68]. For instance, the phonon scattering is mostly by other phonons. In a three-phonon scattering, a phonon could split its energy and create two other phonons. And these scattering events return the distribution to the equilibrium state f_i^0. Then the scattering rates are generally in integral form, with the integral taking over the energy of the final (after-collision) state and the energy of the other participating particles. According to Eq. 2.134, therefore, BTE is an integral-differential equation, and the unknown function in the equation is a probability distribution function in a six-dimensional space of a particle position and momentum. In general, we have to use some approximation methods to solve it.

The relaxation-time τ_i approximation (RTA) is widely used to describe the scattering rate, i.e.,

$$f_i^0 = f_i + \frac{\partial f_i}{\partial t}|_s \tau_i + \cdots$$
$$\frac{\partial f_i}{\partial t}|_s \approx -\frac{f_i - f_i^0}{\tau_i} = -\frac{f_i'}{\tau_i} = -\dot{\gamma}_i f_i'. \tag{2.140}$$

Clearly, it indicates that the smaller τ_i, the faster f_i back to equilibrium, and $\tau_i = \frac{1}{\dot{\gamma}_i}$. This approximation is generally valid for a small force field and under elastic or isotropic scattering (collisions).

Now, we only consider the time dependence, $i.e.$, $\dot{s}_{f,i} = 0$, it yields

$$\frac{df_i(t)}{dt} = \frac{\partial f_i}{\partial t}\Big|_s = -\frac{f_i(t) - f_i^0}{\tau_i}. \tag{2.141}$$

Using $f_i(t = 0) = f_i(0)$, the solution to this equation is

$$f_i(t) = f_i^0 + [f_i(0) - f_i^0]e^{-t/\tau_i}. \tag{2.142}$$

It indicates within a small time constants τ_i, the f_i^0 is restored.

2.7. Lattice Thermal Transport

2.7.1. Anharmonic Effects

Although the harmonic phonon model is useful in many cases, there are many important physical phenomena that cannot be explained in a purely harmonic theory. Especially, for those properties with strong temperature dependent, harmonic approximation is incomplete. For instance, in a rigorously harmonic crystal, the equilibrium size is independent with temperature, however, we find finite thermal expansions in the real materials. And the quantum theory of the harmonic crystal predicts that the lattice specific heat capacity should obey the classical Dulong-Petit law at high temperatures. The failure of the high-temperature specific heat to approach this value indicates that there is an anharmonic effect. A rigorously harmonic crystal would have an infinite thermal conductivity. However, this is incorrect. After considering the anharmonic effects the thermal conductivity of an insulating solid is finite. This is probably the most important transport property determined by the anharmonic effects, but they also play essential roles in almost any of the processes by which the lattice vibrations transmit energy. Beyond the harmonic approximation, the potential energy of lattice can be expanded as

$$\Phi = \Phi^{eq} + \Phi^{harm} + \Phi^{anh}, \tag{2.143}$$

where Φ^{eq}, Φ^{harm}, and Φ^{anh} represent the equilibrium, harmonic, and anharmonic potential energy of the lattice, respectively.

We have recognized that phonon frequencies of a real crystal are volume-dependent. Hence, we can in principle use the quasi-harmonic approximation to describe volume-dependent thermal effects, such as thermal expansion. It is based on the assumption that the harmonic approximation holds for every value of the lattice constant, which is to be viewed as an adjustable parameter. More details will be discussed in the following section. Now, we give a brief discussion of the thermal expansion coefficient (α) [86],

$$\alpha = \frac{C_V \gamma}{3B},\tag{2.144}$$

where $B = -V(\partial P / \partial V)_T$ is the bulk modulus. γ is the overall Grüneisen parameter. The Grüneisen parameter is defined for every phonon mode as

$$\gamma_i = -\frac{\partial \ln \omega_i}{\partial \ln V},\tag{2.145}$$

where i indicates a phonon mode. The total Grüneisen parameter is the sum of all γ_i. It is a measure of the anharmonicity of the system.

How phonon anharmonicity emerges in a real system is complicated to understand. In past decades, people used advanced measurement and computational methods to determine the origin of phonon anharmonicities, such as lone-pair electrons, resonant bindings, polar covalent bonding, and buckling structures [87, 88, 89]. Meanwhile, the concept of phonon "anharmonicity engineering" [90, 91] has also been proposed recently to regulate the thermal properties in numerous materials, like thermoelectric materials and thermal barrier coatings [92].

2.7.2. Phonon-Phonon Interactions

Up to now, by using harmonic and single electron approximations, we have assumed that the energy and propagation properties of any excitation in the system are entirely unaffected by the presence or absence of other excitations, and the excited states of the system are treated as an assembly of completely independent phonons and electrons. In fact, through those approximations, the transport properties are incorrect. Now, we rewrite the full Hamiltonian of a crystal as

$$H = H_n + H_e + H_{ep}\tag{2.146}$$

where H_e is for the electronic Hamiltonian, H_{ep} is for the electron-phonon interactions.

From Eq. 2.89, we know that the third and higher order terms indicate the interactions among phonons. The Hamiltonian for the lattice including anharmonicity can be written as

$$H_n = H_0 + H_A, \tag{2.147}$$

where H_0 is the above discussed harmonic part of the Hamiltonian. H_A is the anharmonic terms

$$H_A = \sum_{n \geq 3} \frac{1}{n!} \sum_{\substack{k_1 \ldots k_n \\ \alpha_1 \ldots \alpha_n \\ \mathbf{R_1} \ldots \mathbf{R_n}}} \Phi^{k_1 \ldots k_n}_{\alpha_1 \ldots \alpha_n}(\mathbf{R_1} \ldots \mathbf{R_n}) u^{k_1}_{\alpha_1}(\mathbf{R_1}) \ldots u^{k_n}_{\alpha_n}(\mathbf{R_n}). \tag{2.148}$$

Usually, it is easy to work with the quantized phonon field by using the second quantization formalism. The atomic displacement can be expressed by using the phonon field operator $A(\lambda) = a(\lambda) + a^\dagger(\lambda)$, which is constructed from the momentum and position operators of the Hamiltonian, $\lambda \equiv \{\mathbf{q}, j\}$, the lower $a(\lambda)$ and raising $a^\dagger(\lambda)$ operators are the phonon annihilation and creation operators, respectively. This is also called the occupation number representation, in which n phonons of wave-vector $\mathbf{q}$ are created with n raising operations as $(a^\dagger(\lambda))^n |0\rangle_\lambda = (n!)^{-1/2} |n\rangle_\lambda$. Then the displacement operators is represented as

$$u^k_\alpha(\mathbf{R}) = \sum_\lambda \sqrt{\frac{\hbar}{2NM_k \omega_\lambda}} \varepsilon \alpha^k(\lambda) e^{i\mathbf{q} \cdot \mathbf{R}} A(\lambda). \tag{2.149}$$

Substitution into the Hamiltonian for the nth order anharmonic term yields:

$$\begin{aligned}
H_A^{(n)} &= \frac{1}{n!} \sum_{\substack{k_1 \ldots k_n \\ \alpha_1 \ldots \alpha_n \\ \mathbf{R_1} \ldots \mathbf{R_n}}} \Phi^{k \ldots k_n}_{\alpha \ldots \alpha_n}(\mathbf{R_1} \ldots \mathbf{R_n}) u^{k_1}_{\alpha_1}(\mathbf{R_1}) \ldots u^{k_n}_{\alpha_n}(\mathbf{R_n}) \\
&= \frac{1}{n!} \left(\frac{\hbar}{2N}\right)^{n/2} \sum_{\lambda_1 \ldots \lambda_n} \sum_{\substack{k_1 \ldots k_n \\ \alpha_1 \ldots \alpha_n \\ \mathbf{R_1} \ldots \mathbf{R_n}}} \frac{\varepsilon^{k_1}_{\alpha_1}(\lambda_1) \ldots \varepsilon^{k_n}_{\alpha_n}(\lambda_n)}{(M_{k_1} \omega_{\lambda_1} \ldots M_{k_n} \omega_{\lambda_n})^{1/2}} \Phi^{k \ldots k_n}_{\alpha \ldots \alpha_n}(\mathbf{R_1} \ldots \mathbf{R_n}) \\
&\quad \times e^{i(\mathbf{q_1} \cdot \mathbf{R_1} + \cdots + \mathbf{q_n} \cdot \mathbf{R_n})} A(\lambda_1) \ldots A(\lambda_n)
\end{aligned} \tag{2.150}$$

We in principle expand the H_A in any chosen coordinate [71]. For instance, the anharmonic Hamiltonian expanded in powers of the Fourier components of the ionic displacement in reciprocal space:

$$H_A = \sum_{n \geq 3} \frac{1}{n!} \sum_{\substack{k_1 \ldots k_n \\ \alpha_1 \ldots \alpha_n \\ \mathbf{q_1} \cdots \mathbf{q_n}}} \Phi_{\alpha_1 \ldots \alpha_n}^{k_1 \ldots k_n}(\mathbf{q_1} \ldots \mathbf{q_n}) u_{\alpha_1}^{k_1}(\mathbf{q_1}) \ldots u_{\alpha_n}^{k_n}(\mathbf{q_n}), \qquad (2.151)$$

where the α-component of the Fourier-transformed displacement vector of atom k of wave vector $\mathbf{q}$ is

$$u_\alpha^k(\mathbf{q}) = \frac{1}{\sqrt{N}} \sum_{\mathbf{R}} e^{-i\mathbf{q} \cdot \mathbf{R}} u_\alpha^k(\mathbf{R}) \qquad (2.152)$$

Interatomic Force-Constants (IFCs) are the derivatives of the potential with respect to the displacements, from Eq. 2.89, the nth order IFCs is expressed as

$$\Phi_{\alpha \cdots \alpha_n}^{k_1 \cdots k_n}(\mathbf{R_1} \ldots \mathbf{R_n}) = \frac{\partial^n \Phi}{\partial u_{\alpha_1}^{k_1}(\mathbf{R_1}) \cdots \partial u_{\alpha_n}^{k_n}(\mathbf{R_n})}. \qquad (2.153)$$

and similarly, the Fourier-transformed IFCs matrix:

$$\Phi_{\alpha \cdots \alpha_n}^{k_1 \cdots k_n}(\mathbf{q_1} \ldots \mathbf{q_n}) = \frac{\partial^n \Phi}{\partial u_{\alpha_1}^{k_1}(\mathbf{q_1}) \cdots \partial u_{\alpha_n}^{k_n}(\mathbf{q_n})}. \qquad (2.154)$$

and we have

$$\Phi_{\alpha \cdots \alpha_n}^{k_1 \cdots k_n}(\mathbf{q_1} \ldots \mathbf{q_n}) = \frac{1}{N} \sum_{\mathbf{R_1} \ldots \mathbf{R_n}} \Phi_{\alpha \cdots \alpha_n}^{k_1 \cdots k_n}(\mathbf{R_1} \ldots \mathbf{R_n}) e^{i(\mathbf{q_1} \cdot \mathbf{R_1} + \cdots + \mathbf{q_n} \cdot \mathbf{R_n})}. \qquad (2.155)$$

Among that, the second order (harmonic) IFCs ($\Phi_{\alpha_1 \alpha_2}^{k_1 k_2}$) are the harmonic response of the force acting on atom k_1 (α_1-direction) resulted form the displacement of atom k_2 (α_2-direction). Based on the finite displacement difference method, the second order IFCs tensor can be obtained as

$$\Phi_{\alpha_1 \alpha_2}^{k_1 k_2} = \frac{\partial^2 \Phi}{\partial u_{\alpha_1}^{k_1} \partial u_{\alpha_2}^{k_2}} = \begin{bmatrix} \frac{\partial^2 \Phi}{\partial u_x^{k_1} \partial u_x^{k_2}} & \frac{\partial^2 \Phi}{\partial u_x^{k_1} \partial u_y^{k_2}} & \frac{\partial^2 \Phi}{\partial u_x^{k_1} \partial u_z^{k_2}} \\ \frac{\partial^2 \Phi}{\partial u_y^{k_1} \partial u_x^{k_2}} & \frac{\partial^2 \Phi}{\partial u_y^{k_1} \partial u_y^{k_2}} & \frac{\partial^2 \Phi}{\partial u_y^{k_1} \partial u_z^{k_2}} \\ \frac{\partial^2 \Phi}{\partial u_z^{k_1} \partial u_x^{k_2}} & \frac{\partial^2 \Phi}{\partial u_z^{k_1} \partial u_y^{k_2}} & \frac{\partial^2 \Phi}{\partial u_z^{k_1} \partial u_z^{k_2}} \end{bmatrix}. \tag{2.156}$$

Based on the second order IFCs the dynamical matrix can be constructed and the phonon dispersion are obtained by diagonalizing the dynamical matrix. The anharmonic nature of the system is described using the third order IFCs, while the contributions of the fourth and higher order terms are usually neglected. The anharmonic IFCs are evaluated based on the third order derivatives of the total potential energy with respect to the atomic displacements

$$\Phi_{\alpha_1 \alpha_2 \alpha_3}^{k_1 k_2 k_3} = \frac{\partial^3 \Phi}{\partial u_{\alpha_1}^{k_1} \partial u_{\alpha_2}^{k_2} \partial u_{\alpha_3}^{k_3}}, \tag{2.157}$$

which is the response along the α_1 direction on atom k due to the displacement of atom k_2 (α_2-direction) and atom k_3 (α_3-direction). Using the anharmonic IFCs, the scattering matrix can be constructed, based on which one can calculate the three-phonon scattering rates and then obtain the phonon lifetime.

Anharmonic Phonon Coupling Tensor

On the other hand, the anharmonic Hamiltonian H_A can also be expanded in powers of phonon field operators $A(\lambda)$, which is

$$H_A = \sum_{\lambda_1 \dots \lambda_n} V_n(\lambda_1, \dots, \lambda_n) A(\lambda_1) \dots A(\lambda_n) \tag{2.158}$$

As mentioned above, the phonon field operator is the sum of an annihilation and creator operator, set up as:

$$A(\lambda) = A(\mathbf{q} j) = a(\mathbf{q} j) + a^\dagger(-\mathbf{q} j) \tag{2.159}$$

as well as

$$V_n(\lambda_1, \dots, \lambda_n) = \frac{1}{n!} \frac{\partial^n \varepsilon}{\partial A(\lambda_1) \dots \partial A(\lambda_n)}. \tag{2.160}$$

Hence, this is the anharmonic phonon coupling tensor, which is the nth derivative of the total energy with respect to the $A(\lambda)$. Now, using Eq. 2.149, we have

$$\sum_{\lambda_1 \dots \lambda_n} V_n(\lambda_1, \dots, \lambda_n) A(\lambda_1) \dots A(\lambda_n)$$

$$= \frac{1}{n!} \sum_{\substack{k_1 \dots k_n \\ \alpha_1 \dots \alpha_n \\ \mathbf{R_1} \dots \mathbf{R_n}}} \Phi_{\alpha \dots \alpha_n}^{k \dots k_n}(\mathbf{R_1} \dots \mathbf{R_n}) u_{\alpha_1}^{k_1}(\mathbf{R_1}) \dots u_{\alpha_n}^{k_n}(\mathbf{R_n})$$

$$= (\frac{\hbar}{2N})^{n/2} \sum_{\substack{k_1 \dots k_n \\ \alpha_1 \dots \alpha_n \\ \mathbf{R_1} \dots \mathbf{R_n}}} \Phi_{\alpha \dots \alpha_n}^{k \dots k_n}(\mathbf{R_1} \dots \mathbf{R_n}) e^{i(\mathbf{q_1} \cdot \mathbf{R_1} + \dots + \mathbf{q_n} \cdot \mathbf{R_n})} \qquad (2.161)$$

$$\times \sum_{\lambda_1 \dots \lambda_n} \frac{\varepsilon_{\alpha_1}^{k_1}(\lambda_1)}{\sqrt{M_{k_1} \omega_{\lambda_1}}} \dots \frac{\varepsilon_{\alpha_n}^{k_n}(\lambda_n)}{\sqrt{M_{k_n} \omega_{\lambda_n}}} A(\lambda_1) \dots A(\lambda_n)$$

which indicates a general expression for $V_n(\lambda_1, \dots, \lambda_n)$:

$$V_n(\lambda_1, \dots, \lambda_n) = \frac{1}{n!} (\frac{\hbar}{2N})^{n/2} \frac{1}{\sqrt{\omega_{\lambda_1} \cdots \omega_{\lambda_n}}} \sum_{\substack{k_1 \dots k_n \\ \alpha_1 \dots \alpha_n \\ \mathbf{R_1} \dots \mathbf{R_n}}} \Phi_{\alpha \dots \alpha_n}^{k_1 \dots k_n}(\mathbf{R_1} \dots \mathbf{R_n})$$

$$\times e^{i(\mathbf{q_1} \cdot \mathbf{R_1} + \dots + \mathbf{q_n} \cdot \mathbf{R_n})} \frac{\varepsilon_{\alpha_1}^{k_1}(\lambda_1)}{\sqrt{M_{k_1}}} \dots \frac{\varepsilon_{\alpha_n}^{k_1}(\lambda_n)}{\sqrt{M_{k_n}}} \qquad (2.162)$$

If we write

$$\widetilde{\Psi}_{\alpha_1 \dots \alpha_n}^{k_1 \dots k_n}(\mathbf{q_1}, \dots, \mathbf{q_n}) = \sum_{\mathbf{R_1} \dots \mathbf{R_n}} \frac{\Phi_{\alpha \dots \alpha_n}^{k_1 \dots k_n}(\mathbf{R_1} \dots \mathbf{R_n}) e^{i(\mathbf{q_1} \cdot \mathbf{R_1} + \dots + \mathbf{q_n} \cdot \mathbf{R_n})}}{\sqrt{M_{k_1} \cdots M_{k_n}}} \qquad (2.163)$$

then

$$V_n(\lambda_1, \dots, \lambda_n) = (\frac{\hbar}{2N})^{n/2} \frac{1}{\sqrt{\omega_{\lambda_1} \cdots \omega_{\lambda_n}}} \sum_{\substack{k_1 \dots k_n \\ \alpha_1 \dots \alpha_n}} \widetilde{\Psi}_{\alpha_1 \dots \alpha_n}^{k_1 \dots k_n}(\mathbf{q_1} \dots \mathbf{q_n}) \varepsilon_{\alpha_1}^{k_1}(\lambda_1) \dots \varepsilon_{\alpha_n}^{k_n}(\lambda_n) \quad (2.164)$$

Therefore, $\widetilde{\Psi}^{k_1...k_n}_{\alpha_1...\alpha_n}(\mathbf{q_1},...,\mathbf{q_n})$ is defined as a nth order dynamical tensor:

$$\widetilde{\Psi}^{k_1...k_n}_{\alpha_1...\alpha_n}(\mathbf{q_1},...,\mathbf{q_n}) = \frac{1}{\sqrt{M_{k_1}\cdots M_{k_n}}}\frac{\partial^n \varepsilon}{\partial u^{k_1}_{\alpha_1}(\mathbf{q_1})...\partial u^{k_n}_{\alpha_n}(\mathbf{q_n})}. \tag{2.165}$$

Harmonic dynamical matrix is hence given by

$$\widetilde{\Psi}^{k_1 k_2}_{\alpha_1 \alpha_2}(\mathbf{q_1}\mathbf{q_2}) = \frac{1}{\sqrt{M_{k_1}M_{k_2}}}\frac{\partial^2 \varepsilon}{\partial u^{k_1}_{\alpha_1}(\mathbf{q_1})\partial u^{k_2}_{\alpha_2}(\mathbf{q_2})}. \tag{2.166}$$

Furthermore, dividing by the square root of the atomic mass, we have the third-order dynamical tensor

$$\widetilde{\Psi}^{k_1 k_2 k_3}_{\alpha_1 \alpha_2 \alpha_3}(\mathbf{q_1}\mathbf{q_2}\mathbf{q_3}) = \frac{1}{\sqrt{M_{k_1}M_{k_2}M_{k_3}}}\frac{\partial^3 \varepsilon}{\partial u^{k_1}_{\alpha_1}(\mathbf{q_1})\partial u^{k_2}_{\alpha_2}(\mathbf{q_2})\partial u^{k_3}_{\alpha_3}(\mathbf{q_3})}. \tag{2.167}$$

Hence, higher order dynamical tensors are derivatives of the harmonic dynamical matrix with respect to atomic displacements with wave vector $\mathbf{q}$ in the Brillouin zone

$$\widetilde{\Psi}^{k_1 k_2 k_3}_{\alpha_1 \alpha_2 \alpha_3}(\mathbf{q_1}\mathbf{q_2}\mathbf{q_3}) = \frac{1}{\sqrt{M_{k_3}}}\frac{\partial}{\partial u^{k_3}_{\alpha_3}(\mathbf{q_3})}\widetilde{\Psi}^{k_1 k_2}_{\alpha_1 \alpha_2}(\mathbf{q_1}\mathbf{q_2}),$$

$$u^k_\alpha(\mathbf{q}) = \sum_j (\frac{\hbar}{2NM_k\omega_\lambda})^{\frac{1}{2}}\varepsilon^k_\alpha(\lambda)A(\lambda), \tag{2.168}$$

$$A(\lambda) = \sum_{k\alpha}(\frac{2NM_k\omega_\lambda}{\hbar})^{\frac{1}{2}}\varepsilon^k_\alpha(\lambda)^* u^k_\alpha(\mathbf{q}),$$

where $\varepsilon^k_\alpha(\lambda)$ is the displacement pattern for mode $\lambda \equiv \{\mathbf{q}, j\}$, where $\mathbf{q}$ is wave vector and j is the phonon branch index. Hence, for example, the third-order anharmonic coupling tensor is

$$V_3(\lambda_1, \lambda_2, \lambda_3) = (\frac{\hbar}{8N^3\omega_1\omega_2\omega_3})^{\frac{1}{2}}\sum_{\substack{k_1...k_n \\ \alpha_1...\alpha_n}}\frac{\partial \Psi^{k_1 k_2}_{\alpha_1 \alpha_2}(\mathbf{q_1}, \mathbf{q_2})}{\partial u^{k_3}_{\alpha_3}(\mathbf{q_3})}\frac{\varepsilon^{k_1}_{\alpha_1}(\lambda_1)}{\sqrt{M_{k_1}}}\frac{\varepsilon^{k_2}_{\alpha_2}(\lambda_2)}{\sqrt{M_{k_2}}}\frac{\varepsilon^{k_1}_{\alpha_3}(\lambda_3)}{\sqrt{M_{k_3}}} \tag{2.169}$$

As a result, a phonon of the wave vector $\mathbf{q}$ and the branch j of the dispersion spectrum $\omega_j(\mathbf{q})$ will decay into other phonons in a finite time. Phonon–phonon interactions involve different number of phonons in different interaction process. Because of the conservation of energy and momentum, details of the phonon dispersions are crucial for calculating the anharmonic behaviour of phonons. If we use a δ function to indicate that the conservation of lattice momentum $\mathbf{q_1} + \mathbf{q_2} + \mathbf{q_3} = \mathbf{g}$, and $\mathbf{g} = 0$ and $\mathbf{g} \neq 0$ represent the Normal and Umklapp process of the three phonon scattering, respectively. Umklapp processes allow many more three-phonon interactions, but the phonon wave-vectors must be of length comparable to the reciprocal lattice vector for this to be possible. Umklapp scattering is one process limiting the thermal conductivity in crystalline materials.

2.7.3. Phonon Boltzmann Transport Equation

In general, the net heat flux vector of a system generated by a change in the distribution function of energy carriers can be expressed as

$$\mathbf{J} = \sum_\alpha \frac{1}{C\pi^3} \int [E_p(\mathbf{k}) - \mu] \mathbf{u}_p(\mathbf{k}) f'_p(\mathbf{k}) \mathrm{d}\mathbf{k}, \tag{2.170}$$

where $C\pi^3$ represents the volume of the system, and $C = 8$ is for phonons and $C = 4$ is for electrons (because of spin degeneracy). E_p means the carrier energy, μ represents its chemical potential, $\mathbf{u}_p$ is the carrier velocity (group), and f'_p is the deviation of the mode population from the equilibrium distribution.

Now, we only consider phonons. The sum is over all mode polarizations, the chemical potential is zero, and the phonon group velocity is defined as carrier speed. And the heat flux (Eq. 2.170) can be compared with the Fourier law ($\mathbf{J} = -\mathbf{K}_p \cdot \nabla T$), and we can have an expression for the thermal conductivity.

The steady-state BTE (with no external force and source), for a single-phonon mode (as listed in Table 2.4) needs

$$\mathbf{u}_p \cdot \nabla f_p = \frac{\partial f_p}{\partial t}\big|_s \quad \text{phonon BTE.} \tag{2.171}$$

If the phonon population is only influenced by the temperature, then introducing temperature gradient we have

$$\mathbf{u}_p \cdot \nabla f_p = \mathbf{u}_p \cdot \frac{\partial f_p}{\partial T} \nabla T = \mathbf{u}_p \cdot \nabla T \frac{\partial f_p}{\partial T} \tag{2.172}$$

Defining $f_p = f_p^\circ + f_p'$, where f_p° is the equilibrium phonon distribution, we assume the deviations from equilibrium f_p' are independent of temperature, then having

$$\frac{\partial f_p}{\partial T} \simeq \frac{\partial f_p^\circ}{\partial T}. \tag{2.173}$$

Using the relaxation-time approximation method for the collision term, we have

$$\frac{\partial f_p}{\partial t}\big|_s = \frac{f_p^\circ - f_p}{\tau_p} = -\frac{f_p'}{\tau_p} \quad \text{SMRT approximation.} \tag{2.174}$$

So this is the single-mode relaxation time (SMRT) approximation for a phonon mode. The relaxation time τ_p describes the temporal response of the system when that particular phonon mode is activated. In this regard, instead of temperature gradient, microwave/ultrasonic driving forces can also lead to thermal conductivity. Under these assumptions, phonon BTE becomes

$$f_p' = -\tau_p \frac{\partial f_p^\circ}{\partial T} \mathbf{u}_p \cdot \nabla T. \tag{2.175}$$

The heat flux vector $\mathbf{J}$ can be rewritten as

$$\mathbf{J} = -\Big(\frac{1}{8\pi^3} \sum_\alpha \int E_p \tau_p \frac{\partial f_p^\circ}{\partial T} \mathbf{u}_p \mathbf{u}_p \mathrm{d}\mathbf{k}\Big) \cdot \nabla T, \tag{2.176}$$

Taking E_p to be independent of temperature, we have

$$\int E_p f_p^\circ \mathrm{d}\mathbf{k} = \frac{\langle E_p \rangle}{V}, \tag{2.177}$$

in which $\langle E_p \rangle$ is the total energy of system. Then the mode specific heat capacity is given by

$$nC_{V,p} = \frac{\partial (E_p f_p^\circ)}{\partial T}\big|_V = E_p \frac{\partial f_p^\circ}{\partial T}. \tag{2.178}$$

Therefore, the heat flux vector is

$$\mathbf{J} = -\Big(\frac{1}{8\pi^3} \sum_\alpha \int C_{V,p} \tau_p \mathbf{u}_p \mathbf{u}_p \mathrm{d}\mathbf{k}\Big) \cdot \nabla T, \tag{2.179}$$

The phonon thermal conductivity tensor is

$$\mathbf{K}_p = \frac{1}{8\pi^3} \sum_\alpha \int C_{V,p} \tau_p \mathbf{u}_p \mathbf{u}_p \mathrm{d}\mathbf{k} \tag{2.180}$$

2.7.4. Phonon Scattering Relaxation Time Models

The thermal transport properties for a solid is determined by the various scattering rates. The Matthiessen's rule can be used for combining the contributions from various scattering mechanisms, as written as

$$\frac{1}{\tau_p} = \sum_j \frac{1}{\tau_{p,j}}, \tag{2.181}$$

where τ_p represents the effective phonon relaxation time and $\tau_{p,j}$ means relaxation time caused by different scattering mechanisms.Several typical phonon scatterings are shown in Figure 2.6, including phonon-crystalline boundary scattering, phonon-impurity scattering, three-phonon scattering and phonon electron scattering, with detailed discussed as follows.

Phonon-boundary scattering

To address the grain size effect dependent phonon transport properties, the phonon boundary scattering due to diffuse boundary absorption/emission should be considered. It is also called Casimir boundary scattering. It gives a mean free path for a phonon equal to the Casimir length L, which is the length of travel of the phonon before the boundary absorption/re-emission. As shown in Figure 2.6 (a), $L = (2/\pi^{1/2})(l_1 l_2)^{1/2}$, the relaxation time is

$$\frac{1}{\tau_{p-b}} = \frac{u_{p,A}}{L} \tag{2.182}$$

This reveals ballistic transport within the crystal, with the scattering bottleneck being the grain boundary scattering. In micro-particles and nano-particles, this boundary scattering dominates at very low temperatures.

Phonon-impurity scattering

Phonon impurity scattering is similar to the Rayleigh scattering of the transverse electromagnetic waves, which is proportional to ω_p^4, the relaxation time can be estimated as

$$\tau_{p-im} = \frac{4\pi u_{p,A}^3}{V \sum_i x_i (1 - \frac{M_i}{M})^2} \omega^{-4}, \tag{2.183}$$

where the impurity i has a molecular weight M_i and mass fraction x_i. The volume is V, and the host molecular weight is M.

Phonon-electron scattering

Based on maximum phonon frequency, the phonon-electron relaxation time is calculated from a momentum balance analysis [93] as

$$\frac{1}{\tau_{p-e}} = \frac{3u_{p,A}^2}{\mu_e^2} \frac{\sigma_e}{c_{v,p}T} \tag{2.184}$$

where σ_e represents the electrical conductivity, μ_e is the electrical mobility, and $c_{v,p}$ represents the phonon heat capacity of the phonons allowed to interact with conduction electrons. The phonon–electron coupling will be discussed in the next section,
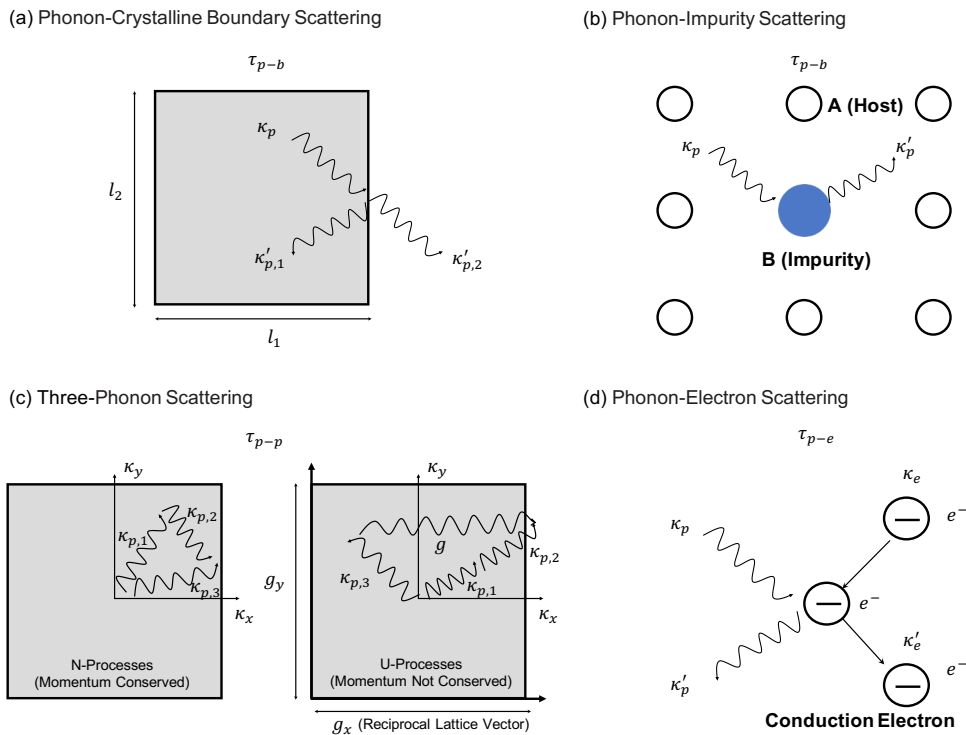
Figure 2.6.: Phonon scattering by (a) crystalline (grain) boundary, (b) impurity, (c) other phonons, and (d) electron.

and the case of acoustic phonons in elastic interaction with the conduction electrons will use a electron-phonon coupling potential. In general, phonons affect conduction electron transport more than electrons affect phonon transport. The coupling potential is weaker for metals than semiconductors, but the conduction electron density is higher in metals [68].

Phonon-phonon scattering

Phonon-phonon scattering dominates the phonon conductivity at high temperature. In general, the three-phonon interaction makes mostly contribution to the interphonon scattering. As shown in Figure 2.6(c), the phonon-phonon scattering can be divided into Normal $\tau_{p-p,N}$ (N) and Umklapp $\tau_{p-p,U}$ (U) process. Because interphonon scatterings change the energy of all phonon modes involved, it is barely expected that these processes could be exactly presented by a relaxation-time approximation. For the N-processes, the crystal momentum and energy are conserved. However, for the U-Processes, the crystal momentum is not conserved, but energy is. Therefore, we have three-phonon N-Processes

$$\boldsymbol{k_1} + \boldsymbol{k_2} = \boldsymbol{k_3} \text{ (momentum)}, \ \omega_1 + \omega_2 = \omega_3 \text{ (energy)} \tag{2.185}$$

and three-phonon U-Processes

$$\boldsymbol{k_1} + \boldsymbol{k_2} = \boldsymbol{k_3} + \boldsymbol{g} \text{ (momentum)}, \ \omega_1 + \omega_2 = \omega_3 \text{ (energy)} \tag{2.186}$$

where $\boldsymbol{g}$ represents the reciprocal lattice vector. The $\boldsymbol{g}$ is not limited to a process that flips the wave-vector summation to the neighboring reciprocal space unit cell only but can involve other cells.

Based on the in-and-out scattering in BTE and the Fermi golden rule (FGR), namely, the Peierls three-phonon scatterings are defined as [94]

$$\begin{aligned}
\frac{\partial \langle f_{p,1} \rangle}{\partial t}|_s = &\sum_{\boldsymbol{k_2}} \sum_{\alpha_2} [\sum_{\alpha_3} \dot{\gamma}_{p,\alpha_1,\alpha_2,\alpha_3}(\boldsymbol{k_1}, \boldsymbol{k_2}, -\boldsymbol{k_3}) \langle f_{p,3}(f_{p,2}+1)(f_{p,1}+1) \\
&- (f_{p,3}+1)f_{p,2}f_{p,1} \rangle \delta_D(\omega_1 + \omega_2 - \omega_3) \\
&+ \frac{1}{2} \sum_{\alpha_3} \dot{\gamma}_{p,\alpha_1,\alpha_2,\alpha_3}(-\boldsymbol{k_1}, \boldsymbol{k_2}, \boldsymbol{k_3}) \langle ((f_{p,1}+1)f_{p,2}f_{p,3} \\
&- f_{p,1}(f_{p,2}+1)(f_{p,3}+1) \rangle \delta_D(\omega_1 - \omega_2 - \omega_3)]
\end{aligned} \tag{2.187}$$

2.8. Electronic Thermal Transport

Heat conduction in solids can be determined through the Fourier law, namely $q_k = -K \cdot \nabla T$. The total conductivity K consisted of electronic thermal conductivity tensor K_e and phonon thermal conductivity tensor K_p, hence, we have $K = K_e + K_p$. Compared with lattice (*i.e.*, phonon), the heat capacity of an electron $c_{v,e}$ is relatively small, except at very high temperatures. In addition, electrons can have a net motion under an external electric field. This process would provide chances for the exchange of their kinetic energy. For example, electrons can exchange energy with lattice (phonon) through inelastic scattering in Joule heating. This electronic and thermal transport coupling is known as thermoelectricity, leading to Peltier heating/cooling.

2.8.1. Free Electron Gas

In the free electron gas model, the Fermi energy E_F is defined as the highest occupied energy level in a quantum system of non-interacting fermions (electrons) at absolute zero temperature. We can use the Fermi sphere to represent the occupied orbitals, the wave vectors at the Fermi surface have a magnitude k_F, and:

$$k_F = (3n_{e,c}\pi^2)^{1/3}, \tag{2.188}$$

where $n_{e,c}$ is the number density of conduction electrons.

$$n_{e,c} = \int_0^\infty D_e(E_e) f_e \mathrm{d}E_e, \tag{2.189}$$

The Fermi energy is defined as

$$E_F = \frac{\hbar^2 k_F^2}{2m_e}. \tag{2.190}$$

For metals, $n_{e,c}$ is found directly from the number of conduction (delocalized) electrons and is independent of temperature. For semiconductors, $n_{e,c}$ depends on temperature and on Fermi energy.

For metals, we have

$$n_{e,c} = \int_0^\infty D_e(E_e) f_e^\circ dE_e = n z_e, \quad D_e(E_e) = \frac{m_e k_F}{\pi^2 \hbar^2} = \frac{2^{1/2} m_e^{3/2} E_e^{1/2}}{\pi^2 \hbar^3}$$
$$= \int_0^{E_F} D_e dE_e = \frac{1}{3\pi^2} \left(\frac{2m_e}{\hbar^2} E_F\right)^{3/2} \tag{2.191}$$

Then the Fermi velocity based on Fermi energy and m_e is

$$u_F = \left(\frac{2E_F}{m_e}\right)^{1/2}. \tag{2.192}$$

The Fermi temperature is

$$T_F = \frac{E_F}{k_B}. \tag{2.193}$$

The Fermi momentum is

$$p_F = 2(m_e E_F)^{1/2}. \tag{2.194}$$

The electron group velocity $u_{e,g}$ is defined similarly to that for phonons as

$$u_{e,g} = \frac{1}{\hbar} \nabla_k E_e(k). \tag{2.195}$$

Further, the Fermi surface separates the occupied from unoccupied energy levels. Increasing the temperature, the kinetic energy of the electron gas increases, correspondingly the occupation of the electron states changes. The Fermi-Dirac distribution function is used to describe the probability that an orbital will be occupied from an ideal electron gas model in thermal equilibrium

$$f_e^\circ = \frac{1}{\exp\left(\frac{E_e - \mu}{k_B T}\right) + 1} = \frac{1}{\exp\left(\frac{E_e - E_F}{k_B T}\right) + 1} \tag{2.196}$$

where μ is the chemical potential and assumed to be equal to E_F.

For semiconductors, at T=0 K, all electrons occupy the valence bands. As the temperature increases, more electrons move to the conduction bands. The conductive electron density is

$$n_{e,c} = \int_0^\infty D_e(E_e) f_e(E_e) \mathrm{d}E_e \equiv \sum_k f_e[E_e(\boldsymbol{k})].$$

In general, the electron energies $E_e(\boldsymbol{x},\boldsymbol{p}) = E_{e,p}(\boldsymbol{x}) + E_{e,k}(\boldsymbol{p})$, is the sum of the potential and kinetic energies, assuming $\mu = E_F$, we have

$$f_e^\circ = \frac{1}{\exp(\frac{E_e(\boldsymbol{x},\boldsymbol{p})-\mu}{k_B T})+1} = \frac{1}{\exp[\frac{E_{e,p}(\boldsymbol{x})+E_{e,k}(\boldsymbol{p})-E_F}{k_B T}]+1}. \tag{2.197}$$

Note that, for the free-electron gas, the $\mu = E_F$, but there is a temperature dependence given by $\mu = E_F[1 - \frac{1}{3}(\frac{\pi k_B T}{2 E_F})^2 + \cdots]$, which is negligible for $T \ll \frac{E_F}{k_B}$. The potential energy $E_{e,p}(\boldsymbol{x})$ is the same as the lowest energy of the conduction band. For $\frac{E_e - E_F}{k_B T} \gg 1$ (the nondegeneracy approximation) and $E_{e,k} = \frac{p^2}{2 m_{e,e}}$ ($m_{e,e} = \frac{\hbar^2}{\frac{\partial^2 E_e(k)}{\partial k^2}|_{k=0}}$ is electron effective mass), we have

$$f_e^\circ = \exp(-\frac{E_e - E_F}{k_B T}) = \exp(\frac{E_F - E_{e,p}}{k_B T})\exp(-\frac{p^2}{2 m_{e,e} k_B T}). \tag{2.198}$$

The conduction band electron density in the nondegeneracy equilibrium is defined as

$$n_{e,c} = \frac{1}{4}(\frac{2 m_{e,e} k_B T}{\pi \hbar^2})^{3/2}\exp(\frac{E_F - E_{e,p}}{k_B T}) \quad \text{for } \frac{E_e - E_F}{k_B T} \gg 1$$
$$\equiv n_{e,F}\exp(\frac{E_F - E_{e,p}}{k_B T}), \ n_{e,F} = 2(\frac{m_{e,e} k_B T}{2\pi \hbar^2})^{3/2}. \tag{2.199}$$

The effective density of conduction band $n_{e,F}$ has a counter-part for the valence band (e.g., the hole density). Therefore, unlike metals, for semiconductor $n_{e,c}$ and E_F are temperature-dependent. The larger the E_F (μ), the larger are the number of conduction electrons (carriers). Compared with metals that have large E_F, semiconductors have a small E_F (or $n_{e,c}$). The density of electronic states in energy space $D_e(E_e)$ is the number of electric states having energy $E_e(\boldsymbol{k})$ and given as

$$D_e[E_e(\boldsymbol{k})] = \frac{2^{1/2} m_{e,e}^{3/2} E_e^{1/2}}{\pi^2 \hbar^3}. \tag{2.200}$$

This is same as electron gas for metals, except here we use the effective mass and bond energy.

2.8.2. Specific Heat Capacity of Electrons

The specific heat heat of the electron gas is defined similarly to phonon and given in terms of electron density of states as

$$n_{e,c}c_{v,e} = \frac{\partial(\langle E_e \rangle - E_F)}{\partial T}\Big|_V, \qquad (2.201)$$

where the energy of a system of electrons is defined as

$$\langle E_e \rangle = \int_0^\infty (E_e - E_F)f_e^\circ D_e(E_e)\mathrm{d}E_e. \qquad (2.202)$$

As one can see, because the Fermi energy is large, the high energy electrons are not excited until very high temperatures and this results in vanishing electronic heat capacity at low and moderate temperatures.

Then,

$$n_{e,c}c_{v,e} = \int_0^\infty (E_e - E_F)\frac{\partial f_e^\circ}{\partial T}D_e(E_e)\mathrm{d}E_e, \qquad (2.203)$$

and we have

$$c_{v,e} = \int_0^\infty (E_e - E_F)D_e(E_e)\frac{\partial}{\partial T}\frac{1}{\exp(\frac{E_e - E_F}{k_B T}) + 1}\mathrm{d}E_e. \qquad (2.204)$$

This equation can be approximated by changing the limit of the integral by using $D_e(E_e) \simeq D_e(E_F)$ and then putting this outside the integral. Then we use a variable substitution $x = (E_e - E_F)/k_B T$, having

$$n_{e,c}c_{v,e} = k_B^2 T D_e(E_F)\int_{-E_F/k_B T}^\infty \frac{x^2 e^x}{(e^x + 1)^2}\mathrm{d}x. \qquad (2.205)$$

On using the density of conduction electrons of metals, we have the electron-gas specific heat capacity as

$$\begin{aligned}
n_{e,c}c_{v,e} &= k_B^2 T \frac{3n_{e,c}}{2E_F}\int_{-E_F/k_B T}^\infty \frac{x^2 e^x}{(e^x + 1)^2}\mathrm{d}x \\
&= k_B^2 T \frac{2^{1/2}m_e^{3/2}E_F^{1/2}}{\pi^2 \hbar^3}\int_{-E_F/k_B T}^\infty \frac{x^2 e^x}{(e^x + 1)^2}\mathrm{d}x.
\end{aligned} \qquad (2.206)$$

As one known, the Fermi temperature of metal is rather large at moderate temperatures, the integral in Eq. 2.206 is small, and hence the specific heat of electron gas is small. This is because electrons with energy less than the Fermi energy are already occupied. So, very small fraction of electrons, those within $k_B T$ of E_F are able to contribute to $c_{v,e}$.

Because at moderate temperatures $k_B T \ll E_F$, and by using $n_{e,c} = \frac{N_e}{V} = \frac{k_F^3}{3\pi^2} = \frac{1}{3\pi^2}(\frac{2m_e}{\hbar^2}E_F)^{3/2}$, we have the low-temperature limit as

$$D_e(E_F) = \frac{3n_{e,c}}{2E_F}. \tag{2.207}$$

and now by using this in Eq. 2.206 for $E_F \gg k_B T$, we have

$$n_{e.c}c_{v,e} = (\frac{\pi^2 k_B T}{2E_F})n_{e,c}k_B, \tag{2.208}$$

which, we use the classical behavior for a particle, would be $3n_{e,c}k_B/2$, which is independent of the temperature and extremely large for low and moderate temperatures.

For a nondegenerate semiconductor with parabolic bands, we can use Eq. 2.199 for $E_F/k_B T \ll 1$ and then we have the specific heat capacity for nondegenerate semiconductors

$$n_{e.c}c_{v,e} = \frac{\pi^2 k_B^2 T}{2E_F}n_{e,c}(T), \tag{2.209}$$

where $n_{e.c}c_{v,e}$ is per unit volume. This equation shows a linear temperature dependence of electron specific heat at moderate temperatures in addition to the $n_{e,c}(T)$ dependence given by Eq. 2.199.

2.8.3. Electron Boltzmann Transport Equation

Similar to our treatment of phonon conductivity, we now discuss the transport properties of electrons in solids. Ziman introduced the theoretical treatment of electron transport in Ref. [95]. And Lundstrom gave an explicit introduction to electron transport in semiconductor [96]. Here, we briefly review the properties of electron transport. Under a steady-state and uniform electric field along the x direction $e_{e,x}$, the conduction

electrons in a semiconductor have $\partial f_e/\partial t = 0$ and $\nabla_x f_e = 0$. Then, using RTA ($F_x = -e_c e_{e,x}$), the Eq. 2.134 is now changed as

$$-e_c e_{e,x} \frac{\partial f_e}{\partial p_x} = -\frac{f_e - f_e^0}{\tau_e} = -\frac{f_e'}{\tau_e}. \tag{2.210}$$

In addition, using the low-field approximation, we assumed $\frac{\partial f_e}{\partial p_x} = \frac{\partial f_e^0}{\partial p_x}$, and $p_x = \hbar k_x$, we have

$$-\frac{e_c e_{e,x}}{\hbar} \frac{\partial f_e^0}{\partial k_x} = -\frac{f_e'}{\tau_e}. \tag{2.211}$$

Further, we obtain

$$f_e' = \frac{e_c}{\hbar} e_{e,x} \tau_e \frac{\partial f_e^0}{\partial k_x} \quad \text{or} \quad f_e = f_e^0 + \frac{e_c}{\hbar} e_{e,x} \tau_e \frac{\partial f_e^0}{\partial k_x}, \tag{2.212}$$

where $\tau_e = \tau_e(k)$. The equilibrium distribution function $f_e^0(k)$ is described in Table 2.5, f_e can be determined.

For instance, a nondegenetate electron energy distribution in semiconductors is considered here. We assume a one-dimensional electron motion, where the total energy in Table 2.5 is

$$E_e = E_{e,p(x)} + E_{e,k(p_x)}. \tag{2.213}$$

Then,

$$f_e^0 = \frac{1}{exp(E_e - E_F - 1)} \approx exp[-\frac{E_{e,p}(x) - E_F}{k_B T}] exp[-\frac{E_{e,k}(p_x)}{k_B T}] \text{ nondegenerate } f_e^0. \tag{2.214}$$

And we know $E_{e,k} = p^2/2m_e = \hbar^2 k_x^2/2m_e$ as well as the nondegenerate electron does not obey Pauli principle (low $n_{e,c}$ semiconductors). Hence, we obtain,

$$\frac{\partial f_e^0}{\partial k_x} = \frac{\hbar^2 k_x}{m_e k_B T} exp[-\frac{E_{e,p}(x) - E_F}{k_B T}] exp(-\frac{\hbar^2 k_x^2}{2m_e k_B T}). \tag{2.215}$$

At last,

$$f_e = f_e^0 (1 - \frac{\hbar e_c e_{e,x} \tau_e}{m_e k_B T} k_x)$$

$$= f_e^0 (1 - \frac{e_c e_{e,x} \tau_e}{m_e k_B T} p_x) \quad\quad\quad (2.216)$$

$$= f_e^0 (1 - \frac{2^{1/2} e_c e_{e,x} \tau_e}{m_e^{1/2} k_B T} E_{e,k}^{1/2}).$$

This represents that f_e is shifted on the $E_{e,k}$ axis when compared with the f_e^0. Using the Eq. 2.216, the directional electron drift velocity $u_{e,x}$, the electron mobility $\mu_{e,x}$, and electrical conductivity $\sigma_{e,x}$ can be found as

$$\mu_{e,x} = -\frac{\langle u_{e,x} \rangle}{e_{e,x}} \equiv -\frac{1}{e_{e,x}} \frac{\sum_p u_{e,x} f_e}{\sum_p f_e}, \quad \sigma_{e,x} = n_{e,c} e_c \mu_{e,x}, \quad\quad (2.217)$$

in which $n_{e,x}$ is the conduction electron density, e_c is the electron charge. Here, the relaxation time $\tau_e = 1/\dot{\gamma}_e$, indicating that the relaxation time approaches zero when the transition rate is enormous. The scattering force the distribution toward equilibrium.

2.8.4. Electronic Thermal Conductivity

For a free-electron gas, the Fermi velocity u_F is given in Eq. 2.192, and specific heat capacity $c_{v,e}$ is defined as Eq. 2.206, for electrons in thermal equilibrium with the lattice. For $T_e \neq T_p$, $c_{v,e} = \frac{3k_B T}{2}$, per electron [68].

Then the mobility is given in terms of the relaxation time by Eq. 2.217 and can in turn be written in terms of the electron mean free path $\lambda_e = u_F \langle\langle \tau_e \rangle\rangle$, and then the electrical conductivity becomes

$$\sigma_e = n_{e,c} e_c^2 \frac{\lambda_e}{m_{e,e} u_F}. \quad\quad\quad (2.218)$$

The electronic thermal conductivity can be defined because of the kinetic form of the thermal conductivity, similar to lattice thermal conductivity. We have

$$\kappa_e = \frac{1}{3} n_{e,c} c_{v,e} u_F \lambda_e. \qu\quad\quad\quad (2.219)$$

Next, combining all the properties together, we have the Wiedemann-Franz law, which is expressed as

$$\frac{\kappa_e}{\sigma_e T} = N_L = \frac{\pi^2}{3} \frac{k_B^2}{e_c^2}. \tag{2.220}$$

N_L is the Lorenz number and $N_{L,0} = 2.442 \times 10^{-8} W\Omega K^{-2}$. The Wiedemann-Franz law states that for metals at the finite temperature, the ratio of the electronic thermal conductivity to the electrical conductivity is proportional to the temperature. $N_{L,0}$ results from the fact that at low temperature. At finite temperature two mechanisms lead to a deviation of the ratio N_L from the theoretical value $N_{L,0}$. First, interactions from other thermal carrier such as phonons. Second, the inelastic scattering process. At higher temperature the contribution of phonon to thermal transport is important, which can lead to $N_L(T) \geq N_{L,0}$. Above the Debye temperature the phonon contribution to thermal transport is constant and the ratio $N_L(T)$ is again found constant.

2.8.5. Thermoelectric Power

Now, the electrical conductivity, electronic thermal conductivity, and phonon thermal conductivity are known in the previous sections. The coupling of electronic and thermal transport is known as thermoelectricity. Thermoelectricity is the direct conversion of heat into electrical energy. Thermoelectric systems are solid-state devices that either convert heat directly into electricity or transform electric power into thermal power for heating or cooling. These phenomena encompass three separately identified effects: the Seebeck effect, the Peltier effect, and the Thomson effect.

The Seebeck effect describes the buildup of a voltage difference (ΔV) across materials due to the diffusion of charge carriers along a temperature gradient (ΔT), which the material experiences because one side of it is heated or cooled. The ratio of the voltage developed to the temperature gradient ($\Delta V / \Delta T$) is related to an intrinsic property of the materials called the Seebeck coefficient S, which is given as

$$S = \frac{\Delta V}{\Delta T} \tag{2.221}$$

Determined by the type of majority carriers (*i.e.*, holes or electrons), the voltage difference (and therefore the Seebeck coefficient) can be positive or negative, *i.e.*, $S > 0$ for p-type semiconductors and $S < 0$ for n-type semiconductors. The Seebeck coefficient, which can be understood as the entropy per charge carrier, is related to the density of states (DOS).

The Peltier effect describes an electric current is passed through a junction of the two different materials, heat is generated at one junction and absorbed at the other junction, which is depended on the direction of the current. The Peltier coefficient is related to the Seebeck coefficient (Π), written as

$$\Pi = ST \tag{2.222}$$

Therefore, the Seebeck effect describes how a temperature difference creates an electrical current. The Peltier effect describes how an electrical current can create a heat flow.

The Thomson effect was predicted by Lord Kelvin, describing an electric current that is passed through a homogeneous circuit in the presence of a temperature gradient. This is now called the Thomson effect and has a minor magnitude among the thermoelectric effects.

At last, the thermoelectric performance of a material at a given absolute temperature T can be determined by the nondimensional figure of merit ZT, which is simply a particular combination of transport coefficients:

$$ZT = \frac{S^2 \sigma T}{\kappa_{tot}} = \frac{S^2 \sigma T}{\kappa_e + \kappa_p}. \tag{2.223}$$

2.9. Electron-Phonon Interaction

In the Born-Oppenheimer approximation, the Hamiltonian of the system is separated into nuclei and electron contributions. However, the interaction between electrons and phonons plays an essential role in many-particle physics, especially in the theory of transport and superconductivity in solids. For example, electron-phonon interactions (EPIs) enable the thermalization of hot carriers, determine the temperature dependence of electron band structure in solids, and give rise to phonon-mediated superconductors. In this section, we briefly review the basic formalism underlying the calculation of EPIs using DFT, and we will also discuss how the solids' superconductivity is calculated by using DFT.

2.9.1. Electron-phonon Interaction in DFT

To discuss the electron-phonon interaction, we start from the standard form of the Hamiltonian describing a coupled electron-phonon system [23]:

$$
\begin{aligned}
\hat{H} = &\sum_{n\mathbf{k}} \varepsilon_{n\mathbf{k}} \hat{c}^{\dagger}_{n\mathbf{k}} \hat{c}_{n\mathbf{k}} + \sum_{\mathbf{q}\nu} \hbar\omega_{\mathbf{q}\nu} (\hat{a}^{\dagger}_{\mathbf{q}\nu} \hat{a}_{\mathbf{q}\nu} + 1/2) \\
&+ N_p^{-1/2} \sum_{\substack{\mathbf{k},\mathbf{q} \\ mn\nu}} g_{mn\nu}(\mathbf{k},\mathbf{q}) \hat{c}^{\dagger}_{m\mathbf{k}+\mathbf{q}} \hat{c}_{n\mathbf{k}} (\hat{a}_{\mathbf{q}\nu} + \hat{a}^{\dagger}_{-\mathbf{q}\nu}) \\
&+ [N_p^{-1} \sum_{\substack{\mathbf{k},\mathbf{q},\mathbf{q}' \\ mn\nu}} g^{DW}_{mn\nu\nu'}(\mathbf{k},\mathbf{q},\mathbf{q}') \hat{c}^{\dagger}_{m\mathbf{k}+\mathbf{q}+\mathbf{q}'} \hat{c}_{n\mathbf{k}} \times (\hat{a}_{\mathbf{q}\nu} + \hat{a}^{\dagger}_{-\mathbf{q}\nu})(\hat{a}_{\mathbf{q}'\nu'} + \hat{a}^{\dagger}_{-\mathbf{q}'\nu'})],
\end{aligned}
\tag{2.224}
$$

where the first line represents the separate electron and phonon subsystems using the second-quantized formalism. The second line describes the first order atomic displacements in electron-phonon coupling. Then the third line specifies the electron-phonon coupling Hamiltonian to second order in the atomic displacements, which is barely used but plays a critical role in the theory of temperature-dependent band structures. Here $\varepsilon_{n\mathbf{k}}$ denotes the single-particle eigenvalue of an electron with crystal momentum $\mathbf{k}$ in the band n, $\omega_{\mathbf{q}\nu}$ is the frequency of a lattice vibration with crystal momentum $\mathbf{q}$ in the branch ν. $\hat{c}^{\dagger}_{n\mathbf{k}}$ and $\hat{c}_{n\mathbf{k}}$ and ($\hat{a}^{\dagger}_{\mathbf{q}\nu}$ and $\hat{a}_{\mathbf{q}\nu}$) are the associated electron (phonon) creation and destruction operators. N_p defines the number of unit cells in the supercell. The $g_{mn\nu}(\mathbf{k},\mathbf{q})$ and $g^{DW}_{mn\nu\nu'}(\mathbf{k},\mathbf{q},\mathbf{q}')$ are electron-phonon coupling matrix elements. Here the superscript "DW" stands for Debye-Waller and relates to the Debye-Waller self-energy [23].

Having outlined the Hamiltonian for electrons and phonons in crystals in previous sections, we now proceed to generate the connection between the coupling Hamiltonian and DFT calculations. The electron-phonon coupling Hamiltonian is obtained by expanding the KS effective potential in term of the nuclear displacement $\Delta\tau_{kp}$ from their equilibrium positions τ_{kp}^0. The potential to fist order in the displacements is

$$
V^{KS}(\{\tau_{kp}\}) = V^{KS}(\{\tau_{kp}^0\}) + \sum_{k\alpha p} \frac{\partial V^{KS}}{\partial \tau_{k\alpha p}} \Delta\tau_{k\alpha p}.
\tag{2.225}
$$

Using ladder operators $\Delta\tau_{k\alpha p}$, in the normal mode coordinates [23], we have

$$V^{KS} = V^{KS}(\Delta\tau^0_{kp}) + N_p^{-1/2}\sum_{\mathbf{q}\nu}\Delta_{\mathbf{q}\nu}V^{KS}(\hat{a}_{\mathbf{q}\nu} + \hat{a}^\dagger_{-\mathbf{q}\nu}),$$

$$\Delta_{\mathbf{q}\nu}V^{KS} = e^{i\mathbf{q}\cdot\mathbf{r}}\Delta_{\mathbf{q}\nu}v^{KS},$$

$$\Delta_{\mathbf{q}\nu}v^{KS} = l_{\mathbf{q}\nu}\sum_{k\alpha}(M_0/M_k)^{1/2}e_{k\alpha,\nu}(\mathbf{q})\partial_{k\alpha,\mathbf{q}}v^{KS},$$

$$l_{\mathbf{q}\nu} = [\hbar/(2M_0\omega_{\mathbf{q}\nu})]^{1/2},$$

$$\partial_{k\alpha,\mathbf{q}}v^{KS} = \sum_p e^{i\mathbf{q}\cdot(\mathbf{r}-\mathbf{R}_p)}\frac{\partial V^{KS}}{\partial\tau_{k\alpha}}|_{\mathbf{r}-\mathbf{R}_p}.$$

(2.226)

In above expressions, the $\Delta_{k\alpha,\mathbf{q}}v^{KS}$ and $\Delta_{\mathbf{q}\nu}v^{KS}$ are lattice-periodic functions. $l_{\mathbf{q}\nu}$ is the "zero-point" displacement amplitude. M_0 is an arbitrary reference mass, ensuring that $l_{\mathbf{q}\nu}$ has the dimensions of a length and is similar in magnitude to $\Delta\tau_{k\alpha p}$.

Hence, we have the electron-phonon coupling Hamiltonian as the usual second-quantized formalism

$$\hat{H}_{ep} = \sum_{n\mathbf{k},n'\mathbf{k}'}\langle\psi_{n\mathbf{k}}\left|V^{KS}(\{\tau_{kp}\}) - V^{KS}(\{\tau^0_{kp}\})\right|\psi_{n'\mathbf{k}'}\rangle\hat{c}^\dagger_{n\mathbf{k}}\hat{c}_{n'\mathbf{k}'},$$

(2.227)

where the bra and ket indicate an integral over the supercell. After introducing the electron-phonon matrix element, we have

$$\hat{H}_{ep} = N_p^{-1/2}\sum_{\substack{\mathbf{k},\mathbf{q}\\mn\nu}}g_{mn\nu}(\mathbf{k},\mathbf{q})\hat{c}^\dagger_{m\mathbf{k}+\mathbf{q}}\hat{c}_{n\mathbf{k}}(\hat{a}_{\mathbf{q}\nu} + \hat{a}^\dagger_{-\mathbf{q}\nu}),$$

(2.228)

where the electron-phonon matrix element $g_{mn\nu}(\mathbf{k},\mathbf{q})$ is defined as

$$g_{mn\nu}(\mathbf{k},\mathbf{q}) = \langle u_{m\mathbf{k}+\mathbf{q}}|\Delta_{\mathbf{q}\nu}v^{KS}|u_{n\mathbf{k}}\rangle_{uc}.$$

(2.229)

Here the subscript "uc" represents that the integral is carried out within one unit cell of the crystal.

2.9.2. Phonon-mediated Superconductivity

Now, we briefly discuss the study of phonon-mediated superconductivity [97] based on the DFT calculations of EPI. Nowadays, a semiempirical expression introduced by McMillan [28] is popular for predicting the superconducting transition temperature. The refined equation [98] is

$$k_{\mathrm{B}} T_c = \frac{\hbar \omega_{log}}{1.2} \exp[-\frac{1.04(1+\lambda)}{\lambda - \mu^*(1+0.62\lambda)}],\tag{2.230}$$

where T_c is the superconducting transition temperature, ω_{log} represents the logarithmic average of the phonon frequencies, λ is the electron-phonon coupling strength, and μ^* is the Coulomb interaction parameter. Under the isotropic version of the Eliashberg function [99], the electron-phonon coupling strength and logarithmic average of the phonon frequencies can be obtained as follows

$$\alpha^2 F(\omega) = \frac{1}{N_F} \int \frac{d\mathbf{k} d\mathbf{q}}{\Omega_{BZ}^2} \sum_{mn\nu} |g_{mn\nu}(\mathbf{k}, \mathbf{q})|^2 \delta(\varepsilon_{n\mathbf{k}} - \varepsilon_F) \times \delta(\varepsilon_{m\mathbf{k}+\mathbf{q}} - \varepsilon_F) \delta(\hbar\omega - \hbar\omega_{\mathbf{q}\nu}),\tag{2.231}$$

$$\lambda = 2 \int_0^\infty \frac{\alpha^2 F(\omega)}{\omega} d\omega,\tag{2.232}$$

$$\omega_{log} = \exp[\frac{2}{\lambda} \int_0^\infty d\omega \frac{\alpha^2 F(\omega)}{\omega} \log\omega],\tag{2.233}$$

where N_F is the DOS at the Fermi level, μ^* is usually treated as an adjustable parameter from 0.05 to 0.2. And from above expressions, it is assumed that the superconductor is isotropic and exhibits a single superconducting gap.

2.10. Machine-learned Accelerator

Machine learning approaches have changed our anticipations of what computational simulations can achieve. In other words, machine learning methods enrich the choice of simulation methods in computational materials science, which can significantly accelerate the speed of calculations and economically extend to accurate large time- and length-scales simulations. Although many successful cases have been reported in computational materials design, such as machine-learned potentials for next-generation

matter simulations [34], combining HTP with ML for novel materials design [4]. This thesis will only focus on the compressive sensing (CS) technique and its application in lattice dynamics.

2.10.1. Compressive Sensing

The CS [39] technique is a recently developed approach in the field of signal processing, which provides a simple, general, and efficient way to model building. Before discussing the power of CS for constructing physical models, the concept of itself is firstly illustrated. Usually, the definition of ℓ_p norms is required for discussing the CS,

$$\|u\|_p = \left(\sum_i |u_i|^p \right)^{1/p}, \tag{2.234}$$

of which ℓ_1 and ℓ_2 norms are special cases. The number of nonzero elements of $\vec{u}$ is often (improperly) referred to as the ℓ_0 "norm" even though it is not a norm in a strict mathematical sense.

The CS technique is used in signal processing to recover sparse signals *exactly* with far fewer samples than required standard spectral methods. Assuming a signal has the functional form

$$f(t) = \sum_{n=1}^{N} u_n e^{i2\pi nt}, \tag{2.235}$$

for a sparse signal, most of the coefficients u_n are 0. The Fourier transform is mathematically equivalent to solving the matrix equation

$$\mathbb{A}\vec{u} = \vec{f}, \tag{2.236}$$

where the matrix $\mathbb{A}$ is constructed by the values of the Fourier basis functions at the sampling times t_m, namely, it consists of rows of n terms of the form $A_{mn} = e^{i2\pi nt_m}$, and $f_m \equiv f(t_m)$ is the sampled signal [40]. The solution vector $\vec{u}$ includes the relative amounts of the different Fourier components. Using Fourier transform methods to catch all relevant frequency components of the signal needs the signal to be sampled regularly and at a frequency at least as high as a specific frequency (Nyquist frequency), a severe restriction stemming from the requirement that the linear system (described in Eq. 2.236) should not be under-determined [41]. Nevertheless, the central conception

of CS is that when the signal is sparse, one can recover the exact signal with several measurements proportional to the number of nonzero components, *i.e.*, with far fewer samples than those given by the Nyquist frequency. Conceptually, it could be achieved by searching for a solution, with which the measured time signal exactly can be reproduced and the number of nonzero Fourier components is minimum. However, this formulation leads to a discrete optimization problem, which cannot be solved in polynomial time. CS converts the problem as a simple minimization of the ℓ_1 norm of the solution, subject ot the constraint given by Eq. 2.236:

$$\min_{u} \left\{ \|\vec{u}\|_1 : \mathbb{A}\vec{u} = \vec{f} \right\}, \tag{2.237}$$

In other words, one is trying to minimize the sum of the components of the solution vector $\vec{u}$ subject to the condition that the measured signal is reproduced exactly. This constitutes the so-called basis pursuit problem. A simple illustration was given in Ref. [40]. And a mathematical theorem proven by Candès, Romberg, and Tao [100] provides the mathematical foundation of CS, which guarantees that with an overwhelming probability, any sparse signal with S nonzero components can be recovered from $M \sim S \ln N$ random measurements. N represents the total number of sensing basis functions.

2.10.2. Compressive Sensing Lattice Dynamics

As discussed above, the starting point of the computational methodology for lattice dynamics is to approximate the potential energy of interacting atoms by a Taylor expansion concerning atomic displacements, shown in Eq. 2.148. In that equation, the IFCs are also defined. Now, let us denote a column vector comprising the N irreducible set of IFCs as Φ. Then, the Taylor expansion potential (TEP) re-defined by Eq. 2.148 is written as

$$U_{TEP} = b^T \Phi, \tag{2.238}$$

where $b \in \mathbb{R}^{1 \times N}$ is a function of atomic displacements $\{u_i\}$ defined as $b = \partial U / \partial \Phi$. The atomic forces based on the TEP is defined as

$$F_{TEP} = -\frac{\partial U_{TEP}}{\partial u} = -\frac{\partial b^T}{\partial u} \Phi = A\Phi, \tag{2.239}$$

where $A \in \mathbb{R}^{3N_s \times N}$, N_s is the number of atoms. $u^T = (u_1^x, u_1^y, u_1^z, \ldots, u_{N_s}^x, u_{N_s}^y, u_{N_s}^z,)$ is the vector containing $3N_s$ atomic displacements in the supercell. It is noted that the matrix

A and force vector F_{TEP} depend on the atomic configuration of the supercell. To make this point clearer, let us denote them as $A(u)$ and $F_{TEP}(u)$. To estimate the IFCs Φ by linear regression, it is usually necessary to consider several different displacement patterns. Supposing we have N_d displacement configurations and atomic forces for each configuration obtained by DFT, Eq. 2.239 defined for each displacement configuration could be combined into a single equation as

$$\mathscr{F}_{TEP} = \mathbb{A}\Phi, \tag{2.240}$$

where $\mathscr{F}_{TEP} = [F^T(u_1), \ldots, F^T(u_{N_d})]$ and $\mathbb{A} = [A^T(u_1), \ldots, A^T(u_{N_d})]$.

To calculate the harmonic phonon frequency, harmonic IFCs are obtained using the finite-displacement approach. Hence, we can extract $\Phi_{\mu\nu}(\ell\kappa; \ell'\kappa')$ by solving the ordinary least-square (OLS) problem

$$\Phi_{\text{OLS}} = \arg\min_{\Phi} \frac{1}{2N_d} \|\mathscr{F}_{\text{DFT}} - \mathscr{F}_{\text{TEP}}\|_2^2 = \arg\min_{\Phi} \frac{1}{2N_d} \|\mathscr{F}_{\text{DFT}} - \mathbb{A}\Phi\|_2^2, \tag{2.241}$$

$\mathbb{F}_{\text{DFT}}$ is is the vector of atomic forces obtained by DFT calculations.

To overcome both of time-consuming calculations by using the finite-displacement approach and overfitting issue in OLS [101], the compressive sensing lattice dynamics (CLSD) method based CS technique is proposed by Zhou [102], which is a more robust approach to estimate anharmonic IFCs. Given training data, CS automatically picks out the relevant signals (*i.e.*, expansion coefficients in physics models) and determines their values *in one shot*. The linear problem $\mathscr{F}_{TEP} = \mathbb{A}\Phi$ is solved by minimizing the ℓ_1 norm of the coefficients,

$$\|\Phi\|_1 \equiv \sum_i |\Phi_i|, \tag{2.242}$$

while demanding a specific level of accuracy for reproducing the data. Noting that only a small fraction of IFCs has non-negligible contributions to atomic forces, and obtained the sparse solution using the least absolute shrinkage and selection operator (LASSO) technique, which is expressed as

$$\Phi_{\text{lasso}} = \arg\min_{\Phi} \frac{1}{2N_d} \|\mathbf{F}_{\text{DFT}} - \mathbb{A}\Phi\|_2^2 + \alpha \|\Phi\|_1. \tag{2.243}$$

Owing to the ℓ_1-regularization term, physically irrelevant IFCs are driven to be exactly zero and important terms are selected and calculated automatically. And the penalty term is added to the OLS equation to avoid the overfitting inherent in the OLS method. The coefficient α is a hyperparameter that controls the trade-off between the sparsity

and accuracy of the model, an optimal value of α can be estimated, for example, by cross-validation (CV).

3. Methodology and Selection of Parameters

As for the employment of the methods described in Section 2, there are lots of options/parameters involved, which deserve to be carefully studied to make sure that the results are converged via good practices of the numerical calculations. In addition, a practical workflow is also very critical for calculating target properties efficiently and economically. In this Section, we first present the workflow of using high-throughput DFT calculations for screening functional materials in detail. Then, the workflows and selection of parameters of thermodynamics and thermal transport calculations are discussed. At last, the workflows of construction of the Wannier function and electron-phonon interaction calculation are briefly discussed. More computational can be found in each corresponding result section.

3.1. High-throughput DFT Calculations

Nowadays, using high-throughput (HTP) computations based on DFT, people have been successfully screened and designed various functional materials, such as thermoelectrics [8], functional magnets [7], and so-on. One of the achievements of this thesis is designing functional magentic materials using the HTP DFT method. Here, we briefly discuss the workflow for designing magnetic materials based on HTP-DFT calculations. In addition, more fundamental aspects and detailed summaries for proper HTP calculations on magnetic materials can be found in the recently published review paper "High-throughput design of magnetic materials [19]." Figure 3.1 shows the general workflow to perform screening on stable magnetic materials used in current work, highlighting how the most fundamental target magnetic properties can be evaluated. The main steps in the workflow are:

- At the starting point, the crystal structures are the only input for the DFT calculations. The structure information can be obtained from (1) known database, such as ICSD [103], OQMD [15], and Materials Projects [104], (2) generated based on
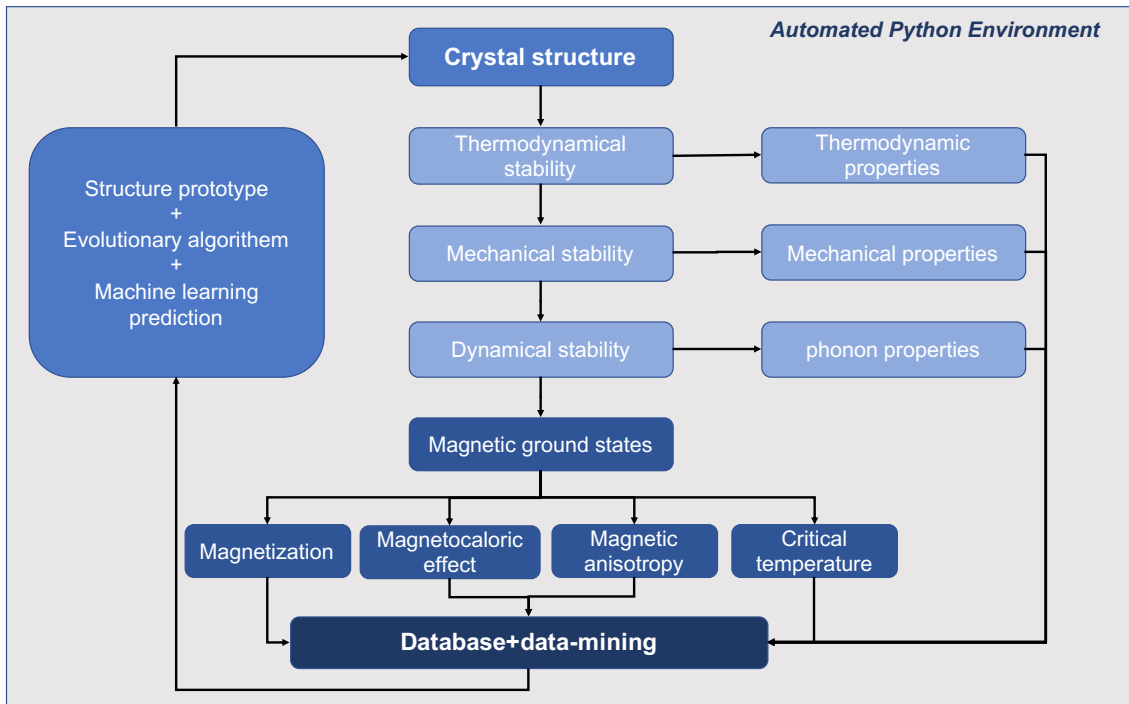
Figure 3.1.: The HTP workflow for screening magnetic materials.

evolutionary algorithms using USPEX [105] and CALYPSO [106], (3) predicted using machine learning algorithm [107], (4) combinatorial substitutions of the crystal structure prototypes.

- Three stability criteria can be evaluated, namely, the thermodynamic, mechanical, and dynamic stabilities. Thermodynamic stability is generally determined using formation energy and convex hull analysis. The mechanical and dynamical stabilities and the related properties can be obtained by evaluating the elastic constants and the phonon spectra.

- Before digging out the promising magnetic properties, the magnetic ground states of stable compounds should be determined. Then the other magnetic properties, such as magnetization, electronic structure, critical temperature, magnetic anisotropy, and magnetocaloric effect, are calculated.

- Finally, a research database is needed to avoid repetitive calculations and to share data. Moreover, the data should be findable, accessible, interoperable, and reusable. Such databases are indispensable for data mining using machine learning techniques.
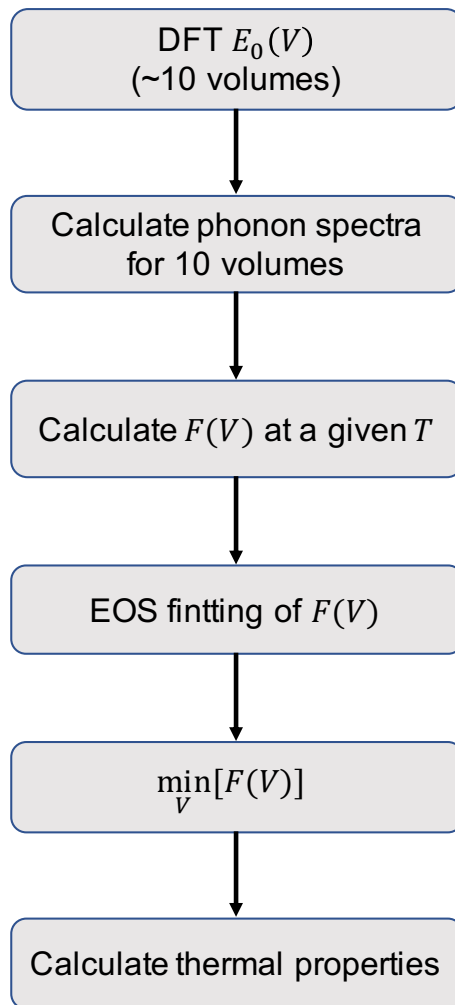
Figure 3.2.: Workflow for phonon quasi-harmonic approximation calculations.

3.2. Lattice Thermodynamics Calculations

The critical aspect in the first-principles thermodynamic calculation for solids is the phonon quasi-harmonic approximation calculations. Before doing the resource-consuming calculations, an important step to avoid possible calculation errors and dynamical instability is to examine the phonon dispersions first. After this step, the general computational protocol for the QHA method is depicted in Figure 3.2, and described below:

1. First, only the electronic ground state energies $E_0(V)$ for approximately ten volumes are calculated using DFT.

2. Next, the phonon dispersion for each volume is calculated.

3. From the phonon dispersion, $F(V)$ of each volume within a specified temperature window is calculated.

4. Then, an EOS is used to fit the calculated $F(V)$ at each considered temperature.

5. Finally, $G = F + PV$ is minimized with respect to volume at each considered temperature, which yields various thermodynamic properties.

The volume interval is usually up to $+/- 5\%$ of the equilibrium volume. Too small volume interval can result in numerical instability due to the numerical uncertainties in the static total energy calculations, particularly when one numerically computes the 1st- and the 2nd-order derivatives of the Helmholtz energy in deriving the thermodynamic quantities. It should be noted that, whenever available, analytic formulas should be used instead of a numerical 2nd-order derivative to avoid numerical errors. For example, when the phonon approach is employed, C_V has an analytic expression regarding the phonon DOS. In addition, for the non-cubic system, the lattice constants of each varied volume, namely c/a, should be optimized for accurate free energies.

3.3. Lattice Thermal Transport Calculations

Over the last decade, based on the first-principles calculations to solve the Boltzmann transport equation, people successfully reproduced experimental thermal conductivities of different materials [108, 89], and predicted many promising thermal transport properties for thermoelectric and thermal management applications [109, 110]. Here, the work flow of calculating the lattice thermal conductivities is presented, as shown in Figure 3.4. To extract the harmonic and anharmonic interatomic force constants (IFCs) from the calculated forces, we use the linear regression or compressive sensing (CS) methods [111, 102, 102], as shown in Figure 3.3. After getting the IFCs, the thermal conductivity can be calculated by solving BTE. Typically, the conventional solution of BTE on the basis of phonons within the harmonic approximation (HA) and required 3-order IFCs has successfully worked for most cases [87, 112], which can give reasonable thermal conductivity (highlighted as HP+BTE in Figure 3.4(a)). However, due to the possible structural instability or strong anharmonicity, the HP+BTE method has failed to gain the correct thermal conductivity in some structures [113], especially for pervoskites [101]. Therefore, the inclusion of lattice anharmonicity is important to be considered in the calculations of the thermal conductivity for such systems. In the last decade, several methods have been proposed to consider the anharmonic effect [114, 115, 116, 117, 113]. Among these methods, the self-consistent phonon

(SCP) theory in Ref. [117] is the one implemented in DFT calculations recently [101, 113]. Combined with the CS lattice dynamics that can train the IFCs swiftly based on the required data set of displacements and forces [111, 102, 102], the SCPH method is even capable of calculating anharmonic phonons quickly in complex systems, such as f the type-I clathrate $Ba_8Ga_{16}Ge_{30}$ [118], and even can be used for high-throughput screening [119]. To solve the SCP equation and estimate the anharmonic phonon frequencies, one has to prepare quartic IFCs. As shown in Figure 3.4, for the calculations of thermal conductivities, the SCP computations are first performed based on quartic IFCs, and then the real-space effective harmonic IFCs at each considered temperature are obtained by Fourier transformation from the temperature-dependent anharmonic dynamical matrices produced by the SCP calculations. Finally, the effective harmonic IFCs at each temperature are used to replace the harmonic IFCs to solve BTE. The whole process is named as SCP+BTE method, the more details will discussed in the Chapter 7.
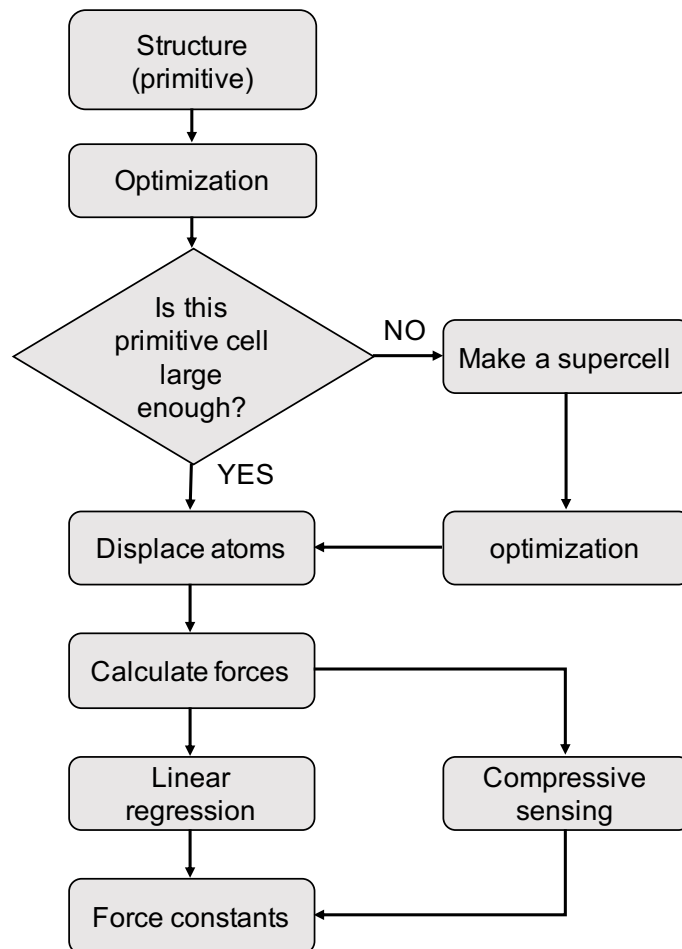
Figure 3.3.: Workflow for force constants calculations.

It is worth noting that many options and parameters are involved in the procedure of applying the HP+BTE or SCP+BTE method. Hence, the selection of parameters is crucial for predicting accurate thermal conductivities. Here, several essential options and parameters are listed as follows

- The selection of exchange-correlation functional.

- Considering long-range van der Waals interactions or not.

- The electronic wavevector grid.

- The planewave cutoff energy.

- The Fermi-Dirac function smearing.

- The thickness of vacuum layer for 2D materials.

- The energy and force tolerances for structure optimization.

- Non-analytical term correction.

- The symmetry tolerance for the structure.

- The supercell size for harmonic and anharmonic IFCs extraction.

- The displacement magnitude for generating displaced supercells for force constant extraction.

- The cutoff distance for evaluating anharmonic IFCs.

- The invariance constraints (translational and rotational invariance) for renormalizing the IFCs.

- The Q-grid size for calculating thermal conductivity.

- The broadening parameter for phonon-phonon scattering delta function.
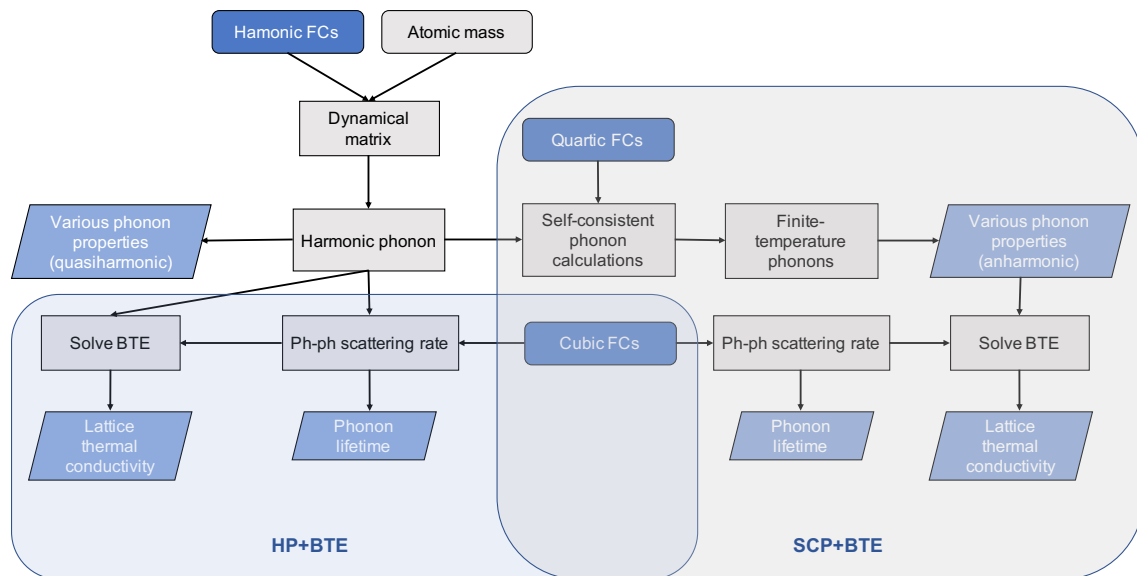
Figure 3.4.: Workflow for the lattice thermal conductivity.

Unfortunately, the list is so long that, in many cases, it is hard to conduct all the tests comprehensively. Some parameters are susceptible to specific systems. People could follow some hints in the previous references [120] to choosing options and parameters. However, some parameters should be carefully tested for convergence, such as the cutoff distance when evaluating the anharmonic IFCs and the Q-grid size when calculating the thermal conductivity. Unfortunately, little work did such thorough tests due to the high computational cost.

3.3.1. State of Art for Calculating Lattice Thermal Conductivity

After using the Debye model to describe the specific heat of crystalline solids, the harmonic oscillator is one of the most successful and most frequently discussed models, where quantum mechanics, quantum field theory, and so on can be applied to tackle real problems in condensed matter physics. It has become a pillar of solid-state physics. Among that, theoretical techniques attracted the attention of the phonon community due to their high flexibility in calculating the thermal conductivity of various materials. A variety of approximations have thus been introduced to develop an understanding of phonon driven thermal properties. For instance, Slack *et al.* proposed a simple model for the lattice thermal conductivity and a simple set of rules for its interpretation based on crystal structures, average atomic mass, bonding strength, and anharmonicity. These are quantified in terms of a material's Debye temperature and average Grüneisen parameter,

which measure the speed of sound of the heat-carrying phonons and anharmonicity, respectively [121].

Nowadays, with the recent advances in theoretical and computational techniques and the exponentially increasing computational power, the thermal conductivities of a wide range of materials can be obtained through theoretical methods. In general, there are two popular numerical methods for calculating the thermal conductivity: first principles calculations by solving the BTE and molecular dynamics (MD) simulations. The BTE method calculates thermal conductivity using force constants usually obtained from DFT. The harmonic and anharmonic interatomic force constants (IFCs) can be calculated numerically either from DFT electronic structure calculations based on supercell perturbations method [122] or from the linear response methods within density functional perturbation theory (DFPT) [123]. Moreover, the solution of BTE has been achieved so substantially beyond the typical relaxation-time approximation, from variational methods [124] to self-consistent iterative procedures [125] and self-consistent phonon (SCP) theory combining compressive sensing (CS) [111]. Various open-source code packages give the ability to calculate thermal conductivity using the BTE method, including but not limited to ShengBTE [125], Phono3py [126], and almaBTE [127]. Beyond these conventional DFT-BTE calculations, state-of-the-art phonon calculations are recently developed to treat more realistic systems. For example, it has been shown that considering four-phonon scattering has a significant contribution to the thermal conductivity of several specific structures [128], which has been implemented in Four-Phonon code [129]. Moreover, for systems with complexity and strong anharmonicity, Hellman *et al.* developed an accurate method, called the temperature-dependent effective potential (TDEP) technique, to determine the temperature-dependent anharmonic free energy, based on *ab initio* molecular dynamics (AIMD) followed by mapping onto an effective model Hamiltonian describing the lattice dynamics [115]. In addition, Tadano et al. developed an open-source code ALAMODE [113], which uses the SCP theory combined with the CSLD to obtain the anharmonic phonons quickly in very large systems [118].

Another popular branch to determine thermal conductivity is the MD approach, in which thermal conductivity is calculated by selecting an appropriate potential function to describe interatomic forces. Equilibrium molecular dynamics (EMD) and non-equilibrium molecular dynamics (NEMD) methods are employed to calculate thermal conductivity. In the EMD method that is based on the linear response theory, a system is maintained at the equilibrium state. The Green-Kubo method is an EMD simulation that can be used by employing the fluctuation-dissipation theorem [130]. The thermal conductivity is calculated based on the Green–Kubo formalism [131], as follows:

$$\kappa = \frac{V}{3k_B T^2} \int_0^\infty \langle J(t)J(0)\rangle \mathrm{d}t, \tag{3.1}$$

where κ is the lattice thermal conductivity, V is the volume of the system, k_B is the Boltzmann constant, T refers to the system temperature, J denotes the heat flux, and $\langle J(t)J(0)\rangle$ is heat-current autocorrelation function (HCACF). Within the length of integral time, HCACF must deteriorate to zero to produce convergence. Therefore, the correlation length is an important parameter to guarantee enough time for the autocorrelation function to deteriorate to zero.

To utilize the NEMD method, a temperature gradient is used in the simulation cell, resembling a measurement mechanism in experimental procedures. The thermal conductivity is inferred based on the Fourier's law as $J = -\kappa \nabla T$. There are multiple methods to calculate thermal conductivity by NEMD. In the first method, two regions are created and their desired temperatures are preserved by adding and subtracting energy to the hot zone and from the cold zone, respectively. The other method is to add and remove a known amount of energy to and from two different regions [132]. Afterward, the temperature gradient in the material is calculated to estimate the thermal conductivity. A reverse non-equilibrium molecular dynamics (RNEMD) as another method is performed using an algorithm suggested by Müller-Plathe [133]. In this method, kinetic energy displacement is imposed to create a temperature gradient within the specimen.

However, one principal limitation of the MD approach for thermal conductivity is the insufficient accuracy of the interatomic potentials, which is usually sacrificed for the simplicity of the potential form and the computational cost. On the other hand, the heavy DFT calculations to obtain the lattice thermal properties are among the limitations of the quantum methods utilized in the BTE method. Lately, with the development of artificial intelligence and machine learning, it has become possible to significantly improve the accuracy of potential functions used in MD simulations and computing IFCs required in the BTE method. Machine-learning interatomic potentials (MLIPs) offer a unique possibility to conduct first-principles multi-scale modeling, in which *ab initio* level of accuracy can be hierarchically bridged to explore lattice thermal conductivity. The main steps within the first principles hierarchical multi-scale modeling framework include four key steps: (1) DFT simulations for training data, (2) development of MLIPs, (3) classical MD simulations, and (4) calculation of effective lattice thermal conductivity. MLIPs are a type of nonparametric designed interatomic potentials to provide accuracy in the order of quantum mechanics computations. At the same time, their computational costs are in the order of empirical interatomic potentials. A nonparametric potential consists of two basic elements. The first element is called "descriptors" and the second element is a regression model that is a function of the descriptors. The goal of every machine-learning potential is the determination of the potential energy surface (PES) that is related to descriptors. Here, we summarised in Table 3.1, which lists the characteristics of four popular machine learning methods in creating interatomic potentials and their prepared software packages.

Table 3.1.: Machine learning methods in creating interatomic potentials.

Method	Descriptor	Regression model	Code
Moment Tensor Potentials (MTPs) [134]	Moment tensor	Linear	MLIP [135]
Spectral Neighbor Analysis Potential (SNAP) [136]	Bispectrum coefficients	Linear	PyXtal_FF [137]
Gaussian Approximation Potentials (GAP) [138]	SOAP kernel	Gaussian process	QUIP [139]
Neural Network Potentials (NNP) [140]	Behler–Parrinello	Artificial neural networks	RuNNer [141]

3.4. Electron-Phonon Interaction Calculations
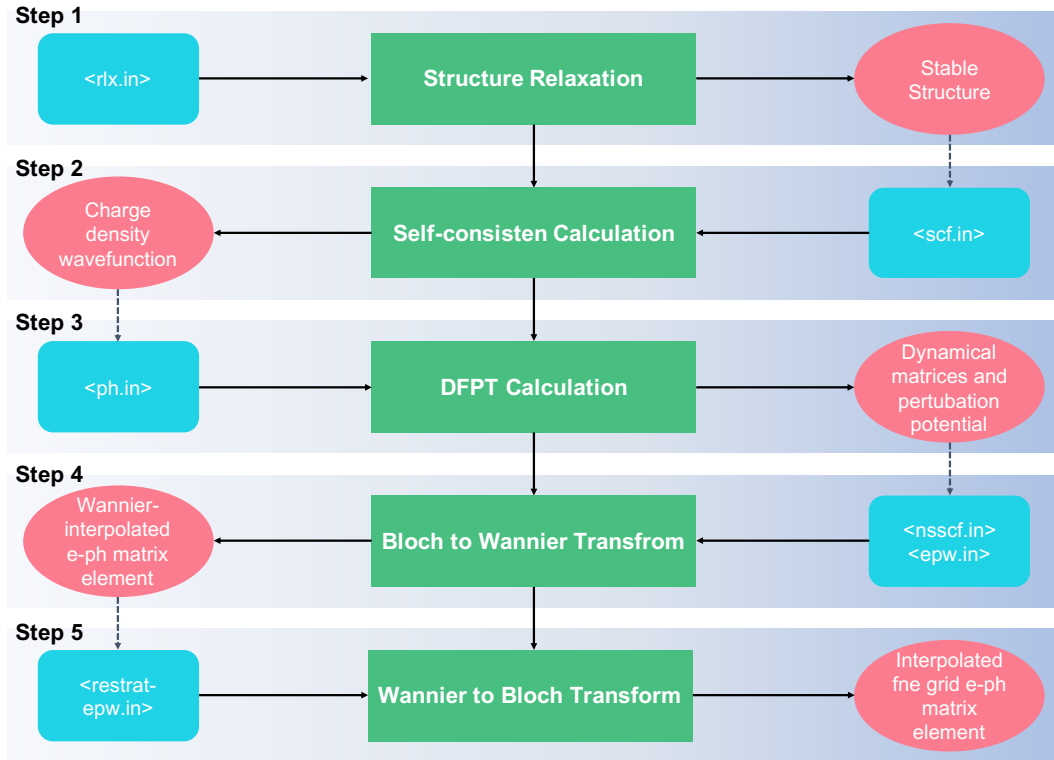
Figure 3.5.: A general workflow for electron-phonon matrix element using EPW. Green, blue, and red blocks denote the main process of calculation, input file, and useful output information, respectively.

In the section 2.9, we discussed the DFT calculation of electron-phonon coupling. There are two important aspects: obtaining the electron-phonon matrix element and using Wannier interpolation techniques to reduce computational resources. These techniques have been implemented in the Electron-Phonon with Wannier functions (EPW) code, allowing previously unpractical calculation of properties related to the electron-phonon interaction [142]. Hence, we present the workflow for calculating the electron-phonon matrix element using EPW code in Figure 3.5.

Note that a fully relaxed structure in Step 1 is essential for the following phonon calculation, which is sensitive to the structure. The self-consistent calculation in Step 2 will generate the charge density for the non self-consistent calculation. The dynamical matrices and deformation potential can be found in the DFPT calculation in Step 3, which are input files for Step 4. And in Step 4 and 5, we do two times Fourier

transform of the electron-phonon matrix elements between reciprocal space and real space.

3.4.1. Wannier Interpolation

The study of EPI from first principles requires evaluating Brillouin-zone integrals of functions that exhibit strong fluctuations. In DFT total energy calculations, we usually discretize the Brillouin zone using meshes of the order of 10^3 points. However, the numerical convergence of EPI calculations demands much denser grids, sometimes with as many as 10^6 wave vectors [143]. Determining phonon frequencies $\omega_{\mathbf{q}v}$ and perturbations $\Delta_{\mathbf{q}v} v^{KS}(\mathbf{r})$ for such a large number of wave vectors is a prohibitive work, since every calculation is roughly as expensive as one total energy minimization. In practical DFT calculations, we use an efficient electron-phonon Wannier interpolation technique based on maximally localized Wannier functions (MLWF) to perform the calculations of EPI.

The Wannier function describes a Fourier transform of the extended Bloch wave functions, given as

$$\mathrm{w}_{mp}(\mathbf{r}) = N_p^{-1} \sum_{n\mathbf{k}} e^{i\mathbf{k}\cdot(\mathbf{r}-\mathbf{R}_p)} U_{nm\mathbf{k}} u_{n\mathbf{k}}(\mathbf{r}), \tag{3.2}$$

where $U_{nm\mathbf{k}}$ expresses a unitary matrix in the indices m and n. One can consider electron bands $\varepsilon_{n\mathbf{k}}$ with eigenfunctions $\psi_{n\mathbf{k}}$, where the index n is restricted to a set of bands that are separated from all other bands by finite energy gaps above and below. These bands are referred to as "composite energy bands" [144]. In addition, we know the $u_{n\mathbf{k}}(\mathbf{r})$ is lattice periodic. Then, Wannier functions have the property $\mathrm{w}_{mp}(\mathbf{r}) = \mathrm{w}_{m0}(\mathbf{r} - \mathbf{R_p})$. The inverse transformation of Eq. 3.2 is

$$u_{n\mathbf{k}}(\mathbf{r}) = \sum_{mp} e^{i\mathbf{k}\cdot(\mathbf{r}-\mathbf{R}_p)} U_{mn\mathbf{k}}^{\dagger} \mathrm{w}_{mp}(\mathbf{r}). \tag{3.3}$$

Note that, the unitary matrix $U_{nm\mathbf{k}}$ is completely arbitrary, and therefore there exists considerable freedom in the construction of Wannier functions. Marzari and Vanderbilt exploited this degree of freedom to construct Wannier functions that are maximally localized. There is a comprehensive and up-to-date review of the theory and applications of MLWFs in Ref. [145].

In 2007, Giustino *et al.* [146, 143] used Wannier functions for evaluation EPI. The electron-phonon matrix element in the Wannier representation is

$$g_{mnk\alpha}(\mathbf{R}_p, \mathbf{R}_{p'}) = \langle \mathrm{w}_{m0}(\mathbf{r}) | \frac{\partial V^{KS}}{\partial \tau_{k\alpha}} (\mathbf{r} - \mathbf{R}_{p'}) | \mathrm{w}_{n0}(\mathbf{r} - \mathbf{R}_p) \rangle_{sc}, \qquad (3.4)$$

where the subscript "sc" represents that the integral is over the supercell. The relation between $g_{mnk\alpha}(\mathbf{R}_p, \mathbf{R}_{p'})$ and $g_{mn\nu}(\mathbf{k}, \mathbf{q})$ is

$$g_{mn\nu}(\mathbf{k}, \mathbf{q}) = \sum_{pp'} e^{i(\mathbf{k} \cdot \mathbf{R}_p + \mathbf{q} \cdot \mathbf{R}'_p)} \times \sum_{m'n'k\alpha} U_{mm'\mathbf{k}+\mathbf{q}} g_{m'n'k\alpha}(\mathbf{R}_p, \mathbf{R}_{p'}) U^{\dagger}_{n'n\mathbf{k}} u_{k\alpha, \mathbf{q}\nu}, \qquad (3.5)$$

where $u_{k\alpha, \mathbf{q}\nu} = (\hbar/2M_k \omega_{\mathbf{q}\nu})^{1/2} e_{k\alpha\nu}(\mathbf{q})$ and $e_{k\alpha\nu}(\mathbf{q})$ are the eigenmodes of phonon. The inverse relation is

$$g_{mnk\alpha}(\mathbf{R}_p, \mathbf{R}_{p'}) = \frac{1}{N_p N_{p'}} \sum_{\mathbf{k},\mathbf{q}} e^{i(\mathbf{k} \cdot \mathbf{R}_p + \mathbf{q} \cdot \mathbf{R}'_p)} \times \sum_{m'n'\nu} u^{-1}_{k\alpha, \mathbf{q}\nu} U^{\dagger}_{mm'\mathbf{k}+\mathbf{q}} g_{m'n'\nu}(\mathbf{k}, \mathbf{q}) U_{n'n\mathbf{k}}. \qquad (3.6)$$

As one can see, these two equations express a generalized Fourier transform of the electron-phonon matrix elements between reciprocal space and real space. The critical idea for solving practically electron-phonon matrix elements is to first evaluate a small number of electron-phonon matrix elements in the MLWF representation, and then perform a generalized Fourier interpolation into the momentum space, *i.e.*, into the Bloch representation.

4. Designing of Functional Materials from Structure Prototypes

Part of this chapter is published in: Designing of magnetic MAB phases for energy applications. Reproduced with permission from Chen Shen et al. [Journal of Materials Chemistry A 9 (13), 8805-8813] Copyright 2022 Royal Society of Chemistry.

Based on high-throughput density functional theory calculations, we performed screening for stable magnetic MAB compounds and predicted potential strong magnets for permanent magnet and magnetocaloric applications. The thermodynamical, mechanical, and dynamical stabilities are systematically evaluated, resulting in 21 unreported compounds on the convex hull, and 434 materials being metastable considering convex hull tolerance to be 100 meV/atom. Analysis based on the Hume-Rothery rules revealed that the valence electron concentration and size factor difference are of significant importance in determining the stability, with good correspondence with the local atomic bonding. We found 71 compounds with the absolute value of magneto-crystalline anisotropy energy above 1.0 MJ/m^3 and 23 compounds with a uniaxial anisotropy greater than 0.4 MJ/m^3, which are potential gap magnets. Based on the magnetic deformation proxy, 99 compounds were identified as potential materials with interesting magnetocaloric performance.

4.1. Introduction

The modern industrial and societal demands for advanced functional magnetic materials are growing faster as we are witnessing the global expansion of hybrid-electric vehicles, robotics, wind turbines, and automation, leading to a strong incentive on the green energy revolution [147, 148]. Particularly, the efficient harvesting of renewable energy (such as wind energy) and endeavor to reduce the greenhouse effect (mainly through the development of e-mobility and magnetic refrigeration) have intensified the impetus to design resource-efficient magnetic materials with optimal performance, such as permanent magnets and magnetocaloric materials. For instance, one interesting

question is to identify the so-called gap magnets [149], *i.e.*, permanent magnets with their energy density (BH)max [150] lying between the widely applied AlNiCo and Ferrites [151] and the high-performance Sm-Co [152] and Nd-Fe-B-based [153] permanent magnets. Potential candidates can be characterized using the dimensionless figure of merit $\kappa = \sqrt{K_1/(\mu_0 M_S^2)}$ [154], providing an effective descriptor for high-throughput screening. Moreover, following the discovery of $Gd_5Si_2Ge_2$ [155] and $LaFeSi_{13}$ [156] with giant magnetocaloric effect (MCE) around room temperature, magnetic refrigeration technology is assumed to be capable of competing with and hopefully surpassing conventional refrigeration in terms of energy efficiency, environmentally friendly and ecological impact in the near future [157, 158, 159]. However, most permanent magnets and potential magnetocaloric materials with high performance are based on the intermetallic compounds containing rare-earths (RE), which are resource critical [160]. Therefore, rare-earth-free permanent magnets and MCE materials with enhanced efficiency over a broad temperature range and useful secondary properties, such as mechanical stability, corrosion resistance, shapeability, sustainability, and recyclability, are still desirable [161, 147, 162].

The MAB phases with nanolaminated crystal structures exhibit intriguing magnetic properties and mechanical deformation behavior, which have attracted considerable attention recently [163]. Such materials are ternary borides comprising stacked M-B layers (M = transition metal, B = Boron) interleaved by monolayers of A atoms. In this regard, the crystal structures are quite similar to those of the well-known MAX phases $M_{n+1}AX_n$ (X = C and N, A denotes a main group element), which host a unique combination of metallic and ceramic properties [164]. The novel magnetic nanolaminates recently discovered in the MAX phases [165], are also expected in the MAB phases. Moreover, Fe_2AlB_2 was found to be a promising magnetocaloric material exhibiting an interesting MCE [166], with the ordering temperature around 300 K confirmed by experimental [167, 168] and theoretical studies [169, 170, 171]. Ke *et.al.* [172] investigated the intrinsic properties of Fe_2AlB_2, and found a MAE as large as -1.34 MJ/cm^3, in good agreement with the experiments [168]. Recently, Cr_4AlB_4 with a novel structure of MAB phase has been synthesized consistent with the theoretical calculations [173]. Khazaei *et.al.* [174] carried out high-throughput (HTP) calculations on Al-containing non-magnetic MAB phases and predicted 9 stable compounds. More recently, Miao *et.al.* [175] reported another HTP screening for Ti-A-B, Zr-A-B, and Hf-A-B and predicted 7 thermodynamically stable compounds. Therefore, an interesting question is whether there exist more stable MAB compounds beyond the above-mentioned cases and whether are they good candidates as potential functional magnetic materials.

In this work, based on HTP density functional theory (DFT) calculations, we systematically studied the stabilities and the magnetic properties of the MAB compounds to identify possible candidates for permanent magnets and magnetocaloric materials.

Six experimentally synthesized MAB phases and three non-MAB phases (as competitive phases) are considered (Figure 4.1), including MAB [176] (space group *Cmcm*), M_2AB_2 [177] (space group *Cmcm*), $M_3A_2B_2$ [178] (space group *Cmcm*), M_3AB_4 [179] (space group *Immm*), M_4AB_4 [173] (space group *Immm*) and M_4AB_6 [180] (space group *Cmcm*); non-MAB phases are M_5AB_2 [181] (space group *I4/mcm*), $M_3A_2B_2$ [182] (space group *P2/m*) and $M_4A_3B_2$ [182] (space group *P4/mmm*). Three non-MAB phases are considered as competitive phases in order to make the prediction of MAB compounds more reliable. Such compounds are flexible in the chemical compositions and have tunable magnetic properties. For example, Fe_5SiB_2 has a T_C higher than 760 K, a M_S larger than 1 MA/m, and a MAE more than 0.30 MJ/m^3 at room temperature [183, 184, 185, 186, 187]. After validating all the experimentally known phases, we identified stable and metastable ternary borides based on the systematic evaluation of the thermodynamical, mechanical, and dynamical stabilities. Taking the M_2AB_2-type compounds as an example, we investigated the effect of magnetic ordering on the thermodynamic stability, followed by a comprehensive analysis of the stability trend following the Hume-Rothery rules and local atomic bonding. The MAE and magnetic deformation proxy are evaluated explicitly, which help to screen for potential permanent magnets and magnetocaloric materials. Our work expands the materials library of rare-earth free permanent magnets and magnetic refrigeration, and thus provides valuable guidance to further theoretical and experimental studies to design advanced magnetic materials in transition metal-based ternary borides for energy applications [162, 159].

4.2. Computational Details

The DFT calculations are performed using an in-house developed HTP environment [188, 189] to determine the thermodynamical stability for the above mentioned six MAB and three non-MAB phases, as demonstrated in recent studies [190, 191, 192]. It is noted that the non-MAB phases are regarded as competitive phases for the MAB phase to obtain the reliable convex hull, which is also applied in designing MAX phases by considering antiperovskites as a competitive phase [191]. Thermodynamical stability is evaluated by considering the formation energy (E_f) and the distance to the convex hull with respect to all the relevant competing phases available in the OQMD database [15]. All the calculations are carried out using the Vienna ab initio simulation package (VASP) code [193, 194]. The MAE of the predicted stable phases is obtained using the full-potential local-orbital (FPLO) [195] code in the force theorem regime, and the recently proposed magnetic deformation proxy [196] is used to evaluate the MCE.
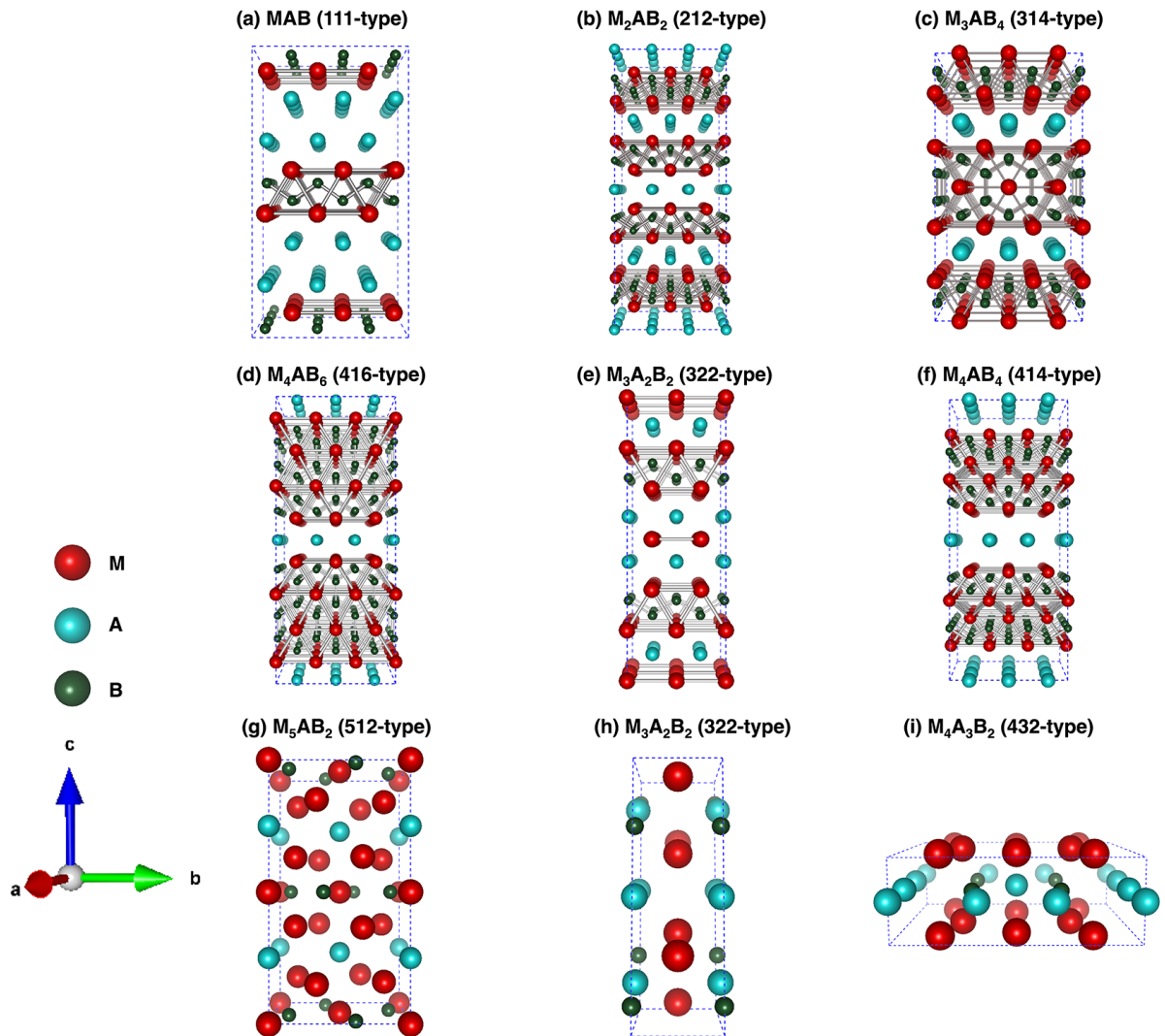
Figure 4.1.: Crystal structures of considered MAB phases(a-f) and non-MAB phases(g-h): (a)222-type [Cmcm], (b)212-type [*Cmcm*], (c)314-type [*Pmmm*], (d)416-type [*Cmmm*], (e) 322-type [*Cmcm*], (f) 414-type [*Immm*], (g) 512-type [*I4/mcm*], (h) 322-type [*P2/m*] and (i) 432-type [*P4/mmm*].

4.3. Results and Discussion

4.3.1. Stabilities of Phases

Thermodynamical Stability

The thermodynamical stability of the MAB and non-MAB phases (shown in Figure 4.1) are obtained based on the formation energy ΔE_f and distance to the convex hull ΔE_h, where $\Delta E_f < 0$ and $\Delta E_h = 0$ are required for the stable phases. In general, $\Delta E_f < 0$ ensures that the target compounds are energetically stable against decomposing into the constituent elements following the reaction $M_x A_y B_z \rightarrow xM + yA + zB$, whereas $\Delta E_h = 0$ denotes the stability upon the decomposition into any binary and ternary phases according to the reaction $\Delta E_h = E_{tot}(\text{predicted phase}) - E_{tot}(\text{competing phases})$. In our calculations, the competing phases include all the relevant compounds found in the OQMD database [15, 197]. As summarized in Table 4.1, there are 21 compounds satisfying the thermodynamic stability criteria, 17 of them are with one of the MAB structures. According to the literature, 15 ternary borides with one of the considered structures have been experimentally synthesized, as listed in Table 4.1. All such compounds exhibit $\Delta E_f < 0$ and $\Delta E_h < 80$ meV/atom (due to the possible numerical errors in DFT, competing phases, and finite-temperature effects), validating our methodology and hence the validity of the newly predicted phases. The resulting lattice parameters are in good agreement with the existing measurements and other theoretical calculations, as listed in Table 4.1. A special case is Co_5PB_2, where the lattice constants are underestimated (overestimated) along [100] ([001]) directions. This is also observed in previous DFT calculations, [198] which may be driven by the missing spin fluctuations as confirmed in $(Fe_{1-x}Co_x)_2B$ [199].

Furthermore, not all the compounds are magnetic, *e.g.*, with finite magnetization larger than 0.05 μ_B per magnetic atom (Table 4.1). It is observed that the nonmagnetic compounds occur mostly for the Cr-, Mn-, and Ni-based cases, whereas $Fe_4Al_3B_2$ and $Co_4Be_3B_2$ are nonmagnetic as well. This can be understood based on the Stoner criteria, where $I\nu(E_F) > 1$ indicate possible itinerant magnetic ordering, with I being the Stoner parameter and $\nu(E_F)$ the density of states (DOS) at the Fermi energy E_F of the nonmagnetic state. For instance, the Stoner parameters of magnetic atoms range between 0.6 and 0.75 from Cr to Ni, [200], thus those compounds with marginal $\nu(E_F)$ smaller than 1.4 states/eV per magnetic atom end up as nonmagnetic (Figure S1 in Appendix) because $I\nu(E_F) < 1$. Moreover, the predicted results agree well with previous experimental and theoretical reports, *e.g.*, Fe_5PB_2 with average magnetization 1.71 μ_B/Fe [186] and $Cr_4AlB_{4/6}$ being nonmagnetic. [180, 173] Furthermore, it is observed that there exist nonzero induced magnetic moments on the nonmagnetic atoms which are antiparallel to the magnetic moments of the $3d$ atoms. For instance, Mn_4BeB_4 has

the smallest ratio $\mathbf{M}_{tot}/\mathbf{M}_{3d}$ of about 0.94, where the magnetic moments of non-metal B atoms are about -0.05 μ_B per B atom and those of metal Be atoms are smaller than -0.01 μ_B per Be atom.

Interestingly, the distance to the convex hull for the experimentally synthesized compounds are finite (Table 4.1), *e.g.*, Cr_4AlB_6, Fe_5PB_2 and Co_5PB_2 with distances to the convex hull of 12, 33 and 79 meV/atom, respectively. Co_5PB_5 with a distance to the convex hull being 79 meV/atom is a special case, where there is also a 3% deviation in the theoretical and experimental lattice constants. In fact, the calculated lattice constants of this compound agree well with previously reported calculations.[198]. Nevertheless, this suggests that a loose tolerance $\Delta E_h < 100$ meV/atom is reasonable, though it is not deliberately chosen to cover the Co_5PB_5 phase.

Critical tolerance with comparable values for the convex hull has also been adopted in other HTP studies [192, 189, 209]. This leads to 434 (335 are MAB phases) stable compounds, as listed in Table S1 in the Appendix. As a consequence, our predictions become consistent with another HTP study[174] focusing on Al-containing MAB phases with early transition metals on the $\mathbf{M}$-sites. For instance, 8 novel MAB phases they found, *i.e.*, CrAlB, MnAlB, $Cr_3Al_2B_2$, $Mn_3Al_2B_2$, $Ni_3Al_2B_2$, Mn_3AlB_4, and Fe_3AlB_4, are also predicted to be stable using the loose tolerance on the convex hull, as listed in the Table S2. It is noted that even if such compounds are metastable, they can still be synthesized using non-equilibrium methods such as MBE and ball milling. Hereafter we will consider the stability trend and magnetic properties for all those compounds. Last but not least, it is essential to consider the non-MAB phases as competing phases beyond those in the OQMD database. It is observed that the 322-MAB $Fe_3Al_2B_2$ is stable with $\Delta E_h = 0$ compared with competing phases in OQMD, whereas it becomes metastable with $\Delta E_h = 33$ meV/atom after considering the non-MAB $Fe_3Al_2B_2$. Certainly there are other competing phases and even novel crystal structures beyond those considered in this work, which will be saved for future investigation after experimental validations.

Another interesting question for predicting stable magnetic materials is whether the magnetic configurations would influence the thermodynamic stability, since most HTP calculations are done assuming the ferromagnetic (FM) state as in the OQMD and the Materials Project [210]. This applies particularly to Mn-based compounds, as revealed by a recent work that the energy landscape of the convex hull is drastically changed after considering the magnetic ground state [211]. According to the literature, the 212-type Mn_2AlB_2 is observed to display an AFM magnetic ground state with Néel temperature about 390 K, [212, 213, 172] thus we performed extensive calculations on the predicted 212-type MAB compounds. As summarized in Table S3, 15 out of 54 magnetic compounds prefer AFM magnetic configurations, including not only Mn-based but also Fe- and Co-based compounds. The magnetic ground states are consistent with those obtained from our Monte Carlo modeling based on the Heisenberg model taking

Table 4.1.: List of MAB and non-MAB phases that we found stable based on relative stability analysis. The present considered phases experimentally synthesized are indicated by asterisks (*). Lattice parameters (Å), formation energy (eV/atom), distance to the convex hull (eV/atom), competing phases, magnetism (Mag.) and magnetic moment (M and the unit as μB per magnetic atom) in considered phases are shown.

Phases	Space group	Lattice			ΔE_f	ΔE_h	Competing phases	Mag.	M
		a	b	c					
FeBeB	63	2.648	12.164	2.925	-0.326	0	FeB, Be$_2$Fe, B	FM	0.422
MnBeB	63	2.811	12.252	2.809	-0.378	0	MnB, Be	NM	0.002
Fe$_2$AlB$_2$ *	65	2.916	11.019	2.851	-0.401	0	FeAl$_6$, AlB$_2$, FeB	FM	1.330
Ref. Exp. [166]		2.928	11.033	2.868					
Ref. Cal. [172]		2.915	11.017	2.851					
Fe$_2$BeB$_2$	65	2.904	9.947	2.749	-0.344	0	Be$_2$Fe, B, FeB	AFM	0.760
Cr$_2$AlB$_2$ *	65	2.923	11.051	2.932	-0.466	0	Cr$_3$AlB$_4$, Cr$_7$Al$_{45}$, CrB	NM	0.010
Ref. Exp. [180]		2.937	11.051	2.968					
Ref. Cal. [172]		2.921	11.034	2.929					
Mn$_2$AlB$_2$ *	65	2.894	11.080	2.831	-0.471	0	Mn$_4$Al$_{11}$, MnB, MnB$_4$	AFM	0.765
Ref. Exp. [170]		2.923	11.070	2.899				AFM	
Ref. Cal. [172]		2.887	11.109	2.830				AFM	
Mn$_2$BeB$_2$	65	2.846	9.969	2.815	-0.435	0	MnB, Be	NM	0.011
Cr$_3$AlB$_4$ *	47	2.939	2.939	8.091	-0.445	0	Cr$_2$AlB$_2$, CrB$_4$, CrB	NM	0.049
Ref. Exp. [180]		2.956	2.978	8.054					
Ref. Cal. [201]		2.938	2.943	8.090					
Cr$_4$AlB$_6$ *	65	2.947	21.328	2.943	-0.422	0.012	CrB$_4$, Cr$_3$AlB$_4$, CrB	NM	0.003
Ref. Exp. [180]		2.952	21.280	3.013					
Ref. Cal. [202]		2.972	21.389	2.961					
Fe$_4$AlB$_4$	71	2.927	18.565	2.870	-0.417	0	AlFe$_2$B$_2$, FeB	FM	1.271
Fe$_4$BeB$_4$	71	2.918	17.513	2.821	-0.377	0	FeB, Be$_2$Fe, B	FM	1.017
Fe$_4$GaB$_4$	71	2.939	18.557	2.883	-0.343	0	FeB, Ga$_3$Fe, B	FM	1.288
Fe$_4$MgB$_4$	71	2.932	19.626	2.875	-0.354	0	FeB, Mg	FM	1.391
Fe$_4$ZnB$_4$	71	2.931	18.726	2.872	-0.348	0	FeB, Zn	FM	1.326
Cr$_4$AlB$_4$ *	71	2.920	18.856	2.939	-0.510	0	AlCr$_2$B$_2$, CrB	NM	0
Ref. Exp. [173]		2.934	18.891	2.973					
Ref. Cal. [173]		2.932	18.912	2.957					
Mn$_4$BeB$_4$	71	2.899	17.591	2.878	-0.467	0	MnB, Be	FM	0.878
Mn$_4$AlB$_4$	71	2.929	18.591	2.889	-0.499	0	MnB, Mn$_2$AlB$_2$	FM	1.014
Mn$_4$IrB$_4$	71	2.959	18.716	2.966	-0.450	0	MnB, Ir	FM	2.003
Ni$_4$AuB$_4$	71	3.012	18.793	2.950	-0.224	0	Au, Ni$_4$B$_3$,	NM	0
Ni$_4$CuB$_4$	71	2.992	18.125	2.875	-0.227	0	B, Cu, Ni$_4$B$_3$	NM	0
Ni$_4$PdB$_4$	71	2.996	18.453	2.931	-0.265	0	Ni$_4$B$_3$, BPd$_2$, B	NM	0
Ni$_4$PtB$_4$	71	2.995	18.351	2.960	-0.267	0	BPt$_2$, Ni$_4$B$_3$, B	NM	0
Ni$_4$ZnB$_4$	71	2.992	18.517	2.880	-0.261	0	Ni$_4$B$_3$, B, ZnNi$_3$B$_2$	NM	0
Fe$_3$Al$_2$B$_2$ *	10	5.685	2.833	8.593	-0.426	0	FeAl$_6$, AlB$_2$, FeB	FM	0.784
Ref. Exp. [182]		5.723	2.857	2.857					
Fe$_4$Al$_3$B$_2$	123	8.083	8.083	2.791	-0.411	0	AlFe, AlFe$_2$B$_2$	NM	0.002
Co$_4$Be$_3$B$_2$	123	7.586	7.586	2.586	-0.395	0	Be$_3$Co, BeCo, CoB	NM	0
Ni$_4$Li$_3$B$_2$	123	8.049	8.049	2.734	-0.252	0	Li, Ni$_2$B	NM	0.0002
Fe$_5$BeB$_2$	140	5.455	5.455	9.914	-0.292	0	Be$_2$Fe, Fe$_2$B, Fe	FM	1.932
Fe$_5$PB$_2$ *	140	5.570	5.570	10.436	-0.392	0.033	Fe$_2$B, FeB, Fe$_2$P	FM	1.705
Ref. Exp. [181]		5.548	5.548	10.332				FM	1.730
Ref. Exp. [186]		5.485	5.485	10.348				FM	1.720
Ref. Exp. [203]		5.492	5.492	10.365				FM	1.658
Ref. Cal. [198]		5.456	5.456	10.296				FM	1.770
Fe$_5$SiB$_2$ *	140	5.509	5.509	10.299	-0.359	0.003	Fe$_2$B, FeSi	FM	1.731
Ref. Exp. [184]		5.551	5.551	10.336				FM	1.808
Ref. Exp. [183]		5.554	5.554	10.343				FM	1.750
Ref. Cal. [185]		5.546	5.546	10.341				FM	1.840
Co$_5$PB$_2$ *	140	5.279	5.279	10.477	-0.357	0.079	Co$_2$P, CoB, Co	FM	0.409
Ref. Exp. [204]		5.420	5.420	10.200					
Ref. Cal. [198]		5.284	5.284	10.541				FM	0.440
Co$_5$SiB$_2$ *	140	5.484	5.484	9.942	-0.337	0.042	CoB, Co$_2$Si, Co	FM	0.394
Ref. Exp. [205]									
Ref. Cal. [185]		5.511	5.511	9.953				FM	0.484
Cr$_5$PB$_2$ *	140	5.537	5.537	10.317	-0.474	0.032	Cr$_3$P, CrB	NM	0.022
Ref. Exp. [206]		5.593	5.593	10.370					
Cr$_5$B$_3$ *	140	5.431	5.431	9.923	-0.418	0	CrB, Cr$_2$B	NM	0
Ref. Exp. [207]		5.460	5.460	10.460					
Mn$_5$PB$_2$ *	140	5.509	5.509	10.287	-0.480	0.033	Mn$_2$B, MnB, Mn$_2$P	FM	1.665
Ref. Exp. [204]		5.540	5.540	10.490					
Ref. Exp. [208]		5.540	5.540	10.490					
Mn$_5$SiB$_2$ *	140	5.559	5.559	10.293	-0.415	0.003	MnSi, Mn$_2$B	FM	1.583
Ref. Exp. [208]		5.540	5.540	10.490					

exchange parameters from DFT calculations (not shown), which will be discussed in detail elsewhere. Nevertheless, the energy difference between the FM and AFM states is less than 20 meV per atom, hence the magnetic ground state has no strong impact on the thermodynamic stability for such compounds. This can be attributed to the nano-laminated crystal structure, where the magnetic interaction between the local Mn-moments is relatively weak, in comparison to the strongly frustrated fcc-lattice from the Cu_3Au lattice considered in Ref. [211]. It is noted that systematic evaluation of the magnetic ground states is a challenge, hereafter we will focus on the physical properties of the FM states, which should be valid for most of the other compounds.

After the thermodynamic stability, mechanical and dynamical stabilities should be addressed as well in order to make systematic predictions. It is observed that mechanical stability plays a marginal role as explicitly demonstrated for 21 stable compounds on the convex hull. This is consistent with our previous studies on the antiperovskite compounds. [192]. For the orthorhombic MAB phases, there are nine independent elastic constants C_{11}, C_{22}, C_{33}, C_{44}, C_{55}, C_{66}, C_{12}, C_{13}, and C_{23}. For the tetragonal non-MAB phases, there are six independent elastic constants C_{11}, C_{33}, C_{44}, C_{66}, C_{12}, and C_{13}. According to the mechanical stability defined in the Ref. [214], none of the novel compounds predicted to be thermodynamically stable is found to be mechanically unstable. In addition, the dynamical stability is verified by examining the the phonon spectra as compiled in Figure S3 for 21 predicted and 15 known cases. Obviously, there is no imaginary modes observed for 35 compounds, indicating that those compounds are stable against local atomic displacements. The resulting phonon spectra for Cr_2AlB_2 and Cr_3AlB_4 are in good agreement with previous reported results [215]. The mechanical (not shown) and dynamical (as indicated by phonon spectra in Figure S3) stabilities seem to be of marginal importance for the newly predicted compounds on the convex hull (cf. Table 4.1), which is consistent with our previous studies on the antiperovskite compounds [192]. Due to the expensive computational cost, we have not performed such detailed evaluations for the other predicted compounds with the distance to the convex hull smaller than 100 meV/atom.

Nevertheless, for $Ni_4Li_3B_2$ there exists an imaginary mode at the M point. This suggests that the compound may end up with other crystal structures or synthesized on certain substrates using molecular beam epitaxy.

Trends in the Stability

To understand the trend of stabilities for the MAB and non-MAB phases, the number of stable compounds ($\Delta E_h < 100$ meV/atom) with respect to the **A** element are shown in Figure S4. It is obvious that most elements in the periodic table act as a constituent

element stabilizing at least one of the considered crystal structures, whereas nine out of 59 elements (*i.e.*, K, Rb, Cs, Sr, Ba, Zr, N, Sb, and Bi) do not form any stable phases. Particularly, each of the five elements like Be, Al, Pt, Zn, and Ir support more than 22 stable phases. Moreover, among all the structure types considered in this work, 136 compounds are stable with the 414-type structure, albeit the first compound Cr_4AlB_4 was reported in 2019. [173].

Figure 4.2.: The stability map of 212-MAB phases (circle symbols represent unstable phases in the present work; triangle symbols represent possible stable phases with convex hull distance below 100 meV/atom in the present work; square symbols represent newly reported novel phases in Ref. [174]).

Taking the 212-type MAB structure as an example, the stability trend with respect to the chemical composition can be understood based on the Hume-Rothery rules [216]. Such rules are formulated based on the difference of size, electronegativity factors and the valence electron concentration (VEC). It is observed that the electronegativity difference between the **M** and **A** elements has no strong correlation with the stability (Figure S5), same as the MAX compounds [217]. On the other hand, as shown in Figure 4.2, both the atomic radius difference of the **M** and **A** elements $\frac{|R_M - R_A|}{R_A}$ and

VEC have significant influence on the stability. Clearly, most stable compounds are within the region $\frac{|R_M - R_A|}{R_A} < 0.4$ and VEC < 5.5. The newly reported novel phases in Ref. [174] also prove the practicality of the current expression factors. Similar behavior is also observed for the 414-type MAB compounds with a slightly smaller tolerance for VEC < 6, as shown in Figure S6. The reason might be due to the fact that the **M**-site and boron-site contributing less valence electrons because of the extended M-B block (Figure 4.1).

The general trend in the stability can be elucidated based on the chemical orbital Hamilton population (COHP) obtained using the LOBSTER code [218], which provides an atomic picture about the bonding. As an example which is representative for all the compounds we considered, the bond-resolved COHP is shown for M_2AlB_2 (where M are Cr, Mn, Fe, Co and Ni) and Fe_2AB_2 (where A are Be, Mg, Ca, Sr and Ba) in Figure S7. Focusing on varying the **M** elements, the number of valence electron on the **M**-sites increases from 6 in Cr_2AlB_2, to 8 in Fe_2AlB_2, and finally to 10 in Ni_2AlB_2. For Cr_2AlB_2, it is obvious that the values of -COHP are all positive below the Fermi energy, indicating only boning states are occupied in the corresponding bonds, which leads to a high overall stability (Figure S7) Increasing the number of valence electron to 10 in Ni_2AlB_2, the negative energies -COHP appeared below the Fermi energy in the Ni-B, Ni-Al, and Ni-Ni bonds. The occupation of such anti-bonding states weakens the bonds and therefore destabilizes the Ni_2AlB_2 compound. Therefore, the ICOHP of M-Al and M-B are increasing within the the number of valence electron increasing, which indicates the corresponding bond strength weakens. Similar behaviour is also observed in the COPH os Fe_2AB_2 compounds with varying A elements being Be, Ca, and Ba (Figure S7). As the atomic size changes from 0.99 Å(Be), 1.74 Å(Ca) and 2.06 Å(Ba), the bond strength of those compounds becomes weaker, which are confirmed by the COHP values of Fe-Fe, Fe-B, Fe-A and A-B.

Hence, with respect to varying both **M** and **A** elements with increasing number of valence electrons and atomic size, the Fermi energy is shifted into the anti-bonding states, leading to instability. This helps to understand the trend observed in Figure 4.2, which provide valuable guidance to guide the synthesis of MAB phases by substituting the **M/A** sites or via forming solid solutions.

4.3.2. Magnetic Properties

MAE

Turning now to the magnetic properties, we focus on the magnetocrystalline anisotropy energy (MAE) and magnetocaloric effect (MCE), in order to identify potential candidates for permanent magnet and magnetocaloric applications. The MAE is caused by the

broken continuous symmetry of magnetization directions due to the spin-orbit coupling (SOC) [219], which is defined (denoted as K) in terms of

$$K_{\hat{n}_1-\hat{n}_2} = E_{\hat{n}_1} - E_{\hat{n}_2}, \qquad (4.1)$$

where $E_{\hat{n}}$ denotes the total energy with the magnetization direction parallel to $\hat{n}$. In the present work, we consider $\hat{n}$ along three crystalline directions, namely, [100], [010] and [001], as MAB compounds have orthorhombic structures (Figure 4.1). This leads to three MAEs, *i.e.*, $K_{001-010}$, $K_{001-100}$ and $K_{010-100}$. Figure 4.3 shows the MAE with respect to the saturation magnetization (M_S), in comparison with the experimentally known permanent magnets. There are in total 71 cases (cf. Table S4 in the Appendix) with the absolute value of at least one MAE greater than 1.0 MJ/m^3. For instance, the MAE of Fe_2AlB_2 has been evaluated by different groups [172, 167, 168], and our result of -1.14 MJ/m^3 is in good agreement with the experimental measurements of -0.9 MJ/m^3 at 50 K by Barua [168] and theoretical calculation -1.34 MJ/m^3 by Ke [172]. In the newly predicted compounds, the MAB phase Mn_4PtB_4 has the largest MAE as 13.498, 11.948 and -1.550 MJ/m^3 for $K_{001-010}$, $K_{001-100}$ and $K_{010-100}$. Additionally, the 111-type FePtB shows the largest MAE in non-Mn-containing compounds as -10.646, 7.225 and -3.421 MJ/m^3 for $K_{010-100}$, $K_{001-010}$ and $K_{001-100}$, suggesting the *b*-direction (c-direction) is easy (hard) axis. Based on the dimensionless figure of merit $\kappa = \sqrt{K_1/(\mu_0 M_S^2)}$ [154], there exist quite a few compounds which can be classified as hard magnets. Particularly, the MAE of such ternary TM borides fill the gap between the widely used low performance magnets (such as AlNiCo and ferrite) and high performance magnets (such as Sm-Co and Nd-Fe-B).

However, not only the absolute values of the MAE but also the sign matters, *e.g.*, the easy axis (direction with the lowest energy) is ideally aligned along a special crystalline axis. For all the MAB compounds, the [001] direction along the stacking direction of the M-B layers (Figure 4.1) is chosen, corresponding to the most-probably exposed surfaces for such nano-laminated structures. For the non-MAB phases of the tetragonal space groups, the special axis is chosen to be the axis of 4-fold rotational symmetry, *i.e.*, the [001] direction in Figure 4.1(g & i). The MAE for the 322-type compounds (Figure 4.1(h)) is overall small thus we do not consider them. Correspondingly, we found 16 MAB and 7 non-MAB phases with a significant out-of-plane MAE (> 0.4 MJ/m^3), as well as 33 (18) MAB (non-MAB) compounds with a reasonable in-plane MAE (absolute value larger than 0.4 MJ/m^3), as listed in Table S5. Among them, the 322-type MAB compound $Mn_3Ir_2B_2$ has the largest out-of-plane MAE of 10.17 MJ/m^3 for $K_{010-001}$, and Fe_2ReB_2 with a large MAE of 9.00 MJ/m^3 in $K_{010-001}$. Interestingly, the MAE value of $Fe_3Zn_2B_2$ is as large as 3.00 MJ/m^3 in $K_{100-001}$ while its M_s is comparable to that of MnAl. It contains no expensive, toxic or critical element, which is a good candidate permanent magnet material. Moreover, Fe_7B_2 has a sizable MAE 0.681 MJ/m^3, which is quite comparable to that of hcp Co. Such a phase is beyond the known

binary Fe-B phase diagram [220], which might be synthesizable under non-equilibrium conditions. Last but not least, our results (Figure 4.3 and Table S4) provides reasonable matrix compounds whose MAE can be further enhanced by proper doping to engineer permanent magnets. For instance, our calculations reveal that Fe_5PB_2 has an MAE of 0.63 MJ/m^3 consistent with the experimental measured value of 0.65 MJ/m^3 [187], whereas a recent work demonstrated that its MAE can be enhanced by substitutionally doping tungsten [221].

As discussed above, most compounds with significant MAE contain $5d$ elements, such as Pt, Ir, and Re. This suggests that the MAE is originated from the enhanced atomic SOC strength for the $5d$-shell of such elements. Following Ref. [222], the atomic resolved SOC energy changes are listed in Table S6 for the 111-type FeXB with **X** =
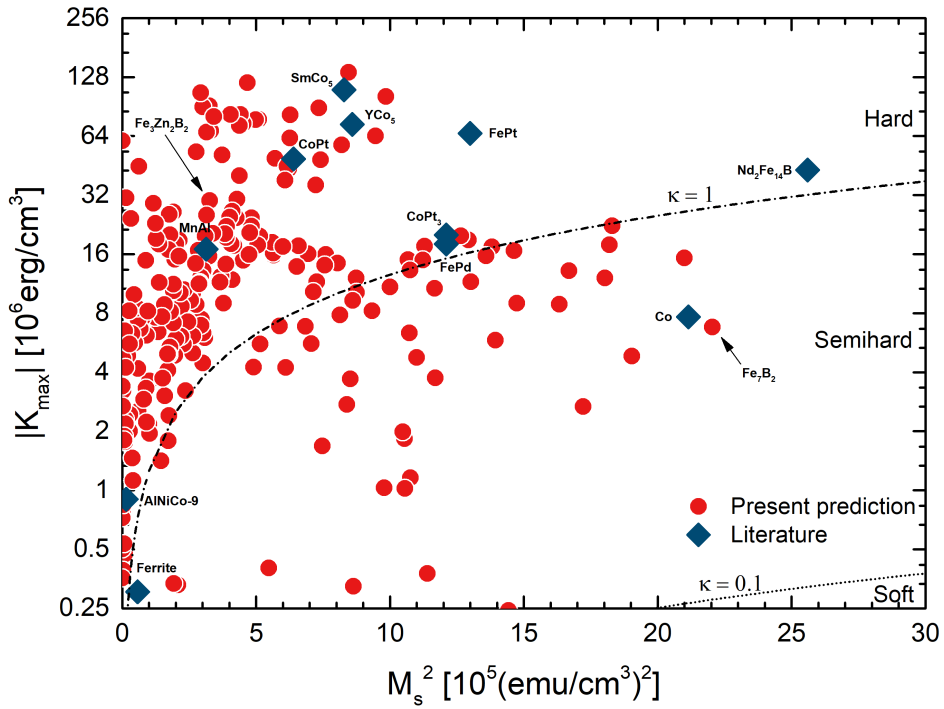
Figure 4.3.: The MAE vs magnetization of the promising candidates of targeted phases. The dashed lines correspond to magnetic hardness parameter $\kappa = \sqrt{K_1/(\mu_0 M_S^2)}$ for values $\kappa = 1$ and 0.1. Hard magnetic materials ($\kappa > 1$) can be used to make efficient permanent magnets of any shape.

Ni, Pd, and Pt. As the atomic SOC strength increases from 98 meV for Ni, 185 meV for Pd, to 533 meV for Pt [223], the contribution from the **X** element to the MAE is becoming more significant, as given by the change of atom-resolved SOC energy $\Delta E_{SOC} = E_{SOC}(\hat{n}_1) - E_{SOC}(\hat{n}_2)$. For FeNiB, ΔE_{SOC}(Fe) (-0.492 meV/at. in [100]-[010] direction) dominants the total ΔE_{SOC} (-0.586 meV/f.u. in [100]-[010] direction) of the compound, as the SOC strength is comparable for Fe (55 meV) and Ni. Furthermore, for FeXB with **X** = Ni, Pd, and Pt, the ΔE_{SOC} of Ni, Pd, and Pt are -0.093, 0.702, and 2.603 meV/atom between two magnetization directions [100] and [010], corresponding to the changes in the total MAE of -0.128, 0.181, and 2.106 meV/atom, respectively. That is, ΔE_{SOC} of **X** has a more dominant contribution to the total ΔE_{SOC} and hence the MAE, when moving down the group from $3d$ to $5d$ elements. In the FePtB, the contribution of ΔE_{SOC} of Pt is 84% in total ΔE_{SOC}. Therefore, like FePt [224], the $5d$ elements have a more significant contribution to the MAE because of enhanced atomic SOC strength, though the magnetic moments on such elements are induced by those of the $3d$ atoms.

MCE

As introduced above, it is postulated that ternary TM borides are promising candidates for MCE applications, such as Fe_5SiB_2 [183] and Fe_2AlB_2 [166, 168, 171, 167]. To search for more candidates in the predicted MAB and non-MAB compounds, we performed screening based on the magnetic deformation proxy [196]. It is demonstrated that the magnetic entropy change ΔS_M upon magneto-structural transitions has a strong correlation with the magnetic deformation $\Sigma_M = \frac{1}{3}(\eta_1^2 + \eta_2^2 + \eta_3^2)^{1/2} \times 100$ and $\eta = \frac{1}{2}(\mathbf{P}^T\mathbf{P} - \mathbf{I})$ where $\mathbf{P} = \mathbf{A}_{nonmag}^{-1} \cdot \mathbf{A}_{mag}$ with $\mathbf{A}_{nonmag}$ and $\mathbf{A}_{mag}$ being the lattice constants of the nonmagnetic and magnetic unit cells. Although there is no direct scaling between ΔS and Σ_M, it is suggested that $\Sigma_M > 1.5\%$ is a reasonable cutoff to select the promising compounds [196]. Figure 4.4 shows the 99 potential MCMs with $\Sigma_M > 1.5\%$ from 434 compounds with convex hull $\Delta E < 100$ meV/atom. Among them, the reported [196] Σ_M of Fe_5SiB_2 (2.14%) and Fe_2AlB_2 (2.05%) are confirmed in our calculations, with the resulting Σ_M of 2.03 % and 1.96 %, respectively. Interestingly, there is positive correlation between the magnetization density and the magnitude of magnetic deformation, *i.e.*, as the magnetic deformation increases, the magnetization of compounds also increase (Figure 4.4). It is noted that 82 out of 99 potential MCMs locating at $\Sigma_M < 3.5\%$, and the magnetization concentrating between 500 to 1000 emu/cm^3. Particularly, there are four compounds, *e.g.*, Fe_5B_2 (322-MAB), $Fe_3Co_2B_2$ (322-MAB), $Mn_3Co_2B_2$ (322-MAB), and Fe_2B (111-MAB), at the upper-right corner, which perform on both large magnetization and magnetic deformation. We suspect such compounds can exhibit significant ΔS_M upon second order phase transition at the corresponding Curie temperature, which will be saved for detailed investigation in the

future. Additionally, isostructural doping can be applied to improve the magnetocaloric performance [225] or to fine tune the the magnetostructural or metamagnetic transitions[226], which enables further design of magnetocaloric materials with optimal performance.
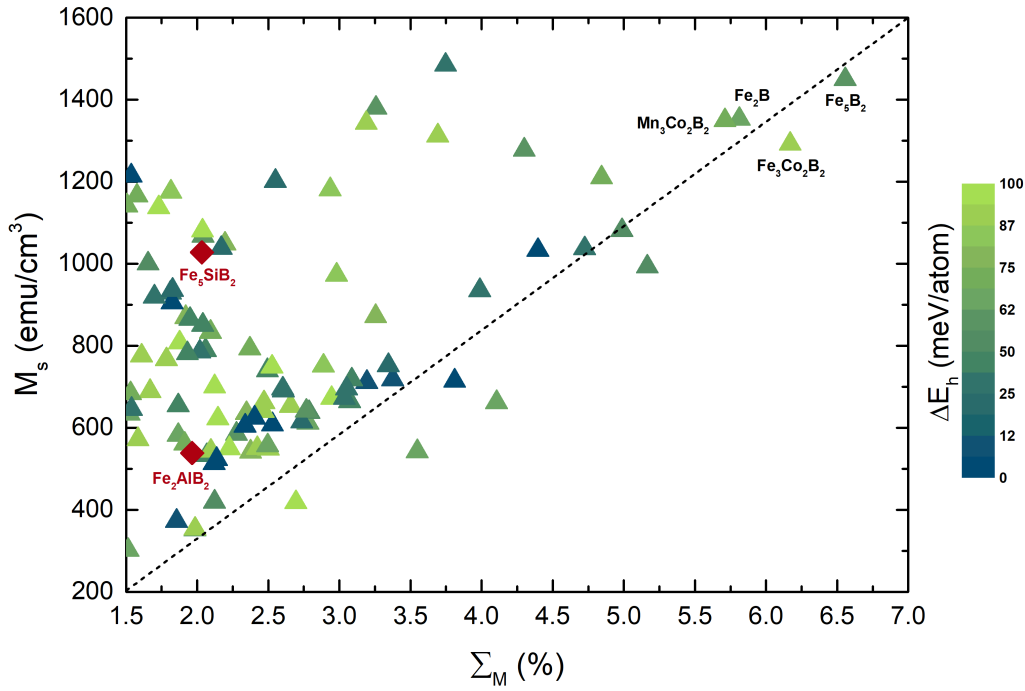
Figure 4.4.: The 99 potential MCMs with magnetic deformation $\sum_M > 1.5\%$. The color bar marks the distance to the convex hull. The dash line indicates a positive correlation between the magnetization density and the magnitude of magnetic deformation.

Several important aspects on possible MCE in such materials are noteworthy, based on the distributing map with respect to the **M** and **A** sites as shown in Figure S8. For instance, compounds with Fe and Mn occupying the **M**-site show a high possibility to posses a large MCE based on the magnetic deformation, which have been confirmed in several reported compounds [208, 227, 228]. Based on the correlations observed in known MCMs in Ref. [196], such materials are likely to show a strong magnetocaloric effect and are therefore excellent candidates for experimental study. Moreover, compounds with Mn/Fe/Co, Ru/Rh/Pd and Os/Ir/Pt occupying the **A**-site also show a high potential to host remarkable magnetocaloric properties. Furthermore, it is noted the fact that Fe_2AlB_2 is composed entirely of earth-abundant elements. This provides a major advantage at least from a cost and resource point of view, over the competing MCMs that contain expensive critical elements (*e.g.*, Gd, $Gd_5Si_2Ge_2$, FeRh). Therefore, such economic

material without critical elements appears especially appealing to us, and the present system $M_xA_yB_z$, when **A** = Al, Zn, Si and Fe should be attracted more attention, such as Fe_4AlB_4 (2.33 %), Fe_3AlB_4 (2.11 %), Fe_4SiB_4 (2.73 %), Fe_3ZnB_4 (2.42 %) and Fe_5B_2 (*Cmmm*, 6.56 %) (Figure S8).

4.4. Conclusions

In summary, our high-throughput screening on 6 types of MAB phases and 3 types of competing non-MAB phases predict 434 magnetic ternary transition metal borides which are potential candidates for permanent magnets and magnetocaloric materials. After validating the 15 reported compounds, 21 novel compounds are identified to be stable based on the systematic evaluation of thermodynamic, mechanical, and dynamical stabilities, and the number of stable compounds is increased to 434 taking the tolerance of convex hull being 100 meV/atom. It is observed that the magnetic ground state for such compounds with layered structures does not have a strong influence on the thermodynamic stability. The trend of stability for the MAB phase can be understood based on the Hume-Rothery rules, where the size factor difference and the valence electron concentration play a critical role. Such a trend can be further attributed to the bond-resolved COHP, providing intuitive guidance for experimental synthesis. The detailed evaluation of the magnetocrystalline anisotropy energy and the magnetic deformations leads to 23 compounds with significant uniaxial anisotropy ($>$ 0.4 MJ/m^3) and 99 systems with reasonable magnetic deformation ($\sum_M > 1.5\%$). For those compounds containing no expensive, toxic, or critical elements, it is observed that $Fe_3Zn_2B_2$ is a reasonable candidate as gap permanent magnet, and Fe_4AlB_4, Fe_3AlB_4, Fe_3ZnB_4, and Fe_5B_2 as potential magnetocaloric materials. This work paves the way for designing more magnetic materials for energy applications. In particular, it also provides a good starting point to search for novel two-dimensional magnetic materials, *i.e.*, MBene, based on detailed evaluation of the exfoliation energy and follow-up experiments.[229] At last, the realistic assessment of the predicted potential MAB phases are conducting and will add to our library [162, 159] soon.

5. Thermal Transport in Novel 2D Systems

Part of this chapter is published in: Two-dimensional layered MSi_2N_4 (M = Mo, W) as promising thermal management materials: a comparative study. Reproduced with permission from Chen Shen et al. [Physical Chemistry Chemical Physics 24 (5), 3086-3093] Copyright 2022 Royal Society of Chemistry.

With the miniaturization and integration of nanoelectronic devices, efficient heat removal becomes a key factor affecting the reliable operation of such devices. Two-dimensional (2D) materials, with the high intrinsic thermal conductivity, good mechanical flexibility, and precisely controllable growth, are widely accepted as ideal candidates for thermal management materials. In this work, by solving the phonon Boltzmann transport equation (BTE) based on first-principles calculations, we investigated the thermal conductivity of novel 2D layered MSi_2N_4 (M = Mo, W). Our results point to a competitive thermal conductivity as large as 162 Wm^{-1}K^{-1} of monolayer $MoSi_2N_4$, which is around two times larger than that of WSi_2N_4 and seven times larger than that of monolayer MoS_2 despite their similar non-planar structures. It is revealed that the high thermal conductivity arises mainly from its large group velocity and low anharmonicity. Our result suggests that $MoSi_2N_4$ could be a potential candidate for 2D thermal management materials.

5.1. Introduction

$MoSi_2N_4$ was synthesized by chemical vapor deposition (CVD) method [230]. It can be structural viewed as 2H-MoS_2-type MoN_2 intercalating into α-InSe-type Si_2N_2 [231]. 2D $MoSi_2N_4$ was reported to exhibit semiconducting behavior, high carrier mobility, high strength, and excellent ambient stability [230, 231]. In addition to that, due to its noncentrosymmetric hexagonal structure and unique electronic structure, several new physical properties such as second harmonic generation [232], valley pseudospin [233, 234] and piezoelectricity [235] were proposed in this system. However, at present,

these researches mainly focus on the electronic properties instead of the phononic properties of $MoSi_2N_4$, which is of great significance to the operating reliability with applications in electronics.

The thermal conductivity of 2D semiconductors is one of the significant phononic properties that have attracted considerable interest [236, 237, 238, 239, 240], which calls for its layered structural feature that is out-of-plane van der Waals bond and in-plane covalent bond. Due to the atomic thin monolayer with van der Waals bond along the out-of-plane direction, thermal conductivities of 2D semiconductors are generally thickness-dependent in both out-of-plane, and in-plane direction [241]. Several 2D semiconductors such as h-BN [242], $PdSe_2$ [25], phosphorene [243], and MoS_2 [244] are experimentally and theoretically reported to have the thickness-dependent thermal conductivity. As for monolayer with an in-plane covalent bond, weak covalent bonds result in lower in-plane thermal conductivity than that of graphene [245]. Therefore, various 2D semiconductor materials with different lattice structures and covalent bonds strength produce different thermal conductivity values. Low thermal conductivity materials can be candidates for thermoelectric (TE) [109], while high thermal conductivity materials can be used as thermal management materials [246, 247]. Particularly, transition metal dichalcogenides (TMDCs) with tunable band gap [248] and the allotropes [249] make possess low or high thermal conductivity. For instance, the thermal conductivity of monolayer $1T$-$ZrSe_2$ and $1T$-$HfSe_2$ at room temperature is 1.2 $Wm^{-1}K^{-1}$ and 1.8 $Wm^{-1}K^{-1}$ [110], which is benefit to thermoelectric application. In contrast, the thermal conductivity of monolayer MoS_2 is 23.2 $Wm^{-1}K^{-1}$ [250], which can be expected to be used in thermal management applications [251]. Among all the 2D materials, graphene holds the highest thermal conductivity, which can be up to 3000-5300 $Wm^{-1}K^{-1}$ [245, 252]. Such superior thermal conductivity promises its application in thermal management. However, the graphene channel field effect transistor has a low on/off ratio (< 100) metal behavior at room temperature [253]. With such consideration, TMDCs can be a candidate for both high heat conduction and excellent on/off ratio compared to graphene [254, 255].

As proposed in Ref. [230] and Ref. [231], $MoSi_2N_4$ monolayer holds 1.74 eV PBE band gap and 2.30 eV HSE band gap, which is comparable to that of MoS_2 (1.8 eV, PBE). And the derived carrier mobility of $MoSi_2N_4$ is four times that of MoS_2. Furthermore the Young's modulus of $MoSi_2N_4$ is about 50 GPa, which is higher than that of MoS_2 by 26.8 GPa [256]. Similarity to MoS_2 of TMDCs, $MoSi_2N_4$ is also a member of MA_2Z_4 family. In addition, both $MoSi_2N_4$ and WSi_2N_4 have been synthesized experimentally by CVD. Geometrically, $MoSi_2N_4$ contains $2H$-MoS_2 type MoN_2 in its monolayer and it is sandwiched by two two-atomic-layer zigzag-SiN. Given the fact that both the $2H$-MoS_2 (23.2 $Wm^{-1}K^{-1}$) and Si_3N_4 (177 $Wm^{-1}K^{-1}$) [257] have excellent thermal conductivity, it is urgently required to study the thermal conductivity of $MoSi_2N_4$ and WSi_2N_4 monolayer for promoting their applications. Although predicting the thermal

conductivity by using machine-learning-based interatomic potentials [258] and solving the phonon BTE based on DFT calculation [259] have been used to study the thermal conductivity of $MoSi_2N_4$ family, more comprehensive analysis and higher precision computation is always required.

In this work, we performed a systematic study of the phonon transport properties of both $MoSi_2N_4$ and WSi_2N_4 by solving the phonon BTE based on first-principles calculations. Firstly, the lattice structure and phonon dispersion of the $MoSi_2N_4$ and WSi_2N_4 were studied. Then, the lattice thermal conductivities of them at different temperatures were calculated. We found that the $MoSi_2N_4$ and WSi_2N_4 are promising thermal management materials with outstanding thermal conductivity. The mechanism underlying the high thermal conductivity of such $MoSi_2N_4$-based materials is explained by analyzing the mode resolved phonon properties. Considering the similar geometry structures of monolayer MoS_2 and silicene, namely, $2H$-MoS_2 corresponds to $2H$-MoN_2 of $MoSi_2N_4$, and silicene corresponds to top or bottom two-atomic-layer SiN unit of $MoSi_2N_4$. We chose these two materials as comparison materials. The thermal transport properties of them are also calculated. Moreover, the electronic structures were further studied to obtain a deep insight into phonon transport. This paper systematically studied the thermal transport properties of 2D MSi_2N_4-based materials for exploring their potential applications in thermal management and many other fields.

5.2. Computational Details

Ab initio calculations based on density functional theory (DFT) were performed using the *Vienna ab initio simulation package* (VASP) [260, 193], which implements the projector augmented wave (PAW) [194]. Exchange-correlation energy functional is treated using the Perdew-Burke-Ernzerhof of generalized gradient approximation (GGA-PBE) [59]. The wave functions are expanded in plane wave basis with a $20{\times}20{\times}1$ Monkhorst-Pack [261] k-sampling grid and cut-off energy of 700 eV. A large vacuum region is set as 35 Å to avoid the interactions between the monolayer and its mirrors induced by the periodic boundary conditions. Precision of total energy convergence for the self-consistent field (SCF) calculations was as high as 10^{-8} eV. All structures are fully optimized until the maximal Hellmann-Feynman force is less than 10^{-8} eVÅ^{-1}. To calculate the phonon dispersion, thermal conductivity, and various phonon properties, it is necessary to extract second- and third- interatomic force constants (IFCs) from first-principles calculations. To this end, $4{\times}4{\times}1$ supercells containing 112 atoms were constructed, which is sufficiently large to allow the out-of-phase tilting motion. To extract second-order IFCs, an atom in the supercell was displaced from its equilibrium position by 0.01 Åand the Hellmann-Feynman forces were calculated based on the displaced configuration. To estimate the anharmonic phonon frequencies of current

systems, we extended the finite-displacement approach to preparing cubic IFCS with appropriately chosen displacement magnitude $\Delta\mu$ ($\Delta\mu = 0.04$ for cubic). A cut-off radius is introduced to disregard the interactions between atoms with a distance larger than a specific value for practical purposes. In principle, the cut-off radii should exceed the range of physically relevant anharmonic interactions to get satisfactory results, which should be carefully tested. ALAMODE only implements the RTA method for calculating thermal conductivity. The previous work [25] mentioned the larger cut-off radius could provide more reasonable thermal conductivity for the RTA method. Based on the convergence test of thermal conductivity *vs.* cut-off radius and numerical consideration, we choose the cutoff interactions up to the 26th nearest neighbors for the anharmonic term. The cut-off radius of 18a0 and 14a0 (where a0 is the Bohr radius) was used for harmonic and cubic IFCs. The cubic IFCs within considering 26th nearest neighbors results in 2771 displacement configurations. And the Q-grid of $101 \times 101 \times 1$ for calculating the thermal conductivity of $M\mathrm{Si_2N_4}$ system. Lattice thermal conductivity (κ_L) and relative phonon properties were determined by solving the phonon BTE, as implemented in the ALAMODE [113] package. The κ_L is estimated by the BTE within RTA through the following equation:

$$\kappa_L^{\alpha\beta}(T) = \frac{1}{NV}\sum_q C_q(T)v_q^{\alpha}(T)v_q^{\beta}(T)\tau_q(T), \qquad (5.1)$$

where V, $C_q(T)$, $v_q(T)$, and $\tau_q(T)$ are the unit cell volume, mode specific heat, phonon group velocity, and phonon lifetime, respectively.

5.3. Results and Discussion

5.3.1. Lattice Structures of Monolayer MoSi$_2$N$_4$ and WSi$_2$N$_4$

MoSi$_2$N$_4$ and WSi$_2$N$_4$ are new septuple-atomic-layer monolayer materials reported in Ref. [230], as shown in Figure 5.1. This monolayer is built up by septuple atomic layers of N-Si-N-M-N-Si-N (M = Mo, W), which can be structurally constructed by inserting 2H-MoS$_2$-type MN$_2$ into α-InSe-type SiN. Interestingly, the space group of MoSi$_2$N$_4$ ($P\bar{6}m2$, No. 187) is consistent with that of 2H-MoS$_2$ and α-InSe monolayer. Note that since MSi$_2$N$_4$, 2HMoS$_2$, and α-InSe holds multiatomic-layer complex lattice structures, instead of the plane group, the space group is used here to describe their lattice structures. In detail, in Figure 5.1(a), Si locates in the center of a tetrahedron formed by four N atoms, and Mo is in a triangular prism consisted of six N atoms. Notably, MoSi$_2$N$_4$ described above is identified as the most energetically favorable

structure among thirty structures proposed in Ref. [231] in combination with first-principles structural optimization (lattice parameters and space group are listed in Table 5.1).
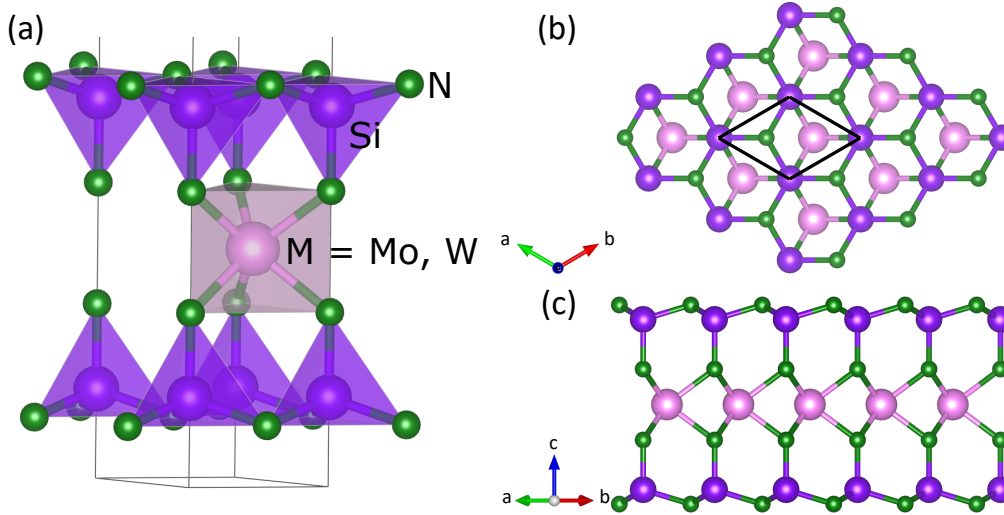
Figure 5.1.: The top and side views of structures of $MoSi_2N_4$ and WSi_2N_4.

Table 5.1.: Lattice parameters of monolayer $MoSi_2N_4$ and WSi_2N_4 (unit Å).

Compound	Space group	a	Thickness
$MoSi_2N_4$	P$\bar{6}$m2	2.91	6.79
WSi_2N_4	P$\bar{6}$m2	2.91	7.02

5.3.2. Phonon Dispersion and Density of States

To study the phonon transport properties of monolayers $MoSi_2N_4$ and WSi_2N_4, phonon dispersion calculations are firstly performed based on the finite displacement difference method. The phonon dispersions are shown in Figure 5.2, it is noted that no imaginary part existing in monolayers $MoSi_2N_4$ and WSi_2N_4, indicating the dynamic stability of the two monolayer compounds. The primitive cell of monolayer $MoSi_2N_4$ (WSi_2N_4) has seven atoms. Thus there are three acoustic phonon branches and eighteen optical branches. The three lowest phonon branches are acoustic phonon branches, *i.e.* the out-of-plane flexural acoustic (FA) branch, the in-plane transverse acoustic (TA) branch, and the in-plane longitudinal acoustic (LA) branch, present linear behavior when approaching the Γ point, while the flexural acoustic (FA) phonon branch shows a quadratic behavior,

which is consistent with our previous results [108]. Similar behaviors are always found in 2D materials, and the consistency ensures the accuracy of the obtained thermal conductivity.
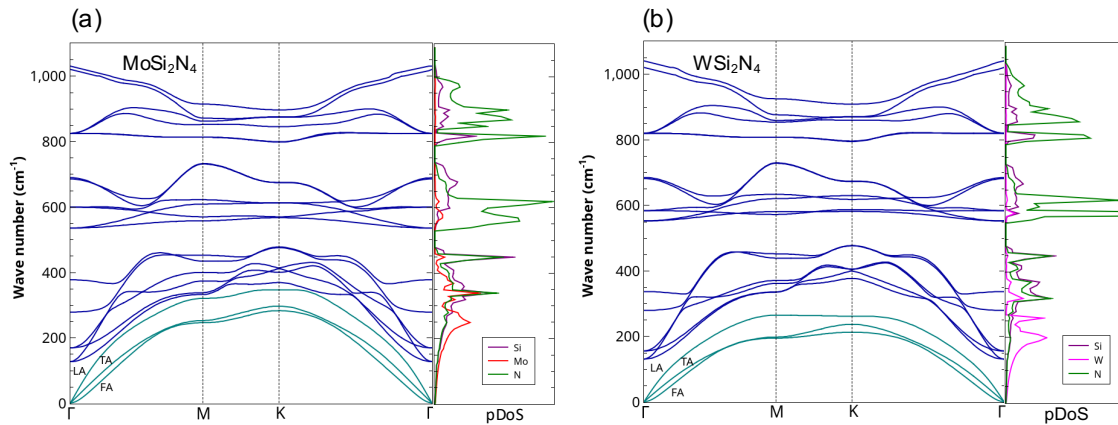
Figure 5.2.: The phonon dispersions adn density of states (pDOS) of $MoSi_2N_4$ and WSi_2N_4.

In addition, the two monolayer compounds show very similar dispersion curves along the path passing through the main high symmetry K-points in the irreducible Brillouin zone (IBZ). The phonon dispersions of monolayer $MoSi_2N_4$ and WSi_2N_4 are separated into three regions. There exists a gap between the regions. The gap between these two compounds is also quite similar. Interestingly, the frequencies of acoustic branches of $MoSi_2N_4$ and WSi_2N_4 are pretty similar and comparable with the common 2D materials, such as WS_2 and MoS_2. The high frequency of acoustic branches indicates that the phonon harmonic vibrations of $MoSi_2N_4$ and WSi_2N_4 are strong, which will significantly affect the phonon transport properties. However, as shown in Figure 5.2, TA, FA, and LA branches (highlighted as a green line) of $MoSi_2N_4$ and WSi_2N_4 are different. The LA branch of $MoSi_2N_4$ interacts with other optical modes, and the frequency is larger than that of WSi_2N_4. This phenomenon will also impact the thermal transport properties; we will discuss them in the next section.

As revealed by the partial density of states (pDOS), high-frequency optical phonon branches above the gap are mainly contributed by the vibration of the light N atom. In the low-frequency range around 200 cm^{-1}, the contribution of W atoms and Mo atoms to the DOS of the $MoSi_2N_4$ and WSi_2N_4 are the main parts. In frequency range around 400 cm^{-1}, partial DOS of Si atoms has the same level with N atoms, while above the frequency of 400 cm^{-1}, partial DOS of N atoms is more significant than that of other atoms, and the transition metals Mo and W contribute rarely.

5.3.3. Phonon Transport Properties

Based on the harmonic and anharmonic IFCs, the lattice thermal conductivities of monolayer $MoSi_2N_4$ and WSi_2N_4 are calculated solving the BTE. In Figure 5.3, thermal conductivities of the two systems at different temperatures with monolayer MoS_2 and silicene as references for comparison are presented. The reason for choosing these two materials is the similar geometry structures. $2H$-MoS_2 corresponds to $2H$-MoN_2 of $MoSi_2N_4$, and silicene corresponds to top or bottom two-atomic-layer SiN unit of $MoSi_2N_4$.
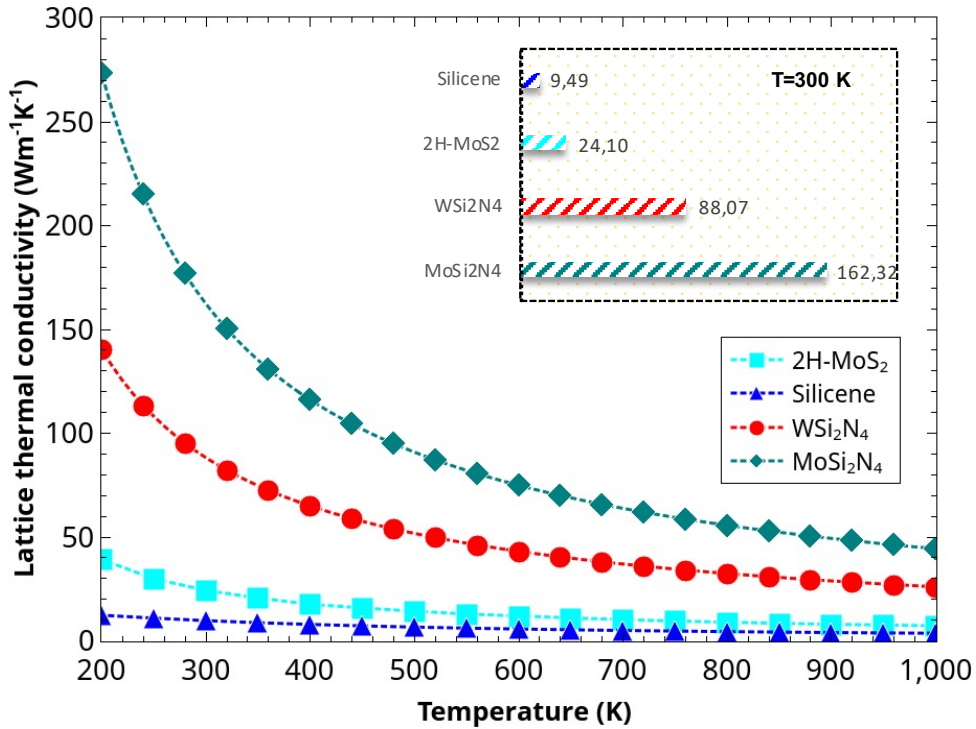
Figure 5.3.: Temperature (200-1000 K) dependent thermal conductivities of monolayer $MoSi_2N_4$, WSi_2N_4, 2H-MoS_2 and silicene.

As one can see that, the intrinsic lattice thermal conductivities are temperature dependent, which is approximately proportional to the inverse temperature of T^{-1}, consistent with the expected behavior of crystalline materials in both bulk and 2D forms. It is noted that $MoSi_2N_4$ has larger thermal conductivities. In contrast, the thermal conductivities of WSi_2N_4 are lower, which may be owing to the low frequencies of TA, FA, and LA branches. Comparing with the common excellent thermoelectric materials, such as $ZrSe_2$ [110] and $HfSe_2$ [262], the thermal conductivities of $MoSi_2N_4$ and WSi_2N_4 are

huge, 162 $Wm^{-1}K^{-1}$ and 88 $Wm^{-1}K^{-1}$ at room temperature respectively. Such large thermal conductivities limit the $MoSi_2N_4$ and WSi_2N_4 being the promising thermoelectric material. However, these two compounds with such larger thermal conductivities present the promising potential for thermal management materials. The $MoSi_2N_4$ and WSi_2N_4 possess rather high thermal conductivity compared to a lot of thermal management materials, such as MoS_2, silicene, phosphorene, *etc* [243]. In this work, the thermal conductivity of silicene as the comparison is plotted in Figure 5.3. As one can see, the intrinsic lattice thermal conductivities of $MoSi_2N_4$ and WSi_2N_4 are 7 and 4 times the one for monolayer MoS_2 (24.10 $Wm^{-1}K^{-1}$, agree with Ref. [250]), 16 and 9 times the one for silicene (9.49 $Wm^{-1}K^{-1}$, agree with Ref. [263]). Furthermore, the intrinsic thermal conductivities of $MoSi_2N_4$ and WSi_2N_4 are much larger than those of the other well-known 2D semiconductors, such as GaN (24 $Wm^{-1}K^{-1}$) [112], and monolayer 2H-$MoTe_2$ (42.2 $Wm^{-1}K^{-1}$) [264]. Especially, the thermal conductivity of $MoSi_2N_4$ is even much higher than those of widely used electronic materials such as Si (142 $Wm^{-1}K^{-1}$), which could guarantee heat transfer in the corresponding nano-electronic devices, which provides the penitential for it to be thermal management materials.

To understand the underlying mechanism responsible for the mode contributed thermal conductivity of monolayers $MoSi_2N_4$ and WSi_2N_4. We plot the spectrum of thermal conductivities and absolute contribution from each acoustic phonon branch [FA, TA, and LA as marked in Figure 5.4] to the overall thermal conductivity in Figure 5.3. As shown in Figure 5.4(a), the low-frequency phonons (below a frequency of 400 cm^{-1}) of $MoSi_2N_4$ and WSi_2N_4 dominate the thermal conductivity contributions. Especially, the contribution from FA, TA, and LA phonon branches (below a frequency of 200 cm^{-1}) contribute the most proportion of thermal conductivities of both of them. Further, the high-frequency phonons of $MoSi_2N_4$ and WSi_2N_4 hardly contribute as heat carriers. In Figure 5.4 (b and c), we compared each acoustic phonon branch (FA, TA, and LA as marked in Figure 5.4) to the overall thermal conductivity. Each acoustic phonon branch contributes quite similarly to both materials. However, the FA, TA, and LA phonon branches of $MoSi_2N_4$ are almost two times larger than the values of WSi_2N_4; the results are also consistent with the deduction from phonon dispersion of them. The main contribution of phonons in the low-frequency region of 2D materials to the thermal conductivity has been confirmed in many materials [265].

Finally, to understand the grain-size effect quantitatively, the cumulative lattice thermal conductivity was analyzed concerning the mean free path (MFP) of phonons. The cumulative thermal conductivities with respect to MFP for the $MoSi_2N_4$ and WSi_2N_4 are plotted in Figure 5.5. The MFPs corresponding to 50% of the cumulative lattice thermal conductivities for $MoSi_2N_4$ and WSi_2N_4 at 300 K are 80 and 50 nm, respectively. The MFP helps study the size effect on the ballistic vs. diffusive phonon transport. This quantity is crucial for the thermal design to modulate the thermal conductivity in the

(a)

(b)　　　　　　　　　　(c)
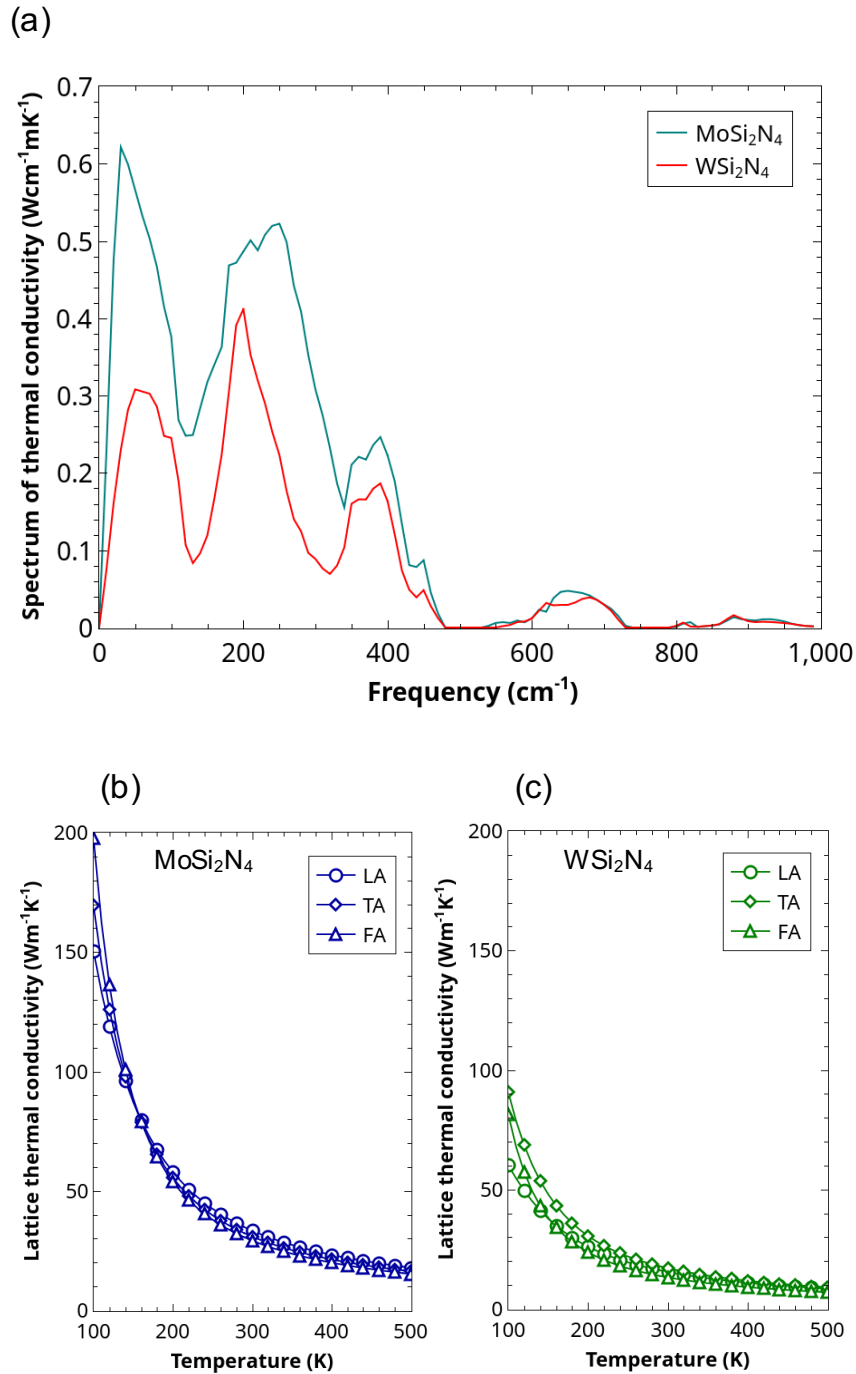
Figure 5.4.: (a) The spectrum of thermal conductivities (at 300 K) and (b,c) acoustic phonon branch contributions for overall thermal conductivities of monolayer $MoSi_2N_4$ and WSi_2N_4.

small-grain limit.
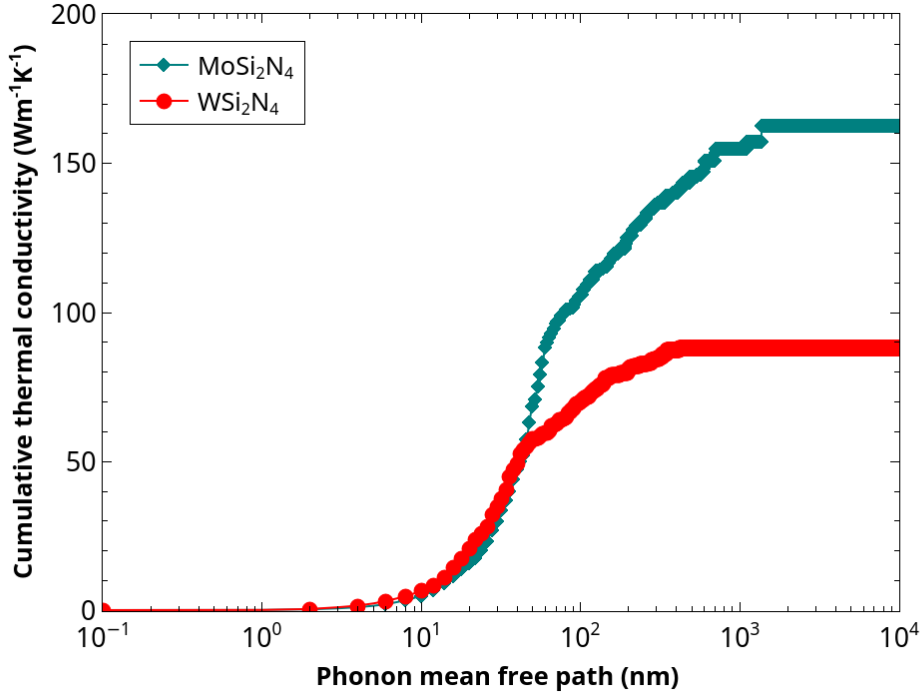
Figure 5.5.: Comparison of the cumulative lattice thermal conductivities of monolayer MoSi$_2$N$_4$ and WSi$_2$N$_4$ with respect to phonon mean free path (MFP) at 300 K.

5.3.4. Mode Level Analysis

To gain insight into the phonon transport in MoSi$_2$N$_4$ and WSi$_2$N$_4$, we performed a detailed analysis on the mode level phonon group velocity and lifetime (relaxation time). Comparison of the mode level phonon group velocity of MoSi$_2$N$_4$, WSi$_2$N$_4$, MoS$_2$ and silicene as a function of frequency at 300 K are shown in Figure 5.6(a). It is worth noted that the overall phonon group velocity of monolayer MoSi$_2$N$_4$, WSi$_2$N$_4$ are on the same order of magnitude, which is larger than that of monolayer MoS$_2$ and silicene. As for these four materials, it is interesting to notice that the acoustic phonon branches have large phonon group velocities. Furthermore, the high-frequency phonon branches (above a frequency of 400 cm^{-1}) for MoSi$_2$N$_4$, WSi$_2$N$_4$ have also relatively large phonon group velocities, which is distinctly different from MoS$_2$ and silicene. Besides, the phonon velocity of acoustic branches of MoSi$_2$N$_4$ is larger than the values of WSi$_2$N$_4$, and the rest of the branches are almost identical. It is also

confirmed that TA, FA, and LA manipulate thermal conductivity between $MoSi_2N_4$ and WSi_2N_4.

(a)

(b)
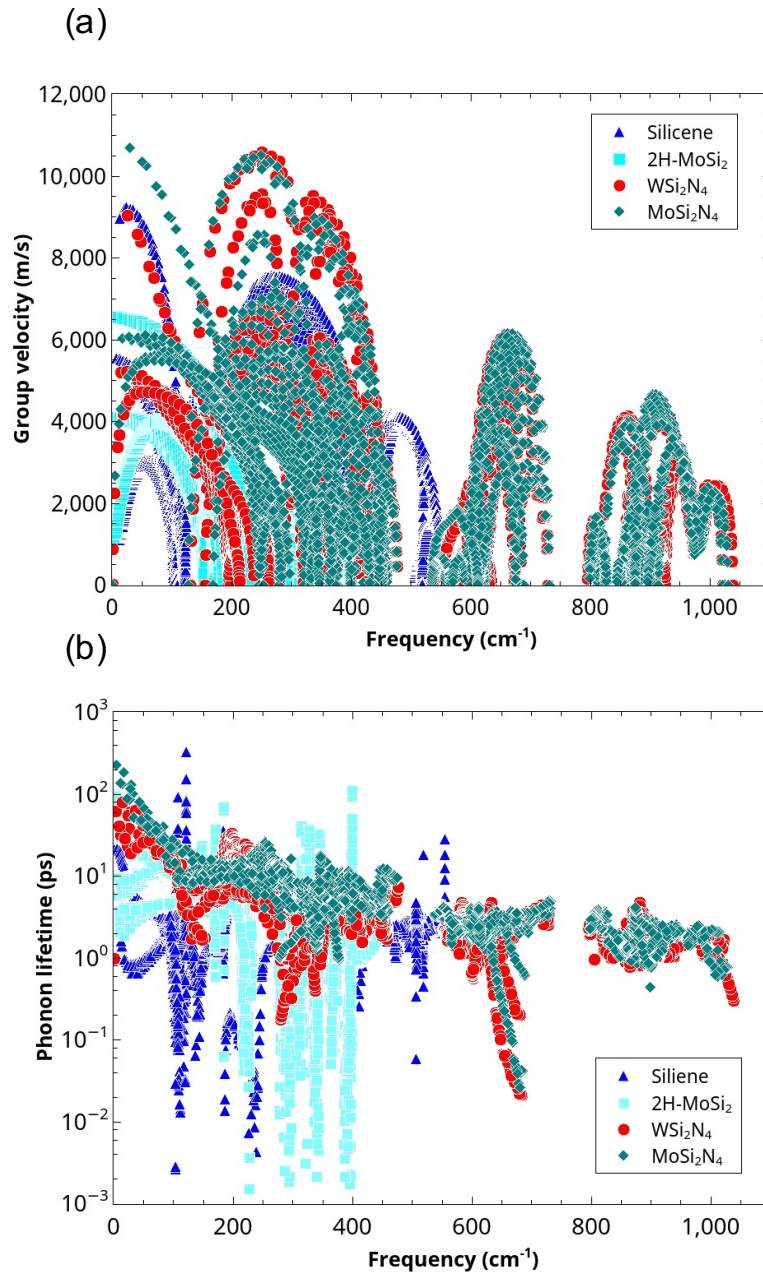
Figure 5.6.: The comparison of mode level (a) phonon group velocity and (b) phonon lifetime of monolayer $MoSi_2N_4$, WSi_2N_4, 2H-MoS_2 and silicene at 300K.

In addition, the phonon lifetimes of $MoSi_2N_4$, WSi_2N_4, MoS_2 and silicene at 300 K are plotted in the Figure 5.6(b). It can be seen that the overall lifetime of phonon branches of MoS_2 and silicene are smaller than that of $MoSi_2N_4$, WSi_2N_4, which might be due to the enhanced phonon-phonon scattering in MoS_2 and silicene, so it has a lower lattice thermal conductivity. Considering the same magnitude of group velocity as $MoSi_2N_4$, WSi_2N_4 possesses lower thermal conductivity due to its small phonon lifetime.

5.3.5. Phonon Anharmonicity
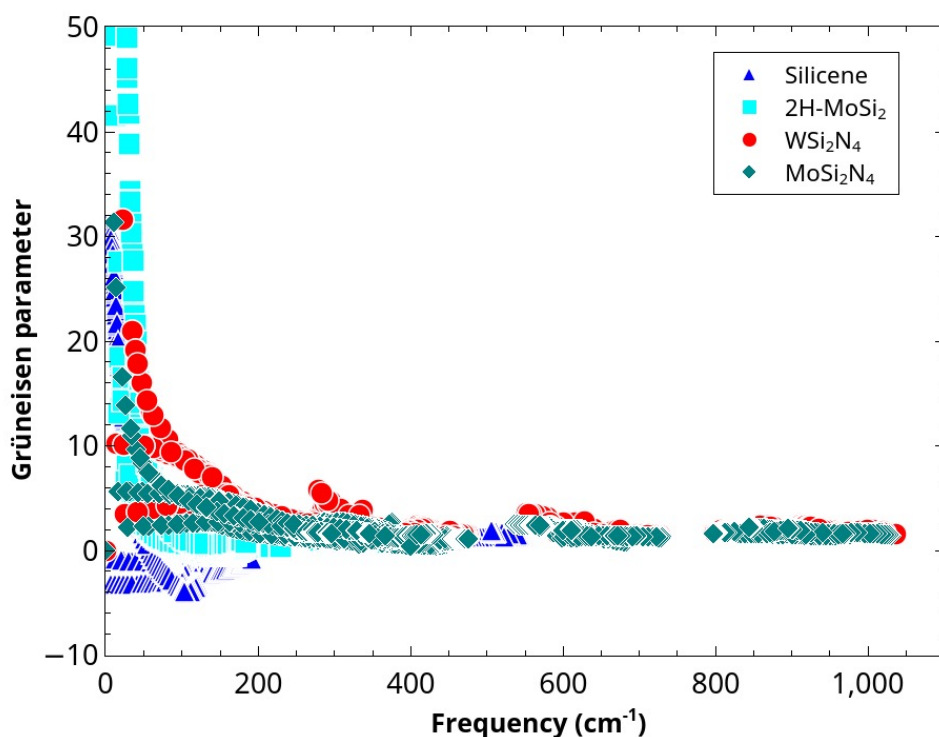
Figure 5.7.: The mode level Grüneisen parameters for $MoSi_2N_4$, WSi_2N_4, 2H-$MoSi_2$ and silicene.

It is well known that the phonon-phonon scattering process is determined by the anharmonic nature of structures, whose magnitude can be roughly quantified by the Grüneisen parameter. To this end, we examine the phonon anharmonicity of these materials by calculating the Grüneisen parameter. As shown in Figure 5.7, the magnitude of Grüneisen parameter for MoS_2 is obviously larger than $MoSi_2N_4$ and WSi_2N_4, meaning

stronger phonon anharmonicity in MoS_2. The strong phonon-phonon scattering due to the anharmonicity leads to the small phonon lifetime of MoS_2 (Figure 5.6(b)), and thus leads to the low thermal conductivity of silicene (Figure 5.3). For the same reason, the Grüneisen parameter of $MoSi_2N_4$ smaller than that of WSi_2N_4, which is the underlying reason for the small phonon lifetime and further lower thermal conductivity of WSi_2N_4 than $MoSi_2N_4$. Significantly, the deviation of the Grüneisen parameter between $MoSi_2N_4$ and WSi_2N_4 mainly occurs at low-frequency range (below a frequency of 200 cm^{-1}), indicating the acoustic phonon branches dominate the thermal transport properties.

5.3.6. Insight from Electronic Structures
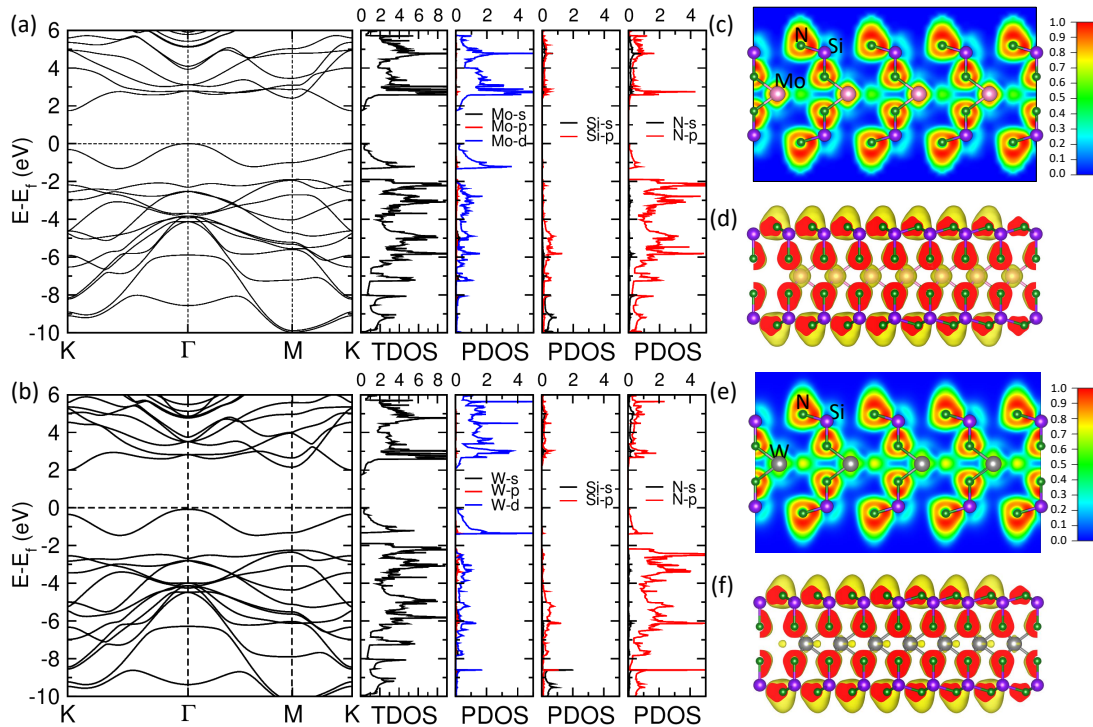
Figure 5.8.: (a,b) The electronic structures for $MoSi_2N_4$, WSi_2N_4, (c,e) 2D ELF images for $MoSi_2N_4$, WSi_2N_4, and (d,f) 3D isosurface images with ELF = 0.6 for $MoSi_2N_4$, WSi_2N_4.

To understand the fundamental mechanism underlying the phonon thermal transport, the electronic structures of $MoSi_2N_4$ and WSi_2N_4 monolayers are derived by first-principles calculations, as comparably shown in Figure 5.8(a and b). $MoSi_2N_4$ and

WSi$_2$N$_4$ are semiconductors with indirect band gap about 1.74 and 2.08 eV, which are also confirmed by the density of states (DOS) as shown in Figure 5.8(c and e). For both MoSi$_2$N$_4$ and WSi$_2$N$_4$ monolayers, we find that the valence bands from -10 to -2 eV mainly originate from p-orbits of N. In contrast, the bands from -1.5 to 6 eV are mainly dominated by the d-orbits of M (M = Mo, W) and are weakly contributed by the p-orbits of N. Such fact implies strong orbital hybridization between N-p and M-d orbits.

To learn more about the bonding formability with respect to the variation of orbital states of atoms, detailed analysis on crystal orbital Hamilton population (COHP) is carried out. A positive -pCOHP value indicates the bonding interaction, while a negative value indicates the antibonding interaction. As shown in Figure 5.9, close to the Fermi level, Mo[4d](W[5d])-N[2p] orbitals hybridize and dominantly contribute to the bonding, which indicates a positive -pCOHP at Fermi level. This scenario can also confirmed by the DOS calculation in Figure 5.8. To further explore the bonding characteristics of MSi$_2$N$_4$ monolayer, the electron localization function (ELF) is plotted in Figure 5.8(c and e) ranging from 0 (blue) to 1 (red). ELF = 1 means perfect localization, while ELF = 0.5 is the probability of electron-gas-like pair. In MSi$_2$N$_4$ monolayers, the electrons are largely localized around N atoms and decayed from M and Si atoms, indicating that the electrons are transferred from M and Si to N to form bonds with ionic characteristics between M, Si and N. Furthermore, compared with Mo atom, smaller ELF value near W atoms indicates stronger ionic bonding of W-N than Mo-N, which is consistent with the TMDCs [266, 267].
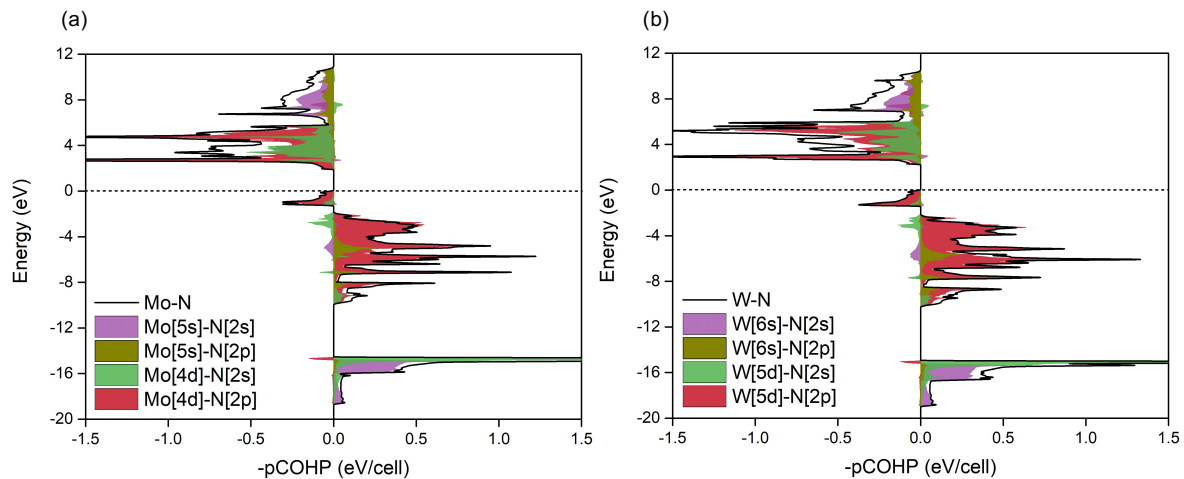
Figure 5.9.: Orbital-resolved COHP of monolayer MoSi$_2$N$_4$ and WSi$_2$N$_4$.

Generally, strong interatomic bonding and low average atomic mass are benefit to high thermal conductivity of 2D materials [268]. Therefore, the Young's modulus

and average atomic mass of MSi_2N_4 are derived in Table 5.2. For more detail, in the linear elastic regime the Young's modulus of 2D materials (Y^{2D}) is possible to estimate by the elastic constants C11 and C12, the form of Y^{2D} as follows [269, 270]

$$Y^{2D} = \frac{C_{11}^2 - C_{12}^2}{C_{11}} \qquad (5.2)$$

Note that, the elastic constant is rescaled by d_0/h to obtain the effective elastic constant, where d_0 is slab model length along thickness direction and h is the thickness of monolayer. As listed in Table 5.2, we can find that the Young's modulus of MSi_2N_4 is more than twice than that of MoS_2 and silicene, which indicates stronger interatomic bonding in MSi_2N_4. Furthermore, the average atomic mass ($\bar{M} = M_t/n$, where M_t is total mass per formula cell, and n is the number of atoms per formula cell) of $MoSi_2N_4$ is about half of MoS_2 and comparable to that of silicene, indicated a higher thermal conductivity of MSi_2N_4. Such a fact is in good agreement with the results derived by first-principle-based BTE calculations that higher thermal conductivity of MSi_2N_4 than that of MoS_2 and silicene.

Table 5.2.: The average atomic mass ($\bar{M}$), Young's modulus (Y^{2D}, GPa) and thickness (h, Å) of MSi_2N_4, MoS_2 and silicene.

Compound	$\bar{M}$	Y^{2D}	h
$MoSi_2N_4$	29.74	474.75	10.28
WSi_2N_4	42.29	499.83	10.29
MoS_2	53.36	205.81	6.04
silicene	28.09	207.94	2.97

5.4. Conclusions

In summary, by solving the phonon BTE based on the first-principles calculations, we have performed a comprehensive study on the phonon transport properties of $MoSi_2N_4$ and WSi_2N_4 and made a thorough comparison with monolayer MoS_2 and silicene. The thermal conductivities of $MoSi_2N_4$ and WSi_2N_4 are found to be 162 $Wm^{-1}K^{-1}$ and 88 $Wm^{-1}K^{-1}$ at room temperature respectively, which are are 7 and 4 times the one for monolayer MoS_2, 16 and 9 times the one for silicene. These results show that, $MoSi_2N_4$ and WSi_2N_4 have promising potential being thermal management materials. To understand the underlying mechanism for the high thermal conductivity of $MoSi_2N_4$ and WSi_2N_4, systematic analysis is performed based on the contribution from each phonon branch and comparison among the mode level phonon group velocity and lifetime. The root reason for the high thermal conductivity of $MoSi_2N_4$ and WSi_2N_4 is

that the high group velocity of these two materials. The phonon Grüneisen parameter is further analyzed to understand the phonon-phonon scattering. And the Grüneisen parameter of $MoSi_2N_4$ smaller than that of WSi_2N_4, which is the underlying reason for the small phonon lifetime and further lower thermal conductivity of WSi_2N_4 than $MoSi_2N_4$. Therefore, our study offers fundamental understanding of thermal transport properties in monolayer $MoSi_2N_4$ and WSi_2N_4 within the framework of BTE and the electronic structures from the bottom, which will enrich the studies and exploring of novel MSi_2N_4 type two dimensional thermal management materials.

6. Mechanism Underlying Phonon Anharmonicity

With the successful synthesis of the two-dimensional (2D) gallium nitride (GaN) in a planar honeycomb structure, the phonon transport properties of 2D GaN have been reported. However, it still remains unclear for the thermal transport in Ga-based materials by substituting N to other elements in the same main group, which is of more broad applications. In this paper, based on first-principles calculations, we performed a comprehensive study on the phonon transport properties of 2D GaX (X = N, P, and As) with planar or buckled honeycomb structures. The thermal conductivity of GaP (1.52 $Wm^{-1}K^{-1}$) is found unexpectedly ultra-low, which is in sharp contrast to GaN and GaAs despite their similar honeycomb geometry structure. Based on PJTE theory, GaP and GaAs stabilize in buckling structure, different from the planar structure of GaN. Compared to GaN and GaAs, strong phonon-phonon scattering is found in GaP due to the strongest phonon anharmonicity. In view of electronic structures, deep insight is gained into the phonon transport that the buckling structure has the most significant influence on the anharmonicity. And the delocalization of electrons in GaP is restricted due to the buckling structure. Thus, non-bonding lone pair electrons of P atoms induce nonlinear electrostatic forces upon thermal agitation, leading to increased phonon anharmonicity in the lattice and thus reducing the thermal conductivity. Our study offers a fundamental understanding of phonon transport in GaX monolayers with honeycomb structure, which will enrich future studies of nanoscale phonon transport in 2D materials.

6.1. Introduction

The effective manipulation of thermal energy and thermal transport plays a pivotal role in the thermal management for advanced energy and nano-electronic devices [271, 246]. On the one hand, materials with enhanced thermal transports are indispensable to maximize the heat transfer or minimize the heat waste, which can be applied to improve the working stability and energy efficiency of microelectronics. On the other hand, systems with low thermal conductivity benefit the performance of the thermal barrier coating and thermoelectric devices [272]. Therefore, insulators with tailored thermal transport properties originated from the crystal lattices are essential, as they can be integrated as thermal management components without causing other complications [273]. There is a strong impetus to gain deeper insights into the thermal transport mediated by phonons and to further treat the appealing thermophysical problems with enormous practical implications, which can be applied in electronic cooling [274], thermoelectrics [272, 275], phase change memories [276, 277], thermal devices (diodes, transistors, logic gates) [278], *etc*.

Particularly, initiated by the discovery of graphene [279], 2D materials have been intensively investigated for promising applications in engineering miniaturised devices [276, 280]. For instance, a variety of 2D materials have been theoretically predicted and successfully fabricated, such as Xenes (*e.g.*, black phosphorus) [281], transition-metal dichalcogenides (TMDCs) (*e.g.*, MoS_2) [282], MXenes (*e.g.*, Ti_3C_2, and Ti_4N_3) [283], and nitrides (*e.g.*, BN, $MoSi_2N_4$) [284, 22, 285], which provide alternative solutions for electronic, spintronic, and optoelectronic applications. Moreover, the more efficient high-throughput density functional theory method is implemented to screen the novel 2D thermoelectric materials [286]. Recently, monolayer GaN with a planar honeycomb structure was successfully fabricated in experiments [287, 288] and has been intensively theoretically studied [112, 108], which shows low thermal conductivity and is considered as potential application in energy conversion such as thermoelectrics. Therefore, an interesting question is how does the thermal transport perform in monolayer GaP and GaAs as the same main group of GaN and whether they are also good candidates as potential thermoelectric applications.

In this work, we performed first-principles calculations on the thermal conductivities in a series of Ga-based 2D materials GaX (X = N, P, and As). It is observed that the lattice thermal conductivity of GaP monolayers is unexpectedly ultra-low, which is in sharp contrast to GaN and GaAs monolayers. Detailed analysis of the crystal structure and mode-resolved thermal conductivities reveals that the lone-pair non-bonding electrons play a critical role in the thermal conductivity. Such lone-pairs are strongly correlated with the crystal structure distortions, which can be attributed to the pseudo Jahn-Teller effect (PJTE). Such mechanistic understanding of the thermal conductivities in GaX monolayers and the established electronic structure descriptors pave the way to optimize

and design novel 2D materials as thermal functional materials and to enrich the studies of nanoscale phonon transport in 2D materials.

6.2. Computational Details

Ab initio calculations based on density functional theory (DFT) were performed using the *Vienna ab initio simulation package* (VASP) [260, 193], which implements the projector augmented wave (PAW) [194]. The outer electrons configurations of Ga, N, P, and As are $4s^2 4p^1$, $2s^2 2p^3$, $3s^2 3p^3$, and $4s^2 4p^3$ respectively. Exchange–correlation energy functional is treated using the Perdew–Burke–Ernzerhof of generalized gradient approximation (GGA-PBE) [59]. The wave functions are expanded in plane wave basis with a $20 \times 20 \times 1$ Monkhorst-Pack [261] k-sampling grid and cut-off energy of 1000 eV. A large vacuum region is set as 20 Å to avoid the interactions between the monolayer and its mirrors induced by the periodic boundary conditions. Precision of total energy convergence for the self-consistent field (SCF) calculations was as high as 10^{-8} eV. All structures are fully optimized until the maximal Hellmann–Feynman force is less than 10^{-8} eVÅ^{-1}. To calculate the phonon dispersion, thermal conductivity, and various phonon properties, it is necessary to extract second- and third-interatomic force constants (IFCs) from first-principles calculations. To this end, $6 \times 6 \times 1$ supercell containing 72 atoms were constructed, which is sufficiently large to allow the out-of-phase tilting motion. To extract harmonic and anharmonic IFCs, an atom in the supercell was displaced from its equilibrium position by 0.01 Å (harmonic) and 0.04 Å (anharmonic), namely the real-space finite displacement difference method, and the Hellmann-Feynman forces were calculated based on the displaced configuration. To get more accurate results, all the possible anharmonic terms (3rd order force constant) between each element are considered in this work, which means the cutoff radius exceeds the range of physically relevant anharmonic interactions. And the Q-grid of $101 \times 101 \times 1$ for calculating the thermal conductivity of GaX. Besides, the Born effective charges (Z*) and dielectric constants (ε) are obtained based on the density functional perturbation theory (DFPT), which is added to the dynamical matrix as a correction to take the long-range electrostatic interactions into account. Lattice thermal conductivity (κ_L) and relative phonon properties were determined by solving the phonon BTE, as implemented in the ALAMODE [113] package. The κ_L is estimated by the BTE within RTA through the following equation:

$$\kappa_L^{\alpha\beta}(T) = \frac{1}{NV} \sum_q C_q(T) v_q^\alpha(T) v_q^\beta(T) \tau_q(T),$$

(6.1)

where V, $C_q(T)$, $v_q(T)$, and $\tau_q(T)$ are the unit cell volume, mode specific heat, phonon group velocity, and phonon lifetime, respectively. When calculating the thermal conductivity, the real thickness of 2D materials can be obtained by considering the van der

Waals radius of the upper and lower atoms plus the distance between the upper and lower atoms (buckling distance in this work). At last, the stabilities of current systems can be checked in the C2DB database [289], which also indicates the GaSb and GaBi unstable.

6.3. Results and Discussion

6.3.1. Lattice Structures of Monolayer Ga-based Compounds

The optimized structures of 2D GaN, GaP, and GaAs monolayers are shown in the Figure 6.1. According to the top views, all three GaX monolayers exhibit honeycomb structures, with the resulting lattice parameters listed in Table 6.2. However, GaN monolayers have a planar structure, whereas the GaP and GaAs monolayers are buckled, *et al.*, the Ga and X sublattices are shifted in opposite directions perpendicular to the monolayers, leading to larger thickness than GaN (as listed in Table 6.2). The lattice constants of the GaN, GaP, and GaAs are in good agreement with previous reports [290, 108]. For instance, the in-plane lattice constant of GaN is 3.21 Å as optimized in this study, which is between 3.20 Å in Ref. [290] and 3.26 Å in Ref. [108].

The origin of such differences (*i.e.*, planar versus buckled) in the crystal structures can be attributed to the electronic structure. Following the theory of PJTE, the curvature of the adiabatic potential energy surface (APES) yields

$$
K = \underbrace{\left\langle \Psi_0 \left| (\frac{\partial^2 H}{\partial Q^2})_0 \right| \Psi_0 \right\rangle}_{K_0} - 2\sum_n \underbrace{\frac{\left| \left\langle \Psi_0 \left| (\frac{\partial H}{\partial Q})_0 \right| \Psi_n \right\rangle \right|^2}{E_n - E_0}}_{K_v} \tag{6.2}
$$

where H represents the Hamiltonian, $\Psi_0(\Psi_n)$ denotes the ground state (excited state) wave function, and all the functions are considered for the high-symmetry configuration. It is noted that for the high-symmetry configuration the K_0 term is greater than zero, [291, 292, 293] and K_v, the vibronic contribution, is smaller than zero and the source of instability. If the resulting $K = K_0 + K_v$ is smaller than zero, the crystal structure is unstable with respect to the distortion mode denoted by Q. Correspondingly, the allowed virtual transitions can be obtained based on the symmetry analysis, *i.e.*, the direct product of the irreducible representations (irrep) of the ground state Γ_0, the excited state Γ_n, and the distortion mode Γ_q should contain the A_{1g} representation. That is, $\Gamma_0 \otimes \Gamma_q \otimes \Gamma_n \supset A_{1g}$. In other words, when the direct product of the representations of the electronic states contains the irrep of the distortion mode, [294] *i.e.*, $\Gamma_0 \otimes \Gamma_n \supset \Gamma_q$, there is possible finite contribution to the K_v term. Besides, in the case of strong PJTE,

the curvature of ground (excited) state in the APES becomes negative (positive) with respect to the q distortion mode.
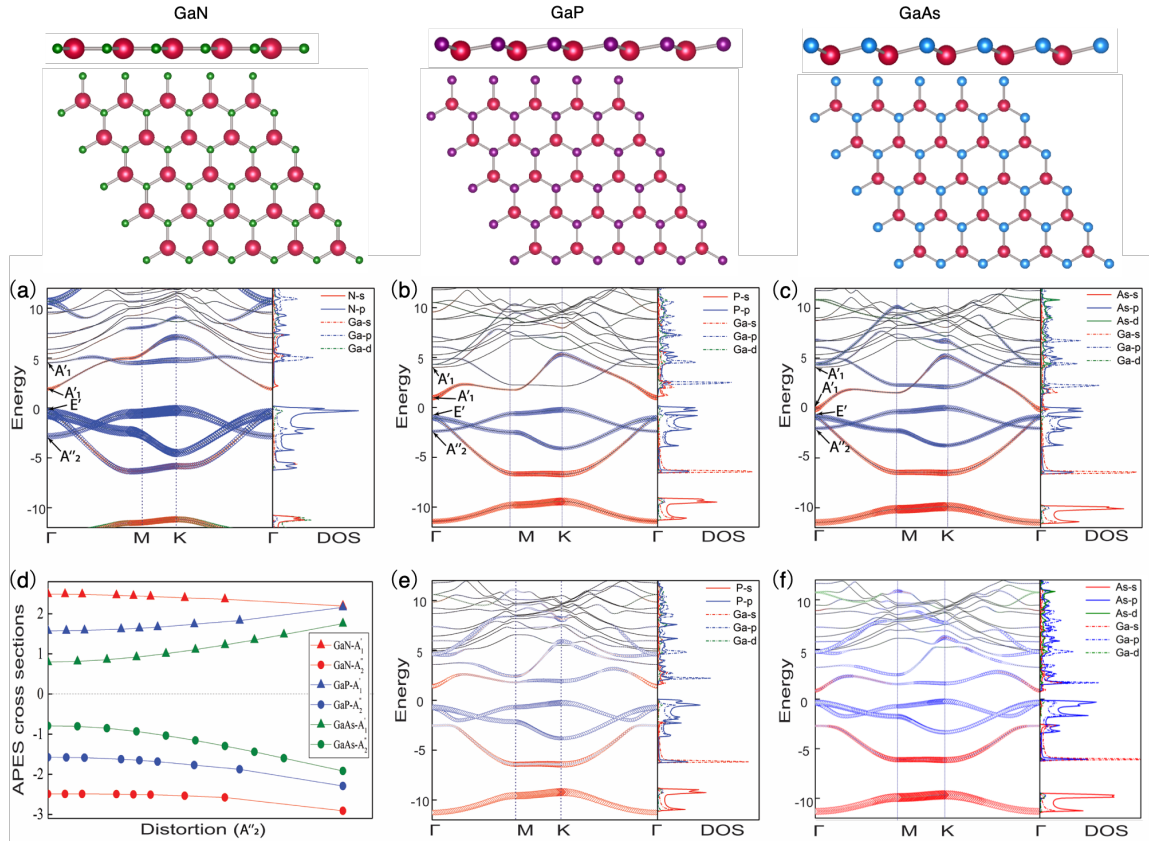
Figure 6.1.: The side and top views of structures, phonon dispersions, and partial density of states (pDOS) of monolayer GaN, GaP and GaAs. Electronic band structures and pDOS of planar monolayer (a) GaN, (b) GaP, and (c) GaAs. (d) The adiabatic potential energy surface cross section of planar GaN, GaP, and GaAs with respect to the $A_2^{''}$ distortion mode. Electronic band structures and pDOS of buckled monolayer (e) GaP and (f) GaAs.

For the GaX monolayers, following the PJTE at the center of the BZ (Γ point), the buckling is induced by the $A_2^{''}$ mode, which causes the phase transition from the high-symmetric $P\bar{6}m2$ structure to the low-symmetric $P3m1$ structure. Based on symmetry analysis and according to the irreps of the electronic states in Figure 6.1(a-c), only the $A_2^{''}$ (originated mostly from the X-p states) and A_1' (mainly of the X-s character) states are allowed to be coupled by the $A_2^{''}$ distortion mode, because $A_2'' \otimes A_1' = A_2''$. The resulting adiabatic potential energy surface cross section with respect to the $A_2^{''}$ distortion amplitude is shown in Figure 6.1(d). Obviously, the softening of the ground

state, with A_2'' irrep, and increasing of the excited state, with A_1' irrep, increases from the GaN to the GaAs monolayers. One main reason is the reduced energy difference between the two electronic states ($E_n - E_0$ in the K_V term), marked as energy gap, *e.g.*,the energy gap changes from 4.98 eV for GaN, to 3.15 eV for GaP, and finally to 1.59 eV for GaAs monolayers. Thus, such an enhanced PJT coupling leads to the buckling of the crystal lattices of GaP and GaAs.

Table 6.1.: Symmetry space group, lattice constant (a in Å), thickness (Å), and buckling distance (Å) of monolayer GaN, GaP, and GaAs. (The real thickness of 2D materials can be obtained by considering the van der Waals radius of the upper and lower atoms plus the distance between the upper and lower atoms.)

Compound	Space group	Thickness	a	Buckling distance
GaN	P6̄m2	3.74	3.21	0
GaP	P3m1	4.06	3.90	0.39
GaAs	P3m1	4.30	4.05	0.58

6.3.2. Phonon Dispersion

Turning now to the lattice dynamics and thermal transport properties. Figure 6.2 shows the phonon spectra of GaX monolayers obtained by diagonalizing the dynamical matrix based on the second order IFCs. As the GaX systems behave more like ionic insulators, the longitudinal optical (LO) - transverse optical (TO) splitting clearly occurs after considering the nonanalytical corrections based on the Born effective charges listed in Table 6.2. This indicates the arising of macroscopic electric fields resulted from the atomic displacements associated with the long-wave LO phonons [295]. Note also that after considering the non-analytical correction, the slightly imaginary mode at Γ point for GaP and GaAs monolayers disappear. This is due to the macroscopic field generated by the strongly polarized covalent bonds, leading to modified force constants and hence dynamical stability at the Γ point.

Interestingly, in comparison to those of GaP and GaAs monolayers, there exists a big gap in the phonon spectra of GaN monolayers between the LO/TO and other phonon bands. This can be attributed to the large difference in the atomic mass of Ga and N atoms. Moreover, the frequencies of the acoustic branches of GaP and GaAs monolayers are lower than those in GaN cases, and much lower than the common 2D materials, such as h-BN [89] and graphene [296]. This implies that the phonon harmonic vibrations of GaP and GaAs are weak, which will have a significant effect on the phonon transport properties. In addition, the longitudinal acoustic (LA) and transverse acoustic (TA)

phonon branches of the GaX systems present linear behavior when approaching to the Γ point, while the flexural acoustic (FA) phonon branch shows a quadratic behavior. This is consistent with our previous results in GaN [108], which is a common behavior for 2D materials.

Table 6.2.: Born effective charges (Z^*) of Ga and X (where X = N, P, and As) atoms and the dielectric constants (ε) of GaP, GaP, and GaAs.

GaN	Z^*(Ga)	Z^*(N)	ε
xx	3.071	-3.071	1.859
yy	3.071	-3.071	1.859
zz	0.337	-0.337	1.148
GaP	Z^*(Ga)	Z^*(P)	ε
xx	2.975	-2.975	3.025
yy	2.975	-2.975	3.025
zz	0.156	-0.156	1.179
GaAs	Z^*(Ga)	Z^*(As)	ε
xx	2.955	-2.955	3.901
yy	2.955	-2.955	3.901
zz	0.107	-0.107	1.193
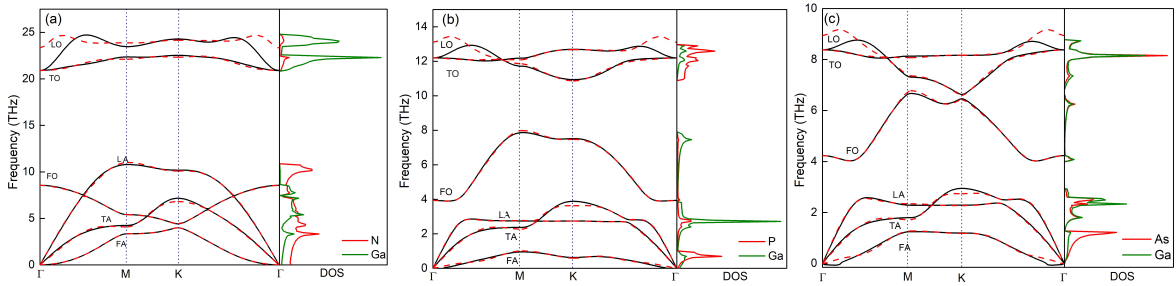
Figure 6.2.: The phonon dispersion considering the effect of Born effective charges and dielectric constants is plotted in a violet dash-dot line, showing LO-TO splitting at the center of the BZ (Γ point). The phonon dispersions not including the dipole correction are also plotted in solid line for comparison.

6.3.3. Anomalous Thermal Conductivity

Figure 6.3 (a) shows the thermal conductivities of the three systems as a function of temperature, evaluated by solving the BTE with Born effective charges considered. Clearly, the temperature dependence of the lattice thermal conductivities presents the typical

1/T behavior, consistent with other crystalline materials in both bulk and 2D forms. Furthermore, GaN has the highest thermal conductivities in the whole temperature range, while those of GaP and GaAs are on average more than five times smaller. The most striking result illustrated in Figure 6.3 (a) is that the thermal conductivity shows a non-monotonous behaviour when moving from N to As, *i.e.*, GaP monolayers possesses the lowest thermal conductivity. For instance, at 300 K, the thermal conductivity of GaP monolayers is 1.52 $Wm^{-1}K^{-1}$, which is half of the value of GaAs monolayers and more than one order of magnitude smaller than that of GaN monolayers. Similarly, Sun *et al.* [297] reported ultra-low thermal conductivities for 2D triphosphides (InP$_3$, GaP$_3$, SbP$_3$, and SnP$_3$), which might be driven by the flatter acoustic phonon branches as expected for the GaP and GaAs monolayers. It is noted that the thermal conductivities of GaP and GaAs monolayers are even lower than those of typical 2D thermoelectric materials such as GeSe [298] and SnSe [299].
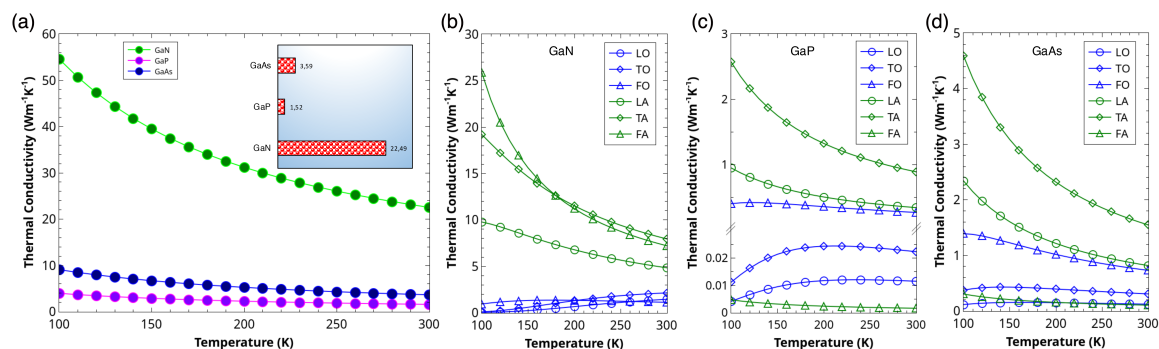
Figure 6.3.: (a) Temperature (100-300 K) dependent thermal conductivities of monolayer GaN, GaP, and GaAs. Inset figure at the right corner shows the thermal conductivity ($Wm^{-1}K^{-1}$) of the three compounds at 300 K. (b-d) The absolute contribution to the total conductivity of monolayer GaN, GaP, and GaAs from each individual phonon branch as a function of temperature

To understand the underlying mechanism responsible for the ultra-low thermal conductivities of GaP monolayers and the anomalous trend for the GaX series, the mode-resolved (FA, TA, LA, FO, TO, and LO modes) contributions to the thermal conductivity are shown in the Figure 6.3 (b-d) for GaX monolayers. Obviously, the acoustic modes exhibit dominant contributions in contrast to the optical modes. Moreover, the FA and TA branches make the most significant contributions to the total thermal conductivity of GaN monolayers, while the TA branch dominates the phonon transport in GaP and GaAs monolayers. The reason for the domination of the FA branch in GaN has been analyzed in previous work, [108] where the reflectional symmetry of the planar honeycomb structure of GaN monolayers leads to the symmetry-based selection rule of phonon-phonon scattering and results in the small scattering rate of FA phonons [296].

On the contrary, the FA branch has drastically reduced contribution to the total thermal conductivities of GaP and GaAs monolayers due to the buckled (non-planar) crystal structures.

6.3.4. Mode Level Analysis
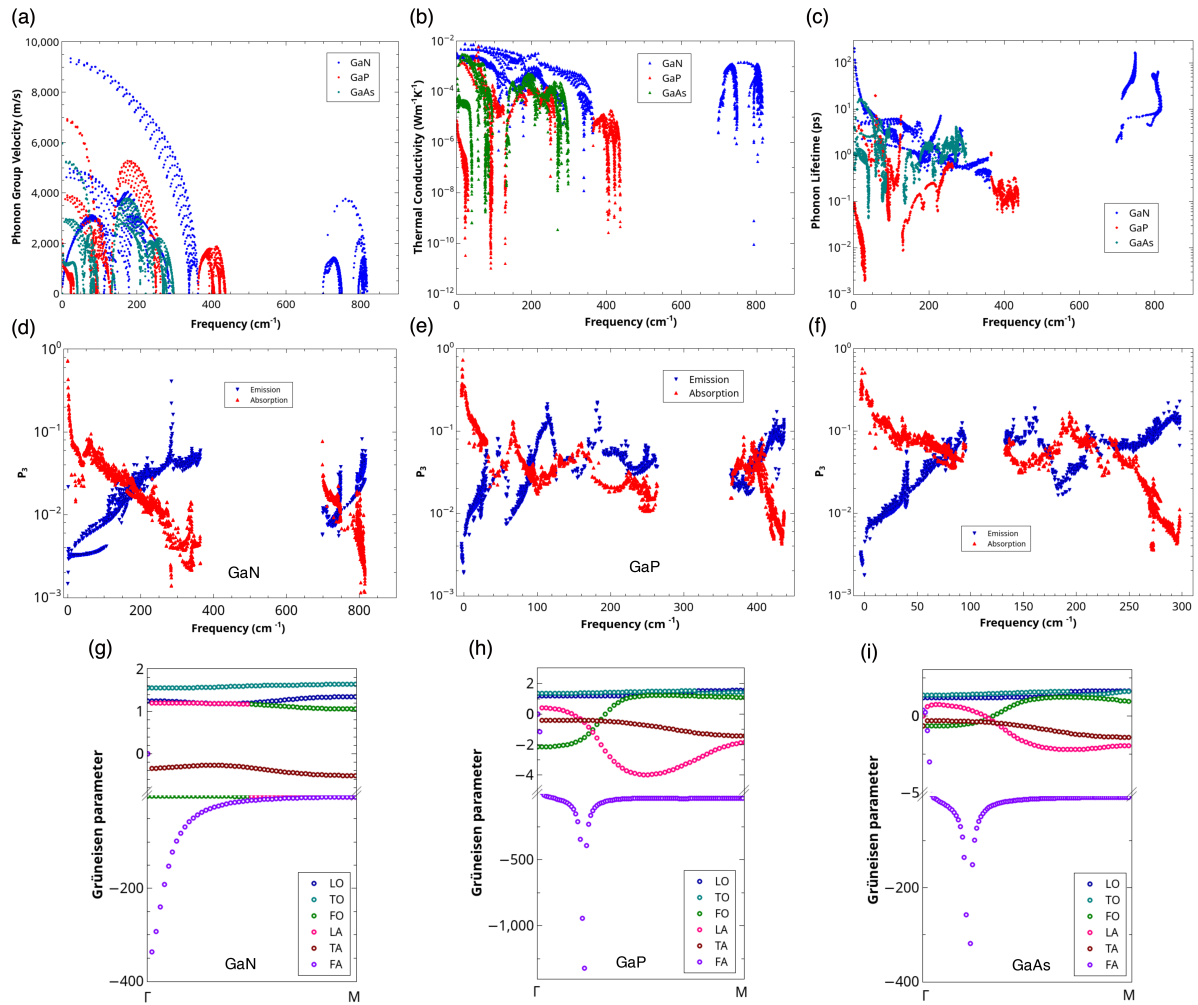
Figure 6.4.: (a) The comparison of mode phonon group velocity, the comparison of the mode-level (b) contributions to thermal conductivity and (c) phonon lifetime of monolayer GaN, GaP, and GaAs at 300K. (d-f) The mode-level scattering phase space of absorption and emission processes, and (g-i) the mode level Grüneisen parameters for three compounds.

To gain further insight into the thermal transport in GaX monolayers, we performed detailed analysis on the mode level phonon properties. Comparison of the mode level phonon group velocity of GaN, GaP and GaAs as a function of frequency at 300 K are shown in Figure 6.4 (a). It is clearly seen that the overall phonon group velocity of monolayer GaP and GaAs are on the same order of magnitude, which is smaller than that of monolayer GaN. Note that, the optical phonon branches of GaN and GaAs have relatively larger group velocities. Besides, the phonon velocity of FO branches of GaN, GaP and GaAs are large among the other branches Interestingly, the contribution of thermal conductivity of FA mode for GaX monolayers are dramatically different, as mentioned in previous section. Hence, we plotted the phonon propeties of FA branch in the Figure 6.5. Note that, the phonon group velocity of FA mode of GaN has larger values and wilder distribution than those of GaP and GaAs. Especially, the phonon group velocity of FA mode of GaP is concentrated in a smaller value area, leading to the lowest thermal conductivity.

The mode-level contribution to thermal conductivity and the corresponding phonon lifetime at 300 K are shown in the Figure 6.4 (b,c). It can be found that the phonon frequencies of monolayer GaN contributing to the thermal conductivity are concentrated at 0-400 cm^{-1}, which is consistent with the results as illustrated in Figure 6.3. And the main contribution of phonon frequencies in GaP and GaN are distributed at a much lower range, which can be confirmed by the phonon dispersion as shown in Figure 6.2. It is worth noting that not only acoustic branches, but also some optical branches with low-frequency play a major role in contributing to the thermal conductivity, which is more pronounced in GaN. Commonly, the phonons with low frequency dominating the main contribution of thermal conductivity is the universal for 2D materials. Figure 6.4 (c) shows the phonon lifetime for GaN, GaP and GaAs at 300 K. Compared to GaN and GaAs, GaP has the lowest phonon relaxation time, which could be an indicator of the strong phonon anharmonicity, leading to an ultra-low lattice thermal conductivity. For GaAs, the phonon relaxation time in the high frequency range above the gap is comparable with that in the low frequency range below the gap. For GaN, the phonon lifetime of optical phonon branches are quite high, some of them are even larger than acoustic phonon modes. Thus, the thermal conductivity of GaN is much higher than the other two. As same as the group velocity of FA mode for GaX monolayers, the FA mode in GaP has the lowest phonon lifetime (as shown in the Figure 6.5 (b)), which also results in the lowest thermal conductivity of GaP in these three materials.

Furthermore, based on phonon dispersion, the scattering phase space has been calculated with the criteria of energy and momentum conservation. As shown in Figure 6.4, the mode level scattering phase space of GaN, GaP and GaAs are presented for the phonon modes available for absorption and emission processes, respectively. It is clearly seen that there is an inverse relationship between phase space for the three-phonon process. As one can see, because of the selection rule applied to the planar honeycomb

structure of monolayer GaN, the phonon scattering processes involving odd numbers of FA phonon modes are largely restricted, which results in the dominant contribution of the FA mode to thermal conductivity. For the buckled GaP and GaAs where symmetry-based selection rule of phonon-phonon scattering are broken, the scattering phase space of FA branches available for both absorption and emission processes is not reduced consequently. As shown in Figure 6.5 (c), the scattering phase space for absorption processes of FA modes of GaP and GaAs are larger, which subsequently leads to the less contribution to thermal conductivity.

As one known, the phonon-phonon scattering process is influenced by the anharmonic nature of structures, which can be roughly quantified by the Grüneisen parameter. In this vein, we analyzed the phonon anharmonicity of the GaN, GaP and GaAs by calculating the Grüneisen parameter. As shown in the Figure 6.4 (g-i), the magnitude of Grüneisen parameter of GaP is much larger than that of other two, especially for the FA phonon branch, which indicates the strongest phonon anharmonicity in GaP. Owing to the strong anharmonicity, the strong phonon-phonon scattering results in the small phonon lifetime, as previously shown in Figure 6.4 (c). Hence, monolayer GaP has the ultra-low thermal conductivity.
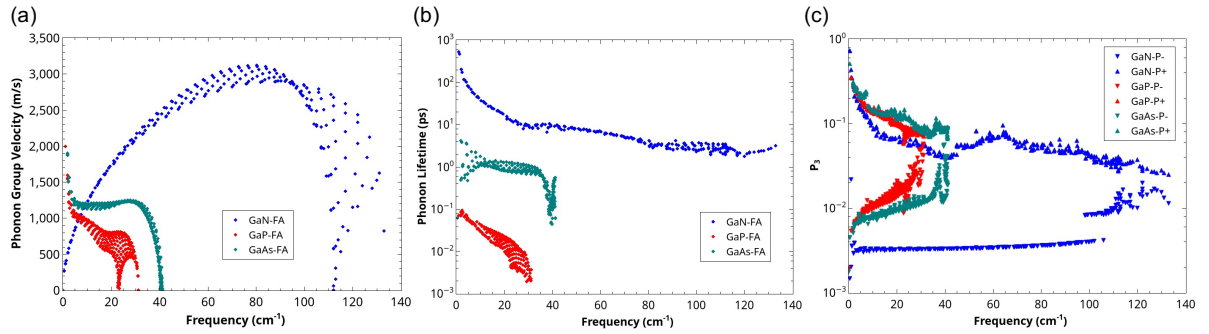
Figure 6.5.: The comparison of (a) phonon group velocity, (b) phonon lifetime, and (c) the scattering phase space of absorption (P+) and emission (P-) processes of FA mode of GaX monolayers.

6.3.5. Insight from Electronic Structures

The systematic investigation of model level phonon transport in the framework of Boltzmann transport theory has been implemented in the above sections to analyze the ultra-low thermal conductivity of monolayer GaP due to strong phonon anharmonicity. In this section, we conduct intensive study on the electronic structures to get deep insight

into the phonon transport and the phonon anharmonicity. We will present that the active lone-pair electrons due to special orbital hybridization and buckling structures drive the remarkable phonon anharmonicity in monolayer GaP.

It was proposed by Petrov and Shtrum that lone-pair electrons could lead to low thermal conductivity [300]. As shown in the Figure 6.6 (a), the electron localization functions (ELF) provides information on the structure of atomic shells, and also displays the location and size of bonding and lone electron pairs [301]. Non-bonding lone-pair electrons arise around N, P, and As atoms. The overlapping wave functions of lone-pair electrons with valence electrons from adjacent atoms Ga induce nonlinear electrostatic forces upon thermal agitation, which leads to increased phonon anharmonicity in the lattice and thus reduces the thermal conductivity [300, 302, 303, 304, 305, 306, 307].
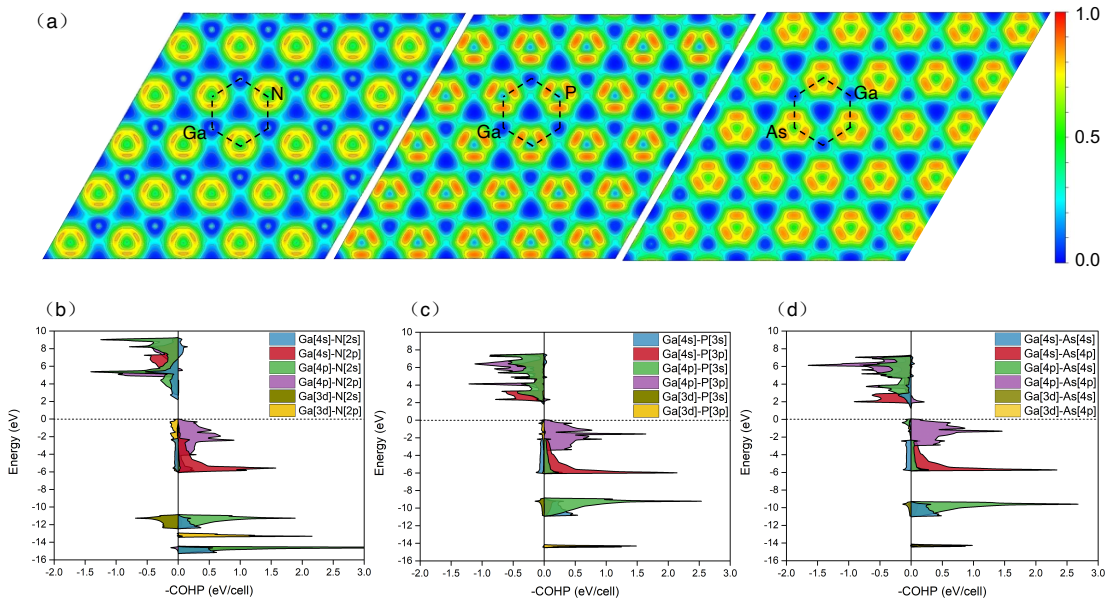
Figure 6.6.: (a) The top view of electron localization functions (ELF), and (b-d) Orbital-resolved COHP of monolayer GaN, GaP, and GaAs

It is noted that there exists difference in the electronegativity between Ga and (N, P, and As), which leads to polarization for the Ga-(N, P, and As) bonds as revealed by charge transfer, as shown in the Table 6.3. The more charge transfer means the covalent bond is more strongly polarized. Considering the largest difference in the electronegativity and charge transfer between Ga and N atoms, the phonon anharmonicity in GaN is expected to be the strongest. However, this does not happen because GaP and GaAs have relatively lower thermal conductivities. The reason might be that the buckled honeycomb structures of GaP and GaAs would induce stronger phonon-phonon scattering, leading

to the much stronger anharmonicity. In our previous work [112], the strongly polarized covalent bond could lead to larger phonon anharmonicity. In this regard, based on the charge transfer and ELF shown in Figure 6 (a), the stronger polarized covalent bond and restrict the delocalization of electrons in GaP leads to the much stronger localization of lone-pairs electrons. Moreover, the bonding electrons for the Ga-P bonds is relatively closer to P atom, which contributes positively to the stronger interaction with the non-bonding P-*s* electrons and thus leads to a stronger phonon anharmonicity. Furthermore, a metavalent boning inducing the low thermal conductivity has been reported recently [308, 309]. And the polarized covalent bonging in the monolayer GaX can be considered as metavalent bonding.

Table 6.3.: The transferred charges between each Ga-X bond (X = N, P, and As).

Compound	Charge on Ga	Charge on X
GaN	-0.4846	0.4846
GaP	-0.2633	0.2633
GaAs	-0.1974	0.1974

To learn more about the bonding formability with respect to the variation of orbital states of atoms, detailed analysis on crystal orbital Hamilton population (COHP) is carried out. A positive -pCOHP value indicate the bonding interaction, while a negative value indicates the antibonding interaction. Thus, the active lone-pair electrons are considered as neither bonding nor anti-bonding interactions. The integrated COHP of orbitals should be zero closing to Fermi energy. Generally, the active lone-pair electrons are dominantly contributed by the *s*-orbital. In this regard, we focus on the *4s* orbital of Ga and outermost *s* orbital of N, P, and As. As shown in Figure 6.6 (b-d), closing to the Fermi level, Ga[p]-(N, P, and As)[p] and Ga[s]-(N, P, and As)[p] orbitals hybridize and dominantly contribute to the bonding, which indicates a positive -pCOHP at Fermi level. In contrast, the (N, P, and As)[s]-Ga[p,d] orbitals present neither bonding nor anti-bonding interactions. Therefore, N, P, and As form the polar covalent bonds with Ga by sharing the *p* electrons, while the s^2 electrons of N, P, and As form isolated (lone pair) bands. Such behavior is also confirmed by the electronic band structures and partial density of states as shown in the Figure 6.1. The *s* orbital is largely (around 10 eV) confined below the valence band, forming an isolated band. However, the situation for the orbitals is different for the N atom where the *s* orbitals hybrid with Ga-*d* orbitals. In this regards, we can find relatively large anti-bonding Ga[3d]-N[2s] as shown in the Figure 6.6 (b).

In this vein, the buckling structure has a high priority influencing the anharmonicity, leading to the low thermal conductivity. Then, due to the buckling structures, the delocalization of electrons in GaP and GaAs are restricted, namely, the bonds are polarized. The

non-bonding lone pair electron of P and As atoms are stronger, which induces nonlinear electrostatic forces upon thermal agitation, leading to increased phonon anharmonicity in the lattice and thus reducing the thermal conductivity.

6.4. Conclusions

In summary, by solving the phonon BTE based on first-principles calculations, we have performed a comprehensive study on the phonon transport properties of 2D GaX with planar and buckled honeycomb structures. The thermal conductivity of GaP is calculated to be $1.52 \, \mathrm{Wm^{-1}K^{-1}}$, which is unexpectedly ultra-low and in sharp contrast to GaN and GaAs. Considering the similar honeycomb geometry structure of GaP to that of GaN and GaAs, it is quite intriguing to find that the thermal conductivity of GaP is very low. Firstly, to understand the underlying mechanism for GaX monolayers having planar or buckling structures, systematic analysis is performed based on PJTE theory. The larger bandgap and smaller the vibronic coupling constant, the less destabilization of the ground state and less stabilization of the excited states. Hence, the GaN exists in planar structure, and GaP and GaAs stabilize in buckling structures. Then, to gain insight into anomalous phenomena of ultra-low thermal conductivity for GaP, we perform a detailed analysis of the underlying mechanisms in the framework of phonon mode-solved investigation. The reason for the low thermal conductivity the of GaP is found to be that: FA dominates the thermal conductivity of GaN but less contributes to the one of GaP, which is due to the symmetry-based selection rule and difference of atomic structure. In particular, the difference originates from the different situations for the phonon lifetime, which is determined by phonon–phonon scattering. The phonon anharmonicity quantified by the Grüneisen parameter is further analyzed to understand the phonon–phonon scattering, indicating the strong phonon-phonon scattering of GaP and the strongest phonon anharmonicity of GaP. Considering that all the properties are fundamentally determined by the atomic structure and the behavior of electrons (such as charge distribution and orbital hybridization), we further perform analysis from the view of electronic structures and orbital bonding to gain deep insight into the phonon transport. The buckling structure has a high priority influencing the anharmonicity, leading to the low thermal conductivity. Then, due to the buckling structures, the delocalization of electrons in GaP and GaAs are restricted, namely, the bonds are polarized. The non-bonding lone pair electron of P and As atoms are stronger, which induces nonlinear electrostatic forces upon thermal agitation, leading to increased phonon anharmonicity in the lattice and thus reducing the thermal conductivity. Our study offers fundamental understanding of phonon transport in GaX monolayers with honeycomb structure within the framework of BTE and the electronic structure from the bottom, which will enrich the studies of nanoscale phonon transport in 2D materials.

7. Quartic Anharmonicity in the Lattice Dynamic

We investigate the role of the quartic anharmonicity in the lattice dynamics and thermal transport of the cubic EuTiO$_3$ by combining ab initio self-consistent phonon theory with compressive sensing techniques and experimental thermal conductivity determination measurement. The anti-ferromagnetic G-type magnetic structure is used to mimic the para-magnetic EuTiO$_3$. We find that the strong quartic anharmonicity of oxygen atoms plays an important role in the phonon quasiparticles free from imaginary frequencies in EuTiO$_3$ and causes the hardening of vibrational frequencies of soft modes. Based on these results, the lattice thermal transport properties are predicted through the Boltzmann transport equation within the relaxation time approximation. The hardened modes thereby affect calculated lattice thermal conductivity significantly, resulting in an improved agreement with experimental results, including the deviation from $\kappa_L \propto T^{-1}$ at high temperature. The calculated thermal conductivity of 8.2 Wm^{-1}K^{-1} at 300 K matched the experimental value of 6.1 Wm^{-1}K^{-1}. When considering the boundary scattering, the calculated thermal conductivity is reduced to 6.9 Wm^{-1}K^{-1} at 300 K, which agrees better with the experimental results.

7.1. Introduction

Thermoelectric materials have attracted intensive attention due to their promising application as green energy materials, *i.e.*, to convert temperature gradient into electricity [310, 311, 312, 313], so that waste heat can be harvested. The efficiency of thermoelectric materials is measured by a dimensionless figure of merit, $ZT = S^2\sigma T/\kappa$, where higher Seebeck coefficient (S) and electrical conductivity (σ), and lower thermal conductivity (κ) are needed for optimal performance. In the last decades, various bulk materials, such as skutterudite (e.g.,CoSb$_3$) [314], clathrates (e.g., Ba$_8$Ga$_{16}$Ge$_{30}$) [315], heusler alloys (*e.g.*, NbCoSn) [316], chalcogenides (*e.g.*, Bi$_2$TeSe$_2$) [317], zintl phases (*e.g.*, YbZn$_2$Sb$_2$) [318], and oxides (*e.g.*, SrTiO$_3$) [319], have been intensively investigated [313]. Oxides are particularly applicable in the high-temperature range

(800~1200 K), which is unreachable for well-known bismuth telluride based materials, thereby leading to a high Carnot efficiency that somewhat compensates for the low ZT [320, 321]. Among them, perovskite-type titanates with a chemical formula of ABO_3, such as $SrTiO_3$ and $EuTiO_3$, exhibit significant thermoelectric figures of merit which are promising for thermoelectric applications [310, 321]. For instance, they present optimal charge carrier concentrations, high flexibility in their structure and composition, and their properties can be easily tuned by ionic substitutions [310, 321], such as $SrTi_{1-x}Nb_xO_3$ performing $ZT = 0.25$ at 1200K [310].

Europium titanate ($EuTiO_3$) is one of the perovskite oxides as promising high-temperature thermoelectric materials, which has the typical perovskite structure of space group $Pm\bar{3}m$ (as shown in Figure 7.1) [322]. Despite its similar crystal structure to $SrTiO_3$, $EuTiO_3$ is more attractive owing to its rich magnetic structure induced by $4f$ shell electrons and strong coupling between spin magnetic moments and surrounding lattices, *e.g.* phonons. In $EuTiO_3$, the Eu^{2+} ions possess a half-filled $4f$ shell thus a large spin magnetic moment ($7~\mu B$) [322, 323], with a second order phase transition at 5.3 K from the paramagnetic to the antiferromagnetic states [324]. The shape of Eu $4f$ band near the Fermi level suggests a giant Seebeck coefficient [325]. In addition, the electrical conductivity and thermal conductivity of $EuTiO_3$ can be tuned by cation or anion substitutions and several substitutions have been reported (*e.g.*, $EuTi(O,N)_{3+\delta}$ [326], $Eu_{1-x}Ba_xTiO_3$ [327]). For instance, the thermoelectric properties of $EuTiO_3$ were studied and a high Seebeck coefficient was found -1053 μV/K at 300 K [327]. The electrical conductivity was improved by partial Nb substitution at the Ti site, resulting in a ZT of $EuTi_{0.98}Nb_{0.02}O_{3-\lambda}$ equals to 0.4 at T =1040 K [328]. Although the thermoelectric properties of pristine and doped $EuTiO_3$ have been extensively explored, there is no detailed experimental and theoretical study on thermal transport properties of magnetic $EuTiO_3$. Therefore, an imperative question is how the intrinsic magnetic behavior play with lattice vibrations, especially anharmonic phonons, and build a quantitative thermal conductivity dependence on them.

Like the other perovskite oxides [101, 329], one challenge to evaluate the thermal conductivity of $EuTiO_3$ is how to properly deal with the strong anharmonic effect, particularly in the high-temperature range where the phonon-phonon interaction is enhanced. In this regard, the recently implemented self-consistent phonon (SCP) theory [101] offers an effective way to systematically consider the anharmonic effects, where the high-ordered interatomic force constants (IFCs) can be obtained based on the compressive sensing technique [111]. Such techniques have been employed to tackle systems with strong anharmonicity, such as $SrTiO_3$ [330], ScF_3 [331] and $Ba_8Ga_{16}Ge_{30}$ [118], where thermal expansion, thermal transport properties, anharmonic vibrational free-energy are accurately predicted and explained.

In this paper, to elucidate the lattice thermal transport properties of $EuTiO_3$, we performed accurate first-principles calculations to evaluate the lattice dynamics of $EuTiO_3$,

including the anharmonic effects. We used the efficient implementation of the SCP theory [101], which employs anharmonic force constants calculated using the compressive sensing lattice dynamics method [111], to calculate the thermal transport properties. And the role of the quartic anharmonicity in the lattice dynamics and thermal transport of the $EuTiO_3$ was comprehensively analyzed. We found that the strong quartic anharmonicity of oxygen atoms plays an important role in the phonon quasiparticles free from imaginary frequencies in $EuTiO_3$ and causes the hardening of vibrational frequencies of soft modes. Further, by using the effective harmonic force constants corrected under anharmonic force constants, the accurate thermal conductivity and relative phonon properties of $EuTiO_3$ are obtained. Meanwhile, the $EuTiO_3$ sample is experimentally synthesized. The thermal conductivity is measured to compare with the predicted results, which have a good agreement.
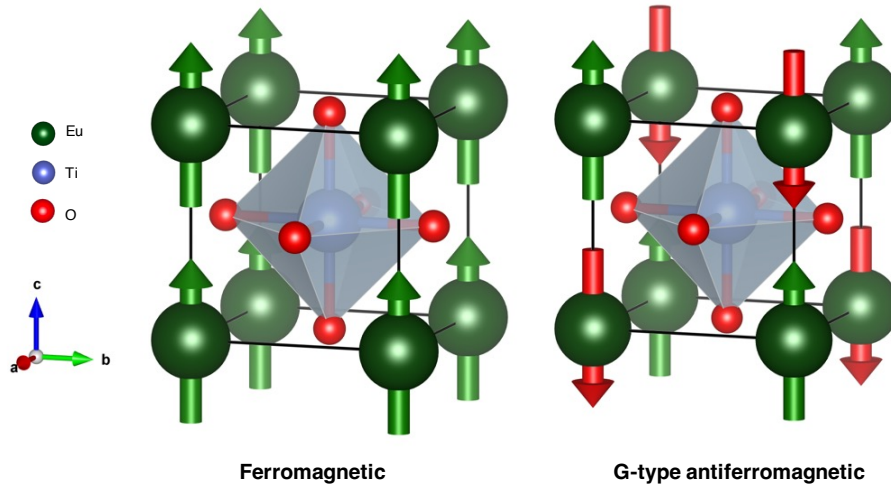
Figure 7.1.: Crystal structure of cubic $EuTiO_3$ with different magnetic structures. The corner atoms represent Eu, and the atoms at the body-centred and the face-centred positions represent Ti and O, respectively.

7.2. Self-consistent Phonon Theory

Let us briefly restart by expressing the potential energy of an interacting ions system U as a Taylor expansion with respect to the atomic displacement u:

$$U = U_0 + U_2 + U_3 + U_4 + \dots, \tag{7.1}$$

$$U_n = \frac{1}{n!} \sum_{\{\ell,\kappa,\mu\}} \Phi_{\mu_1 \cdots \mu_n}(\ell_1 \kappa_1; \ldots; \ell_n \kappa_n) \times u_{\mu_1}(\ell_1 \kappa_1) \cdots u_{\mu_n}(\ell_n \kappa_n). \tag{7.2}$$

Here, $\Phi_{\mu_1 \cdots \mu_n}(\ell_1 \kappa_1; \cdots; \ell_n \kappa_n)$ is the nth-order derivative of the nth-order potential energy U_n with respect to displacement, which is called the interatomic force constant (IFC). The IFCs are determined at the ground state and therefore have no temperature dependence. $u_\mu(\ell\kappa)$ is the atomic displacement of atom κ in the ℓth cell along μ direction.

In the harmonic approximation, only the second order term U_2 is considered, and all of the anharmonic terms are neglected. Then, the Hamiltonian of the system $H_0 = T + U_2$ can be represented in terms of the harmonic phonon frequency ω, which can be obtained for the dynamical matrix

$$D_{\mu\nu}(\kappa\kappa'; \boldsymbol{q}) = \frac{1}{\sqrt{M_\kappa M_{\kappa'}}} \sum_{\ell'} \Phi_{\mu\nu}(\ell\kappa; \ell'\kappa') \exp\left[i\boldsymbol{q} \cdot (\boldsymbol{r}(\ell') - \boldsymbol{r}(\ell))\right], \tag{7.3}$$

where M_κ is the mass of atom κ, and $\boldsymbol{r}(\ell)$ is a translation vector of the primitive lattice. By diagonalizing the dynamical matrix, we can obtain the squared harmonic phonon frequencies and the polarization vector as

$$\omega_{\boldsymbol{q}j}^2 = (e_{\boldsymbol{q}j}^*)^{\mathrm{T}} D(\boldsymbol{q}) e_{\boldsymbol{q}j}, \tag{7.4}$$

where the index j labels the phonon modes for each crystal momentum vector $\boldsymbol{q}$ and $e_{\boldsymbol{q}j}$ is the polarization vector of the phonon mode $\boldsymbol{q}j$. Since the harmonic IFCs are independent with temperatures, there is no the intrinsic temperature dependence of phonon frequencies and polarization vectors $\{\omega_{\boldsymbol{q}j}, e_{\boldsymbol{q}j}\}$ in the harmonic approximation.

In order to derive the SCP equation, the many-body Green's function theory is addressed. The one-phonon imaginary-time Green's function is expressed as

$$\begin{aligned} G_{\boldsymbol{q}j,\boldsymbol{q}j'}(\tau) &= \left\langle T_\tau A_{\boldsymbol{q}j}(\tau) A_{\boldsymbol{q}j'}^\dagger(0) \right\rangle_H \\ &= Z^{-1} \mathrm{Tr}\left\{ e^{-\beta H} T_\tau [A_{\boldsymbol{q}j}(\tau) A_{\boldsymbol{q}j'}^\dagger(0)] \right\}, \end{aligned} \tag{7.5}$$

where T_τ represents the time-ordering operator, $A_{\boldsymbol{q}j}(\tau)$ is the displacement operator in the Heisenberg picture, $Z = \mathrm{Tr}e^{-\beta H}$ is for the partition function, and $\beta = \frac{1}{kT}$. $A_{\boldsymbol{q}j} = b_{\boldsymbol{q}j} +$

$b_{qj}^{\dagger}$ where $b_{qj} + b^{\dagger}$ and $b_{qj}^{\dagger}$ are the annihilation and creation operators of the phonon qj. It is clear to show that the Green's function satisfies

$$G_{qjj'}(\tau) = G_{qjj'}(\tau + \beta\hbar) \text{ for } -\beta\hbar < \tau < 0, \tag{7.6}$$

$$G_{qjj'}(\tau) = G_{qjj'}(\tau - \beta\hbar) \text{ for } 0 < \tau < \beta\hbar, \tag{7.7}$$

where we simply denote $G_{qj,qj'}$ as $G_{qjj'}$. Because of these properties, we can also show the following result for the Fourier transform of the Matsubara Green's function

$$G_{qjj'}(i\omega_m) = \int_0^{\beta\hbar} d\tau G_{qjj'}(\tau) e^{i\omega_m \tau}, \tag{7.8}$$

where $\omega_m = 2\pi m/\beta\hbar$ is the Matsubara frequency.

To get the Green's function for anharmonic systems, one needs to solve the Dyson equation. When one obtains $G_{qjj'}(i\omega_m)$ within some approximations, it is possible to obtain the retarded Green's function $G_{qjj'}(\omega)$ by analytic continuation to the real axis as $G_{qjj'}(\omega) = G_{qjj'}(i\omega_m \rightarrow \omega + i\varepsilon)$ with a positive infinitesimal ε. $G_{qjj'}$ has a pole at the energy corresponding to the renormalized frequency Ω_{qj}. In the harmonic approximation, the $G_{qjj'}$ is expressed as

$$G^0_{qjj'}(\omega) = -\frac{2\omega_{qj}}{\omega^2 - \omega_{qj}^2}\delta_{jj'}. \tag{7.9}$$

Hence, the free-phonon Green's function is diagonal in the phonon polarization index j and can be obtained from the harmonic phonon frequencies.

To estimate the phonon Green's function $G_{qjj'}(\omega)$, and thereby obtain the anharmonic frequency Ω_{qj}, we solve the Dyson equation

$$[G_q(\omega)]^{-1} = [G^0_q(\omega)]^{-1} - \Sigma_q(\omega). \tag{7.10}$$

The retarded Green's functions are denoted in the matrix form. And $\Sigma_q(\omega)$ represents for the phonon self-energy, estimated within a systematic diagrammatic approximation. Since $[G_q(\omega)]^{-1}$ becomes 0 at the frequencies of the renormalized phonons, finding the solution $\{\Omega_{qj}\}$ is equivalent to solving the following equation:

$$\det\left\{\left[G_q^0(\omega)\right]^{-1} - \Sigma_q(\omega)\right\} = 0. \tag{7.11}$$

By multiplying $\det(\Lambda_q^{\frac{1}{2}})$ from the left and right of above equation with the diagonal matrix $\Lambda_{qjj'} = 2\omega_{qj}\delta_{jj'}$, we obtain the SCP equation:

$$\det[\omega^2 - \mathbf{V}_q(\omega)] = 0, \tag{7.12}$$

$$V_{qjj'}(\omega) = \omega_{qj}^2\delta_{jj'} - (2\omega_{qj})^{\frac{1}{2}}(2\omega_{qj'})^{\frac{1}{2}}\Sigma_{qjj'}(\omega). \tag{7.13}$$

This equation needs to be solved self-consistently because the self-energy is a function of the solution ω.

To solve the SCP equation, we use a diagrammatic approximation to the phonon self-energy. Now considering the anharmonicity up to the fourth order, U_n is expressed in terms of the displacement operator A. This can be obtained by substituting for Eq. 7.2 as

$$u_\mu(\ell\kappa) = (NM_\kappa)^{-\frac{1}{2}}\sum_q\sqrt{\frac{\hbar}{2\omega_q}}A_q e_\mu(\kappa;q)e^{iq\cdot r(\ell)}, \tag{7.14}$$

where q labels the phonon modes, and N is the number of $\mathbf{q}$ points. Then U_n is obtained as

$$U_n = \frac{1}{n!}\left(\frac{\hbar}{2}\right)^{\frac{n}{2}}\sum_{\{q\}}\Delta(\mathbf{q}_1+\cdots+\mathbf{q}_n)\frac{\Phi(q_1;\ldots;q_n)}{\sqrt{\omega_{q_1}\ldots\omega_{q_n}}}\times A_{q_1}\cdots A_{q_n}. \tag{7.15}$$

The Δ functions is 1 when $\mathbf{q}$ is an integral multiple of the reciprocal vector $\mathbf{G}$ and 0 for others.

In solving the SCP equation, one consider only the 1st order contribution to the phonon self-energy due to the quartic term,

$$\Sigma_{\mathbf{q}jj'}^{(a)}(i\omega_m) = -\frac{q}{w}\sum_{q_q}\frac{\hbar\Phi(\mathbf{q}j;-\mathbf{q}j';q_1;-q_1)}{4\sqrt{\omega_{\mathbf{q}j}\omega_{\mathbf{q}j'}}\omega_{q-1}}\times[1+2n(\omega_1)], \tag{7.16}$$

where $n(\omega) = (e^{\beta\hbar\omega}-1)^{-1}$ is the Bose-Einstein distribution function. Since the iteration cycle of the self consistent equation continues to calculate until obtaining a

anharmonic frequency convergence, the SCP equation automatically includes an infinite class of anharmonic self energies that can be generated from the loop diagram. Without considering polarization mixing, the SCP equation is reduced to the diagonal form:

$$\Omega_q^2 = \omega_q^2 + 2\Omega_q I_q^{(a)}, \tag{7.17}$$

$$I_q^{(a)} = \frac{1}{2}\sum_{q_1}\frac{\hbar\Phi(q;-q;q_1;-q_1)}{4\Omega_q\Omega_{q_1}}[1+2n(\Omega_{q_1})] \tag{7.18}$$

7.3. Computational Details

7.3.1. DFT Calculations

Ab initio calculations based on density functional theory (DFT) were performed using the *Vienna ab initio simulation package* (VASP) [260, 193], which implements the projector augmented wave (PAW) [194] potentials. We employed the PBEsol exchange-correlation functional [332], which was reported to work exceedingly well for predicting the equilibrium volume and harmonic phonon frequency of $BaTiO_3$, $SrTiO_3$ and ScF_3 [333, 331]. To account for the strong electron correlation effects on the *f* shells of Eu atoms, we performed the DFT+U scheme [334] in Dudarev's approach [335] with an on-site Coulomb parameter U = 5.7 eV and Hund's exchange J_H = 1.0 eV, which has been checked out in the previous works [336, 337]. The cubic structure (space group Pm3̄m) of $EuTiO_3$ is stable at room temperature [322], which is considered in this work. The experimental lattice parameter of the cubic phase of $EuTiO_3$, 3.90 Å [324, 338, 339] was used to perform all the calculations. The magnetic ground state of cubic $EuTiO_3$ was considered as G-type anti-ferromagnetic to mimic the paramagnetic state of practical observation, and the results of ferromagnetic structure as references were considered in this work (as shown in Figure 7.1). For forces calculations, the self-consistent field loop was continued until the total electronic energy change between two steps became smaller than 10^{-8} eV under a cutoff energy of 600 eV.

7.3.2. Force Constants Calculation

To calculate the thermal conductivity, temperature-dependent phonon frequencies and various phonon properties, it is necessary to extract harmonic and anharmonic interatomic force constants (IFCs) from first-principles calculations. To this end, a

2×2×2 cubic supercell containing 40 atoms was constructed, which was also considered as the conventional cell for G-type antiferromagneitc structure. To extract second-order IFCs, we used frozen phonon method, namely, an atom in the supercell was displaced from its equilibrium position by 0.01 Åand the Hellmann-Feynman forces were calculated for the displaced configuration. From the data sets comprising the displacements and forces, we estimated the second-order terms by the least-squares fitting [340], as implemented in the ALAMODE [113] package. The anharmonic IFCs were calculated using the CSLD method [111]. To this end, we employed the following procedure: First, we performed *ab initio* molecular dynamics (AIMD) to generate physically relevant atomic configurations. The AIMD simulation was performed with $2 \times 2 \times 2$ Monkhorst-Pack k-grid and 4000 steps at 500 K with the time step 2 fs. Second, we uniformly sampled 110 snapshots from the AIMD trajectory. In each sampled snapshot, we further displaced all atoms by 0.1 Åin random directions to decrease cross-correlations between the sampled configurations. Third, we performed static DFT calculations for the 110 snapshots and calculated Hellmann-Feynman forces accurately. Finally, we estimated anharmonic IFCs by using the LASSO [101, 118]. The hyperparameter for the LASSO was selected from cross-validation scores [341]. From the gained harmonic, cubic, and quartic IFCs, the SCP calculations are performed to obtain the anharmonic frequencies.

7.3.3. Phonon Calculations

The lattice thermal conductivity κ_L is estimated by the Boltzmann transport equation (BTE) within the relaxation-time approximation (RTA). A 20×20×20 **q** mesh was used to obtain the converged κ_L, as implemented in the ALAMODE code [113]. Unlike the conventional BTE approach (HP+BTE), we solved the BTE on the top of SCP. That is, after the SCP iteration converges, the resulting renormalized harmonic force constants were used to evaluate the phonon spectra, whereas the phonon self-energy was obtained by considering the three-phonon processes with the anharmonic IFCs as an input, resulting in the phonon lifetime. This is the so-called SCP+BTE method, more detailed computational procedures are described in Ref. [118].

7.4. Experimental Details

7.4.1. Sample Synthesis and Preparation

The polycrystalline $EuTiO_3$ was synthesized via a modified Pechini method. Eu_2O_3 (Alfa Aesar, 99.9 %), titanium(IV) bis (ammonium lactato) dihydroxide solution (Sigma-

Aldrich, 50 wt. % in H_2O), citric acid (Sigma-Aldrich, 99 %), and ethylene glycol (Sigma-Aldrich, $\geq$ 99 %) were chose as raw materials. First, a stoichiometric amount of Eu_2O_3 (0.01 mol) and citric acid were weighted separately and placed into a round-bottom flask. Then 200 ml of demineralized water was added into the flask. Afterwards, the flask containing the mixture was heated up to 373 K in an oil bath under vigorous magnetic stirring. When the solution was completely transparent, the flask was transferred to a room temperature environment without vigorous stirring. Subsequently, the stoichiometric ratio of titanium (IV) bis (ammonium lactato) dihydroxide solution and ethylene glycol were added into the flask. The flask was then placed in an oil bath at 338 K with vigorously stirring for another 2 hours. Finally, the transparent solution was transferred to a Pyrex crystallizing dish and heated at 473 K for 12 h followed by calcination at 753 K for 6 h in a muffle furnace, leaving a white powdery residue as oxide precursors for further preparation. To obtain the polycrystalline $EuTiO_3$ powders, the white precursors were annealed at 1273 K for 12 h under a reducing atmosphere (5 vol.% H_2 in Ar) in a tube furnace with a flow rate of 100 ml/min. The obtained black powder materials were densified to bulk samples by cold isostatic pressing at 205 MPa pressure following by conventional sintering at 1673 K with a forming gas flow for the thermal conductivity measurement and characterization afterwards.

7.4.2. Sample Characterization

Powder X-ray diffraction (XRD) pattern of the obtained $EuTiO_3$ compound was obtained using a Rigaku Smartlab X-ray diffractometer using Cu-Ka$_{1,2}$ radiation. The morphology of the sintered $EuTiO_3$ was characterized by scanning electron microscopy (SEM, Zeiss Merlin) The thermal conductivity κ was calculated by the formula $\kappa = \lambda d C_p$, where λ is the thermal diffusivity, d is the density of samples and C_p is the specific heat. Experimental densities (d) of the bulk sample was determined by the Archimedes method. The λ was measured by a laser flash analyzer (LFA 457, Netzsch) under a forming gas atmosphere (5 vol% H_2 in Ar) in the temperature range of 300 K to 1173 K. C_p was measured by a high-temperature differential scanning calorimeter (DSC404, Netzsch).

Table 7.1.: Current experimental lattice parameters of $EuTiO_3$ comparing with literature.

Compound	Space group	Lattice constant (Å)	Method
$EuTiO_3$	$Pm\bar{3}m$	3.90	EXP
	$Pm\bar{3}m$	3.94	DFT[337]
	$Pm\bar{3}m$	3.90	EXP[324, 339]

7.5. Results and Discussion

7.5.1. Crystal Structure and Microstructure

Figure 7.2 shows the collected PXRD data of synthesized $EuTiO_3$ compound. The crystal symmetry of the synthesized $EuTiO_3$ was found to be cubic perovskite structure with space group $Pm\bar{3}m$. All reflections shown in Figure 7.2 can be indexed into corresponding Miller indices (hkl) of $EuTiO_3$. The profile fitting of the patterns revealed the cell parameters of $EuTiO_3$ is 3.90 Å, as listed in the Table 7.1. The result is agreed well with previous experimental and theoretical results.
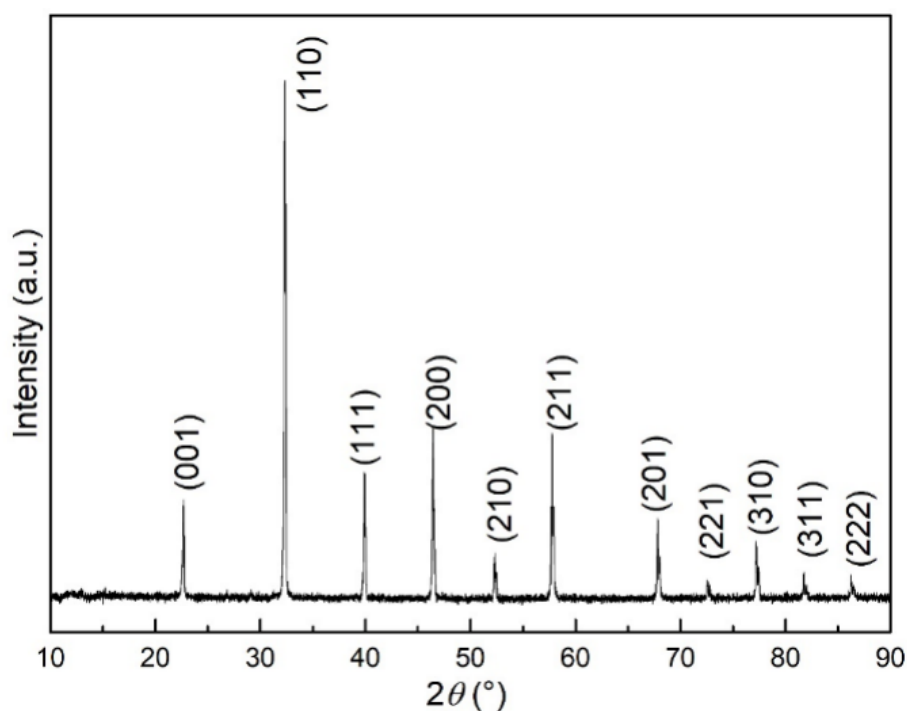
Figure 7.2.: Powder X-ray diffraction (PXRD) pattern of the synthesized $EuTiO_3$ with the corresponding *hkl* indexes.

Figure 7.3 (a and b) are SEM micrographs illustrating the grain size and microstructure of the sintered bulk $EuTiO_3$. The grains were connected well under the given sintering condition, and the relative density of the sintered $EuTiO_3$ is around 90 %. The SEM images also show clear porous in the sintered bulk sample and the sizes of the porous are in the range of 200 nm – 10 μm. Such multi-scale porous structure can scatter phonons with different wavelengths.
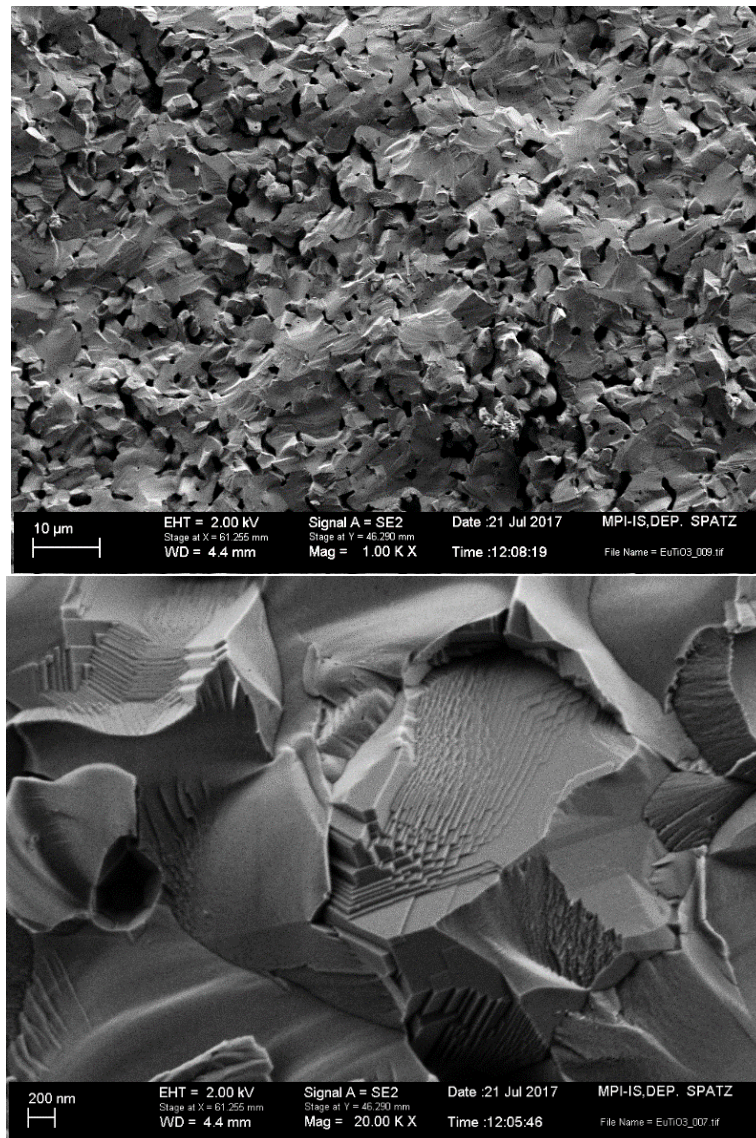
Figure 7.3.: SEM micrographs of the sintered $EuTiO_3$ bulk sample.

7.5.2. Phonon Dispersion and Density of States

The calculated phonon dispersion curves of G-type cubic $EuTiO_3$ within the harmonic approximation (dotted lines) and SCP theory (solid lines) are shown in Figure 7.4. For the harmonic approximation, it indeed reveals strong structural instabilities, which is the same as the results of $EuTiO_3$ within the ferromagnetic state in Ref. [337, 342]. Evidently, the low-lying modes around the Γ (0,0,0) and M (0.5,0.5,0) points in G-type

EuTiO$_3$ are unstable ($\omega^2 < 0$), *e.g.*, with the respective imaginary frequencies of 123.6i cm^{-1} and 73.7i cm^{-1} for the softest mode at Γ and M in which only oxygen atoms vibrate (Γ_{5-} and M_{5-}). In addition, the calculated harmonic phonon density of states (HPDOS) reveals that the imaginary phonons in G-type EuTiO$_3$ are contributed dominantly by the collective motions of the oxygen atoms, which indicates that these instabilities are nonpolar and arise from the displacements of oxygen atoms.
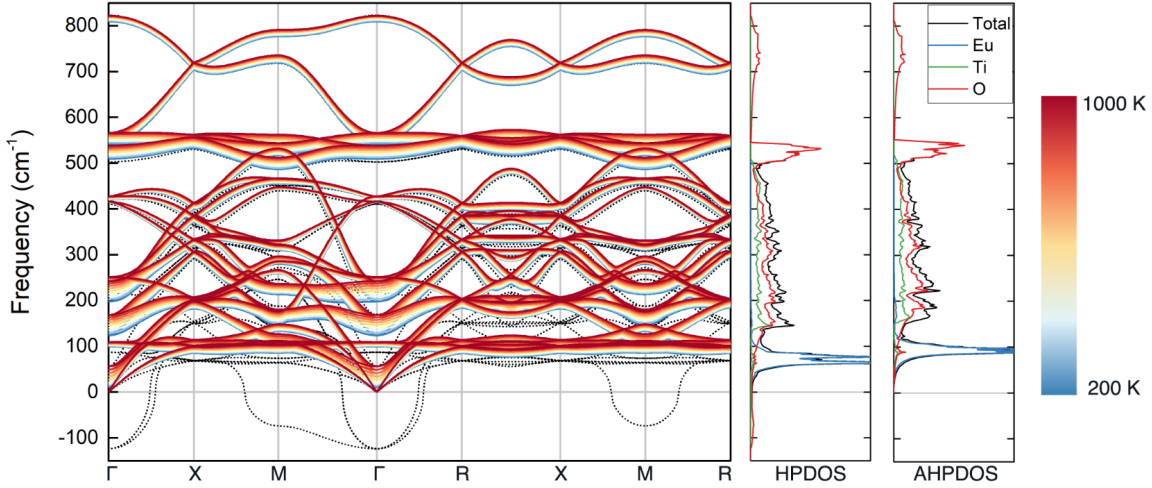
Figure 7.4.: Harmonic and anharmonic phonon dispersions, harmonic phonon density of states (HPDOS), and anharmonic phonon density of states (AHPDOS) (unit: states/cm^{-1}). Temperature-dependent phonon dispersion of cubic EuTiO$_3$ calculated with the PBEsol exchange-correlation functional. The colorful lines represent the SCP solutions at different temperatures ranging from 200 to 1000 K. The grey dotted lines are harmonic lattice dynamics results. In both HPDOS and AHPDOS, the blue, green, and red lines represent the partial phonon density of states of the Eu atoms, Ti atoms, and oxygen atoms, respectively. For the AHPDOS, only the result at 300 K is displayed.

The anharmonic phonon dispersion with temperature dependency is shown in Figure 7.4 from 200 to 1000 K in steps of 100 K. To investigate the convergence of the anharmonic phonon frequency Ω_q concerning the number of $\mathbf{q}_1$ points, the results for the lowest energy soft modes at Γ and M points are summarized in Table 7.2. Our results indicate that at least 4×4×4 $\mathbf{q}_1$ points are needed to obtain convergence and a less dense 2×2×2 $\mathbf{q}_1$-point grid significantly overestimates the Ω_q values. Therefore, the anharmonic phonon dispersion calculated within the 4×4×4 in Figure 7.4 is well convergent. Obviously, the quartic anharmonicity shift of the softest modes in EuTiO$_3$ is particularly

predominant in low-energy optical modes at Γ (0,0,0), and M (0.5,0.5,0) points, and no imaginary frequency appear anymore.

In the present SCP theory, only quartic phonon interactions are considered, which causes frequency shifts, while cubic and other terms that causes phonon lifetime broadening and frequency shift as well as lattice thermal expansion are neglected. Quartic anharmonicity generally boost the frequencies of low-lying modes due to the positive and dominant contribution from the diagonal terms of the force constants [101, 330, 118]. In Figure 7.4, compared with HPDOS in which softest phonon modes arise completely from oxygen atoms, there are no soft modes in the calculated anharmonic phonon density of states (AHPDOS) at 300K. It reveals that the oxygen atoms in the $EuTiO_3$ have significantly strong quartic anharmonicity, which plays an important role in the structural stability of $EuTiO_3$. In addition, the collective motions of europium atoms dominate the acoustic modes and low-frequency optical modes. The high-frequency phonon branches are governed primarily by the motions of oxygen atoms. Furthermore, the low-frequency anharmonic modes harden with the temperature increase, while the high-frequency modes have relatively small anharmonic renormalization. These results indicate that anharmonicity is very significant for phonon frequency and also influence the thermal conductivity consequently.

Table 7.2.: Anharmonic phonon frequency (cm^{-1}) of the soft modes at 300 K calculated using the SCPH equation with various $\mathbf{q}_1$ grid densities. The harmonic phonon frequency is also shown for comparison.

$\mathbf{q}_1$ points	Γ_{5-}	M_{5-}
2×2×2	26.1	35.1
3×3×3	19.3	20.2
4×4×4	14.5	14.6
5×5×5	14.3	14.4
6×6×6	14.3	14.4
Frozen phonon	123.6i	73.7i

7.5.3. Lattice Thermal Conductivity

After obtaining the hardened low-lying modes, the accurate thermal transport properties of the $EuTiO_3$ can be evaluated. As one known, the lattice thermal conductivity is a crucial quantity for optimizing the thermoelectric figure-of-merit ZT. Therefore, we carried out experimental measurements and theoretical calculations to evaluate the lattice thermal conductivity of cubic $EuTiO_3$. In the theoretical work, the lattice

thermal conductivity κ_L is estimated by the BTE within RTA through the following equation:

$$\kappa_L^{\alpha\beta}(T) = \frac{1}{NV} \sum_q C_q(T) v_q^\alpha(T) v_q^\beta(T) \tau_q(T), \tag{7.19}$$

where V, $C_q(T)$, $v_q(T)$, and $\tau_q(T)$ are the unit cell volume, mode specific heat, phonon group velocity, and phonon lifetime, respectively.
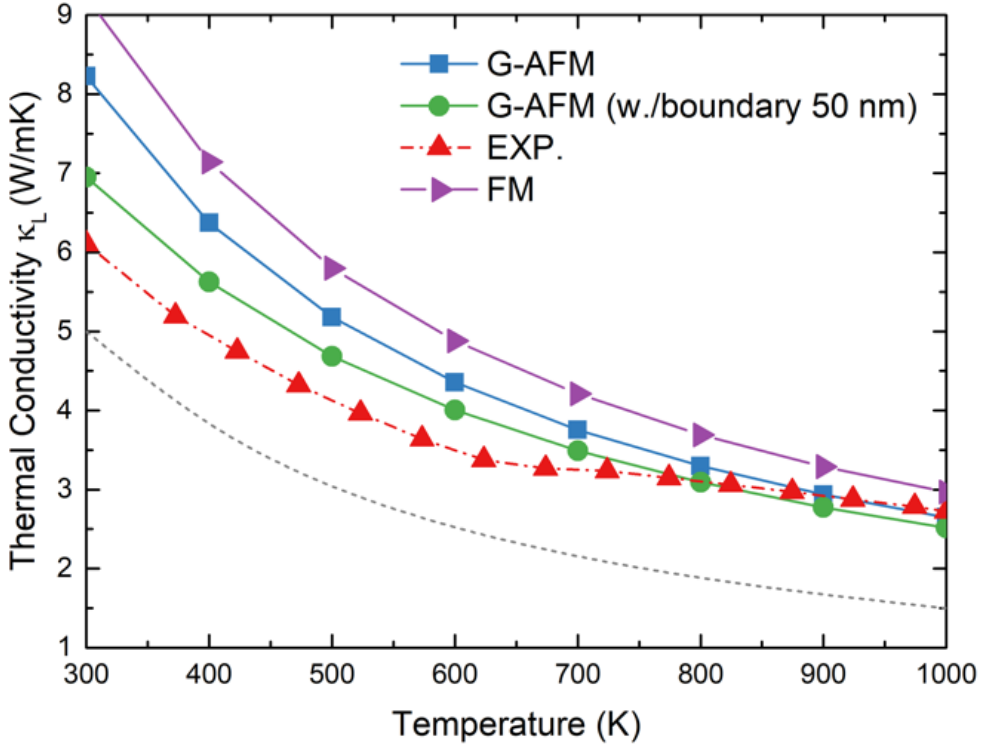
Figure 7.5.: Temperature dependence of lattice thermal conductivities of EuTiO$_3$ from experimental measurements and theoretical calculations are presented. The phonon-boundary scattering result is also shown for comparison.

Due to the sizeable imaginary mode in the harmonic phonon dispersion, we performed SCP+BTE methods to obtain the lattice thermal conductivity. This SCP+BTE method is different from the conventional harmonic phonon-based BTE method (HP+BTE), where the phonon group velocity and lifetime are estimated using harmonic frequencies and eigenvectors as the ground state. Namely, the SCP frequencies and eigenvectors are employed as inputs for the BTE, leading to $v_q(T) = \partial\Omega_q(T)/\partial\mathbf{q}$. Therefore, the group velocity also shows an intrinsic T dependence. The phonon lifetime $\tau_q(T)$ is estimated using Matthiessen's rule $1/\tau_q = 1/\tau_q^{anh} + 1/\tau_q^{iso} + 1/\tau_q^{bun}$. The anharmonic scattering rate $1/\tau_q^{anh}$ is calculated from the imaginary part of the bubble self-energy from the

cubic IFCs (see Eq. (2) in Ref. [118]), and the phonon-isotope scattering rate $1/\tau_q^{iso}$ is evaluated in a manner of perturbation [343]. For the phonon-boundary scattering rate $1/\tau_q^{bun} = 2|v_q|/L$, where L is the grain size.

The calculated lattice thermal conductivity κ_L of G-type cubic EuTiO$_3$ comparing experimentally measured values are shown in Figure 7.5. As can be seen in the Figure 7.5, the G-AFM results are overall good agreement with experimental values. The experimental thermal conductivity value was calculated by using the measured λ, d, and C_p. Obviously, the LTC values calculated by the SCP+BTE method are generally higher than those obtained by the experimental method, which is due to the reason of the pore and boundary scatterings in the practical sample. The calculated κ_L value of G-type AFM EuTiO$_3$ by the SCP+BTE method is 8.2 Wm^{-1}K^{-1}, which matches well with the experimental value 6.1 Wm^{-1}K^{-1}. In Figure 7.5, we also show a theoretical result of EuTiO$_3$ (green cycle) with the effect of phonon-boundary scattering considered by using Matthiessen's rule. The result agrees better with the experimental values in a wide temperature range. Note that κ_L values of EuTiO$_3$ with magnetism in the ferromagnetic state (shown in Figure 7.1) are also plotted in Figure 7.5, which is far from experimental results. Hence, the G-type AFM chosen in this work is more reasonable. These results above clearly reveal that the frequency renormalization plays an essential role in the thermal transport properties of EuTiO$_3$, and the SCP+BTE method works very well for the system with a strong quartic anharmonic effect. Another critical point is that the κ_L exhibits a temperature dependence in EuTiO$_3$. The κ_L decreases with the increase of temperature in both theoretical and experimental results, and at high temperature (e.g., T > 600 K), the κ_L follows the trend of T^{-1}, indicating the phonon-phonon scattering is the dominated phonon scattering processes. We can approximately describe the temperature dependence by a power law $\kappa_L \propto T^{-1}$. When the temperature approaches room temperature, the κ_L deviates from the trend of $\kappa_L \propto T^{-1}$. It can be attributed to boundary phonon scattering and/or defect phonon scattering. Such temperature dependence is known as a common behavior of crystals in the high-temperature regime (in which phonon-phonon scattering is dominant) [344, 345]. Obliviously, a platform exists above 700 K in the experimental measurement. We do not fully understand why a plateau shows around 700 K. The DSC curve and heat capacity are pretty smooth and do not show any visible transition. The known phase transitions are below 300 K. But the thermal diffusivity of EuTiO$_3$ is repeatable, and the plateau always shows around 700 K. Another interesting aspect that needs to be mentioned is the thermal conductivity of EuTiO$_3$ prepared by solid-state reaction does not have a plateau of around 700 K. We guess the plateau might be related to the microstructure (nanodomain structure), which will be studied in further work.

To understand the underlying mechanism responsible for the presence of strong quartic anharmonic renormalization of the soft modes through the SCP+BTE method, thermal conductivity spectra ($\kappa_L(\omega)$) and corresponding cumulative values calculated by the

SCP+BTE method for EuTiO$_3$ at 300 K, 600 K, and 900 K are shown in Figure 7.6. As one can see, the dispersive phonon modes at the low/medium frequency range contribute more than 90% to the total thermal conductivity at three temperatures. Furthermore, below < 100 cm^{-1} the hardened soft modes enhanced the thermal conductivity obviously. Meanwhile, the temperature dependence of thermal conductivity is also shown in character in the figure. Consequently the difference between the κ_L values at the three considered temperatures results primarily from the temperature-induced changes in the $\kappa_L(\omega)$ for the modes with frequencies below 500 cm^{-1}. In principle, in the conventional method (HP+BTE), the increase of temperature leads to the uniform enlargement of the three phonon scattering phase space with the Bose distribution function, and thus the enhanced three-phonon scattering and reduced phonon lifetime of all phonon modes [346]. However, in the current SCP+BTE methods, due to the presence of strong quartic anharmonic renormalization of the soft modes, the effect of the changes in the Bose distribution function is offset by the frequency enhancement.
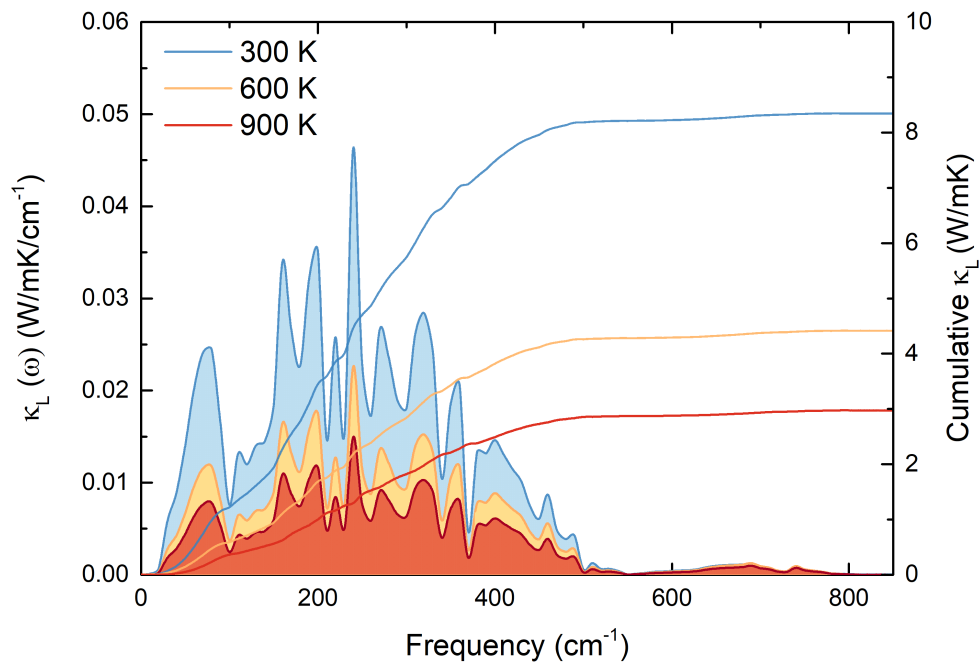
Figure 7.6.: Thermal conductivity spectra $\kappa_L(\omega)$ (the curves below which the areas are filled) and corresponding cumulative values (the bare curves). The SCP+BTE results for EuTiO$_3$ at 300 K, 600 K, 900 K.

As shown in Figure 7.7, the phonon lifetime of the soft modes (below 100 cm^{-1}) are less sensitive to the increase of temperatures. In addition, the phonon lifetime shows a characteristic feature in the low-frequency region (< 100 cm^{-1}). When the phonon lifetimes are above 3 ps, the phonon mode corresponds to the acoustic modes exhibiting ω^2 dependence, which is in good agreement with Klemens' formula and other calculations [347, 348, 349, 113]. As the phonon lifetime is around 0.5 ps, the phonon modes correspond to the phonon modes around the M point, which indicates the severe anharmonicity induced by the Oxygen atoms, which is the same as SrTiO$_3$ in Ref. [101]. Therefore, considering the anharmonicity of the soft modes in the current calculations plays a significant role in the final thermal conductivity. Moreover, it is worth noting that other factors also play crucial roles in determining the temperature dependence of the κ_L, for instance, thermal expansion and additional four-phonon scattering induced by the quartic anharmonicity [350].
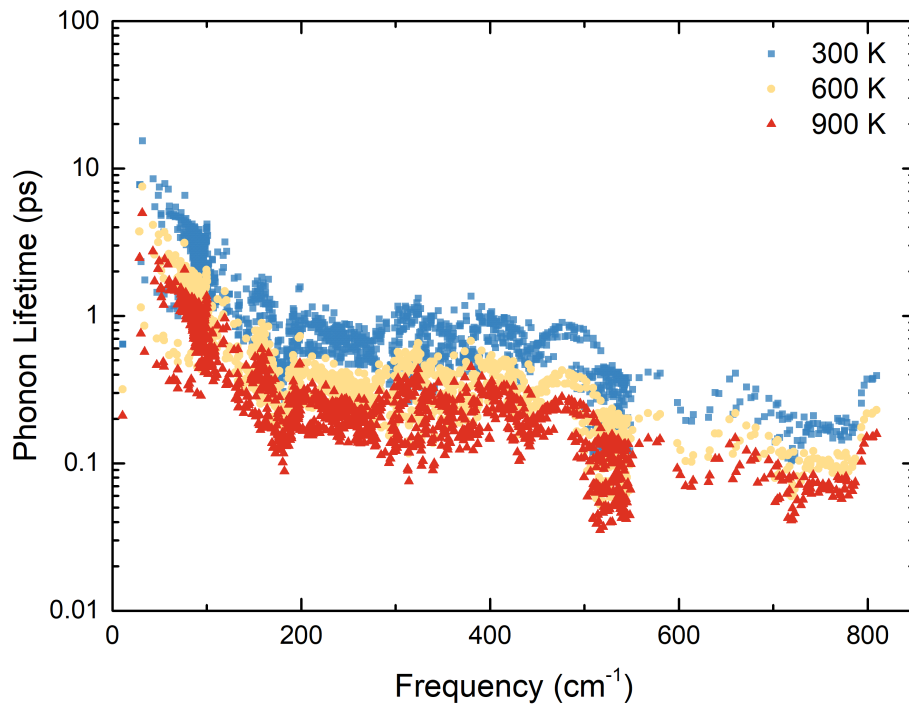
Figure 7.7.: Phonon lifetimes with respect to frequency in EuTiO$_3$ at 300 K, 600 K, 900 K.

7.6. Conclusions

In this work, it is the first time to calculate the thermal conductivity of pristine $EuTiO_3$. And the role of the quartic anharmonicity in the lattice dynamics and thermal transport of the cubic $EuTiO_3$ was studied by combining ab initio self-consistent phonon theory with compressive sensing techniques and experimental thermal conductivity determination measurement. The anti-ferromagnetic G-type magnetic structure is used to mimic the para-magnetic $EuTiO_3$. We find that the strong quartic anharmonicity of oxygen atoms plays an important role in the phonon quasiparticles free from imaginary frequencies in $EuTiO_3$ and causes the hardening of vibrational frequencies of soft modes. Based on these results, the lattice thermal transport properties are predicted through the Boltzmann transport equation within the relaxation time approximation. The hardened modes thereby affect calculated lattice thermal conductivity significantly, resulting in an improved agreement with experimental results, including the deviation from $\kappa_L \propto T^{-1}$ at high temperature. The calculated thermal conductivity of 8.2 $Wm^{-1}K^{-1}$ at 300 K matched the experimental value of 6.1 $Wm^{-1}K^{-1}$. When considering the boundary scattering, the calculated thermal conductivity is reduced to 6.9 $Wm^{-1}K^{-1}$ at 300 K, which agrees better with the experiment.

8. Electron-phonon driven Superconductivity

Antiperovskites are one of the well known and most commonly explored families of ternary compounds. In contrast to ternary oxides, the number of known ternary nitrides is an order of magnitude lower, partially due to their higher free energy of formation and lower thermodynamic stability. This challenges experimentalists to continuously explore the synthetic parameter space and push toward research on new nitride phases. Recently, we demonstrated synthesizing a hitherto unknown orthorhombic structure (space group *Cmcm*) of GeNCr$_3$, which typically crystallizes in a tetragonal (space group *P*$\bar{4}$2$_1$*m*) structure. In this work, we derived from DFT calculations that the formation energies of both phases are similar. The orthorhombic GeNCr$_3$ is a metastable phase, which can be stabilized by choosing lower reaction temperatures. According to detailed thermodynamic analysis, the new compound is stable up to 500 °C and exhibits the same phase transitions as the tetragonal phase at higher temperatures. Moreover, motivated by the occurrence of superconductivity in MgCNi$_3$ [351], antiperovskites are recognized as possible candidates of superconductors. As a matter of fact, many carbide, boride, nitride, and oxide antiperovskites were proved experimentally to be superconductors, and a few others were predicted by theory [46]. Hence, we performed calculations on the electron-phonon interaction for the new orthorhombic compound and found that it is a superconductor with a T_c of 8.2 K.

8.1. Introduction

Perovskites are a well-known and extensively studied family of ternary compounds. Due to the simple cubic *ABO*$_3$ lattice, the tunability of their physical properties can be easily achieved by incorporating intercalations, dopants, and defects [352]. Hence, a multitude of remarkable applications of perovskites have been explored in recent years, such as advanced magnets [353], thermoelectrics [354], lasing [355], ferroelectrics [356], and photovoltaics [357], *etc.* Analogous to perovskites, the antiperovskites (APVs) also attract intensive attention in the last two decades. The essential difference between

perovskites and antiperovskites is that the positions of the cation and anion constituents are reversed in the unit cell structure. APVs also exhibit a lot of exciting physical properties, such as negative thermal expansion, high ionic conductivity, superconductivity, and gaint barocaloric effect [358, 359].
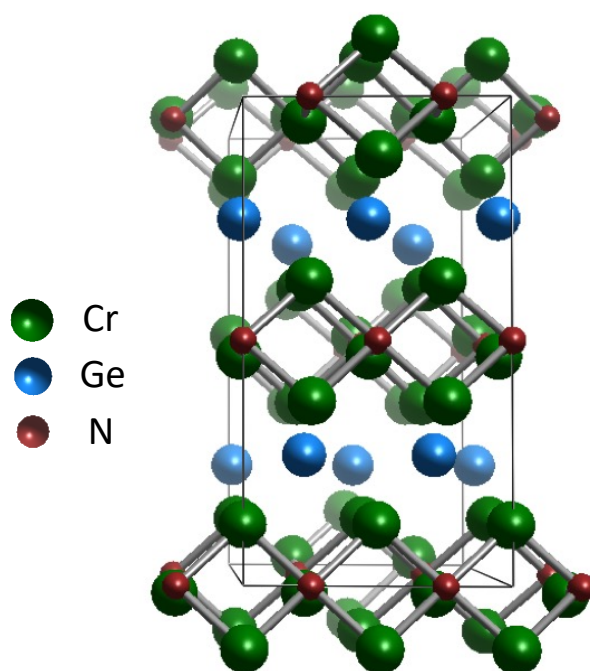
Figure 8.1.: The crystal structures of orthorhombic $GeNCr_3$.

In 2001, He et al. eported $MgCNi_3$ as a superconductor, which crystallizes in the cubic antiperovskite structure [351], which is considered as an *s*-wave superconductor with a paring mechanism mediated by the electron-phonon interaction [360]. This surprising discovery sparked the interest of researchers, and more and more people turned their attention to the antiperovskites superconductors in the following years. Several other carbon-, boron-, nitrogen- and oxygen-based antiperovskites were experimentally found to be superconductors, for example, transition temperature of $CdCNi_3$ is 3.2 K [361]. In addition, based on first-principles calculations and machine learning methods, people predicted more antiperovskites superconductors [46]. Recently, we reported a synthesis strategy to stabilize a hitherto unknown $GeNCr_3$ in the orthorhombic antiperovskite structure with a space group *Cmcm* (as shown in Figure 8.1). Together with our experimental collaborators, we also showed the metastability of the *Cmcm*-$GeNCr_3$ phase, including all expected phase transitions, through detailed thermal analyses coupled with subsequent X-ray powder diffraction data. Further, magnetometry data and electron transport measurements indicated this new structure of a nitride antiperovskite having

the potential as a new superconductor with a remarkably high critical temperature T_c = 7.2 K.

Therefore, we theoretically investigated the thermodynamical stability of *Cmcm*-GeNCr$_3$. Moreover, based on density-functional perturbation theory calculations and Wannier interpolation methods, we estimated the superconducting transition temperature using the commonly used Allen-Dynes formula and further solved the Eliashberg equations using the isotropic average of the Eliashberg function. We predicted *Cmcm*-GeNCr$_3$ having superconducting behavior with a T_c of 8.2 K due to electron-phonon coupling.

8.2. Computational Details

For formation energies, DFT calculations were performed using the Vienna *Ab-Initio* Simulation Package (VASP) code [332]. The exchange correlation interactions and the ion–electron interactions were solved by the Perdew–Burke–Ernzerhof functionals [59] and the projected-augmented wave method [362], respectively. A plane-wave kinetic-energy cutoff value of 520 eV was taken to guarantee good convergence The electron phonon interaction calculations were performed using the QUANTUM ESPRESSO [363] package. We adopted relativistic norm-conserving pseudopotentials [364] with the Perdew-Burke-Ernzerhof [59] exchange-correlation functional in the generalized gradient approximation (GGA). A plane-wave kinetic-energy cutoff value of 90 Ry was taken to guarantee good convergence, where a gamma centered $10 \times 10 \times 10$ Monkhorst-Pack k-mesh [261] and a Methfessel and Paxton smearing [365] of 0.02 Ry were used for the Brillouin-zone (BZ) integration. The atomic positions and lattice parameters were optimized until the total energies converged within 10^{-6} eV, and the maximum Hellmann-Feynman force less than 10^{-6} eV/Å. The dynamical matrices for phonons and electron-phonon coupling (EPC) potential were calculated within the framework of density-functional perturbation theory [123] on the irreducible set of a regular $3 \times 3 \times 3$ q-mesh. The isotropic Migdal-Eliashberg (ME) equation [24, 366] was solved to evaluate the superconducting properties using the EPW code [142]. To obtain the electron-phonon matrix elements on dense grids and hence the accurate superconducting properties, we performed Wannier interpolation [144, 145] on a $30 \times 30 \times 30$ k-mesh and $15 \times 15 \times 15$ q-mesh with 68 maximally localized Wannier functions constructed on a uniform gamma-centered $6 \times 6 \times 6$ k-mesh. An effective Coulomb potential $\mu_c^* = 0.16$ was used for solving the isotropic ME equations. The Matsubara frequency cutoff was chosen to be 0.2 eV and the Dirac deltas were replaced by Lorentzians of width 50 meV (for electrons) and 0.1 meV (for phonons). And vibrational free energies for $P\bar{4}2_1m$ and *Cmcm* phases are calculated by using the quasi-harmonic approximation (QHA) method as implemented in the software Phonopy [367].

8.3. Results and Discussion

8.3.1. Structure Stability

In the previous experimental synthesis process [368], the polycrystalline GeNCr$_3$ (synthesized at a temperature around 1,000 °C) crystallizes in space group $P\bar{4}2_1m$-GeNCr$_3$ and shows subsequent structural transition to $I4/mcm$, $P4/mbm$ and ultimately cubic $Pm\bar{3}m$. Beyond this, our recent work presented a synthesis strategy to stabilize the pure nitride GeNCr$_3$ in the orthorhombic antiperovskite structure (typically only found for the respective carbide or carbon-rich carbonitride). The orthorhombic GeNCr$_3$ phase exhibits a crystal structure with space group $Cmcm$ (No. 63), as shown in Figure 8.1. The structure can be derived from the cubic antiperovskite structure ($Pm\bar{3}m$) by tilting of the Cr$_6$N octahedra. To evaluate the thermodynamic stability of $Cmcm$-GeNCr$_3$, we performed DFT calculations to obtain the formation energies for all five allotropes of GeNCr$_3$, with the resulting optimized lattice parameters consistent with the experimental values (cf. Table 8.1) [368, 369]. It is noted that magnetism is not considered in our current calculations. As listed in Table 8.1, GeNCr$_3$ in the $P\bar{4}2_1m$ structure has the lowest formation energy, indicating that it is the most stable phase. This confirms in our recent submitted paper. Furthermore, the energy difference between $P\bar{4}2_1m$-GeNCr$_3$ and Cmcm-GeNCr$_3$ is only about 0.013 eV/atom, which is comparable with the energy fluctuation at room temperature (about 26 meV).

Table 8.1.: Calculated formation energies (E$_f$, eV/atom) and lattice constants (Å) of three allotropes of GeNCr$_3$.

Space group	E$_f$	DFT			EXP.		
		a	b	c	a	b	c
$P\bar{4}2_1m$	-0.347	5.289	5.289	3.996	5.373	5.373	4.015 [368]
$Cmcm$	-0.334	2.850	10.397	7.544	2.892	10.400	7.670
$Pm\bar{3}m$	-0.309	3.822	3.822	3.822	3.876	3.876	3.876 [368]
$I4/mcm$	-0.312	5.336	5.336	7.824	5.393	5.393	8.017 [368]
$P4/mbm$	-0.293	5.367	5.367	3.869	5.497	5.497	3.948 [368]

In addition, we performed quasi-harmonic approximation (QHA) to calculate the vibrational free energy for the $P\bar{4}2_1m$ and $Cmcm$-GeNCr$_3$ phases. As one can see, from Figure 8.2, the Gibbs free energy difference between these two phases is 11 meV/atom, which has the same magnitude of formation energy difference at 0 K. Therefore, $Cmcm$-GeNCr$_3$ is a metastable phase which is accessible by controlled experimental synthesis, as accomplished in this work.
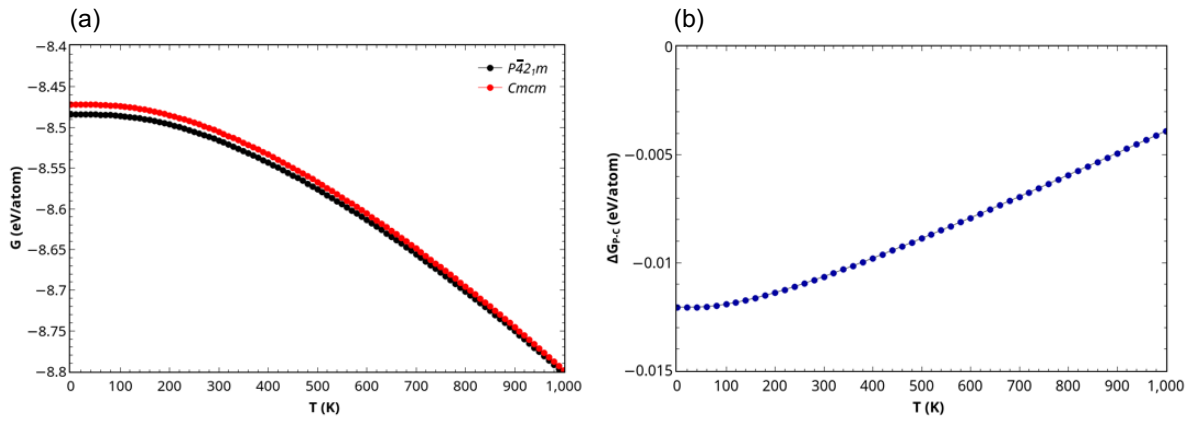
Figure 8.2.: (a) The Gibbs free energies for the $P\bar{4}2_1m$- and $Cmcm$-GeNCr$_3$ phases. (b) The Gibbs free energy difference between these two phases.

8.3.2. Superconducting Behavior
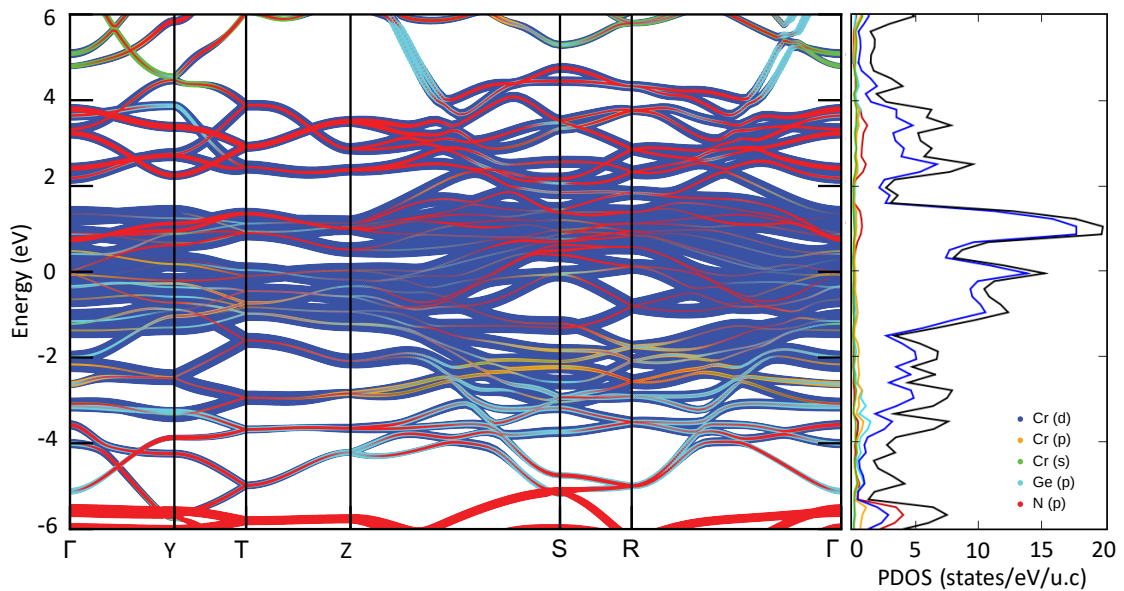
Figure 8.3.: The electronic structure and partial density of states (PDOS) of Cmcm-GeNCr$_3$ phases.

To confirm whether *Cmcm*-GeNCr$_3$ is a superconductor, we performed first-principles calculations to evaluate the electron-phonon interaction and to solve the isotropic Migdal-Eliashberg equation to evaluate the superconducting transition temperature explicitly. Figure 8.3 shows the band structure of *Cmcm*-GeNCr$_3$, displaying hole and electron bands crossing the Fermi level in the whole Brillouin zone. Such electronic states around the Fermi level are dominated by the bands originating from the Cr-*3d* orbitals, with marginal contributions from the *p* orbitals of Ge and N atoms.
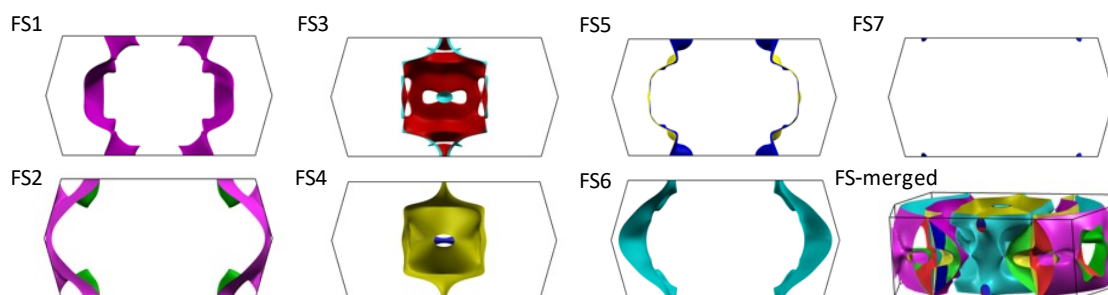
Figure 8.4.: The Fermi surface of *Cmcm*-GeNCr$_3$ phases.
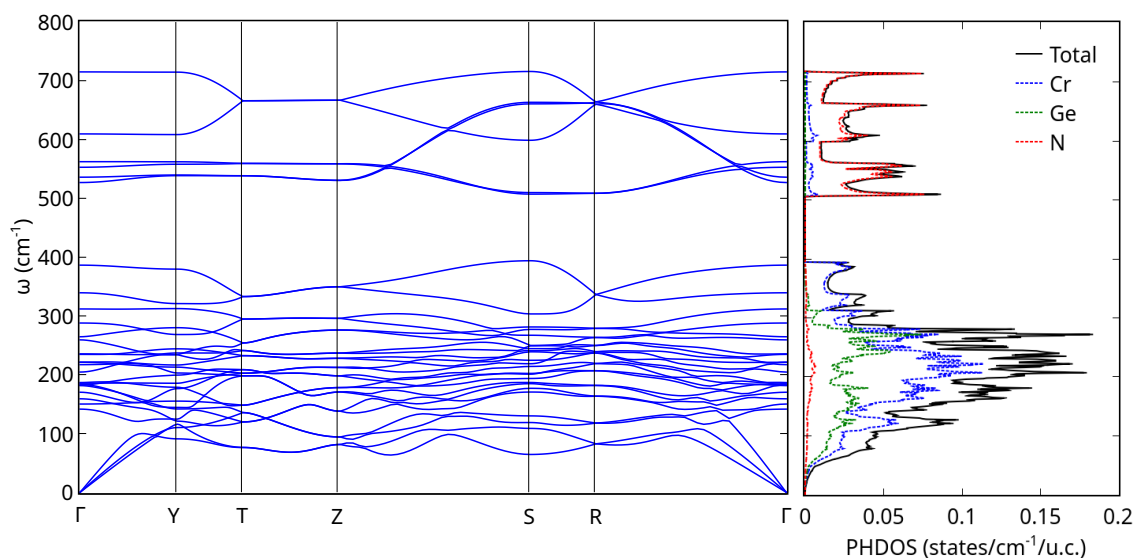
Figure 8.5.: Phonon dispersion and phonon density of states (PHDOS) for *Cmcm*-GeNCr$_3$.

Correspondingly, as shown in Figure 8.4, the Fermi surfaces comprise seven sheets with two butterfly-like (FS3, FS4), four two-dimensional cylinder-like (FS1, FS2, FS5, FS6),

and one small electron pocket (FS7) geometries. The two-dimensional cylinder-like Fermi surface sheets reflect the underlying nano-laminated crystal structure (Figure 8.1), which are similar to those of MgB_2 [24], where the strong EPC in two-dimensional Fermi surface sheets give rise to the two-gap superconductivity [24]. The phonon spectra and density of states (PHDOS) for *Cmcm*-GeNCr$_3$ are shown in Figure 8.5. Obviously, no imaginary mode exists in the phonon spectra, indicating *Cmcm*-GeNCr$_3$ is dynamically stable.
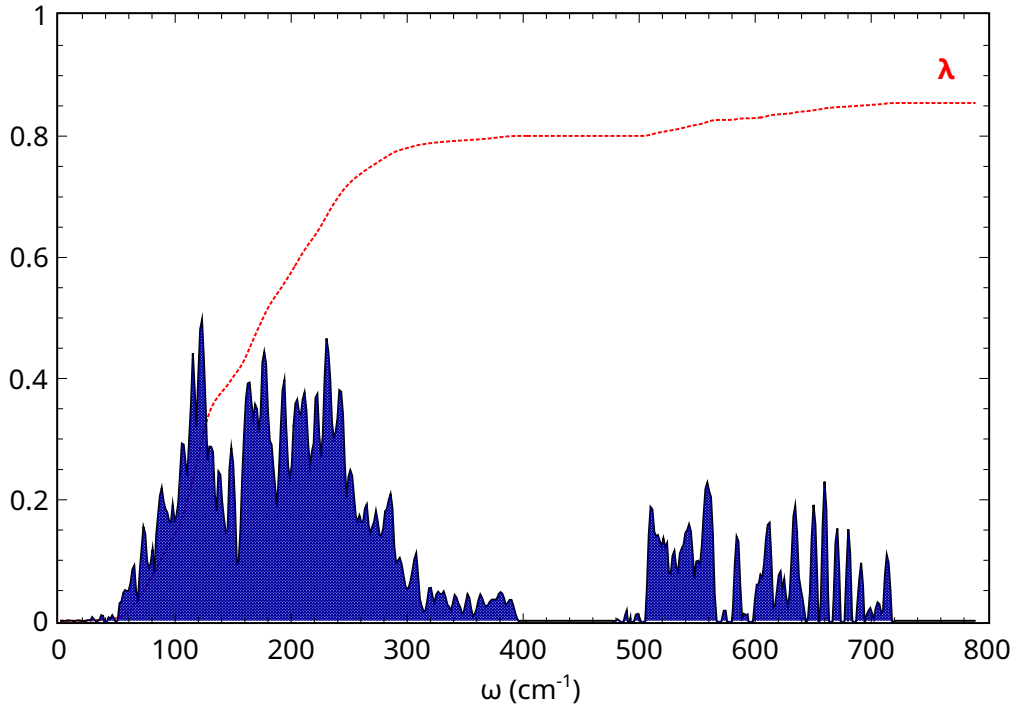
Figure 8.6.: The isotropic Eliashberg spectral function $\alpha^2 F(\omega)$ and electron-phonon coupling strength $\lambda(\omega)$.

The Eliashberg spectral function $\alpha^2 F(\omega)$ is obtained in terms of the mode-specific EPC $\lambda(\omega)$, by evaluating

$$\alpha^2 F(\omega) = \frac{1}{2N_q} \sum_{qv} \lambda_{qv} \omega_{qv} \delta(\omega - \omega_{qv}), \tag{8.1}$$

and the total EPC constant is assessed by

$$\lambda = 2 \int_0^\infty d\omega \frac{\alpha^2 F(\omega)}{\omega}. \tag{8.2}$$

The resulting Eliashberg spectral function together with the frequency-dependent integrated EPC are plotted in Figure 8.6. The total EPC for *Cmcm*-GeNCr$_3$ is estimated to be 0.81, which is bigger than 0.75 for MgB$_2$ [24]. Two cluster peaks are found in the whole frequency range in $\alpha^2 F(\omega)$: One from 50 to 300 cm^{-1} and another from 500 to 700 cm^{-1}. That is, the low-frequency range contributes more significantly to the total EPC. A comparison of $\alpha^2 F(\omega)$ with PHDOS suggests an enhanced EPC to the vibrational modes below 400 cm^{-1}, which are originated mostly from the Cr and Ge atoms. After obtaining EPC, we estimated the superconducting transition temperature T_c using the Allen-Dynes modified McMillan equation:

$$T_c = \frac{\omega_{log}}{1.2} \exp\left[\frac{-1.04(1+\lambda)}{\lambda - \mu_c^*(1+0.62\lambda)}\right].$$ (8.3)

With the EPC being 0.81 and an effective Coulomb parameter $\mu_c^* = 0.16$, T_c is estimated to be 7.6 K.
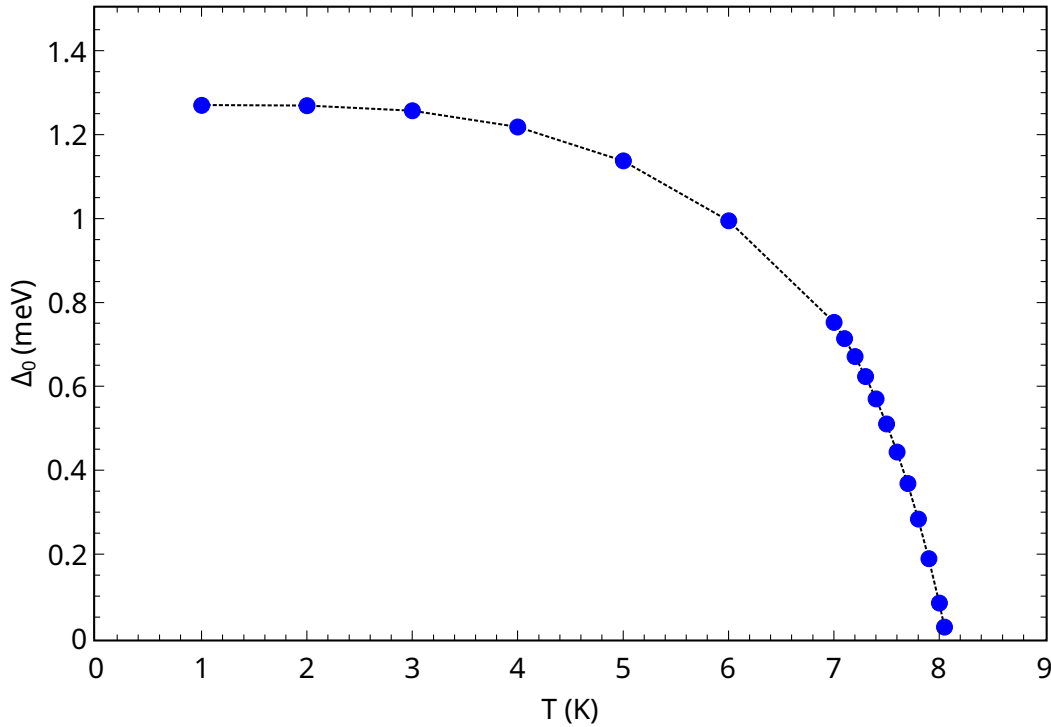
Figure 8.7.: The calculated superconducting gap at the Fermi level as a function of temperature.

Figure 8.7 shows the isotropic superconducting gap function at the Fermi level as a function of temperature, where the leading edge of the gap at $T = 0$ K is found to be

$\Delta_0 = 1.24$ meV. Correspondingly, $T_c = 8.2$ K as identified by the temperature where the gap vanishes, consistent with the estimated T_c of 7.6 K based on the McMillan equation. Hence, a fine superconducting critical temperature for *Cmcm*-GeNCr$_3$ is predicted, indicating that the superconductivity in *Cmcm*-GeNCr$_3$ is likely driven by the electron-phonon interactions. Recently, people used the same strategy through a high-throughput DFT framework to screen novel superconductors, such as antipervoskites [46] and MAX phases [370].

8.4. Conclusions

In this chapter, we derived from DFT calculations the formation energies of a newly synthesized orthorhombic compound GeNCr$_3$, and confirmed that the nitride is similarly stable in $P\bar{4}2_1m$- and *Cmcm*-GeNCr$_3$ phases. In accordance with the experimentally discovered superconductivity in antiperovskite MgCNi$_3$, we performed calculations to evaluate the electron-phonon interaction and the resulting superconducting critical temperature of GeNCr$_3$. The electron-phonon interaction calculations suggest *Cmcm*-GeNCr$_3$ is likely a BCS superconductor with a T_c of 8.2 K. Correspondingly, it is suspected that superconductivity may exist in the other MAX, MAB, and APV compounds, which will be investigated in the future based on the established workflow to evaluate the electron phonon coupling.

9. Thermodynamic Phase Diagram of the Fe-Sn System

Part of this chapter is published in: Thermodynamical and topological properties of metastable Fe$_3$Sn. Reproduced with permission from Chen Shen et al. [npj computational materials, in press] Copyright 2022 Springer Nature.

Considering the thermodynamic properties where the lattice free energy plays a dominant role at finite temperatures, the integrated computational paradigm that combines the DFT calculations, phonon theory, and CALPHAD methods is employed to construct the thermodynamic database, which can be validated with experiments and bridged to phase field simulations to map out the processing-microstructure-property relationships. Combining experimental data, first-principles calculations, and Calphad assessment, thermodynamic and topological transport properties of the Fe-Sn system were investigated. DFT calculations were performed to evaluate the intermetallics' finite-temperature heat capacity (C_p). A consistent thermodynamic assessment of the Fe-Sn phase diagram was achieved by using the experimental and DFT results, together with all available data from previous publications. Hence, the metastable phase Fe$_3$Sn was firstly introduced into the current metastable phase diagram, and corrected phase locations of Fe$_5$Sn$_3$ and Fe$_3$Sn$_2$ under the newly measured corrected temperature ranges.

9.1. Introduction

The kagome lattice is a 2D network of corner-sharing triangles that has been intensively investigated the last years. Due to its unusual geometry, it offers a playground to study interesting physics including frustrated, correlated [371, 372], exotic topological quantum [373, 379, 380, 381, 382, 383, 384, 385, 386, 381, 371, 374, 375, 376, 377, 378], topological Chern [387], insulating and Weyl semimetal [375, 388] phases, originating from the interplay between magnetism and electronic topology. In fact, the kagome lattice has been realized in several materials including metal stannides,

germannides [389, 390] as well as $T_m X_n$ compounds with T=Mn, Fe, Co, X=Sn, Ge (m:n=3:1, 3:2, 1:1) [391]. Recent studies demonstrated that Fe-Sn-based kagome compounds exhibiting interesting properties, such as large magnetic tunability [371]. Furthermore they can host Dirac fermions and flat bands, as found in Fe_3Sn_2 [392, 393] and FeSn [394, 391]. The existence of spin degenerate band touching points was linked to the generation of several interesting phenomena. Specifically, the anomalous Hall effect (AHE) results in a transverse spin polarized charge current (charge current and spin current due to the imbalance of spin up and spin down electrons in ferromagnets) in response to a longitudinal charge current, in the absence of an external magnetic field [395, 396, 397, 398, 399]. This applies also to its thermal counterpart, the anomalous Nernst effect (ANE), in which the external stimuli is replaced by a thermal gradient [400] as well as the Seebeck effect [401].

Interestingly, the Fe-Sn-based intermetallics compounds exhibit not only attractive topological transport properties but also show rich magnetic properties. In our previous studies [402, 403], a DFT screening of the Fe-Sn phase diagram was used to identify Fe-Sn based phases with the potential to be stabilized upon alloying, and their magnetization and magnetocrystalline anisotropy were evaluated. The results revealed that a strong anisotropy as observed in Fe_3Sn might also be found in other Fe-Sn based phases, having high potential to be used as hard magnetic materials. Meanwhile, we applied the reactive crucible melting (RCM) approach to the Fe-Sn binary system, and observed 3 metastable intermetallic compounds, namely Fe_3Sn, Fe_5Sn_3, Fe_3Sn_2, which are ferromagnetic and exist between 873 K and 1173 K. We found that such metastable phases can be synthesized using the RCM method at specific temperature ranges. What's more, the phase diagram of the Fe-Sn system reported in the literature [389, 404, 405] has mentioned that the Fe_3Sn was considered to be a metastable phase, and presented the relevant so-called metastable composition range and phase relations. According to Fayyazi's [402] work, the reactive crucible reproduced the corresponding phase relations as in the bulk samples at 998 K (α-Fe, Fe_3Sn_2, FeSn and Sn) and 1023 K (Fe_3Sn_2, Fe_3Sn, and FeSn), of which Fe_3Sn can only be stabilized between 1023-1098 K during a non-equilibrium process as a metastable phase but disappears at 1123 K due to the presence of Fe_5Sn_3 phase. Accordingly, adding more details to the phase diagram of the metastable Fe_3Sn phase, with the discovered temperature range based on the reported phase diagram is of great significance. Therefore, to further explore the interesting properties of metastable Fe-Sn phases, it is important to understand the phase diagram and thermodynamical properties of the Fe-Sn system.

In this work, we adopted our new measurements [402, 403] on the equilibria states of Fe_3Sn, Fe_5Sn_3, Fe_3Sn_2, combined with the thermodynamic properties of such intermetallic phases obtained based on first-principles calculations. A consistent thermodynamic assessment of the Fe-Sn system was then developed based on all available experimental and first-principles results.

9.2. Methodology

9.2.1. First-principles Calculations

Our calculations were performed using the generalized gradient approximation (GGA) for the exchange-correlation functional, in the parameterization of Perdew-Burke-Ernzerhof [406] for the Vienna ab−initio Simulation Package (VASP) [362, 367]. The energy cutoff is set at 600 eV and at least 5000 k-points in the first Brillouin zone with Γ-centered k-mesh were used for the hexagonal lattices (Fe_3Sn, FeSn, and Fe_5Sn_3), while for all the other structures, Monkhorst-Pack grids were used. The energy convergence criterion was set as 10^{-6} eV, and 10^{-5} eV/Åwas set as the tolerance of forces during the structure relaxation. The enthalpy of formation, $\Delta_f H(Fe_xSn_y)$, for the Fe_xSn_y intermetallic compounds was obtained following

$$\Delta_f H(Fe_xSn_y) = E_{Fe_xSn_y} - \frac{x}{x+y}E_{Fe} - \frac{y}{x+y}E_{Sn}, \tag{9.1}$$

where all the total energies for the equilibrium phases in their corresponding stable structures were obtained after structural relaxation.

For the phonon calculations, the frozen phonon approach was applied using the PHONOPY package [367]. The temperature-dependent thermodynamical properties were calculated by using the quasi-harmonic approximation [407]. The Gibbs free energy $G(T,P)$ at temperature T and pressure P can be obtained from the Helmholtz free energy $F(T,V)$ as follows: [75]

$$G(P,T) - PV = F(T,V) = E_0(V) + F_{vib}(V,T) + F_{el}(V,T) + F_{magn}(V,T), \tag{9.2}$$

where E_0(V) is the total energy at zero Kelvin without the zero-point energy contribution, which were determined by fitting of the energies with respect to the volume data using the Birch-Murnaghan equation of state (EOS) [74]. F_{vib} corresponds to the lattice vibration contribution to the Helmholtz energy, which can be derived from the phonon density of states (PhDOS), $g(\omega,V)$, by using the following equation [75]:

$$F_{vib}(V,T) = k_B T \int_0^\infty \ln\left[2\sinh\frac{\hbar\omega}{2k_B T}\right]g(\omega,V)d\omega, \tag{9.3}$$

where k_B and $\hbar$ are the Boltzmann constant and reduced Planck constant, respectively, and ω denotes the phonon frequency for a given wave vector q. The PhDOS $g(\omega,V)$ can be obtained by integrating the phonon dispersion in the Brillouin zone. The third term F_{el} represents the electronic contribution to the Helmholtz free energy, obtained by [76]:

$$F_{el}(V,T) = E_{el}(V,T) - T \cdot S_{el}(V,T) \tag{9.4}$$

where $E_{el}(V,T)$ and $S_{el}(V,T)$ indicate the electronic energy and electronic entropy, respectively. With the electronic *DOS*, both terms can be formulated as [76]:

$$E_{el}(V,T) = \int n(\varepsilon) f \varepsilon d\varepsilon - \int_{-\infty}^{\varepsilon_F} n(\varepsilon,V) d\varepsilon, \qquad (9.5)$$

$$S_{el}(V,T) = -k_B \int n\varepsilon[f lnf + (1-f)ln(1-f)]d\varepsilon, \qquad (9.6)$$

where $n(\varepsilon)$ is the electronic *DOS*, f represents the Fermi-Dirac distribution function and ε_F is the Fermi energy.

Finally, based on the original Inden–Hillert–Jarl (IHJ) model [77, 78] and further improved expression by Xiong [79], the magnetic Gibbs energy can be formulated as:

$$G_{magn} = RT ln(\beta^* + 1)f(\tau), \qquad (9.7)$$

where τ is T/T^*, T^* is the critical temperature (the Cutie temperature T_C for ferromagnetic materials or the Neel temperature T_N for antiferromagnetic materials). β^* is the effective magnetic moment per atom [79]. And the relative parameters are summarized in Table 9.1. Note that, we adopted the experimental critical temperatures and calculated magnetic moments.

Table 9.1.: Magnetic moment (μB per Fe atom) and critical temperature (K) of intermetallic phases.

Phases	Magnetism	Magnetic moment	Critical temperature
Fe_3Sn	FM	2.35	743 [403]
Fe_5Sn_3	FM	2.34	601 [403]
Fe_3Sn_2	FM	2.22	650 [403]
FeSn	AFM	2.01	368 [408]
$FeSn_2$	AFM	1.92	378 [409]

9.2.2. CALPHAD Modeling

Pure elements

The Gibbs free energies for pure Fe and Sn were taken from the Scientific Group Thermodata Europe (SGTE) pure element database [82], which was described by:

$$^\circ G_i^\phi(T) = G_i^\phi(T) - H_{i,SER}(298.15\,K) = a + bT + cT ln(T) + dT^2 + eT^3 + fT^{-1} + gT^7 + hT^{-9}, \quad (9.8)$$

where i represents the pure elements Fe or Sn, $H_{i,SER}(298.15\ K)$ is the molar enthalpy of element i at 298.15 K in its standard element reference (SER) state, and a to h are known coefficients.

Solution Phases

The solution phases, Liquid, BCC_A2, FCC_A1 and BCT_A5 phases are described using the substitutional solution model, with the corresponding molar Gibbs free energy formulated as:

$$G_m^{\varphi} = x_{Fe}G_{Fe}^{\varphi}(T) + x_{Sn}G_{Sn}^{\varphi}(T) + RT(x_{Fe}lnx_{Fe} + x_{Sn}lnx_{Sn}) + G^{ex} + G^{magn}, \tag{9.9}$$

where x_{Fe} and x_{Sn} are the mole fraction of Fe and Sn in the solution, respectively. Taken from SGTE [82], G_i^{φ} denotes the molar Gibbs free energy of pure Fe and Sn in the structure φ at the given temperature. G^{ex} denotes the excess Gibbs energy of mixing, which measures the deviation of the actual solution from the ideal solution behaviour, modelled using a Redlich-Kister polynomial [83]:

$$G^{ex} = x_{Fe}x_{Sn} \sum_{j=0}^{n} {}^{(j)}L_{Fe,Sn}^{\varphi}(x_{Fe} - x_{Sn})^j. \tag{9.10}$$

The $j-th$ interaction parameter between Fe and Sn is described by ${}^{(j)}L_{Fe,Sn}^{\varphi}$, which is modelled in terms of a^*+b^*T.

Stoichiometric intermetallic compounds

Fe_5Sn_3, Fe_3Sn_2, Fe_3Sn, $FeSn$, and $FeSn_2$ were considered as stoichiometric phases. The Gibbs free energies per mole atom of these phases were thus expressed as follows:

$$G_m^{Fe_xSn_y} = \frac{x}{x+y}G_{Fe,SER} + \frac{y}{x+y}G_{Sn,SER} + \Delta G_f^{Fe_xSn_y}(T) , \tag{9.11}$$

where $\Delta G_f^{Fe_xSn_y}(T)$ is the Gibbs free energy of formation of the stoichiometric compound Fe_xSn_y which can be expressed as:

$$\Delta G_f^{Fe_xSn_y}(T) = A_3 + B_3T , \tag{9.12}$$

where the coefficients A_3, B_3 are the parameters to be optimized. Since there is no experimental data of the thermodynamic properties for such intermetallic phases, the calculated enthalpies of formation for these phases from DFT calculations were treated as initial values of the coefficient A_3 in Eq. 9.12 in the present optimization.

9.3. Results and Discussion

Most end-members in the sublattice models are not stable and their thermodynamic data are impossible to be determined by experiments. First-principles are hence performed to estimate the Gibbs energies of the compounds and end-members at finite temperatures. In order to benchmark the current DFT calculations, the calculated crystallographic information of phases in the binary Fe-Sn system are listed in Table 9.2, in comparison with the available experimental data.

Table 9.2.: Lattice parameters of intermetallics from first-principles calculations compared with experimental values.

| Phases | Space group | Magnetism | Lattice parameters (Å) | | k-point mesh | Refs. |
			a	c		
Fe_3Sn	$P6_3/mmc$	FM	5.457	4.362		[410]
			5.461	4.347		[411]
			5.421	4.434		[412]
			5.440	4.372		[413]
			5.464	4.352		[389]
			5.475	4.307	10×10×12	This work
Fe_5Sn_3	$P6_3/mmc$	FM	4.223	5.253		[414]
Fe_3Sn_2	R-3 m	FM	5.344	19.845		[415]
			5.340	19.797		[389]
			5.315	19.703		[372]
			5.328	19.804	10×10×3	This work
FeSn	P6/mmm	AFM	5.307	4.445		[410]
			5.297	4.481		[416]
			5.288	4.420		[417]
			5.300	4.450		[418]
			5.298	4.448		[389]
			5.297	4.449		[419]
			5.299	4.449	10×10×10	This work
$FeSn_2$	I4/mcm	AFM	6.502	5.315		[420]
			6.539	5.325		[421]
			6.539	5.325		[409]
			6.542	5.326		[416]
			6.542	5.386		[417]
			6.536	5.323		[389]
			6.533	5.320		[422]
			6.545	5.326		[423]
			6.561	5.338	8×8×10	This work

The calculated lattice parameters of the solid phases at 0 K are in good agreement with the experimental results at room temperature. As one can see, the differences between the theoretical and experimental lattice constants are within 0.5 % for all the phases. Note that, in our earlier study [402, 403], we showed, that the crystal structure of "Fe_5Sn_3" synthesized by the equilibrated alloy method, is not of the typically assumed hexagonal Laves structure (as shown in Table 9.2). We rather observed superstructure reflections in the powder XRD spectra that could not be explained by the hexagonal structure and we assigned to a modulated orthorhombic unit cell with lattice parameters of a = 4.221 Å, b = 7.322 Å, c = 5.252 Å. More details and explanations can be found in Ref. [402, 403]. Hence, we used this structure to do phonon calculations. Furthermore, the calculated phonon bands of such phases are shown in Figure 9.1. To prove the validity of the calculations, as shown in Figure 9.1, the phonon dispersion of BCC-Fe is compared with the experimental data [424], presenting good agreement. Therefore, it is expected that the thermodynamical properties of the Fe-Sn intermetallic phases can also be accurately obtained based on DFT calculations. As shown in Figure 9.1, no imaginary phonon modes exist for all the compounds, indicating that all the intermetallics are dynamically stable. And the quasi-harmonic approximation (QHA) can be used to calculate the thermodynamic properties.

The thermodynamic properties at finite temperatures are evaluated based on the Gibbs free energies specified in Eq. 9.2. And from the thermodynamical point of view, we can derive the Gibbs free energies from the heat capacity. To obtain the accurate heat capacity of the intermetallics, we firstly compare the calculated heat capacity of the BCC-Fe with the available experimental data [425], as shown in Figure 9.2. Among that, the magnetic contribution to the heat capacity is analyzed following the theory of IHJ model [77, 78] and further improved version by Xiong [79]:

$$C_{p_{mag}} = Rln(\beta^* + 1)c(\tau). \tag{9.13}$$

Figure 9.2 shows isobaric heat capacity obtained from our DFT calculations. It can be observed that the lattice vibrations dominate other contributions to the heat capacity. Interestingly, the correction made by adding electronic and magnetic heat capacities shifted the result toward bigger values and after that calculations show an excellent agreement with the experimental data [425]. More interestingly, the magnetic contribution to the heat capacity presents at the magnetic phase transition of BCC-Fe. These results prove the accuracy of the current methods and justify the following calculations for intermetallics. Using the same strategy, we calculate heat capacities of Fe_5Sn_3, Fe_3Sn_2, Fe_3Sn, $FeSn_2$, and FeSn at finite temperatures, as shown in Figure 9.2, with the magnetic heat capacity evaluated using Inden model [78].
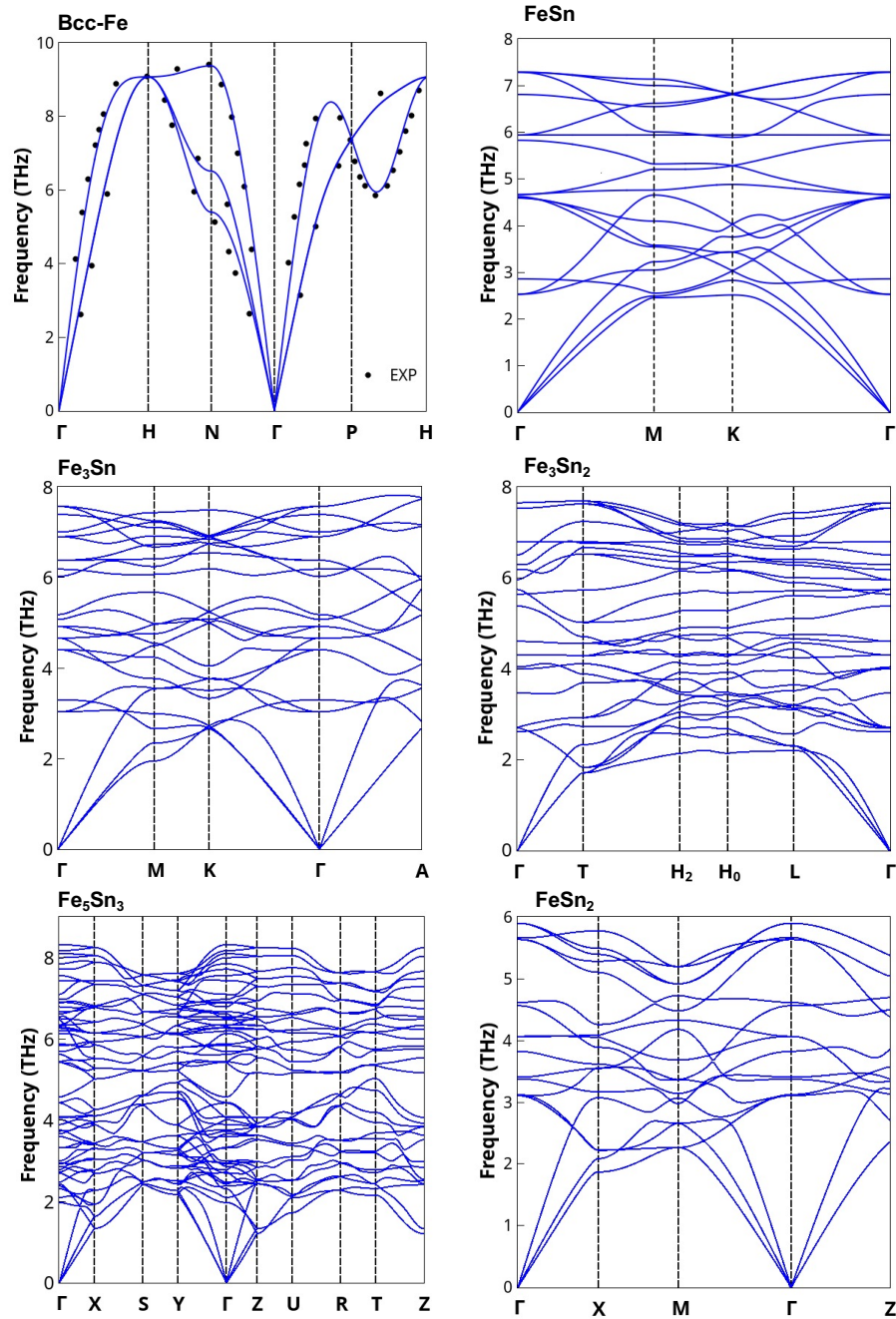
Figure 9.1.: Phonon dispersions of the pure elements and intermetallic phases in the Fe-Sn system. The black solid points represent the experimental data from Ref. [425].

The heat capacity of Fe_3Sn shows a good consistency between our calculations and experiments at low temperature, which also confirms the accuracy of current theoretical

results. We note that such good agreements are supported by considering the magnetic contributions in the magnetic system.
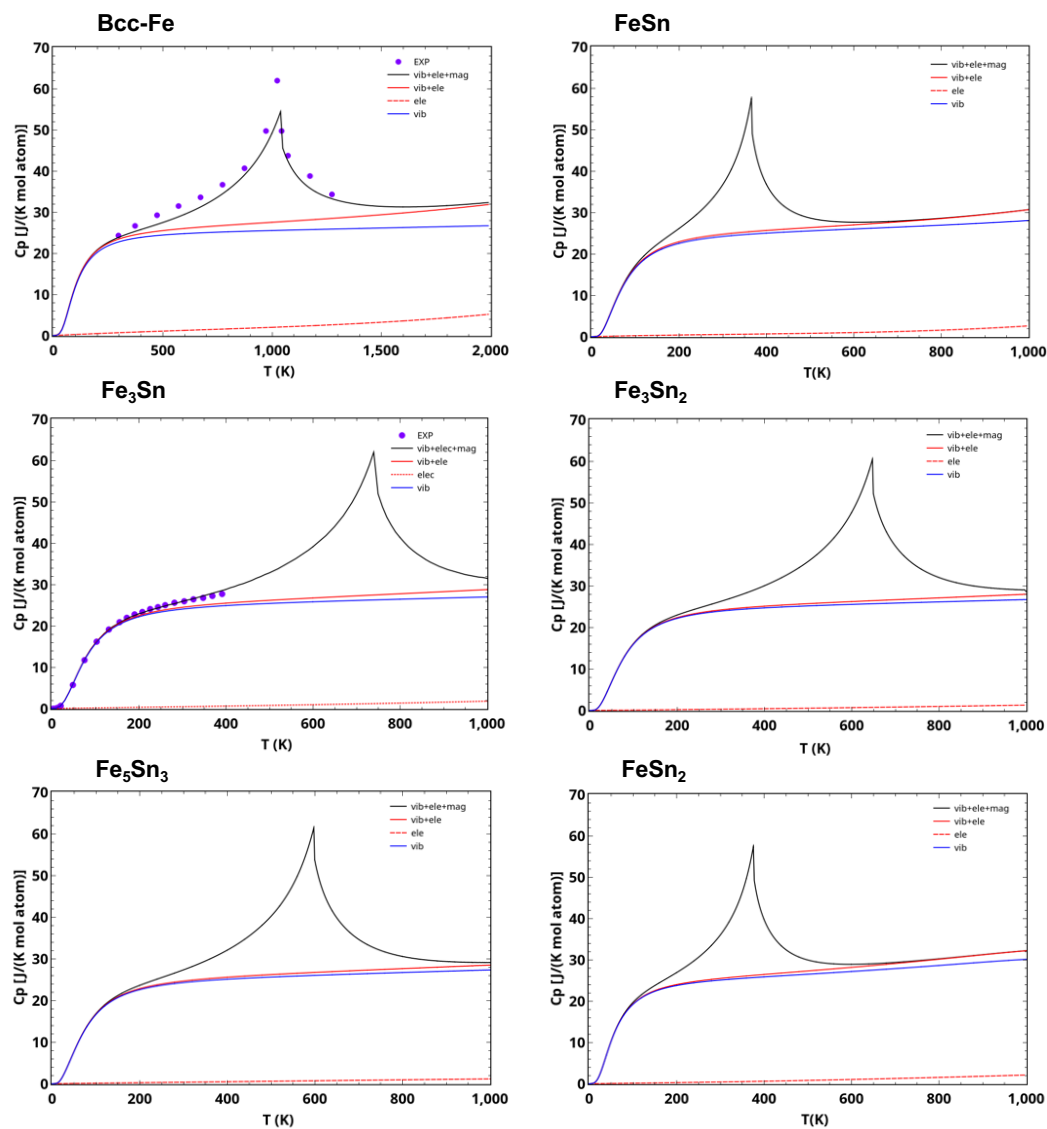
Figure 9.2.: Heat capacity of pure Fe and Sn from DFT calculations in comparison with the experiment data [425]. Those for all the intermetallics are also shown, experimental data of Fe_3Sn is obtained from our previous studies [402, 403].

After getting the thermodynamical properties of intermetallics, we used CALPHAD method [21] to evaluate the thermodynamic model parameters of the Fe-Sn system,

and the phase diagram and thermodynamic properties are calculated by Thermo-Calc [426]. Combining DFT and CALPHAD methods has already been successfully applied in different systems [427, 428]. Thermodynamic database in Appendix lists the modelled thermodynamic parameters of the Fe-Sn system. The calculated Fe-Sn phase diagram is presented in Figure 9.3 along with the experimental data [429, 434, 435, 436, 437, 438, 439, 440, 434, 430, 431, 432, 433, 402].
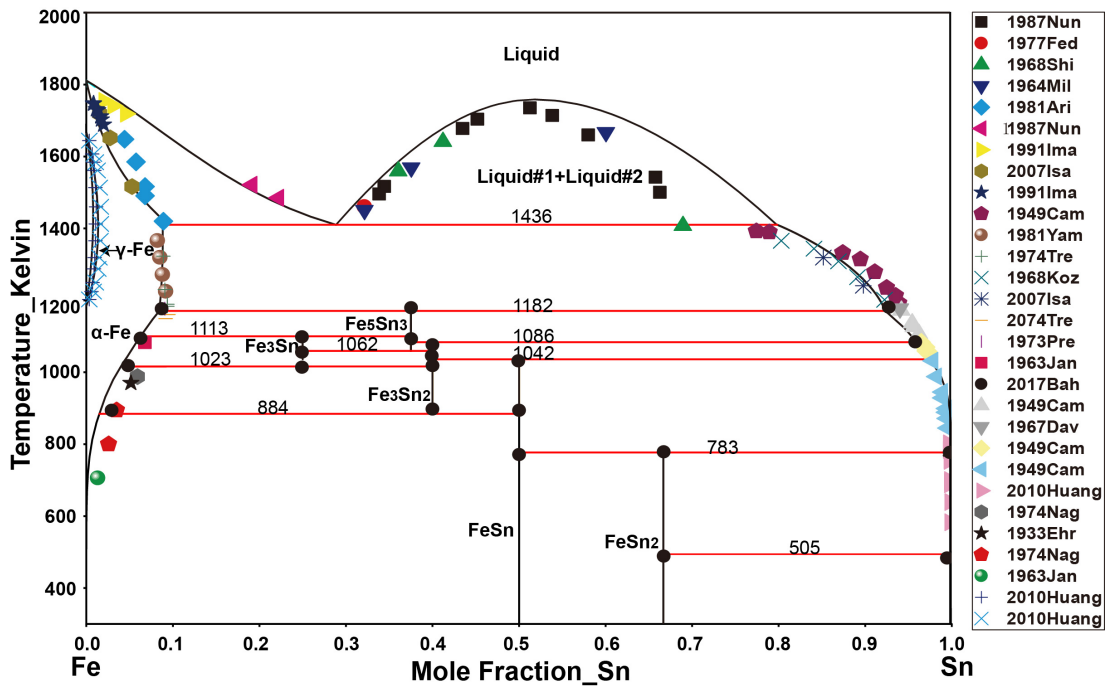
Figure 9.3.: The optimized Fe-Sn phase diagram based on our thermodynamic modelling, in comparison with the experiment data [429, 434, 435, 436, 437, 438, 439, 440, 430, 431, 432, 433, 402].

The comparison of the calculated temperatures and compositions of invariant reactions with experimental data [429, 434, 435, 436, 437, 438, 439] as well as results from previous thermodynamic assessments [441, 405] are listed in Table 9.3. Using the reactive crucible melting (RCM) approach, it is found that 3 metastable intermetallic compounds, i.e., Fe_3Sn, Fe_5Sn_3, and Fe_3Sn_2, can be stabilized between 873 K and 1173 K. Furthermore, we are convinced that the phase diagram reported in the literature is inaccurate in the temperature interval 1023-1038 K and Fe_3Sn can exist at 1023 K. Thus, the meta-stable phase Fe_3Sn is introduced by considering the current accurate experimental results. Obviously, good agreement between the optimized and experimental Figure S1 and S2 in Appendix show the calculated thermodynamic properties of the compounds in current CALPHAD modeling, first-principles calculations, previous CAL-

PHAD modeling and the experimental data. The calculated thermodynamic properties in this work are consistent with experimental data.

Table 9.3.: Summary of the invariant reactions in the Fe-Sn system.

Invariant Reaction	Reaction type	Composition at % Sn			Temperature (K)	Refs.
Liquid#1 →BCC_A2+Liquid#2	Eutectic	0.312	0.083	0.811	1395.9	[441]
					1381	[429]
					1404	[434]
					1403	[435]
					1403	[431]
					1407	[405]
					1413	[436]
	Eutectic	0.297	0.095	0.796	1436	This work
BCC_A2 + Liquid →Fe$_5$Sn$_3$	Peritectic	0.081	0.929	0.375	1174.1	[441]
					1166	[436]
					1168	[405]
					1183	[438]
					1183	[437]
	Peritectic	0.088	0.948	0.375	1182	This work
BCC_A2 + Fe$_5$Sn$_3$ →Fe$_3$Sn	Peritectic	0.064	0.375	0.250	1111	[402]
	Peritectic	0.062	0.375	0.250	1113	This work
Fe$_5$Sn$_3$ + Liquid →Fe$_3$Sn$_2$	Peritectic	0.375	0.967	0.400	1074.8	[441]
					1072	[439]
					1079	[438]
					1079	[437]
					1080	[405]
	Peritectic	0.375	0.979	0.400	1086	This work
Fe$_5$Sn$_3$ → Fe$_3$Sn + Fe$_3$Sn$_2$	Eutectoid	0.375	0.250	0.400	1055	[402]
	Eutectoid	0.375	0.250	0.400	1062	This work
Fe$_3$Sn$_2$ + Liquid →FeSn	Peritectic	0.400	0.980	0.500	1024.7	[441]
					1013	[435]
					1034	[405]
					1043	[438]
					1043	[437]
	Peritectic	0.400	0.979	0.500	1042	This work
Fe$_3$Sn → BCC_A2 +Fe$_3$Sn$_2$	Eutectoid	0.250	0.046	0.400	1023	[402]
	Eutectoid	0.250	0.046	0.400	1023	This work
Fe$_3$Sn$_2$ → BCC_A2 +FeSn	Eutectoid	0.400	0.017	0.500	874.9	[441]
					870	[439]
					873	[435]
					880	[438]
					880	[437]
					880	[405]
	Eutectoid	0.400	0.015	0.500	884	This work
FeSn + Liquid →FeSn$_2$	Peritectic	0.500	0.999	0.666	775.4	[441]
					769	[436]
					769	[429]
					769	[435]
					786	[437]
					786	[438]
					786	[405]
	Peritectic	0.500	0.999	0.666	783	This work
Liquid → FeSn$_2$ +BCT_A5	Eutectic	0.999	0.666	1.000	504.9	[441]
					501	[436]
					505	[437]
					505	[438]
					505	[405]
	Eutectic	0.999	0.666	1.000	505	This work

9.4. Conclusions

In this chapter, based on DFT calculations, the thermodynamical properties of the Fe-Sn system are studied. First-principles phonon calculations with the QHA approach were performed to calculate the heat capacities of pure elements and intermetallics at finite temperatures. The calculated formation energies and Gibbs free energies were then fed into the CALPHAD method as initial input values, which can make up the shortage of experimental data. Hence, thermodynamic modeling of the Fe-Sn phase diagram has been re-established. The problems concerning invariant reactions of intermetallics Fe_5Sn_3 and Fe_3Sn_2 are remedied under recently newly measured temperature ranges. We reported that the metastable phase Fe_3Sn was introduced into the current metastable phase diagram. At latst, a set of self-consistent thermodynamic parameters of Fe-Sn system is obtained by the CALPHAD approach. Taking Fe-Sn as a prototype system, the integrated computational paradigm that combines the HTP DFT calculations, phonon theory, and CALPHAD methods is employed to construct the thermodynamic database, which can be validated with experiments and bridged to phase field simulations to map out the processing-microstructure-property relationships.

10. Summary and Future Work

10.1. Summary

In this thesis, we established a computational paradigm to treat the lattice degree of freedom systematically and explored it via performing high-throughput density functional theory calculations to design novel functional materials, in particular those materials for energy applications. Such a paradigm can tackle the magnetocaloric, thermodynamic, and non-equilibrium transport properties by considering the magneto-structural coupling, quasi-harmonic approximations, and phonon-phonon coupling, as well as superconductivity driven by the electron-phonon interaction. Eventually, such a paradigm can be bridged to large-scale simulations, and also to experimental synthesis.

Considering lattice as crystal structures, our HTP DFT calculations on 6 types of MAB phases and 3 types of competing non-MAB phases predict 434 magnetic ternary transition metal borides which are potential candidates for permanent magnets and magnetocaloric materials. After a comprehensive validation, 21 novel compounds are predicted to be stable based on the systematic evaluation of thermodynamic, mechanical, and dynamical stabilities, and the number of stable compounds is increased to 434 taking the tolerance of convex hull being 100 meV/atom. The trend of stability for the MAB phase can be understood based on the Hume-Rothery rules, where the size factor difference and the valence electron concentration play a critical role. Such a trend can be further attributed to the bond-resolved COHP, providing intuitive guidance for experimental synthesis. From the magneto-structural coupling point of view, the detailed evaluation of the magnetocrystalline anisotropy energy (MAE) and the magnetic deformations ($\sum_M$) leads to 23 compounds with significant uniaxial MAE larger 0.4 MJ/m^3 and 99 systems with reasonable $\sum_M$ over 1.5 %. For those compounds containing no expensive, toxic, or critical elements, it is observed that $Fe_3Zn_2B_2$ is a reasonable candidate as gap permanent magnet, and Fe_4AlB_4, Fe_3AlB_4, Fe_3ZnB_4, and Fe_5B_2 as potential magnetocaloric materials. This work paves the way for designing more magnetic materials using HTP DFT for energy applications. In particular, it also

provides a good starting point to search for novel two-dimensional magnetic materials, *i.e.*, MBene, based on detailed evaluation of the exfoliation energy and follow-up experiments.[229]

Furthermore, considering the lattice degree of freedom as elementary excitations of lattice vibrations, *i.e.*, phonons, the phonon-phonon interaction governed by phonon anharmonicity is employed to design functional materials within many intriguing properties. The thermal transport properties of novel materials of 2D layered MSi_2N_4 (M = Mo, W) are investigated. The thermal conductivities of $MoSi_2N_4$ and WSi_2N_4 are calculated by solving BTE based on the DFT calculations, and found to be 162 $Wm^{-1}K^{-1}$ and 88 $Wm^{-1}K^{-1}$ at 300 K, respectively, which are 7 and 4 times the one for monolayer MoS_2, 16 and 9 times the one for silicene. These results indicate these two novel 2D materials have the potential to be thermal management materials. To understand the underlying mechanism for the high thermal conductivity of $MoSi_2N_4$ and WSi_2N_4, systematic analysis is performed based on the contribution from each phonon branch and comparison among the mode level phonon group velocity and lifetime. The root reason for the high thermal conductivity of $MoSi_2N_4$ and WSi_2N_4 is that the high group velocity of these two materials. The phonon Grüneisen parameter is further analyzed to understand the phonon-phonon scattering. And the Grüneisen parameter of $MoSi_2N_4$ smaller than that of WSi_2N_4, which is the underlying reason for the small phonon lifetime and further lower thermal conductivity of WSi_2N_4 than $MoSi_2N_4$. Therefore, our study offers fundamental understanding of thermal transport properties in monolayer $MoSi_2N_4$ and WSi_2N_4 within the framework of BTE and the electronic structures from the bottom, which will enrich the studies and exploring of novel MSi_2N_4 type two dimensional thermal management materials.

In addition, to gain insight into the phonon anharmonicity in 2D materials, we performed DFT calculations for 2D GaX (X= N, P, As) to investigate the mechanism of anharmonicity from the fundamental phonon mode and electronic structure level. The thermal conductivity of GaP is calculated to be 1.52 $Wm^{-1}K^{-1}$, which is unexpectedly ultra-low and in sharp contrast to GaN and GaAs. Considering the similar honeycomb geometry structure of GaP to that of GaN and GaAs, it is quite intriguing to find that the thermal conductivity of GaP is very low. To understand the underlying mechanism for GaX monolayers having planar or buckling structures, systematic analysis is performed based on PJTE theory. The larger bandgap and smaller the vibronic coupling constant, the less destabilization of the ground state and less stabilization of the excited states. Hence, the GaN exists in planar structure, and GaP and GaAs stabilize in buckling structures. Moreover, in order to gain insight into anomalous phenomena of ultra-low thermal conductivity for GaP, we perform a detailed analysis of the underlying mechanisms in the framework of phonon mode-solved investigation. The reason for the low thermal conductivity ofthe GaP is found to be that: FA dominates the thermal conductivity of GaN but less contributes to the one of GaP, which is due to the symmetry-

based selection rule and difference of atomic structure. In particular, the difference originates from the different situations for the phonon lifetime, which is determined by phonon–phonon scattering. The phonon anharmonicity quantified by the Grüneisen parameter is further analyzed to understand the phonon–phonon scattering, indicating the strong phonon-phonon scattering of GaP and the strongest phonon anharmonicity of GaP in GaX. Considering that all the properties are fundamentally determined by the atomic structure and the behavior of electrons (such as charge distribution and orbital hybridization), we further perform analysis from the view of electronic structures and orbital bonding to gain deep insight into the phonon transport. The buckling structure has a high priority influencing the anharmonicity, leading to the low thermal conductivity. Then, due to the buckling structures, the delocalization of electrons in GaP and GaAs are restricted, namely, the bonds are polarized. The non-bonding lone pair electron of P and As atoms are stronger, which induces nonlinear electrostatic forces upon thermal agitation, leading to increased phonon anharmonicity in the lattice and thus reducing the thermal conductivity. Our study offers fundamental understanding of phonon transport in GaX monolayers with honeycomb structure within the framework of BTE and the electronic structure from the bottom, which will enrich the studies of nanoscale phonon transport in 2D materials.

Besides 2D materials, the pervoskites materials always show the phase instability. High order phonon anharmonicity could have significant effect on the thermal transport properties in such materials. In this work, it is the first time to calculate the thermal conductivity of pristine $EuTiO_3$. And the role of the quartic anharmonicity in the lattice dynamics and thermal transport of the cubic $EuTiO_3$ was studied by combining *ab initio* self-consistent phonon theory with compressive sensing techniques and experimental thermal conductivity determination measurement. The anti-ferromagnetic G-type magnetic structure is used to mimic the para-magnetic $EuTiO_3$. We found that the strong quartic anharmonicity of oxygen atoms plays an important role in the phonon quasiparticles free from imaginary frequencies in $EuTiO_3$ and causes the hardening of vibrational frequencies of soft modes. Based on these results, the lattice thermal transport properties are predicted through the Boltzmann transport equation within the relaxation time approximation. The hardened modes thereby affect calculated lattice thermal conductivity significantly, resulting in an improved agreement with experimental results, including the deviation from $\kappa_L \propto T^{-1}$ at high temperature. The calculated thermal conductivity of 8.2 $Wm^{-1}K^{-1}$ at 300 K matched the experimental value of 6.1 $Wm^{-1}K^{-1}$. When considering the boundary scattering, the calculated thermal conductivity is reduced to 6.9 $Wm^{-1}K^{-1}$ at 300 K, which agrees better with the experimental values.

Furthermore, the interaction between electrons and phonons also plays an essential role in materials properties. In this thesis, based on DFT calculations we investigated the thermodynamical stability of a newly synthesised orthorhombic compound $GeNCr_3$,

and found this new compound is a metastable phase. The finding of superconductor $MgCNi_3$ and more antiperovskites showing superconducting behavior sparked our interest. Hence, we preformed calculations to evaluate the electron-phonon interaction for the new orthorhombic compound and predicted its superconducting behavior with a T_c of 8.2 K. This study offers a fundamental understanding of electron-phonon coupling in materials in the antiperovskite structure, which also invokes our suspecting and imagination of whether the superconductivity may exist in the other MAX, MAB, and APV compounds.

Last but not least, considering the thermodynamic properties where the lattice free energy plays a dominant role at finite temperatures, the integrated computational paradigm that combines the HTP calculations, phonon theory, and CALPHAD methods is employed to construct the thermodynamic database, which can be validated with experiments and bridged to phase field simulations to map out the processing-microstructure-property relationships. Combining experimental data, first-principles calculations, and Calphad assessment, thermodynamic properties of the Fe-Sn system were investigated. First-principles phonon calculations with the QHA approach were employed to calculate the heat capacity of each pure element and intermetallic phase at finite temperatures, which make up for the shortage of experimental data. A set of self-consistent thermodynamic parameters are obtained by the CALPHAD approach. Thermodynamic modeling of the Fe-Sn phase diagram has been re-established. In this work, we reported that the metastable phase Fe_3Sn was introduced into the current metastable phase diagram, and corrected phase locations of Fe_5Sn_3 and Fe_3Sn_2 under the newly measured corrected temperature ranges.

10.2. Future Work

Despite the fact that we can design functional materials from the lattice degree of freedom, they mostly focus on crystalline or ordered structures within the atomic level. In the future, we plan to extend the current paradigm to many more large-scale simulations, which are more realistic for experimental synthesis. To achieve this, we plan to combine the DFT, CALPHAD, and phase field methods to map the composition-processing relationships based on thermodynamics. In addition, a more accurate MLIP will be developed for MD simulations, which could be used to study heat and mass transport properties. Hence, we are going to integrate the DFT, MLIP, and MD for atomistic lattice (and possibly spin) modeling to understand the dynamical and kinetic processes. This is critical for the rapidly developed energy materials industry. Meanwhile, the study of thermal transport properties for 2D and bulk materials has been demonstrated in the current work. More fundamental interactions between the elementary excitations should be further investigated, such as (a) electron-phonon interaction for electronic

transport, thermal conductivity, BCS superconductivity and high-Tc superconductivity; (b) magnon-phonon interaction for spin-driven thermoelectric materials; (c) phonon-phonon driven thermal conductivity in the quantum limit, and at interfaces, which is critical for thermal management materials; (d) ultra-fast processes at the picosecond time scale for photovoltaic materials. For disorder and complex materials, such as multicomponent and high entropy alloys, we plan to use the Exact Muffin-Tin Orbitals (EMTO) theory within the spherical cell approximation and combine it with the Full Charge Density technique and the Coherent Potential Approximation (CPA) to treat the complex alloys. To implement the above plans, more knowledge about theories and techniques should be solid. For instance, from the technical point of view to model the potential energy surfaces, such as advanced algorithms for MLIP, phonon calculations under electric fields, quantum Monte Carlo, and non-adiabatic molecular dynamics, should be learned and understood deeper.

A. Supporting Information for MAB

Table S1.: List of MAB and non-MAB phases that we found stable and meta-stable based convex hull distance < 0.1 eV/atom. Lattice parameters (Å), formation energy (eV/atom), distance to the convex hull (eV/atom), and magnetic moment (the unit as μB per magnetic atom) in considered phases are shown.

Compounds	Space Group	Lattice Constant			Convex Hull	Formation Energy	Magnetic moment
		a	b	c			
FeBeB	63	2.925	2.648	12.164	0.000	-0.326	0.422
MnBeB	63	2.809	2.811	12.252	0.000	-0.378	0.002
CrAlB	63	2.969	3.004	13.881	0.011	-0.377	0.011
CoBeB	63	3.058	2.539	12.098	0.014	-0.284	0.087
CoPtB	63	3.133	2.822	14.347	0.037	-0.250	0.092
FeMgB	63	2.902	2.871	17.037	0.040	-0.211	0.908
FeCrB	63	2.912	2.926	13.261	0.041	-0.310	2.254
FeZnB	63	2.904	2.857	14.631	0.045	-0.206	1.151
Cr2B	63	2.900	2.892	13.469	0.047	-0.328	0.002
NiPtB	63	3.053	3.024	14.015	0.048	-0.227	0.002
NiLiB	63	2.996	2.714	15.995	0.052	-0.149	0.003
CrReB	63	2.881	2.905	15.108	0.052	-0.299	0.003
NiCuB	63	3.037	2.881	13.038	0.054	-0.111	0.000
FeMnB	63	2.912	2.904	13.354	0.057	-0.301	3.889
CrBeB	63	2.860	2.860	12.584	0.060	-0.291	0.012
FeIrB	63	2.896	2.856	14.896	0.061	-0.190	1.451
MnIrB	63	2.926	2.925	14.755	0.062	-0.271	1.992
FePtB	63	2.951	2.974	14.720	0.063	-0.242	1.887
CrNiB	63	2.927	2.983	12.697	0.066	-0.297	0.020
MnAlB	63	2.988	2.953	13.908	0.066	-0.329	0.997
FeAlB	63	2.856	2.729	15.972	0.067	-0.281	0.644
Fe2B	63	2.919	2.868	13.357	0.068	-0.244	4.078
CrPtB	63	2.850	3.124	14.749	0.069	-0.330	0.100
NiAuB	63	3.057	2.995	15.082	0.070	-0.095	0.002
NiPdB	63	3.044	2.965	14.116	0.070	-0.211	0.003
FeLiB	63	2.837	2.797	15.498	0.071	-0.180	0.356
CoMgB	63	2.930	2.834	16.933	0.072	-0.201	0.001
MnPtB	63	2.954	3.071	14.596	0.073	-0.340	2.441
CrTcB	63	2.888	2.915	14.819	0.075	-0.289	0.002
CrRhB	63	2.869	2.892	15.040	0.077	-0.295	0.005
NiZnB	63	2.973	2.788	14.808	0.078	-0.132	0.002
NiIrB	63	3.164	2.828	13.941	0.079	-0.139	0.016
CoPdB	63	3.017	2.847	14.528	0.081	-0.217	0.185
CoRhB	63	2.988	2.811	14.250	0.084	-0.191	0.006
MnCoB	63	2.930	2.891	13.195	0.084	-0.255	3.540
NiMnB	63	2.950	2.942	12.894	0.086	-0.278	2.448
CoLiB	63	2.962	2.679	15.351	0.087	-0.186	0.031
CoIrB	63	2.950	2.845	14.489	0.087	-0.186	0.000
MnZnB	63	2.872	2.868	14.626	0.087	-0.246	0.039
FePdB	63	2.946	2.938	14.740	0.088	-0.216	1.739
MnRhB	63	2.938	2.950	14.468	0.089	-0.273	2.236
MnPdB	63	2.958	3.015	14.701	0.090	-0.296	2.435

CrPdB	63	2.913	2.982	14.950	0.091	-0.270	0.185
CoZnB	63	2.980	2.818	14.328	0.092	-0.181	0.002
FeRuB	63	2.863	2.854	14.744	0.095	-0.155	1.528
MnReB	63	2.832	2.790	15.606	0.096	-0.237	0.049
MnMgB	63	2.883	2.887	17.126	0.096	-0.237	0.265
FeNiB	63	2.957	2.896	12.742	0.097	-0.209	1.977
CoCrB	63	2.927	2.963	12.754	0.097	-0.254	1.379
FeRhB	63	2.913	2.866	14.666	0.098	-0.201	1.852
Fe2BeB2	65	2.749	2.904	9.947	0.000	-0.344	0.760
Mn2BeB2	65	2.815	2.846	9.969	0.000	-0.435	0.011
Fe2AlB2	65	2.851	2.916	11.019	0.000	-0.401	1.330
Mn2AlB2	65	2.831	2.894	11.080	0.000	-0.471	0.400
Cr2AlB2	65	2.932	2.924	11.051	0.000	-0.466	0.010
Cr2SiB2	65	2.931	2.923	10.441	0.029	-0.414	0.001
Cr2BeB2	65	2.911	2.895	9.911	0.034	-0.387	0.131
Cr2ReB2	65	2.916	2.885	11.474	0.034	-0.387	0.006
Fe2MgB2	65	2.849	2.895	12.019	0.035	-0.266	0.910
Co2BeB2	65	2.542	3.017	10.196	0.043	-0.300	0.016
Cr2TcB2	65	2.916	2.887	11.376	0.045	-0.385	0.005
Mn2IrB2	65	2.950	2.960	11.131	0.046	-0.354	2.068
Fe2ZnB2	65	2.853	2.905	11.158	0.054	-0.248	1.046
Cr2IrB2	65	2.933	2.876	11.456	0.055	-0.377	0.009
Ni2LiB2	65	2.667	2.999	11.874	0.058	-0.182	0.002
Ni2PtB2	65	2.962	3.028	10.878	0.060	-0.214	0.006
Co2AlB2	65	2.687	2.971	11.351	0.063	-0.347	0.149
Cr2FeB2	65	2.927	2.913	10.586	0.064	-0.357	1.334
Fe2IrB2	65	2.878	2.917	11.246	0.065	-0.236	1.684
Ni2CuB2	65	2.800	2.995	10.754	0.065	-0.133	0.001
Ni2ZnB2	65	2.819	2.977	11.145	0.066	-0.169	0.005
Cr3B2	65	2.884	2.901	10.773	0.066	-0.374	0.008
Fe2PtB2	65	2.914	2.974	11.188	0.067	-0.267	1.598
Cr2WB2	65	2.926	2.899	11.646	0.068	-0.353	0.007
Co2MgB2	65	2.795	2.932	12.069	0.069	-0.259	0.017
Cr2MoB2	65	2.929	2.903	11.593	0.071	-0.357	0.007
Mn2CoB2	65	2.909	2.934	10.500	0.071	-0.336	2.717
Mn2FeB2	65	2.906	2.926	10.588	0.071	-0.344	2.830
Mn2RhB2	65	2.947	2.961	11.070	0.071	-0.346	2.170
Fe3B2	65	2.840	2.931	10.679	0.074	-0.265	2.899
Cr2RuB2	65	2.917	2.882	11.312	0.075	-0.346	0.013
Cr2OsB2	65	2.916	2.883	11.372	0.077	-0.344	0.007
Mn2PtB2	65	3.015	2.984	11.158	0.067	-0.384	2.354
Fe2GaB2	65	2.877	2.944	10.995	0.078	-0.237	1.360
Ni2BeB2	65	2.712	2.964	10.174	0.080	-0.207	0.001
Ni2PdB2	65	2.928	3.019	10.958	0.080	-0.199	0.005
Mn2SiB2	65	2.734	2.937	10.668	0.081	-0.354	0.004
Mn2ReB2	65	2.907	2.926	11.306	0.081	-0.319	1.647
Cr2RhB2	65	2.934	2.877	11.407	0.082	-0.352	0.034
Cr2VB2	65	2.908	2.927	10.971	0.083	-0.475	0.005
Ni2AuB2	65	2.958	3.044	11.262	0.084	-0.114	0.014
Cr2CoB2	65	2.934	2.904	10.520	0.085	-0.336	1.111
Cr2NiB2	65	2.971	2.917	10.347	0.085	-0.344	0.009
Co2PtB2	65	2.819	3.059	11.026	0.085	-0.252	0.307
Cr2MnB2	65	2.885	2.878	10.698	0.087	-0.360	0.034
Fe2ReB2	65	2.826	2.870	11.552	0.088	-0.232	1.386
Fe2NiB2	65	2.862	2.941	10.376	0.090	-0.244	1.537
Mn2ScB2	65	2.891	2.873	12.668	0.092	-0.432	0.323
Cr2PtB2	65	3.061	2.881	11.283	0.093	-0.357	0.185
Fe2RhB2	65	2.886	2.911	11.204	0.095	-0.248	1.899
Mn2RuB2	65	2.929	2.938	11.061	0.096	-0.304	1.798
Mn2NiB2	65	2.910	2.953	10.404	0.096	-0.322	2.096
Mn2WB2	65	2.790	2.833	12.067	0.099	-0.328	0.006
Mn2TcB2	65	2.899	2.927	11.270	0.099	-0.320	1.605

Cr3AlB4	47	2.939	2.939	8.091	0.000	-0.445	0.049
Cr3BeB4	47	2.915	2.916	7.571	0.011	-0.403	0.006
Mn3BeB4	47	2.911	2.830	7.591	0.025	-0.364	0.636
Cr3SiB4	47	2.954	2.918	7.787	0.035	-0.392	0.010
Mn3AlB4	47	2.937	2.834	8.164	0.038	-0.396	0.758
Fe3BeB4	47	2.953	2.792	7.586	0.047	-0.240	1.198
Fe3AlB4	47	2.961	2.818	8.149	0.065	-0.27975	1.255
Cr3IrB4	47	2.911	2.911	8.359	0.067	-0.37507	0.007
Cr3GaB4	47	2.948	2.950	8.100	0.071	-0.34263	0.099
Cr3ZnB4	47	2.932	2.944	8.162	0.083	-0.33128	0.200
Cr3PtB4	47	2.921	2.968	8.335	0.086	-0.36613	0.245
Fe3ZnB4	47	2.953	2.851	8.198	0.088	-0.19442	1.364
Fe3IrB4	47	2.949	2.854	8.245	0.091	-0.19070	1.436
Fe3MgB4	47	2.940	2.855	8.675	0.092	-0.21718	1.259
Mn3IrB4	47	2.963	2.966	8.165	0.093	-0.32952	2.219
Mn3PtB4	47	2.976	3.011	8.176	0.094	-0.33546	2.258
Mn3SiB4	47	2.982	2.824	7.826	0.095	-0.31629	0.975
Cr3B5	47	2.922	2.920	7.239	0.095	-0.33817	0.013
Mn3MgB4	47	2.911	2.887	8.683	0.098	-0.30260	0.526
Mn3GaB4	47	2.940	2.838	8.228	0.099	-0.29042	0.791
Cr3NiB4	47	2.936	2.944	7.785	0.099	-0.36333	0.019
Cr3ReB4	47	2.916	2.902	8.358	0.099	-0.37916	0.011
Fe3PtB4	47	2.961	2.888	8.264	0.099	-0.21703	1.450
Fe3Al2B2	65	2.872	2.912	16.537	0.033	-0.393	0.735
Mn3Al2B2	65	2.832	2.853	17.788	0.007	-0.406	0.962
Cr5B2	65	2.881	2.889	16.320	0.044	-0.277	0.006
Cr3Al2B2	65	2.950	2.936	17.311	0.046	-0.326	1.024
Mn3Ir2B2	65	3.012	2.979	17.063	0.050	-0.302	2.731
Mn3Rh2B2	65	3.022	2.981	16.960	0.052	-0.299	2.968
Co3Al2B2	65	2.781	2.931	16.884	0.056	-0.412	0.006
Fe5B2	65	2.854	2.914	16.253	0.057	-0.211	3.519
Ni3Pt2B2	65	2.969	3.077	16.525	0.059	-0.202	0.161
Co3Be2B2	65	2.596	2.894	15.185	0.066	-0.287	0.076
Fe3Be2B2	65	2.624	2.914	15.157	0.067	-0.266	0.879
Mn3Be2B2	65	2.787	2.820	15.315	0.068	-0.321	0.950
Mn3Co2B2	65	2.920	2.915	16.092	0.070	-0.248	3.321
Mn3Si2B2	65	2.808	2.883	16.009	0.071	-0.391	0.022
Co3Pt2B2	65	2.775	3.191	16.604	0.072	-0.195	0.477
Fe3Ir2B2	65	2.883	2.912	17.631	0.074	-0.174	2.108
Cr3V2B2	65	2.921	2.920	16.757	0.080	-0.397	0.002
Cr3W2B2	65	2.980	2.985	17.281	0.082	-0.232	0.004
Ni3Zn2B2	65	2.793	2.965	17.255	0.084	-0.174	0.004
Cr3Re2B2	65	2.945	2.940	17.330	0.084	-0.230	0.260
Mn3Pt2B2	65	2.946	2.940	18.452	0.087	-0.351	2.794
Ni3Al2B2	65	2.831	2.961	16.872	0.087	-0.368	0.000
Cr3Tc2B2	65	2.942	2.932	17.178	0.088	-0.229	0.234
Fe3Co2B2	65	2.859	2.900	16.112	0.088	-0.182	3.101
Cr3Mo2B2	65	2.977	2.976	17.263	0.089	-0.226	0.013
Fe3Zn2B2	65	2.816	2.874	17.849	0.090	-0.156	1.484
Fe3Si2B2	65	2.762	2.914	16.035	0.091	-0.315	0.819
Cr3Mn2B2	65	2.881	2.878	16.063	0.094	-0.240	0.000
Mn3Ga2B2	65	2.830	2.848	18.356	0.095	-0.249	1.111
Fe3Rh2B2	65	2.795	2.841	17.976	0.096	-0.172	2.168
Ni3Be2B2	65	2.615	2.945	15.349	0.100	-0.240	0.001
Fe4BeB4	71	2.821	2.918	17.513	0.000	-0.377	1.017
Fe4AlB4	71	2.870	2.927	18.565	0.000	-0.417	1.271
Mn4BeB4	71	2.878	2.899	17.591	0.000	-0.467	0.878
Fe4MgB4	71	2.875	2.932	19.626	0.000	-0.354	1.391
Cr4AlB4	71	2.939	2.920	18.856	0.000	-0.510	0.000
Mn4AlB4	71	2.889	2.929	18.591	0.000	-0.500	1.014

Ni4ZnB4	71	2.880	2.992	18.517	0.000	-0.261	0.000
Fe4ZnB4	71	2.872	2.931	18.726	0.000	-0.348	1.326
Ni4CuB4	71	2.875	2.992	18.125	0.000	-0.227	0.000
Ni4PtB4	71	2.960	2.995	18.351	0.000	-0.267	0.001
Ni4AuB4	71	2.950	3.012	18.793	0.000	-0.224	0.000
Fe4GaB4	71	2.883	2.939	18.557	0.000	-0.343	1.288
Ni4PdB4	71	2.931	2.996	18.453	0.000	-0.266	0.001
Fe5B4	71	2.880	2.932	18.163	0.001	-0.354	2.135
Ni4CdB4	71	2.914	3.004	19.570	0.001	-0.219	0.001
Fe4IrB4	71	2.887	2.930	18.791	0.003	-0.332	1.530
Cr4BeB4	71	2.919	2.896	17.837	0.003	-0.465	0.002
Mn4IrB4	71	2.966	2.959	18.716	0.005	-0.439	2.004
Fe4NiB4	71	2.878	2.938	17.924	0.007	-0.346	1.453
Fe4PtB4	71	2.914	2.950	18.827	0.009	-0.344	1.565
Ni4AgB4	71	2.904	2.997	19.167	0.009	-0.211	0.000
Cr4SiB4	71	2.925	2.932	18.249	0.010	-0.470	0.000
Mn4FeB4	71	2.929	2.940	18.189	0.013	-0.439	2.237
Ni4BeB4	71	2.828	2.969	17.582	0.013	-0.257	0.000
Mn4CoB4	71	2.932	2.949	18.134	0.013	-0.435	2.246
Cr4ReB4	71	2.922	2.895	19.306	0.014	-0.454	0.001
Ni4LiB4	71	2.812	2.991	19.253	0.015	-0.252	0.000
Co4MgB4	71	2.823	2.994	19.214	0.019	-0.346	0.006
Cr4FeB4	71	2.925	2.914	18.438	0.019	-0.449	0.668
Mn4RhB4	71	2.966	2.962	18.697	0.019	-0.435	2.072
Fe4RhB4	71	2.887	2.933	18.798	0.020	-0.338	1.614
Mn4GaB4	71	2.906	2.946	18.573	0.021	-0.423	1.004
Mn4SiB4	71	2.885	2.974	17.913	0.022	-0.442	1.124
Cr4IrB4	71	2.927	2.895	19.312	0.023	-0.451	0.002
Co4AlB4	71	2.844	2.987	18.182	0.023	-0.387	0.001
Co4BeB4	71	2.787	2.999	17.096	0.024	-0.349	0.006
Cr4TcB4	71	2.924	2.898	19.231	0.024	-0.449	0.000
Fe4SiB4	71	2.869	2.938	17.935	0.025	-0.342	1.253
Ni5B4	71	2.884	2.984	17.819	0.025	-0.251	0.005
Fe4PdB4	71	2.901	2.941	18.845	0.025	-0.327	1.507
Fe4ReB4	71	2.871	2.898	19.036	0.026	-0.322	1.436
Co4ZnB4	71	2.817	3.010	18.275	0.027	-0.338	0.001
Mn4NiB4	71	2.943	2.959	18.024	0.027	-0.428	1.963
Cr4NiB4	71	2.947	2.908	18.228	0.027	-0.445	0.001
Cr5B4	71	2.903	2.905	18.629	0.028	-0.451	0.001
Fe4CoB4	71	2.882	2.933	18.044	0.028	-0.335	1.922
Mn4ReB4	71	2.932	2.947	18.884	0.028	-0.416	1.727
Cr4CoB4	71	2.932	2.912	18.356	0.029	-0.439	0.676
Cr4WB4	71	2.925	2.900	19.518	0.029	-0.439	0.000
Fe4LiB4	71	2.856	2.915	19.111	0.029	-0.306	1.385
Mn4ZnB4	71	2.919	2.918	18.694	0.030	-0.414	1.103
Co4PtB4	71	2.838	3.054	18.233	0.030	-0.339	0.001
Cr4GaB4	71	2.951	2.924	18.875	0.031	-0.437	0.000
Fe4CuB4	71	2.873	2.935	18.316	0.031	-0.304	1.437
Cr4MoB4	71	2.927	2.902	19.483	0.031	-0.442	0.001
Fe4MnB4	71	2.877	2.923	18.396	0.032	-0.351	2.163
Mn4MgB4	71	2.918	2.921	19.595	0.032	-0.412	0.983
Cr4VB4	71	2.916	2.919	18.857	0.033	-0.514	0.001
Mn4PtB4	71	2.989	2.978	18.796	0.034	-0.437	2.074
Fe4TcB4	71	2.875	2.904	18.986	0.036	-0.322	1.485
Cr4RhB4	71	2.930	2.893	19.287	0.036	-0.439	0.002
Cr4OsB4	71	2.923	2.896	19.189	0.038	-0.430	0.002
Cr4MnB4	71	2.906	2.893	18.541	0.038	-0.444	0.181
Fe4RuB4	71	2.882	2.922	18.768	0.038	-0.304	1.528
Mn4RuB4	71	2.956	2.953	18.649	0.039	-0.405	1.897
Cr4RuB4	71	2.924	2.895	19.153	0.039	-0.429	0.003
Mn4OsB4	71	2.953	2.953	18.676	0.040	-0.404	1.867
Fe4CdB4	71	2.882	2.939	20.057	0.041	-0.294	1.418
Fe4OsB4	71	2.879	2.916	18.762	0.042	-0.293	1.410

Cr4ZnB4	71	2.944	2.912	18.995	0.042	-0.426	0.005
Ni4GaB4	71	2.931	3.005	18.282	0.043	-0.218	0.000
Ni4IrB4	71	2.922	2.984	18.389	0.045	-0.217	0.000
Ni4MgB4	71	2.883	2.986	19.384	0.045	-0.274	0.000
Mn4TcB4	71	2.934	2.949	18.842	0.046	-0.411	1.717
Ni4AlB4	71	2.880	2.986	18.490	0.046	-0.273	0.000
Co4NiB4	71	2.804	3.033	17.487	0.046	-0.328	0.024
Fe4AuB4	71	2.903	2.952	19.333	0.047	-0.288	1.461
Co4RhB4	71	2.828	3.015	18.211	0.049	-0.316	0.024
Cr4PtB4	71	2.977	2.900	19.288	0.049	-0.435	0.003
Fe4CaB4	71	2.897	2.947	21.118	0.050	-0.285	1.278
Mn5B4	71	2.922	2.941	18.363	0.051	-0.417	2.127
Fe4MoB4	71	2.861	2.896	19.370	0.052	-0.331	1.380
Co4GaB4	71	2.860	3.006	18.043	0.053	-0.321	0.001
Ni4NaB4	71	2.823	3.024	20.975	0.053	-0.177	0.000
Co4PdB4	71	2.836	3.024	18.360	0.054	-0.319	0.003
Fe4WB4	71	2.864	2.890	19.388	0.057	-0.323	1.387
Co4IrB4	71	2.849	3.006	18.193	0.057	-0.308	0.016
Mn4WB4	71	2.858	2.903	19.560	0.057	-0.403	1.084
Ni4InB4	71	2.958	3.024	19.418	0.057	-0.163	0.000
Mn4PdB4	71	2.976	2.967	18.895	0.060	-0.402	2.017
Cr4ScB4	71	2.964	2.934	20.212	0.061	-0.468	0.007
Mn4ScB4	71	2.923	2.913	20.264	0.062	-0.487	0.981
Fe4InB4	71	2.891	2.947	19.867	0.063	-0.272	1.300
Ni4HgB4	71	2.945	3.018	19.498	0.066	-0.154	0.000
Fe4B5	71	2.839	2.938	16.717	0.066	-0.269	1.046
Fe4AgB4	71	2.882	2.933	19.644	0.066	-0.269	1.419
Ni4RhB4	71	2.904	2.988	18.424	0.067	-0.240	0.001
Mn4MoB4	71	2.861	2.902	19.542	0.068	-0.406	1.064
Mn4TaB4	71	2.878	2.894	19.978	0.068	-0.470	0.955
Fe4NbB4	71	2.863	2.907	19.876	0.068	-0.381	1.298
Co4LiB4	71	2.776	2.984	18.980	0.068	-0.297	0.041
Cr4NbB4	71	2.937	2.907	20.085	0.069	-0.464	0.000
Cr4B5	71	2.917	2.906	17.160	0.070	-0.415	0.003
Co4CuB4	71	2.799	3.026	17.758	0.070	-0.295	0.001
Mn4NbB4	71	2.885	2.894	20.064	0.071	-0.458	0.945
Cr4PdB4	71	2.967	2.907	19.260	0.071	-0.401	0.006
Cr4MgB4	71	2.962	2.920	19.743	0.071	-0.397	0.001
Cr4TaB4	71	2.932	2.908	19.968	0.072	-0.480	0.001
Fe4ScB4	71	2.863	2.937	20.181	0.072	-0.416	1.154
Co5B4	71	2.792	3.032	17.541	0.073	-0.292	0.431
Fe4TaB4	71	2.857	2.907	19.773	0.073	-0.386	1.241
Co4CdB4	71	2.847	3.007	19.419	0.075	-0.290	0.001
Mn4YB4	71	2.954	2.938	21.025	0.075	-0.401	0.958
Mn4CuB4	71	2.932	2.951	18.281	0.075	-0.369	1.615
Cr4TiB4	71	2.937	2.932	19.267	0.075	-0.530	0.002
Mn4B5	71	2.888	2.937	16.811	0.078	-0.379	1.069
Fe4CrB4	71	2.868	2.917	18.422	0.080	-0.309	1.811
Co4AuB4	71	2.860	3.035	18.681	0.080	-0.285	0.003
Cr4CuB4	71	2.944	2.910	18.580	0.082	-0.386	0.037
Mn4VB4	71	2.863	2.931	18.869	0.083	-0.459	1.144
Co4FeB4	71	2.765	3.047	17.871	0.084	-0.290	0.753
Co4ReB4	71	2.811	2.985	18.529	0.084	-0.285	0.000
Fe4YB4	71	2.906	2.965	20.832	0.085	-0.334	1.243
Fe4VB4	71	2.870	2.912	18.813	0.086	-0.374	1.592
Co4CaB4	71	2.837	3.014	20.640	0.087	-0.278	0.245
Fe4GeB4	71	2.903	2.961	18.490	0.088	-0.247	1.372
Mn4CdB4	71	2.915	2.918	20.248	0.088	-0.356	0.926
Mn4AuB4	71	2.973	2.972	19.285	0.089	-0.355	1.781
Ni4FeB4	71	2.874	2.976	18.178	0.090	-0.214	0.633
Mn4CrB4	71	2.897	2.940	18.401	0.090	-0.384	1.619
Co4TcB4	71	2.805	2.993	18.540	0.091	-0.285	0.002
Mn4LiB4	71	2.902	2.904	18.789	0.092	-0.352	0.881

Mn4InB4	71	2.928	2.930	20.097	0.092	-0.352	1.039
Co4RuB4	71	2.830	3.002	18.227	0.093	-0.272	0.003
Co4MnB4	71	2.768	3.024	18.463	0.094	-0.292	0.960
Ni4B5	71	2.962	2.987	16.367	0.096	-0.124	0.000
Cr4AlB6	65	2.943	2.947	21.328	0.012	-0.422	0.003
Cr4BeB6	65	2.925	2.932	20.320	0.020	-0.391	0.013
Cr4SiB6	65	2.924	2.961	20.743	0.043	-0.377	0.018
Mn4BeB6	65	2.853	2.935	20.351	0.044	-0.341	0.912
Mn4AlB6	65	2.869	2.948	21.493	0.055	-0.362	1.071
Cr4IrB6	65	2.930	2.930	21.783	0.060	-0.371	0.008
Cr4GaB6	65	2.955	2.955	21.334	0.062	-0.349	0.003
Cr4ZnB6	65	2.951	2.943	21.439	0.066	-0.345	0.004
Cr4PtB6	65	2.969	2.938	21.766	0.069	-0.370	0.158
Cr4CuB6	65	2.947	2.941	21.072	0.079	-0.332	0.008
Cr4NiB6	65	2.943	2.943	20.747	0.080	-0.365	0.023
Cr4MgB6	65	2.958	2.942	22.329	0.082	-0.339	0.004
Cr4B7	65	2.929	2.938	19.646	0.085	-0.339	0.011
Mn4IrB6	65	2.939	2.960	21.583	0.089	-0.319	1.973
Mn4PtB6	65	2.958	2.965	21.737	0.092	-0.322	2.033
Cr4PdB6	65	2.965	2.940	21.726	0.092	-0.348	0.036
Cr4OsB6	65	2.918	2.932	21.731	0.093	-0.348	0.004
Fe4BeB6	65	2.803	2.970	20.364	0.093	-0.184	1.242
Mn4SiB6	65	2.909	2.964	20.680	0.094	-0.307	1.321
Mn4ZnB6	65	2.893	2.938	21.635	0.094	-0.291	1.085
Mn4GaB6	65	2.884	2.953	21.564	0.097	-0.288	1.153
Cr4FeB6	65	2.930	2.950	20.905	0.099	-0.366	0.726
Mn4MgB6	65	2.897	2.935	22.512	0.099	-0.303	0.996
Cr4AuB6	65	2.961	2.945	22.225	0.100	-0.311	0.011
Cr5B3	140	5.431	5.431	9.923	0.000	-0.418	0.000
Fe5BeB2	140	5.455	5.455	9.914	0.000	-0.292	1.932
Fe5SiB2	140	5.509	5.509	10.299	0.003	-0.359	1.731
Mn5SiB2	140	5.559	5.559	10.293	0.003	-0.415	1.583
Cr5BeB2	140	5.500	5.500	10.002	0.008	-0.313	0.001
Fe5B3	140	5.337	5.337	9.959	0.020	-0.308	1.837
Mn5GeB2	140	5.624	5.624	10.504	0.020	-0.303	1.731
Fe5GeB2	140	5.553	5.553	10.576	0.024	-0.242	1.825
Ni5SiB2	140	5.510	5.510	10.110	0.031	-0.367	0.002
Cr5PB2	140	5.537	5.537	10.317	0.033	-0.474	0.022
Fe5PB2	140	5.444	5.444	10.303	0.033	-0.392	1.705
Mn5PB2	140	5.509	5.509	10.287	0.033	-0.480	1.665
Ni5B3	140	5.191	5.191	10.296	0.036	-0.253	0.000
Mn5B3	140	5.352	5.352	9.990	0.037	-0.391	1.433
Cr5AsB2	140	5.603	5.603	10.619	0.038	-0.292	0.098
Ni5BeB2	140	5.443	5.443	9.757	0.039	-0.299	0.000
Mn5BeB2	140	5.456	5.456	9.916	0.040	-0.309	1.337
Co5GeB2	140	5.545	5.545	10.187	0.040	-0.224	0.462
Co5SiB2	140	5.484	5.484	9.942	0.042	-0.337	0.394
Fe5AsB2	140	5.536	5.536	10.652	0.044	-0.244	1.807
Co5BeB2	140	5.451	5.451	9.487	0.045	-0.238	0.680
Ni5PB2	140	5.412	5.412	10.334	0.045	-0.356	0.000
Ni5AsB2	140	5.514	5.514	10.609	0.054	-0.246	0.001
Ni5GeB2	140	5.559	5.559	10.372	0.055	-0.267	0.001
Ni5GaB2	140	5.568	5.568	10.336	0.056	-0.273	0.000
Cr5SiB2	140	5.586	5.586	10.359	0.061	-0.384	0.023
Fe5GaB2	140	5.583	5.583	10.507	0.062	-0.219	1.885
Ni5LiB2	140	5.598	5.598	9.565	0.065	-0.179	0.000
Co5B3	140	5.169	5.169	10.115	0.070	-0.238	0.549
Co5AsB2	140	5.510	5.510	10.283	0.070	-0.212	0.242
Cr5GeB2	140	5.623	5.623	10.571	0.070	-0.259	0.009
Mn5GaB2	140	5.626	5.626	10.502	0.074	-0.253	1.616
Fe5AlB2	140	5.570	5.570	10.436	0.076	-0.241	1.830

Co5GaB2	140	5.566	5.566	10.095	0.076	-0.201	0.620
Ni5ZnB2	140	5.611	5.611	10.138	0.078	-0.209	0.001
Co5PB2	140	5.279	5.279	10.477	0.080	-0.357	0.409
Cr5CB2	140	5.364	5.364	9.960	0.083	-0.232	0.003
Ni5SnB2	140	5.361	5.361	12.718	0.088	-0.196	0.001
Cr5CoB2	140	5.602	5.602	10.063	0.090	-0.192	0.010
Cr5NiB2	140	5.611	5.611	10.084	0.090	-0.192	0.000
Ni5AlB2	140	5.581	5.581	10.177	0.096	-0.311	0.001
Fe5ZnB2	140	5.605	5.605	10.364	0.098	-0.142	1.996
Ni5InB2	140	5.356	5.356	12.785	0.098	-0.174	0.000
Co5ZnB2	140	5.590	5.590	9.972	0.099	-0.110	0.699
Fe3Al2B2	10	5.685	2.833	8.593	0.000	-0.426	0.523
Fe3Pt2B2	10	6.221	2.829	8.657	0.091	-0.216	2.059
Mn3Al2B2	10	5.745	2.877	8.524	0.003	-0.410	0.420
Co3Be2B2	10	5.264	2.587	8.327	0.004	-0.349	0.050
Co3Mg2B2	10	6.309	2.806	8.722	0.006	-0.232	0.013
Fe3Be2B2	10	5.239	2.705	8.066	0.006	-0.327	0.402
Ni3Li2B2	10	6.234	2.721	8.582	0.011	-0.201	0.000
Co3Zn2B2	10	6.007	2.743	8.472	0.029	-0.224	0.012
Co3Al2B2	10	5.812	2.781	8.555	0.031	-0.437	0.106
Ni3Zn2B2	10	6.009	2.768	8.591	0.037	-0.221	0.000
Mn3Re2B2	10	6.114	2.775	8.533	0.038	-0.279	0.024
Fe3Re2B2	10	6.119	2.737	8.574	0.043	-0.214	0.617
Mn3Be2B2	10	5.268	2.826	7.835	0.043	-0.346	0.003
Cr3Re2B2	10	5.894	2.920	8.735	0.046	-0.268	0.005
Ni3Pt2B2	10	6.056	2.903	8.580	0.048	-0.213	0.002
Cr3Tc2B2	10	5.848	2.918	8.702	0.053	-0.264	0.017
Ni3Be2B2	10	5.386	2.660	8.271	0.057	-0.283	0.000
Fe5B2	10	5.558	2.861	8.483	0.059	-0.210	3.349
Ni3Cu2B2	10	5.779	2.804	8.395	0.065	-0.140	0.000
Co3Y2B2	10	6.735	3.047	9.550	0.067	-0.279	0.020
Cr3Al2B2	10	5.916	2.957	8.384	0.067	-0.305	0.007
Mn3Tc2B2	10	6.055	2.780	8.508	0.069	-0.268	0.029
Fe3Ir2B2	10	6.082	2.827	8.507	0.071	-0.178	1.851
Cr3Os2B2	10	5.976	2.883	8.588	0.071	-0.243	0.004
Fe3Tc2B2	10	6.078	2.734	8.532	0.071	-0.211	0.616
Cr5B2	10	5.553	2.883	8.553	0.076	-0.245	0.006
Cr3Ru2B2	10	5.951	2.880	8.532	0.078	-0.236	0.002
Fe3Mo2B2	10	6.285	2.700	8.604	0.078	-0.208	0.046
Fe3Zn2B2	10	6.030	2.803	8.425	0.079	-0.167	1.130
Ni3Mg2B2	10	6.276	2.870	8.855	0.079	-0.254	0.001
Ni3Pd2B2	10	6.002	2.902	8.572	0.083	-0.193	0.000
Fe3W2B2	10	6.276	2.703	8.640	0.083	-0.197	0.066
Fe3Rh2B2	10	6.023	2.848	8.521	0.084	-0.184	2.233
Fe3Co2B2	10	5.589	2.824	8.345	0.084	-0.186	2.794
Cr3Mn2B2	10	5.594	2.848	8.356	0.085	-0.249	0.011
Ni3Al2B2	10	5.848	2.817	8.626	0.085	-0.370	0.001
Cr3Ir2B2	10	6.216	2.816	8.544	0.088	-0.303	0.046
Mn3Ir2B2	10	6.090	2.843	8.545	0.089	-0.263	1.391
Co3Pt2B2	10	6.134	2.815	8.587	0.091	-0.176	0.663
Mn3Co2B2	10	5.534	2.935	8.434	0.091	-0.227	3.310
Co3Tc2B2	10	6.087	2.690	8.602	0.092	-0.172	0.281
Mn3Os2B2	10	6.077	2.758	8.549	0.095	-0.221	0.211
Cr3W2B2	10	5.891	2.969	8.866	0.096	-0.218	0.009
Cr3Mo2B2	10	5.861	2.968	8.869	0.096	-0.219	0.007
Mn3Si2B2	10	5.398	2.818	8.550	0.096	-0.366	0.016
Co3Rh2B2	10	5.987	2.786	8.542	0.097	-0.139	1.060
Co3Fe2B2	10	5.629	2.705	8.674	0.098	-0.160	2.565
Mn3Rh2B2	10	6.029	2.914	8.477	0.098	-0.242	2.156
Co3Re2B2	10	6.106	2.724	8.587	0.098	-0.159	0.032
Co5B2	10	5.633	2.629	8.641	0.099	-0.136	1.905

Co4Be3B2	123	7.586	7.586	2.586	0.000	-0.395	0.001
Fe4Al3B2	123	8.083	8.083	2.791	0.000	-0.411	0.001
Ni4Li3B2	123	8.049	8.049	2.734	0.000	-0.203	0.000
Fe4Be3B2	123	7.487	7.487	2.697	0.028	-0.287	0.530
Fe7B2	123	7.917	7.917	2.875	0.037	-0.171	3.606
Co4Zn3B2	123	8.273	8.273	2.679	0.042	-0.162	0.003
Ni4Be3B2	123	7.643	7.643	2.649	0.049	-0.320	0.001
Mn4V3B2	123	8.067	8.067	2.850	0.063	-0.384	0.198
Co4Al3B2	123	8.181	8.181	2.736	0.063	-0.437	0.420
Mn4Cr3B2	123	7.948	7.948	2.786	0.072	-0.197	0.250
Ni4Zn3B2	123	8.398	8.398	2.687	0.074	-0.187	0.000
Co4Fe3B2	123	8.118	8.118	2.640	0.075	-0.145	2.677
Co4Mg3B2	123	8.486	8.486	2.791	0.075	-0.112	0.001
Mn4Al3B2	123	8.250	8.250	2.823	0.075	-0.306	1.181
Co7B2	123	8.146	8.146	2.571	0.075	-0.107	2.106
Ni4Cu3B2	123	8.282	8.282	2.614	0.085	-0.111	0.000
Cr7B2	123	7.963	7.963	2.890	0.086	-0.163	0.020
Ni4Pt3B2	123	8.479	8.479	2.838	0.087	-0.138	0.002
Fe4Co3B2	123	7.855	7.855	2.851	0.088	-0.136	3.111
Mn7B2	123	7.937	7.937	2.764	0.089	-0.180	1.288
Ni7B2	123	7.482	7.482	3.099	0.091	-0.146	0.007

Table S2.: Comparing the current MAB results with previous predicted results from Ref. [174]

Compounds	Space Group	Lattice Constant (Å)			Convex Hull (eV/atom)	Source
		a	b	c		
CrAlB	63	2.969	3.004	13.881	0.011	This work
		2.969	3.003	13.889	0.008	Ref. [174]
MnAlB	63	2.988	2.953	13.908	0.066	This work
		2.989	2.955	13.859	0.065	Ref. [174]
Cr2AlB2	65	2.932	2.924	11.051	0	This work
		2.934	2.924	11.051	0	Ref. [174]
Mn2AlB2	65	2.831	2.894	11.080	0	This work
		2.831	2.896	11.074	0	Ref. [174]
Fe2AlB2	65	2.851	2.916	11.019	0	This work
		2.853	2.917	11.024	0	Ref. [174]
Cr3Al2B2	65	2.950	2.936	17.311	0.046	This work
		2.951	2.936	17.313	0.038	Ref. [174]
Mn3Al2B2	65	2.832	2.853	17.788	0.007	This work
		2.833	2.851	17.863	0.004	Ref. [174]
Fe3Al2B2	65	2.872	2.912	16.537	0.033	This work
		2.875	2.913	16.536	0	Ref. [174]
Ni3Al2B2	65	2.831	2.961	16.872	0.087	This work
		2.840	2.962	16.926	0.084	Ref. [174]
Cr3AlB4	47	2.939	2.939	8.091	0	This work
		2.939	2.939	8.088	0	Ref. [174]
Mn3AlB4	47	2.937	2.834	8.164	0.038	This work
		2.937	2.835	8.153	0.036	Ref. [174]
Fe3AlB4	47	2.961	2.818	8.149	0.065	This work
		2.960	2.819	8.144	0.063	Ref. [174]
Cr4AlB6	65	2.943	2.947	21.328	0.012	This work
		2.944	2.947	21.325	0.008	Ref. [174]

Here, we found that there are two kind of AFM structures (interlayer and intralayer) existing in 212-type MAB phase, as shown in Figure S2.
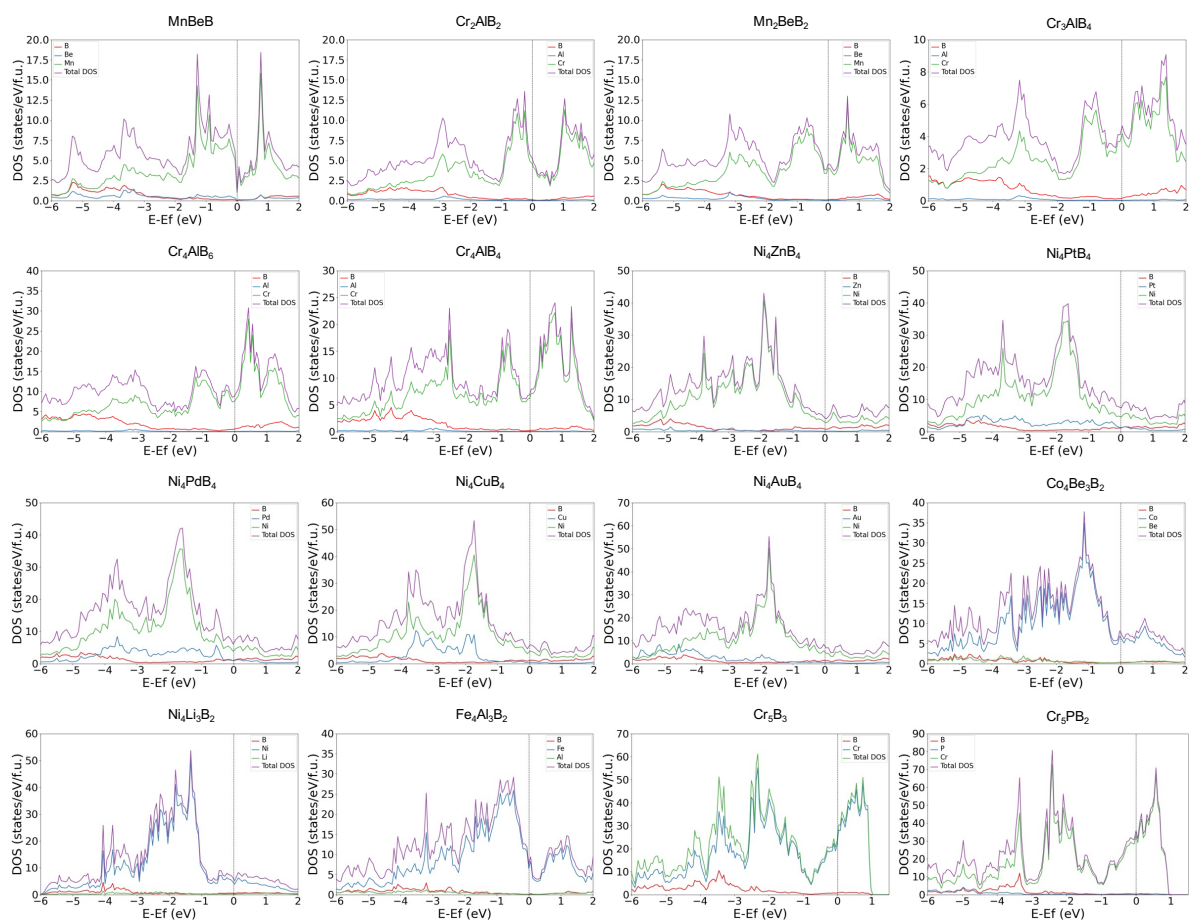
Figure S1.: Density of states of predicted non-magnetic MAB phases.
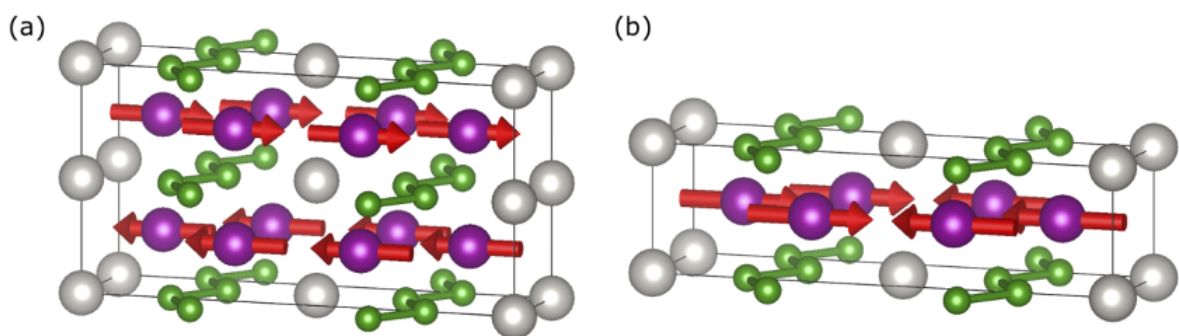
Figure S2.: Antiferromagnetic structure of 212-type MAB (a) intralyer: the antiferromagnetic direction exists in two layers; (b) interlayer: the antiferromagnetic direction exists in single layer. The red arrow presents magnetic direction.

Table S3.: The magnetic ground state of stable 212-MAB phases.

Compounds	AFM-1(interlayer)	AFM-2 (intralayer)	FM	NM
Co2AlB2	-65.88683765	-65.88739406	-65.89295922	-65.88713772
Fe2BeB2	-70.64633821	-70.819765	-70.70739773	-70.62268063
Mn2BeB2	-74.58037508	-74.580124	-74.58040138	-74.58040414
Fe2AlB2	-71.13230669	-71.09418939	-71.22404215	-70.89307686
Mn2AlB2	-74.8532619	-74.98085613	-74.88387864	-74.84775026
Cr2AlB2	-76.85518352	-76.86093353	-76.85519078	-76.86519042
Cr2SiB2	-79.71707885	-79.7170405	-79.71708159	-79.71708801
Cr2BeB2	-76.13809946	-76.13763057	-76.13897144	-76.13825155
Cr2ReB2	-93.44839084	-93.44947192	-93.4483936	-93.4484053
Fe2MgB2	-65.35932093	-65.487255	-65.40892677	-65.22253462
Co2BeB2	-65.46095924	-65.46052103	-65.46096941	-65.46096508
Cr2TcB2	-89.32741701	-89.32863	-89.32741413	-89.32742021
Mn2IrB2	-84.04569417	-83.71480308	-83.93695103	-83.29687721
Fe2ZnB2	-64.29285113	-64.3351	-64.4243543	-64.06986852
Cr2IrB2	-86.19893738	-86.19928	-86.19893654	-86.19894242
Ni2LiB2	-54.27823214	-54.277735	-54.27824987	-54.27825027
Ni2PtB2	-62.98827476	-62.98661738	-62.98827225	-62.98825967
Cr2FeB2	-84.74945681	-84.74946883	-84.77690838	-84.2112152
Fe2IrB2	-79.92897498	-79.74748988	-79.79422707	-79.42577378
Ni2CuB2	-57.44034817	-57.43990365	-57.44036768	-57.44036423
Ni2ZnB2	-52.56202703	-52.56513507	-52.56201213	-52.56202985
Cr3B2	-87.43351322	-87.43396514	-87.43798357	-87.43751847
Fe2PtB2	-74.70423426	-74.62013806	-74.59938047	-74.22282814
Cr2WB2	-94.30228641	-94.29669283	-94.30228909	-94.30228437
Co2MgB2	-60.52900881	-60.52999946	-60.52899462	-60.52898785
Cr2MoB2	-90.20335062	-90.19891642	-90.20335146	-90.20335561
Mn2CoB2	-79.69489999	-79.35527983	-80.1317531	-78.96686236
Mn2FeB2	-81.85999957	-81.93613345	-82.61290818	-81.17754211
Mn2RhB2	-80.76741383	-80.42217598	-80.70689175	-80.09631274
Fe3B2	-78.20603462	-77.97281357	-78.85399875	-77.44795282
Cr2RuB2	-86.69911492	-86.70007	-86.69911455	-86.69911566
Cr2OsB2	-90.66864023	-90.668995	-90.66864015	-90.66865212
Mn2PtB2	-78.79303215	-78.45515068	-78.58993224	-77.82327552
Fe2GaB2	-67.88642365	-67.75845476	-67.92364477	-67.62770421
Ni2BeB2	-58.26200763	-58.26036285	-58.26200875	-58.2619976
Ni2PdB2	-61.07432402	-61.0729872	-61.07429402	-61.0742564
Mn2SiB2	-77.09190803	-77.26047303	-77.09190222	-77.09192171
Mn2ReB2	-90.6081387	-90.7066324	-90.74289642	-90.60827896
Cr2RhB2	-82.79945631	-82.799195	-82.79944198	-82.79945691
Cr2VB2	-87.46225672	-87.46198938	-87.46225834	-87.46226062
Ni2AuB2	-56.23165208	-56.22294795	-56.2316556	-56.23166659
Cr2CoB2	-82.01197093	-82.01197657	-82.16236059	-81.79494385
Cr2NiB2	-79.102105	-79.10211	-79.10212617	-79.10191962
Co2PtB2	-69.63778263	-69.65924301	-69.63859647	-69.63785776
Cr2MnB2	-86.38774777	-86.389125	-86.28089684	-86.28099021
Fe2ReB2	-86.89963676	-86.69655193	-86.90407834	-86.44485698
Fe2NiB2	-73.2030513	-73.05261169	-73.10598643	-72.71702075
Mn2ScB2	-79.49799809	-79.47839842	-79.51282108	-79.48712127
Cr2PtB2	-80.49575377	-80.496715	-80.49590885	-80.49575249
Fe2RhB2	-76.83798018	-76.64636958	-76.77048282	-76.27060534
Mn2RuB2	-84.07773177	-84.02944525	-84.24640701	-83.72690734
Mn2NiB2	-77.03817855	-76.59623733	-76.85380813	-76.52395167
Mn2WB2	-92.01502458	-92.015225	-92.01504492	-92.01504981
Mn2TcB2	-86.50318745	-86.60635618	-86.64415689	-86.50455953

194
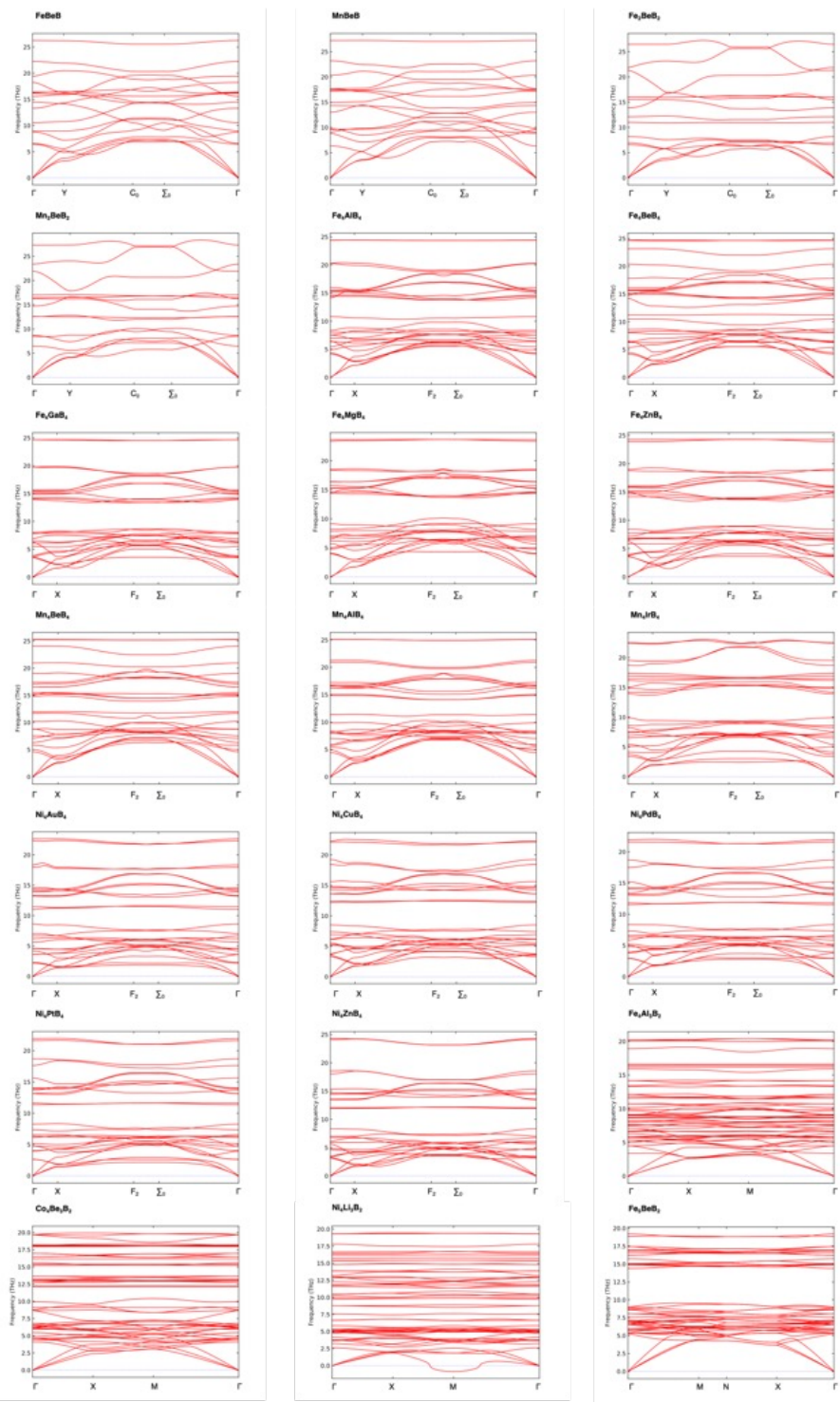
Figure S3.: Phonon bands of unreported MAB and non-MAB phases.
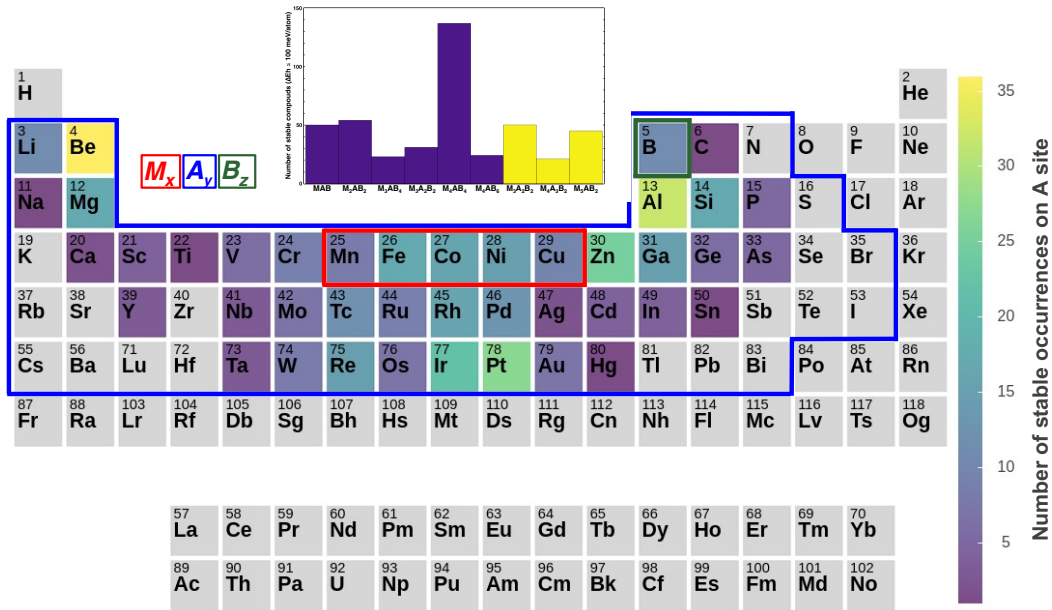
Figure S4.: Elements are color-coded as a function of the number of stable compounds with the respective element on the A sites. (Above) Histogram representation of number of stable compounds of different systems calculated in this work, purple bar means MAB phases and yellow bar means non-MAB phases.

Table S4.: The novel MAB and non-MAB phases with $|K_{i-j}| > 1$ MJ/m^3.

Compounds	Space Group	MAE (MJ/m^3)			Magnetic moment (μB/f.u)	Magnetic density (emu/cm^3)
		$K_{001-100}$	$K_{001-010}$	$K_{010-100}$		
CoCrB	63	-1.884	-1.884	0.000	5.514	462.330
Fe2B	63	2.230	1.865	0.365	16.310	1.352.627
FeIrB	63	-2.627	-1.258	-1.369	5.805	436.918
FeNiB	63	0.834	-0.654	1.488	7.909	672.329
FePtB	63	-3.421	7.225	-10.646	7.550	542.026
FeRhB	63	2.528	0.309	2.220	7.409	561.255
FeZnB	63	0.300	-1.997	2.297	4.602	351.641
CoMnB	63	1.292	1.743	-0.451	14.160	1.174.969
MnIrB	63	4.135	8.049	-3.914	7.967	584.998
MnNiB	63	1.245	1.767	-0.521	9.792	811.435
MnPdB	63	0.790	1.592	-0.802	9.739	688.735
MnPtB	63	9.126	11.969	-2.843	9.763	683.691
MnRhB	63	2.863	4.016	-1.153	8.943	661.411
Co2PtB2	65	-2.412	-3.102	0.690	1.228	119.739
Fe2AlB2	65	-1.110	0.031	-1.141	5.319	538.463
Fe2BeB2	65	-1.917	-0.047	-1.869	3.043	355.462
Fe3B2	65	0.245	1.666	-1.421	11.596	1.209.796
Fe2GaB2	65	-1.122	0.096	-1.218	5.439	541.505
Fe2IrB2	65	5.056	7.245	-2.190	6.736	661.715
Fe2MgB2	65	-2.438	0.470	-2.908	3.640	340.502
Fe2NiB2	65	-2.443	0.010	-2.453	6.147	652.780
Fe2PtB2	65	-3.924	1.211	-5.135	6.392	611.442
Fe2ReB2	65	-4.958	-8.999	4.042	5.541	548.443

Fe2RhB2	65	0.619	1.838	-1.219	7.597	748.423
Fe2ZnB2	65	-1.919	0.636	-2.555	4.183	419.456
Mn2CoB2	65	1.981	1.756	0.225	10.868	1.124.732
Mn2FeB2	65	1.446	1.565	-0.119	11.320	1.165.646
Mn2IrB2	65	1.803	-2.559	4.362	8.270	789.006
Mn2NiB2	65	1.407	0.101	1.305	8.382	869.483
Mn2PtB2	65	20.271	20.271	0.000	9.414	869.433
Mn2ReB2	65	-8.247	-2.133	-6.114	6.589	635.442
Mn2RhB2	65	1.609	1.609	0.000	8.678	833.085
Mn2TcB2	65	-1.424	-0.811	-0.613	6.417	622.289
Fe3BeB4	47	-1.672	0	1.672	3.594	532.907
Fe3IrB4	47	1.021	-5.786	-6.807	4.307	575.519
Fe3MgB4	47	-1.054	-0.099	0.954	3.778	481.034
Fe3PtB4	47	-1.921	7.214	9.134	4.350	570.827
Fe3ZnB4	47	-1.324	-0.056	1.269	4.093	550.002
Mn3IrB4	47	0.965	-3.888	-4.853	6.657	860.514
Mn3PtB4	47	-3.324	-8.892	-5.568	6.773	857.270
Mn4AlB6	65	-1.123	-1.123	0.000	8.566	436.975
Mn4GaB6	65	-1.004	0.010	-1.014	9.221	465.665
Mn4IrB6	65	3.816	3.768	0.047	15.786	779.608
Mn4PtB6	65	6.258	4.738	1.519	16.260	790.929
Mn4ZnB6	65	-0.892	0.149	-1.041	8.680	437.764
Co3Pt2B2	65	-2.429	-1.745	-0.685	2.864	180.640
Co3Pt2B2	65	-2.429	-1.745	-0.685	2.864	180.640
Fe3Al2B2	65	-1.420	0.066	-1.487	4.410	295.705
Fe3Be2B2	65	-2.012	-2.012	0.000	5.274	421.961
Fe3Co2B2	65	-0.159	1.158	-1.317	18.609	1.291.798
Fe5B2	65	0.774	1.528	-0.754	21.114	1.448.993
Fe3Ir2B2	65	8.212	6.782	1.430	12.651	792.503
Fe3Rh2B2	65	0.131	1.027	-0.896	13.009	845.070
Fe3Zn2B2	65	-3.001	-1.361	-1.640	8.907	571.752
Mn3Al2B2	65	-0.197	0.950	-1.148	5.771	372.455
Mn3Co2B2	65	1.788	1.666	0.122	19.929	1.348.995
Mn3Ir2B2	65	-10.171	-7.582	-2.589	16.385	992.463
Mn3Pt2B2	65	6.415	4.767	1.648	16.765	972.699
Mn4PtB4	71	11.948	-1.550	13.498	16.588	919.450
Fe4OsB4	71	4.573	-3.677	8.251	11.281	664.139
Fe4IrB4	71	7.789	4.471	3.318	12.238	714.201
Fe4ReB4	71	-7.417	-1.875	-5.543	11.486	672.519
Fe4TaB4	71	1.785	6.706	-4.921	9.930	560.842
Co4IrB4	71	-6.061	-3.840	-2.221	0.129	7.657
Mn4IrB4	71	-5.757	-3.647	-2.109	16.027	905.022
Mn4ReB4	71	0.411	4.484	-4.073	13.815	785.087
Mn4OsB4	71	-3.608	-0.049	-3.560	14.938	850.492
Fe4AuB4	71	0.570	3.051	-2.481	11.687	654.290
Fe4WB4	71	2.543	2.647	-0.103	11.096	641.107
Fe4AgB4	71	0.927	2.465	-1.538	11.353	633.953
Fe4PdB4	71	0.098	2.453	-2.355	12.053	695.196
Fe4TcB4	71	-0.746	1.474	-2.220	11.881	695.087
Fe4ZnB4	71	0.311	2.213	-1.902	10.608	624.239
Fe4CuB4	71	0.375	2.059	-1.684	11.498	690.269
Fe4NbB4	71	0.528	2.038	-1.511	10.379	581.800
Fe4CdB4	71	1.125	2.030	-0.905	11.340	619.058
Fe4RuB4	71	1.976	1.591	0.385	12.221	717.097
Fe4B5	71	-0.741	1.231	-1.973	8.371	556.735
Fe4MgB4	71	1.086	1.942	-0.856	11.129	623.970
Fe4MoB4	71	0.857	1.809	-0.952	11.036	637.712
Co4FeB4	71	1.379	-0.420	1.799	6.020	370.788
Fe4NiB4	71	0.243	1.776	-1.533	11.622	711.144
Fe4LiB4	71	0.710	1.774	-1.064	11.077	645.627
Mn4CoB4	71	1.568	-0.188	1.756	17.969	1.062.915
Mn4AuB4	71	1.749	0.153	1.596	14.244	775.212
Fe4VB4	71	-0.111	1.511	-1.622	12.732	750.986

Fe4CrB4	71	0.151	1.591	-1.439	14.488	871.794
Fe4RhB4	71	1.582	1.526	0.056	12.909	752.215
Co4MnB4	71	1.562	0.209	1.353	7.677	460.624
Fe4InB4	71	0.156	1.560	-1.404	10.395	569.677
Fe5B4	71	1.017	1.497	-0.480	17.079	1.032.848
Mn4FeB4	71	1.491	0.226	1.265	17.898	1.059.765
Mn4PdB4	71	1.202	-0.237	1.439	16.137	8.971.075
Fe4BeB4	71	-0.182	1.253	-1.435	8.133	523.344
Fe4MnB4	71	0.982	1.326	-0.344	17.299	1.036.999
Fe4GaB4	71	0.170	1.235	-1.065	10.306	607.816
Fe4CoB4	71	0.792	1.209	-0.416	15.379	934.922
Fe4GeB4	71	0.029	1.182	-1.153	10.975	640.336
Fe4AlB4	71	0.063	1.153	-1.090	10.166	604.617
Mn4VB4	71	0.513	-0.616	1.130	9.149	535.797
Mn5B4	71	1.090	0.352	0.738	17.017	999.941
Mn4RhB4	71	0.335	-0.685	1.019	16.572	935.596
Fe4YB4	71	0.575	1.014	-0.438	9.945	513.817
Co5BeB2	140	1.810	1.810	0	13.608	447.646
Co5ZnB2	140	1.689	1.689	0	13.972	415.771
Fe5ZnB2	140	1.889	1.889	0	39.919	1.136.984
Co3Fe2B2	10	1.072	0.000	-1.072	15.387	1.080.426
Co3Pt2B2	10	4.492	1.922	-2.570	3.979	249.501
Fe3Ir2B2	10	3.395	7.741	4.346	11.105	706.387
Fe3Pt2B2	10	4.931	2.545	-2.386	12.353	755.315
Fe3Rh2B2	10	-0.115	1.043	1.157	13.396	852.345
Fe3Zn2B2	10	-1.503	-0.368	1.135	6.781	443.081
Mn3Co2B2	10	1.210	0.628	-0.582	19.858	1.342.777
Mn3Ir2B2	10	5.313	0.000	-5.313	8.346	525.648
Mn3Rh2B2	10	-0.846	-1.380	-0.533	12.938	807.529
Co4Fe3B2	123	1.156	1.156	0.000	21.417	1.141.436

Table S5.: The novel MAB and non-MAB phases with uniaxial MAE.

Compounds	Space Group		MAE (MJ/m^3)		
			$K_{001-100}$	$K_{001-010}$	$K_{010-100}$
CoCrB	63	Out-of-plane	-1.884	-1.884	0.000
FeIrB	63	Out-of-plane	-2.627	-1.258	-1.369
MnPtB	63	In-plane	9.126	11.969	-2.843
MnRhB	63	In-plane	2.863	4.016	-1.153
Fe2B	63	In-plane	2.230	1.865	0.365
CoMnB	63	In-plane	1.292	1.743	-0.451
MnNiB	63	In-plane	1.245	1.767	-0.521
Co2PtB2	65	Out-of-plane	-2.412	-3.102	0.690
Fe2ReB2	65	Out-of-plane	-4.958	-8.999	4.042
Mn2CoB2	65	In-plane	1.981	1.756	0.225
Mn2RhB2	65	In-plane	1.609	1.609	0.000
Mn2FeB2	65	In-plane	1.446	1.565	-0.119
Cr2CoB2	65	In-plane	0.697	0.697	0.000
Cr2FeB2	65	In-plane	0.446	0.446	0.000
Ni3Pt2B2	65	Out-of-plane	-0.467	-0.467	0.000
Fe3Be2B2	65	Out-of-plane	-2.012	-2.012	0.000
Co3Pt2B2	65	Out-of-plane	-2.429	-1.745	-0.685
Fe3Zn2B2	65	Out-of-plane	-3.001	-1.361	-1.640
Mn3Ir2B2	65	Out-of-plane	-10.171	-7.582	-2.589
Fe3Ir2B2	65	In-plane	8.212	6.782	1.430
Mn3Pt2B2	65	In-plane	6.415	4.767	1.648
Mn3Co2B2	65	In-plane	1.788	1.666	0.122
Fe3MgB4	47	Out-of-plane	-1.054	-0.099	0.954
Fe4PtB4	71	Out-of-plane	-0.442	-0.557	0.115
Ni4CoB4	71	Out-of-plane	-0.502	-0.801	0.299
Fe4ReB4	71	Out-of-plane	-7.417	-5.543	-1.875

Mn4PtB4	71	In-plane	11.948	13.498	-1.550
Mn4AuB4	71	In-plane	1.749	1.596	0.153
Mn4CoB4	71	In-plane	1.568	1.756	-0.188
Co4MnB4	71	In-plane	1.562	1.353	0.209
Mn4FeB4	71	In-plane	1.491	1.265	0.226
Co4FeB4	71	In-plane	1.379	1.799	-0.420
Mn4PdB4	71	In-plane	1.202	1.439	-0.237
Mn4PB4	71	In-plane	0.975	0.924	0.051
Co4CrB4	71	In-plane	0.890	1.015	-0.125
Mn4GeB4	71	In-plane	0.788	0.742	0.046
Mn4NiB4	71	In-plane	0.769	0.928	-0.159
Mn4TiB4	71	In-plane	0.731	0.590	0.141
Mn4SiB4	71	In-plane	0.679	0.694	-0.015
Mn4AlB4	71	In-plane	0.556	0.500	0.055
Mn4NbB4	71	In-plane	0.482	0.491	-0.009
Mn4GaB4	71	In-plane	0.461	0.609	-0.148
Mn4HgB4	71	In-plane	0.429	0.510	-0.081
Mn4ZrB4	71	In-plane	0.415	0.256	0.158
Mn4MgB6	65	Out-of-plane	-0.768	-0.768	0.000
Mn4AlB6	65	Out-of-plane	-1.123	-1.123	0.000
Fe4BeB6	65	Out-of-plane	-0.745	-0.745	0.000
Mn4IrB6	65	In-plane	3.816	3.768	0.047
Mn4PtB6	65	In-plane	6.258	4.738	1.519
Fe5PB2	140	Out-of-plane	-0.634	-0.634	0.000
Co5AsB2	140	In-plane	0.486	0.486	0.000
Fe5AlB2	140	In-plane	0.475	0.475	0.000
Mn5BeB2	140	In-plane	0.559	0.559	0.000
Co5PB2	140	In-plane	0.665	0.665	0.000
Co5GaB2	140	In-plane	0.642	0.642	0.000
Co5B3	140	In-plane	0.762	0.762	0.000
Co5GeB2	140	In-plane	0.755	0.755	0.000
Mn5GaB2	140	In-plane	0.783	0.783	0.000
Fe5BeB2	140	In-plane	0.898	0.898	0.000
Co5BeB2	140	In-plane	1.810	1.810	0.000
Co5ZnB2	140	In-plane	1.689	1.689	0.000
Fe5ZnB2	140	In-plane	1.889	1.889	0.000
Fe3Tc2B2	10	Out-of-plane	-0.581	0.162	0.742
Co5B2	10	Out-of-plane	-0.595	-0.684	-0.089
Mn3Rh2B2	10	Out-of-plane	-0.846	-1.380	-0.533
Fe3Al2B2	10	Out-of-plane	-0.971	0.025	0.996
Fe3Zn2B2	10	Out-of-plane	-1.503	-0.368	1.135
Fe3Pt2B2	10	In-plane	4.931	2.545	-2.386
Co3Pt2B2	10	In-plane	4.492	1.922	-2.570
Fe3Ir2B2	10	In-plane	3.395	7.741	4.346
Mn3Co2B2	10	In-plane	1.210	0.628	-0.582
Fe5B2	10	In-plane	0.408	0.482	0.074
Fe7B2	123	Out-of-plane	-0.681	-0.681	0.000
Co4Fe3B2	123	In-plane	1.156	1.156	0.000
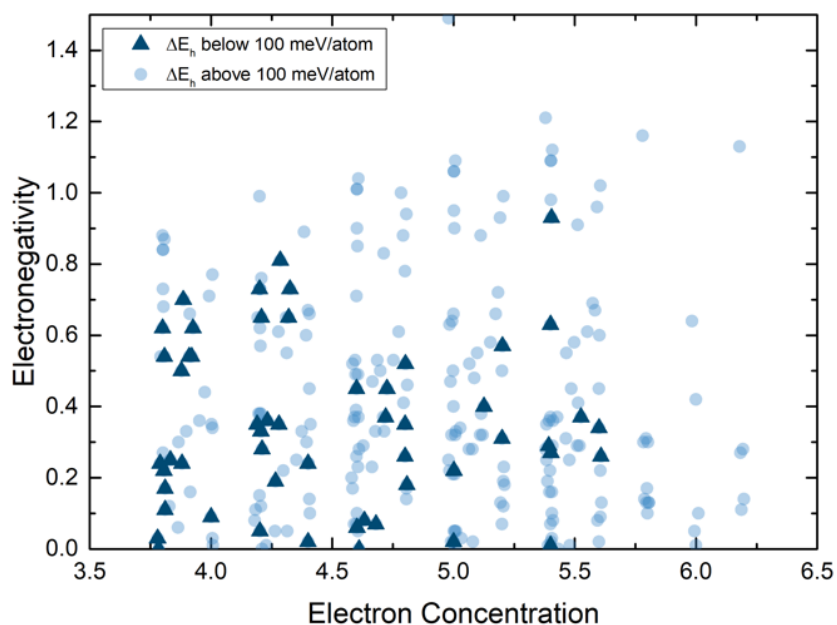
Figure S5.: The stability map of 212-MAB phases according to the feature factors electronegativity and electron concentration (circle symbols represent unstable phases in the present work; triangle symbols represent possible stable phases with convex hull distance below 100 meV/atom in the present).
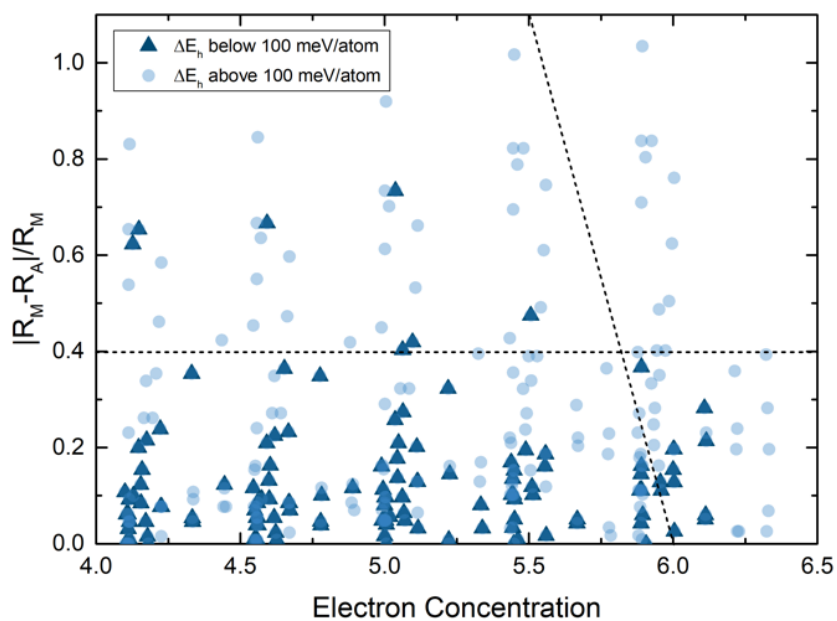
Figure S6.: The stability map of 414-MAB phases (the meaning of symbols is same as above Figure).

Table S6.: The MAE and E_{SOC} for the FeXB (where X are Ni, Pd, and Pt).

		FeNiB	FePdB	FePtB
MAE (meV/f.u.)	[100]-[001]	-0.028	0.002	0.579
	[100]-[010]	-0.128	0.181	2.106
	[001]-[010]	-0.100	0.179	1.526
E_{SOC} (Fe) (meV/atom)	[100]	-10.660	-10.443	-6.934
	[001]	-10.391	-10.230	-6.787
	[010]	-10.167	-10.026	-7.424
ΔE_{SOC} (Fe) (meV/atom)	[100]-[001]	-0.269	-0.213	-0.147
	[100]-[010]	-0.492	-0.417	0.490
	[001]-[010]	-0.223	-0.204	0.637
E_{SOC} (X) (meV/atom)	[100]	-18.892	-338.919	-4223.153
	[001]	-18.918	-339.122	-4224.317
	[010]	-18.799	-339.621	-4225.756
ΔE_{SOC} (X) (meV/atom)	[100]-[001]	0.026	0.203	1.164
	[100]-[010]	-0.093	0.702	2.603
	[001]-[010]	-0.119	0.499	1.439
E_{SOC} (FeXB) (meV/f.u.)	[100]	-29.569	-349.380	-4230.111
	[001]	-29.326	-349.369	-4231.125
	[010]	-28.983	-349.665	-4233.204
ΔE_{SOC} (FeXB) (meV/f.u.)	[100]-[001]	-0.243	-0.011	1.014
	[100]-[010]	-0.586	0.284	3.092
	[001]-[010]	-0.343	0.296	2.078
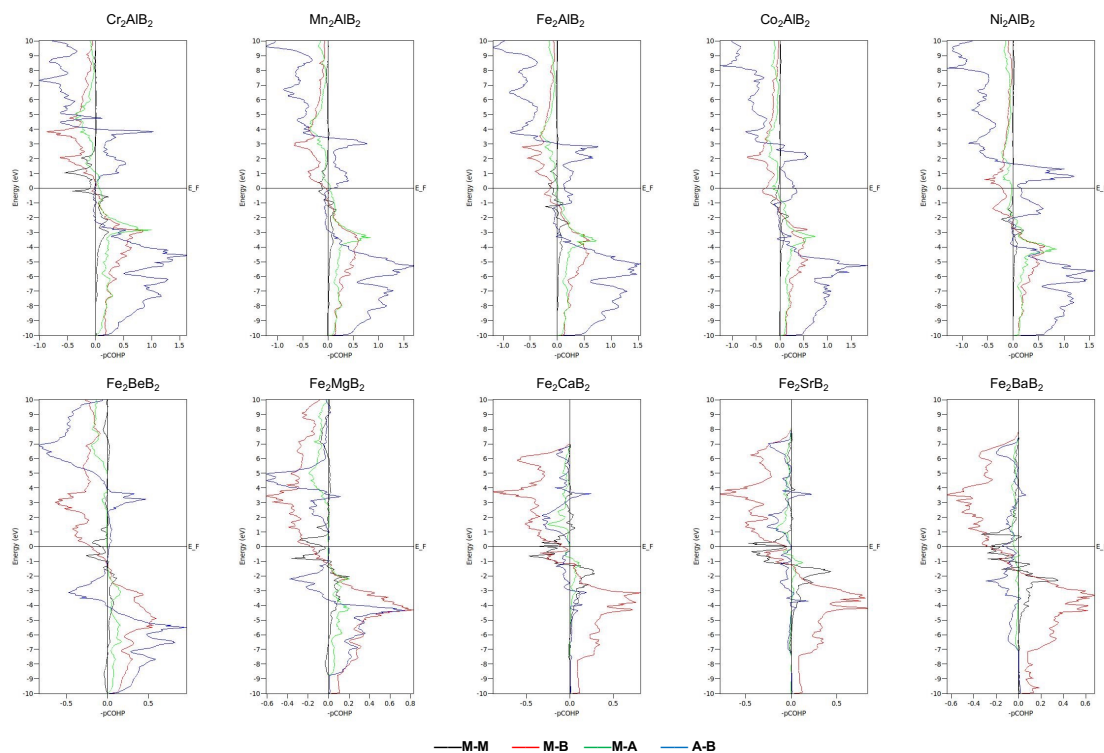
Figure S7.: The COHP results of (upper) M_2AlB_2 (where **M** are Cr, Mn, Fe, Co and Ni) and (bottom) Fe_2AB_2 (where **A** are Be, Mg, Ca, Sr and Ba).
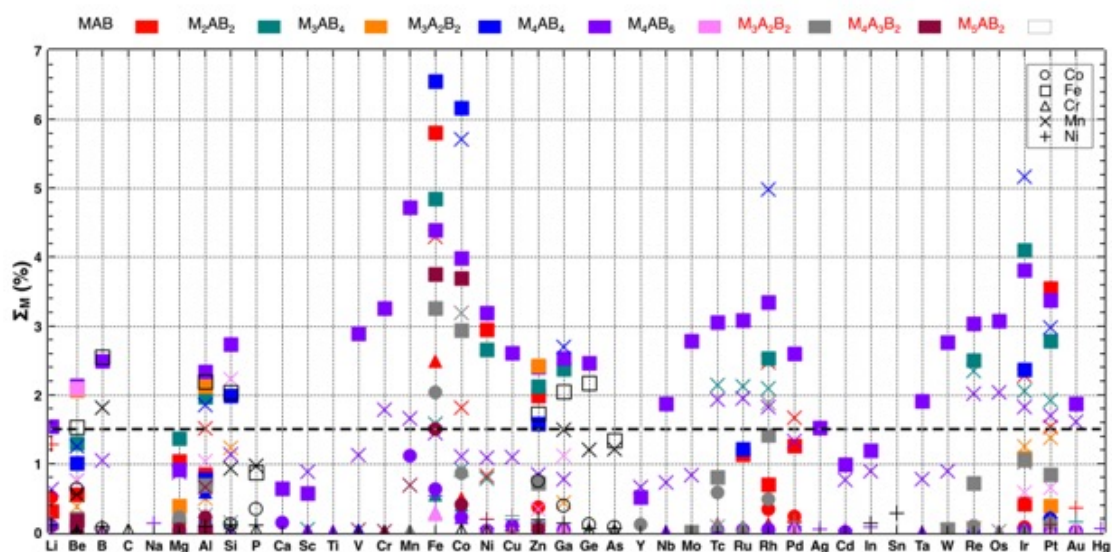
Figure S8.: The calculated $\sum_M$ for all 434 compounds with convex hull tolerance of ΔE_h meV/atom. Different structures were presented with different color in the square above the figure. Magnetic elements were shown in different symbols. The black bold dash line indicates $\sum_M > 1.5\%$; candidates above this line are predicted to show large ΔS_M values.

A. Supporting Information for Fe-Sn

The thermodynamic database of the meta-stable Fe-Sn system is listed as follows:

```
$————THERMODYNAMICAL AND TOPOLOGICAL PROPERTIES OF MATA–STABLE FE3SN————
$ Chen Shen, Ilias Samathrakis, Kun Hu, Harish K. Singh, Nuno Fortunato,
Huashan Liu, Oliver Gutfleisch and Hongbin Zhang
$ —————————————————FE–SN.TDB—————————————————————————————

 TYPE_DEFINITION % SEQ *!
 DEFINE_SYSTEM_DEFAULT ELEMENT 2 !
 DEFAULT_COMMAND DEF_SYS_ELEMENT VA /− !

$—————————————————————————————————————————————————————————
 ELEMENT /−    ELECTRON_GAS              0.0000E+00  0.0000E+00  0.0000E+00!
 ELEMENT VA    VACUUM                    0.0000E+00  0.0000E+00  0.0000E+00!
 ELEMENT FE    BCC_A2                    5.5847E+01  4.4890E+03  2.7280E+01!
 ELEMENT SN    BCT_A5                    1.1871E+02  6.3220E+03  5.1195E+01!

$—————————————————————————————————————————————————————————
$ FUNCTION FE
$—————————————————————————————————————————————————————————
 FUNCTION GHSERFE  298.15
    1225.7+124.134*T−23.5143*T*LN(T)−4.39752E−3*T**2−0.058927E−6*T**3
    +77359*T**(−1); 1811 Y
    −25383.581+299.31255*T−46*T*LN(T)+2296.03E28*T**(−9);  6000 N !
 FUNCTION GFCCFE   298.15
    −236.7+132.416*T−24.6643*T*LN(T)−3.75752E−3*T**2−0.058927E−6*T**3
    +77359*T**(−1); 1811 Y
    −27097.3963+300.252559*T−46*T*LN(T)+2788.54E28*T**(−9);  6000 N !
 FUNCTION GLIQFE 298.15 12040.17−6.55843*T−367.516E−23*T**7+GHSERFE; 1811 Y
    −10838.83+291.302*T−46*T*LN(T);  6000 N !

$—————————————————————————————————————————————————————————
$ FUNCTION SN
$—————————————————————————————————————————————————————————
 FUNCTION GHSERSN  100.00
    −7958.517+122.765451*T−25.858*T*LN(T)+0.51185E−3*T**2−3.192767E−6*T**3
    +18440*T**(−1);   250 Y
    −5855.135+65.443315*T−15.961*T*LN(T)−18.8702E−3*T**2+3.121167E−6*T**3
    −61960*T**(−1);   505.078 Y
    2524.724+4.005269*T−8.2590486*T*LN(T)−16.814429E−3*T**2+2.623131E−6*T**3
    −1081244*T**(−1)−123.07E23*T**(−9);   800 Y
    −8256.959+138.99688*T−28.4512*T*LN(T)−123.07E23*T**(−9);  3000 N !
 FUNCTION GLIQSN 100 7103.092−14.087767*T+147.031E−20*T**7+GHSERSN; 505.078 Y
    9496.31−9.809114*T−8.2590486*T*LN(T)−16.814429E−3*T**2+2.623131E−6*T**3
    −1081244*T**(−1);   800 Y
    −1285.372+125.182498*T−28.4512*T*LN(T);  3000 N !
 FUNCTION GFCCSN 100 +5510−8.46*T+GHSERSN;   3000 N !
 FUNCTION GBCCSN 100 +4400−6*T+GHSERSN;      3000 N !
```

```
$————————————————————————————————————————————————————————————————
$   LIQUID     (FE,SN)1
$————————————————————————————————————————————————————————————————
 PHASE   LIQUID % 1 1        !
   CONSTITUENT   LIQUID :FE,SN    :   !
 PARAMETER G(LIQUID,FE;0)    298.15 +GLIQFE;          6000 N !
 PARAMETER G(LIQUID,SN;0)    100    +GLIQSN;          3000 N !
 PARAMETER G(LIQUID,FE,SN;0) 298.15
 +72347.042−202.434261∗T+22.9803823∗T∗LN(T); 6000 N !
 PARAMETER G(LIQUID,FE,SN;1) 298.15
 −9133.33753+1.97377668∗T+0.104808067∗T∗LN(T); 6000 N !
 PARAMETER G(LIQUID,FE,SN;2) 298.15 +1041.92838−6.34102594∗T; 6000 N !


$————————————————————————————————————————————————————————————————
$   BCC_A2     (FE,SN)1
$————————————————————————————————————————————————————————————————
 TYPE_DEFINITION " GES A_P_D BCC_A2 MAGNETIC −1.0  4.00000E−01 !
 PHASE   BCC_A2 %" 1   1       !
   CONSTITUENT   BCC_A2 :FE,SN    :   !
 PARAMETER G(BCC_A2,FE;0)  298.15 +GHSERFE;         6000 N !
 PARAMETER TC(BCC_A2,FE;0) 298.15 +1043;            6000 N !
 PARAMETER BM(BCC_A2,FE;0) 298.15 +2.22;            6000 N !
 PARAMETER G(BCC_A2,SN;0)  100    +GBCCSN;          3000 N !
 PARAMETER G(BCC_A2,FE,SN;0)  298.15 +24853.4276+4.7843622∗T; 6000 N !
 PARAMETER G(BCC_A2,FE,SN;1)  298.15 −17676.7821;          6000 N !
 PARAMETER TC(BCC_A2,FE,SN;0) 298.15 +932.545;            6000 N !
 PARAMETER BM(BCC_A2,FE,SN;0) 298.15 −5.688;              6000 N !


$————————————————————————————————————————————————————————————————
$   FCC_A1     (FE,SN)1
$————————————————————————————————————————————————————————————————
 TYPE_DEFINITION & GES A_P_D FCC_A1 MAGNETIC −3.0  2.80000E−01 !
 PHASE   FCC_A1 %&   1 1       !
   CONSTITUENT   FCC_A1 :FE,SN  :   !
 PARAMETER G(FCC_A1,FE;0)  298.15 +GFCCFE; 6000 N !
 PARAMETER TC(FCC_A1,FE;0) 298.15 −201;   6000 N !
 PARAMETER BM(FCC_A1,FE;0) 298.15 −2.10;   6000 N !
 PARAMETER G(FCC_A1,SN;0)  100    +GFCCSN; 3000 N !
 PARAMETER G(FCC_A1,FE,SN;0)  298.15 +24140.28; 6000 N !


$————————————————————————————————————————————————————————————————
$   FE5SN3     (FE)5(SN)3
$————————————————————————————————————————————————————————————————
 PHASE   FE5SN3 % 2 5 3     !
   CONSTITUENT   FE5SN3 :FE:SN :    !
 PARAMETER G(FE5SN3,FE:SN;0) 298.15
 −97000+51∗T+5∗GHSERFE+3∗GHSERSN; 6000 N !


$————————————————————————————————————————————————————————————————
$   FE3SN2     (FE)3(SN)2
$————————————————————————————————————————————————————————————————
 PHASE   FE3SN2 % 2 3 2     !
   CONSTITUENT   FE3SN2 :FE:SN:    !
 PARAMETER G(FE3SN2,FE:SN;0) 298.15
  −9.45194246E+04+6.25316153E+01∗T+3∗GHSERFE+2∗GHSERSN; 6000 N !


$————————————————————————————————————————————————————————————————
$   FE3SN1     (FE)3(SN)1 INVENTED
$————————————————————————————————————————————————————————————————
 PHASE   FE3SN1 % 2 3 1     !
   CONSTITUENT   FE3SN1 :FE:SN:    !
  PARAMETER G(FE3SN1,FE:SN;0) 298.15
```

```
 −38822.9184+21.3557*T+3*GHSERFE+GHSERSN; 6000 N !

$————————————————————————————————————————————
$   FESN      (FE)1(SN)1
$————————————————————————————————————————————
 PHASE  FE1SN1 % 2 1 1     !
   CONSTITUENT  FE1SN1 :FE:SN:    !
 PARAMETER G(FE1SN1,FE:SN;0) 298.15
 −55704.5693+41.6671059*T+GHSERFE+GHSERSN; 6000 N !

$————————————————————————————————————————————
$   FESN2      (FE)1(SN)2
$————————————————————————————————————————————
 PHASE  FE1SN2 % 2 1 2     !
   CONSTITUENT  FE1SN2 :FE:SN:    !
 PARAMETER G(FE1SN2,FE:SN;0) 298.15
 −80135.4578+67.9318396*T+GHSERFE+2*GHSERSN; 6000 N !

$————————————————————————————————————————————
$   BCT_A5 (SN)1
$————————————————————————————————————————————
 PHASE  BCT_A5 % 1 1      !
   CONSTITUENT  BCT_A5 :SN:    !
 PARAMETER G(BCT_A5,SN;0) 100 +GHSERSN; 3000 N !
```
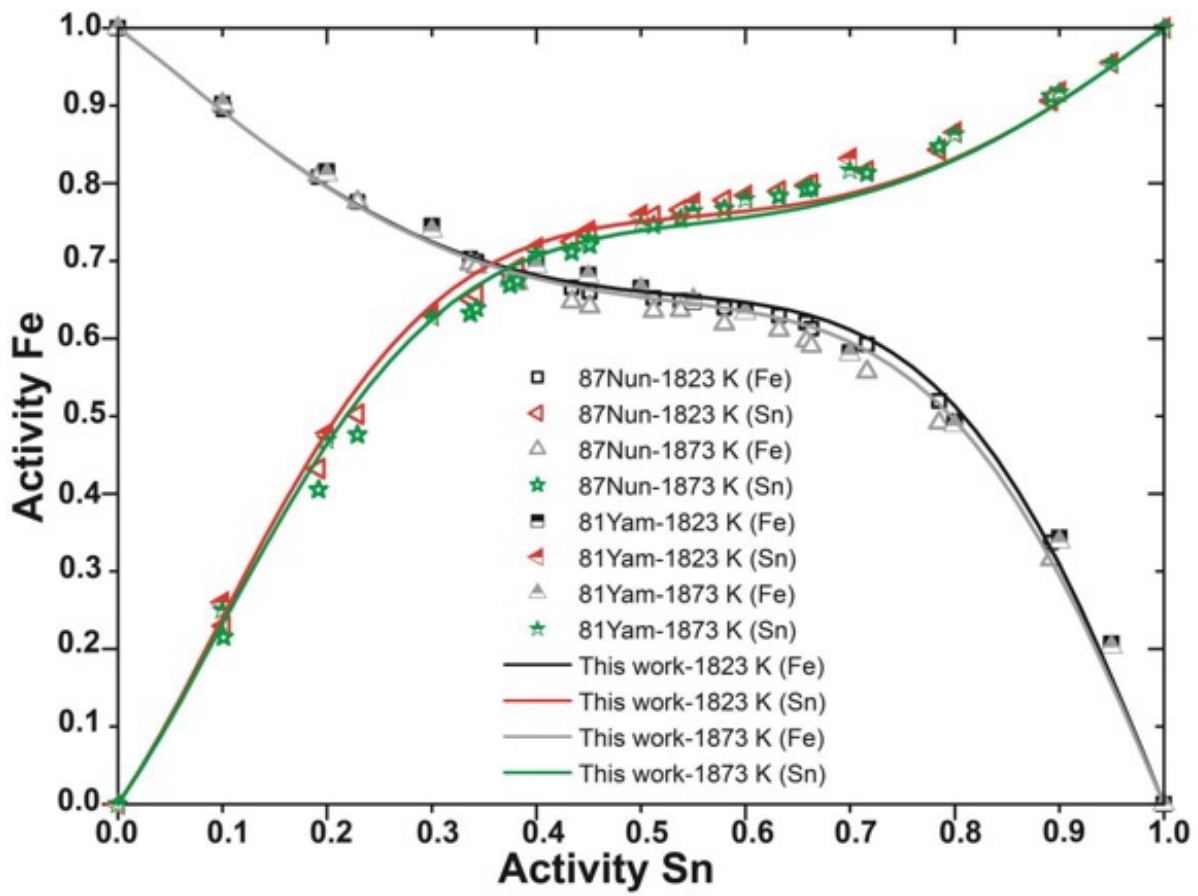
Figure S1.: Calculated activities of Fe and Sn in liquid Fe-Sn system compared with the experimental data at 1823 K and 1873 K [440, 432]. Reference state: Liquid Fe and Liquid Sn.
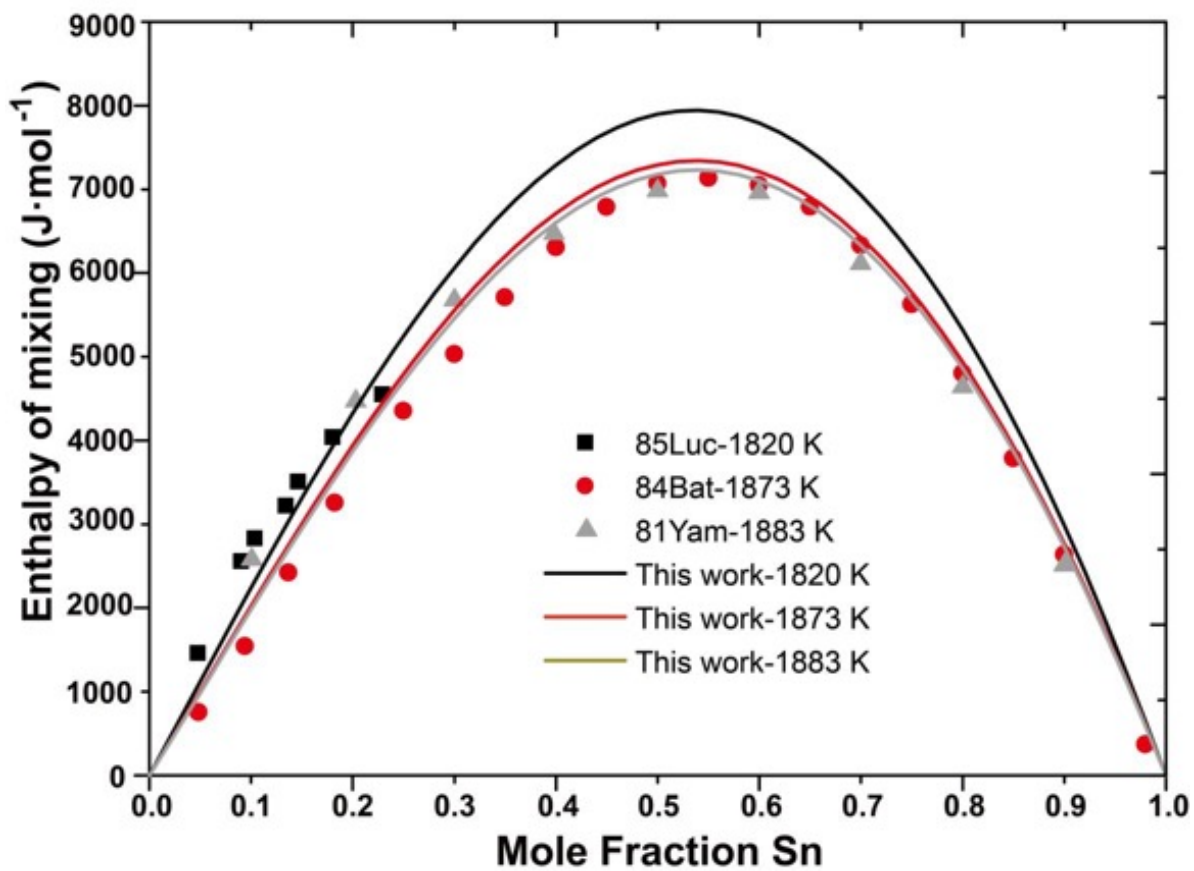
Figure S2.: Calculated enthalpies of mixing of liquid phase compared with the experimental data at 1820 K, 1873 K and 1883 K [432, 442, 443]. Reference state: Liquid Fe and Liquid Sn.

Bibliography

[1] Juan J de Pablo et al. "New frontiers for the materials genome initiative". In: *Npj Comput. Mater.* 5.1 (2019), pp. 1–23.

[2] Yanjing SU et al. "Progress in materials genome engineering in China". In: *Acta Metall Sin* 56.10 (2020), pp. 1313–1323.

[3] William Yi Wang et al. "Integrated computational materials engineering for advanced materials: A brief review". In: *Comput. Mater. Sci.* 158 (2019), pp. 42–48.

[4] Steven G Louie et al. "Discovering and understanding materials through computation". In: *Nat. Mater.* 20.6 (2021), pp. 728–735.

[5] Nicola Marzari, Andrea Ferretti, and Chris Wolverton. "Electronic-structure methods for materials design". In: *Nat. Mater.* 20.6 (2021), pp. 736–749.

[6] Jeff Greeley et al. "Computational high-throughput screening of electrocatalytic materials for hydrogen evolution". In: *Nat. Mater.* 5.11 (2006), pp. 909–913.

[7] Chen Shen et al. "Designing of magnetic MAB phases for energy applications". In: *J. Mater. Chem. A* 9.13 (2021), pp. 8805–8813.

[8] Prashun Gorai, Vladan Stevanović, and Eric S Toberer. "Computationally guided discovery of thermoelectric materials". In: *Nat. Rev. Mater.* 2.9 (2017), pp. 1–16.

[9] Arunima K Singh et al. "Robust and synthesizable photocatalysts for CO_2 reduction: a data-driven materials discovery". In: *Nat. Commun.* 10.1 (2019), pp. 1–9.

[10] Ling Qiao, Yong Liu, and Jingchuan Zhu. "A focused review on machine learning aided high-throughput methods in high entropy alloy". In: *J. Alloys Compd.* 877 (2021), p. 160295.

[11] Jiajun Linghu et al. "High-throughput computational screening of vertical 2D van der Waals heterostructures for high-efficiency excitonic solar cells". In: *ACS Appl. Mater. Interfaces* 10.38 (2018), pp. 32142–32150.

[12] Anubhav Jain et al. "A high-throughput infrastructure for density functional theory calculations". In: *Com. Mat. Sci.* 50.8 (2011), pp. 2295–2310.

[13] Stefano Curtarolo et al. "AFLOWLIB. ORG: A distributed materials properties repository from high-throughput ab initio calculations". In: *Comput. Mater. Sci.* 58 (2012), pp. 227–235.

[14] Claudia Draxl and Matthias Scheffler. "The NOMAD laboratory: from data sharing to artificial intelligence". In: *Journal of Physics: Materials* 2.3 (2019), p. 036001.

[15] James E Saal et al. "Materials design and discovery with high-throughput density functional theory: the open quantum materials database (OQMD)". In: *JOM* 65.11 (2013), pp. 1501–1509.

[16] Giovanni Pizzi et al. "AiiDA: automated interactive infrastructure and database for computational science". In: *Comput. Mater. Sci.* 111 (2016), pp. 218–230.

[17] Kiran Mathew et al. "Atomate: A high-level interface to generate, execute, and analyze computational materials science workflows". In: *Comput. Mater. Sci.* 139 (2017), pp. 140–152.

[18] Stefano Curtarolo et al. "The high-throughput highway to computational materials design". In: *Nat. Mater.* 12.3 (2013), pp. 191–201.

[19] Hongbin Zhang. "High-throughput design of magnetic materials". In: *Electronic Structure* 3.3 (2021), p. 033001.

[20] Geoffroy Hautier. "Finding the needle in the haystack: Materials discovery and design through computational ab initio high-throughput screening". In: *Comput. Mater. Sci.* 163 (2019), pp. 108–116.

[21] Bo Sundman, HL Lukas, and SG Fries. *Computational thermodynamics: the Calphad method*. Cambridge university press Cambridge, 2007.

[22] Yixuan Zhang et al. "Thermal conductivity of h-BN monolayers using machine learning interatomic potential". In: *J. Condens. Matter Phys.* 33.10 (2020), p. 105903.

[23] Feliciano Giustino. "Electron-phonon interactions from first principles". In: *Rev. Mod. Phys.* 89.1 (2017), p. 015003.

[24] Elena Roxana Margine and Feliciano Giustino. "Anisotropic migdal-eliashberg theory using wannier functions". In: *Phys. Rev. B* 87.2 (2013), p. 024505.

[25] Kai-Cheng Zhang et al. "Thickness-dependent anisotropic transport of phonons and charges in few-layered $PdSe_2$". In: *Phys. Chem. Chem. Phys* 23.34 (2021), pp. 18869–18884.

[26] Marios Zacharias and Feliciano Giustino. "One-shot calculation of temperature-dependent optical spectra and phonon-induced band-gap renormalization". In: *Phys. Rev. B* 94.7 (2016), p. 075125.

[27] Philip W Anderson. "Theory of dirty superconductors". In: *J. Phys. Chem. Solids* 11.1-2 (1959), pp. 26–30.

[28] WL McMillan. "Transition temperature of strong-coupled superconductors". In: *Physical Review* 167.2 (1968), p. 331.

[29] AB Migdal. "Interaction between electrons and lattice vibrations in a normal metal". In: *Sov. Phys. JETP* 7.6 (1958), pp. 996–1001.

[30] GM Eliashberg. "Interactions between electrons and lattice vibrations in a superconductor". In: *Sov. Phys. JETP* 11.3 (1960), pp. 696–702.

[31] M Lüders et al. "Ab initio theory of superconductivity. I. Density functional formalism and approximate functionals". In: *Phys. Rev. B* 72.2 (2005), p. 024545.

[32] MAL Marques et al. "Ab initio theory of superconductivity. II. Application to elemental metals". In: *Phys. Rev. B* 72.2 (2005), p. 024546.

[33] Tammie R Nelson et al. "Non-adiabatic excited-state molecular dynamics: Theory and applications for modeling photophysics in extended molecular materials". In: *Chem. Rev.* 120.4 (2020), pp. 2215–2287.

[34] Pascal Friederich et al. "Machine-learned potentials for next-generation matter simulations". In: *Nat. Mater.* 20.6 (2021), pp. 750–761.

[35] Heather Kulik et al. "Roadmap on machine learning in electronic structure". In: *Electronic Structure* (2022).

[36] Teng Long et al. "Constrained crystals deep convolutional generative adversarial network for the inverse design of crystal structures". In: *Npj Comput. Mater.* 7.1 (2021), pp. 1–7.

[37] Teng Zhou, Zhen Song, and Kai Sundmacher. "Big data creates new opportunities for materials research: a review on methods and applications of machine learning for materials design". In: *Engineering* 5.6 (2019), pp. 1017–1026.

[38] Tian Wang et al. "Machine learning approaches for thermoelectric materials research". In: *Adv. Funct. Mater.* 30.5 (2020), p. 1906041.

[39] Emmanuel J Candès and Michael B Wakin. "An introduction to compressive sampling". In: *IEEE signal processing magazine* 25.2 (2008), pp. 21–30.

[40] Lance J Nelson et al. "Compressive sensing as a paradigm for building physics models". In: *Phys. Rev. B* 87.3 (2013), p. 035125.

[41] Lance J Nelson et al. "Cluster expansion made easy with Bayesian compressive sensing". In: *Phys. Rev. B* 88.15 (2013), p. 155105.

[42] Hongxiang Zong et al. "Hcp→ ω phase transition mechanisms in shocked zirconium: A machine learning based atomic simulation study". In: *Acta Mater.* 162 (2019), pp. 126–135.

[43] Venkat Kapil et al. "The first-principles phase diagram of monolayer nanocon-fined water". In: *Nature* (2022), pp. 1–5.

[44] Linfeng Zhang et al. "End-to-end symmetry preserving inter-atomic potential energy model for finite and extended systems". In: *Adv. Neural Inf. Process. Syst.* 31 (2018).

[45] SR Xie et al. "Machine learning of superconducting critical temperature from Eliashberg theory". In: *Npj Comput. Mater.* 8.1 (2022), pp. 1–8.

[46] Noah Hoffmann et al. "Superconductivity in antiperovskites". In: *Npj Comput. Mater.* 8.1 (2022), pp. 1–10.

[47] Stephan R Xie et al. "Functional form of the superconducting critical temperature from machine learning". In: *Phys. Rev. B* 100.17 (2019), p. 174513.

[48] Brandon Bocklund et al. "ESPEI for efficient thermodynamic database develop-ment, modification, and uncertainty quantification: application to Cu–Mg". In: *MRS Communications* 9.2 (2019), pp. 618–627.

[49] Douglas R Hartree. "The wave mechanics of an atom with a non-Coulomb central field. Part I. Theory and methods". In: *Mathematical Proceedings of the Cambridge Philosophical Society*. Vol. 24. 1. Cambridge university press. 1928, pp. 89–110.

[50] Pierre Hohenberg and Walter Kohn. "Inhomogeneous electron gas". In: *Physical review* 136.3B (1964), B864.

[51] Walter Kohn and Lu Jeu Sham. "Self-consistent equations including exchange and correlation effects". In: *Physical review* 140.4A (1965), A1133.

[52] Seymour H Vosko, Leslie Wilk, and Marwan Nusair. "Accurate spin-dependent electron liquid correlation energies for local spin density calculations: a critical analysis". In: *Can. J. Phys.* 58.8 (1980), pp. 1200–1211.

[53] John P Perdew and Alex Zunger. "Self-interaction correction to density-functional approximations for many-electron systems". In: *Phys. Rev. B* 23.10 (1981), p. 5048.

[54] Lee A Cole and JP Perdew. "Calculated electron affinities of the elements". In: *Phys. Rev. A* 25.3 (1982), p. 1265.

[55] John P Perdew and Yue Wang. "Accurate and simple analytic representation of the electron-gas correlation energy". In: *Phys. Rev. B* 45.23 (1992), p. 13244.

[56] Axel D Becke. "Density-functional exchange-energy approximation with correct asymptotic behavior". In: *Phys. Rev. A* 38.6 (1988), p. 3098.

[57] Michael Filatov and Walter Thiel. "Exchange-correlation density functional beyond the gradient approximation". In: *Phys. Rev. A* 57.1 (1998), p. 189.

[58] Axel D Becke. "Density functional calculations of molecular bond energies". In: *J. Chem. Phys.* 84.8 (1986), pp. 4524–4529.

[59] John P Perdew, Kieron Burke, and Matthias Ernzerhof. "Generalized gradient approximation made simple". In: *Phys. Rev. Lett.* 77.18 (1996), p. 3865.

[60] Ulf Von Barth and Lars Hedin. "A local exchange-correlation potential for the spin polarized case. i". In: *J. Solid State Phys.* 5.13 (1972), p. 1629.

[61] MM Pant and AK Rajagopal. "Theory of inhomogeneous magnetic electron gas". In: *Solid State Commun.* 10.12 (1972), pp. 1157–1160.

[62] O Gunnarsson, BI Lundqvist, and JW Wilkins. "Contribution to the cohesive energy of simple metals: Spin-dependent effect". In: *Phys. Rev. B* 10.4 (1974), p. 1319.

[63] Carsten A Ullrich. "Density-functional theory for systems with noncollinear spin: Orbital-dependent exchange-correlation functionals and their application to the Hubbard dimer". In: *Phys. Rev. B* 98.3 (2018), p. 035140.

[64] H Eschrig, M Richter, and I Opahle. "Relativistic solid state calculations". In: *Theoretical and Computational Chemistry*. Vol. 14. Elsevier, 2004, pp. 723–776.

[65] Jürgen Kübler. *Theory of itinerant electron magnetism*. Vol. 106. Oxford University Press, 2017.

[66] Steven H Simon. *The Oxford solid state basics*. OUP Oxford, 2013.

[67] AP French. "Vibrations and waves, New York". In: *NY: Norton.[Google Scholar]* (1971).

[68] Massoud Kaviany. *Heat transfer physics*. Cambridge University Press, 2014.

[69] *Phonons*. Wikipedia. URL: https://en.wikipedia.org/wiki/Phonon#Acoustic_and_optical_phonons (visited on 2010).

[70] Mildred S Dresselhaus, Gene Dresselhaus, and Ado Jorio. *Group theory: application to the physics of condensed matter*. Springer Science & Business Media, 2007.

[71] Max Born and K Huang. *Dynamical Theory of Crystal Lattices, Oxford*. 1954.

[72] Neil W Ashcroft, ND Mermin, and Dan Wei. "Solid State Physics, revised ed". In: *Cengage Learning, Singapore* (2016).

[73] Guillermo Bozzolo, Ronald D Noebe, and Phillip B Abel. *Applied computational materials modeling: theory, simulation and experiment*. Springer Science & Business Media, 2007.

[74] Y Wang, Z.K. Liu, and L.Q. Chen. "Thermodynamic properties of Al, Ni, NiAl, and Ni_3Al from first-principles calculations". In: *Acta Mater.* 52.9 (2004), pp. 2665–2671.

[75] Y.J. Hu et al. "First-principles calculations and thermodynamic modeling of the Yb-Ni binary system". In: *Calphad* 59 (2017), pp. 207–217.

[76] S.M. Liang et al. "Phase equilibria of the Zn-Ti system: Experiments, first-principles calculations and Calphad assessment". In: *Calphad* 64 (2019), pp. 213–224.

[77] G Inden. "Approximate description of the configurational specific heat during a magnetic order-disorder transformation". In: *Proceeding of the 5th project meeting CALPHAD*. Vol. 3. 1976, pp. 4–1.

[78] Mats Hillert and Magnus Jarl. "A model for alloying in ferromagnetic metals". In: *Calphad* 2.3 (1978), pp. 227–238.

[79] Wei Xiong et al. "An improved magnetic model for thermodynamic modeling". In: *Calphad* 39 (2012), pp. 11–20.

[80] Fritz Körmann et al. "Lambda transitions in materials science: Recent advances in CALPHAD and first-principles modelling". In: *Phys. Status Solidi B* 251.1 (2014), pp. 53–80.

[81] Larry Kaufman and Harold Bernstein. "Computer calculation of phase diagrams. With special reference to refractory metals". In: (1970).

[82] A.T. Dinsdale. "SGTE data for pure elements". In: *Calphad* 15.4 (1991), pp. 317–425.

[83] O Redlich and A.T. Kister. "Algebraic representation of thermodynamic properties and the classification of solutions". In: *Ind. Eng. Chem. Res.* 40.2 (1948), pp. 345–348.

[84] D McQuarrie. "Statistical mechanics university science books". In: *Sausalito, CA* (2000), pp. 222–223.

[85] Mark Lundstrom. *Fundamentals of carrier transport*. 2002.

[86] Martin T Dove and Martin T Dove. *Introduction to lattice dynamics*. 4. Cambridge university press, 1993.

[87] Chen Shen et al. "Two-dimensional buckling structure induces the ultra-low thermal conductivity: a comparative study of the group GaX (X= N, P, As)". In: *J. Mater. Chem. C* 10.4 (2022), pp. 1436–1444.

[88] Fuqing Duan et al. "Hydrodynamically enhanced thermal transport due to strong interlayer interactions: A case study of strained bilayer graphene". In: *Phys. Rev. B* 105.12 (2022), p. 125406.

[89] Guangzhao Qin et al. "Lone-pair electrons induced anomalous enhancement of thermal transport in strained planar two-dimensional materials". In: *Nano Energy* 50 (2018), pp. 425–430.

[90] Chen W Li et al. "Orbitally driven giant phonon anharmonicity in SnSe". In: *Nat. Phys.* 11.12 (2015), pp. 1063–1069.

[91] Joseph P Heremans. "The anharmonicity blacksmith". In: *Nat. Phys.* 11.12 (2015), pp. 990–991.

[92] Eric S Toberer, Alex Zevalkink, and G Jeffrey Snyder. "Phonon engineering through crystal chemistry". In: *J. Mater. Chem.* 21.40 (2011), pp. 15843–15852.

[93] DP White. "The effect of ionizing and displacive radiation on the thermal conductivity of alumina". In: *J. Appl. Phys.* 73.5 (1993), pp. 2254–2258.

[94] Vadim L'vovich Gurevich. "Transport in phonon systems". In: (1986).

[95] John M Ziman. *Electrons and phonons: the theory of transport phenomena in solids*. Oxford university press, 2001.

[96] Mark Lundstrom. *Fundamentals of Carrier Transport*. 2nd ed. Cambridge University Press, 2000.

[97] J Schrieffer. *Theory of Superconductivity (Advanced Book Program Series)*. 1983.

[98] Philip B Allen and Jean Paul Nery. "Low-temperature semiconductor band-gap thermal shifts: T 4 shifts from ordinary acoustic and T 2 from piezoacoustic coupling". In: *Phys. Rev. B* 95.3 (2017), p. 035211.

[99] G Grimvall. "The electron-phonon interaction in normal metals". In: *Physica Scripta* 14.1-2 (1976), p. 63.

[100] Emmanuel J Candès, Justin Romberg, and Terence Tao. "Robust uncertainty principles: Exact signal reconstruction from highly incomplete frequency information". In: *IEEE Transactions on information theory* 52.2 (2006), pp. 489–509.

[101] Terumasa Tadano and Shinji Tsuneyuki. "Self-consistent phonon calculations of lattice dynamical properties in cubic $SrTiO_3$ with first-principles anharmonic force constants". In: *Phys. Rev. B* 92.5 (2015), p. 054301.

[102] Fei Zhou et al. "Compressive sensing lattice dynamics. I. General formalism". In: *Phys. Rev. B* 100.18 (2019), p. 184308.

[103] Mariette Hellenbrandt. "The inorganic crystal structure database (ICSD)—present and future". In: *Crystallogr. Rev.* 10.1 (2004), pp. 17–22.

[104] Anubhav Jain et al. "The materials project: Accelerating materials design through theory-driven data and tools". In: *Handbook of Materials Modeling: Methods: Theory and Modeling* (2020), pp. 1751–1784.

[105] Colin W Glass, Artem R Oganov, and Nikolaus Hansen. "USPEX—Evolutionary crystal structure prediction". In: *Comput. Phys. Commun.* 175.11-12 (2006), pp. 713–720.

[106]   Yanchao Wang et al. "CALYPSO: A method for crystal structure prediction". In: *Comput. Phys. Commun.* 183.10 (2012), pp. 2063–2070.

[107]   Jake Graser, Steven K Kauwe, and Taylor D Sparks. "Machine learning and energy minimization approaches for crystal structure predictions: a review and new horizons". In: *Chem. Mater.* 30.11 (2018), pp. 3601–3612.

[108]   Guangzhao Qin et al. "Anomalously temperature-dependent thermal conductivity of monolayer GaN with large deviations from the traditional 1/T law". In: *Phys. Rev. B* 95.19 (2017), p. 195416.

[109]   Myoung-Jae Lee et al. "Thermoelectric materials by using two-dimensional materials with negative correlation between electrical and thermal conductivity". In: *Nat. Commun* 7.1 (2016), pp. 1–7.

[110]   Guangqian Ding et al. "Thermoelectric properties of monolayer MSe_2 (M= Zr, Hf): low lattice thermal conductivity and a promising figure of merit". In: *Nanotechnology* 27.37 (2016), p. 375703.

[111]   Fei Zhou et al. "Lattice anharmonicity and thermal conductivity from compressive sensing of first-principles calculations". In: *Phys. Rev. Lett.* 113.18 (2014), p. 185501.

[112]   Zhenzhen Qin et al. "Orbitally driven low thermal conductivity of monolayer gallium nitride (GaN) with planar honeycomb structure: a comparative study". In: *Nanoscale* 9.12 (2017), pp. 4295–4309.

[113]   Terumasa Tadano, Yoshihiro Gohda, and Shinji Tsuneyuki. "Anharmonic force constants extracted from first-principles molecular dynamics: applications to heat transfer simulations". In: *J. Condens. Matter Phys* 26.22 (2014), p. 225402.

[114]   Olle Hellman, IA Abrikosov, and SI Simak. "Lattice dynamics of anharmonic solids from first principles". In: *Phys. Rev. B* 84.18 (2011), p. 180301.

[115]   Olle Hellman et al. "Temperature dependent effective potential method for accurate free energy calculations of solids". In: *Phys. Rev. B* 87.10 (2013), p. 104111.

[116]   Petros Souvatzis et al. "Entropy driven stabilization of energetically unstable crystal structures explained from first principles theory". In: *Phys. Rev. Lett.* 100.9 (2008), p. 095901.

[117]   NR Werthamer. "Self-consistent phonon formulation of anharmonic lattice dynamics". In: *Phys. Rev. B* 1.2 (1970), p. 572.

[118]   Terumasa Tadano and Shinji Tsuneyuki. "Quartic anharmonicity of rattlers and its effect on lattice thermal conductivity of clathrates from first principles". In: *Phys. Rev. Lett* 120.10 (2018), p. 105901.

[119] Yi Xia et al. "High-throughput study of lattice thermal conductivity in binary rocksalt and zinc blende compounds including higher-order anharmonicity". In: *Phys. Rev. X* 10.4 (2020), p. 041029.

[120] Ankit Jain and Alan JH McGaughey. "Effect of exchange–correlation on first-principles-driven lattice thermal conductivity predictions of crystalline silicon". In: *Comput. Mater. Sci.* 110 (2015), pp. 115–120.

[121] Glen A Slack. "Nonmetallic crystals with high thermal conductivity". In: *J. Phys. Chem. Solids* 34.2 (1973), pp. 321–335.

[122] J Gerratt and Ian M Mills. "Force constants and dipole-moment derivatives of molecules from perturbed Hartree–Fock calculations. I". In: *J. Chem. Phys.* 49.4 (1968), pp. 1719–1729.

[123] Stefano Baroni et al. "Phonons and related crystal properties from density-functional perturbation theory". In: *Rev. Mod. Phys* 73.2 (2001), p. 515.

[124] Giorgia Fugallo et al. "Ab initio variational approach for evaluating lattice thermal conductivity". In: *Phys. Rev. B* 88.4 (2013), p. 045430.

[125] Wu Li et al. "ShengBTE: A solver of the Boltzmann transport equation for phonons". In: *Comput. Phys. Commun.* 185.6 (2014), pp. 1747–1758.

[126] Atsushi Togo, Laurent Chaput, and Isao Tanaka. "Distributions of phonon lifetimes in Brillouin zones". In: *Phys. Rev. B* 91.9 (2015), p. 094306.

[127] Jesús Carrete et al. "almaBTE: A solver of the space–time dependent Boltzmann transport equation for phonons in structured materials". In: *Comput. Phys. Commun.* 220 (2017), pp. 351–362.

[128] Tianli Feng, Lucas Lindsay, and Xiulin Ruan. "Four-phonon scattering significantly reduces intrinsic thermal conductivity of solids". In: *Phys. Rev. B* 96.16 (2017), p. 161201.

[129] Zherui Han et al. "FourPhonon: An extension module to ShengBTE for computing four-phonon scattering rates and thermal conductivity". In: *Comput. Phys. Commun.* 270 (2022), p. 108179.

[130] Rep Kubo. "The fluctuation-dissipation theorem". In: *Rep. Prog. Phys.* 29.1 (1966), p. 255.

[131] Fatemeh Jabbari, Ali Rajabpour, and Seifollah Saedodin. "Thermal conductivity and viscosity of nanofluids: a review of recent molecular dynamics studies". In: *Chem. Eng. Sci.* 174 (2017), pp. 67–81.

[132] Jean-Pierre Hansen and Ian Ranald McDonald. *Theory of simple liquids: with applications to soft matter*. Academic press, 2013.

[133] Florian Müller-Plathe. "A simple nonequilibrium molecular dynamics method for calculating the thermal conductivity". In: *J. Chem. Phys.* 106.14 (1997), pp. 6082–6085.

[134] Alexander V Shapeev. "Moment tensor potentials: A class of systematically improvable interatomic potentials". In: *Multiscale Model. Sim.* 14.3 (2016), pp. 1153–1173.

[135] Ivan S Novikov et al. "The MLIP package: moment tensor potentials with MPI and active learning". In: *Mach. learn.: sci. technol.* 2.2 (2020), p. 025002.

[136] Aidan P Thompson et al. "Spectral neighbor analysis method for automated generation of quantum-accurate interatomic potentials". In: *J. Comput. Phys.* 285 (2015), pp. 316–330.

[137] Howard Yanxon et al. "PyXtal_FF: a python library for automated force field generation". In: *Mach. learn.: sci. technol.* 2.2 (2020), p. 027001.

[138] Albert P Bartók et al. "Gaussian approximation potentials: The accuracy of quantum mechanics, without the electrons". In: *Phys. Rev. Lett.* 104.13 (2010), p. 136403.

[139] Albert P Bartók and Gábor Csányi. "Gaussian approximation potentials: A brief tutorial introduction". In: *Int. J. Quantum Chem.* 115.16 (2015), pp. 1051–1057.

[140] Jörg Behler. "Constructing high-dimensional neural network potentials: a tutorial review". In: *Int. J. Quantum Chem.* 115.16 (2015), pp. 1032–1050.

[141] Nongnuch Artrith, Tobias Morawietz, and Jörg Behler. "High-dimensional neural-network potentials for multicomponent systems: Applications to zinc oxide". In: *Phys. Rev. B* 83.15 (2011), p. 153101.

[142] Samuel Poncé et al. "EPW: Electron–phonon coupling, transport and superconducting properties using maximally localized Wannier functions". In: *Comput. Phys. Commun.* 209 (2016), pp. 116–133.

[143] Feliciano Giustino et al. "Electron-phonon interaction via electronic and lattice Wannier functions: Superconductivity in boron-doped diamond reexamined". In: *Phys. Rev. Lett.* 98.4 (2007), p. 047005.

[144] Nicola Marzari and David Vanderbilt. "Maximally localized generalized Wannier functions for composite energy bands". In: *Phys. Rev. B* 56.20 (1997), p. 12847.

[145] Nicola Marzari et al. "Maximally localized Wannier functions: Theory and applications". In: *Rev. Mod. Phys.* 84.4 (2012), p. 1419.

[146] Feliciano Giustino, Steven G Louie, and Marvin L Cohen. "Electron-phonon renormalization of the direct band gap of diamond". In: *Phys. Rev. Lett.* 105.26 (2010), p. 265501.

[147] Oliver Gutfleisch et al. "Magnetic materials and devices for the 21st century: stronger, lighter, and more energy efficient". In: *Adv. Mater.* 23.7 (2011), pp. 821–842.

[148] KP Skokov and O Gutfleisch. "Heavy rare earth free, free rare earth and rare earth free magnets-vision and reality". In: *Scr. Mater.* 154 (2018), pp. 289–294.

[149] JMD Coey. "Permanent magnets: Plugging the gap". In: *Scr. Mater.* 67.6 (2012), pp. 524–529.

[150] Oliver Gutfleisch. "Controlling the properties of high energy density permanent magnetic materials by different processing routes". In: *J. Phys. D Appl. Phys.* 33.17 (2000), p. 157.

[151] S Sugimoto. "Current status and recent topics of rare-earth permanent magnets". In: *J. Phys. D Appl. Phys.* 44.6 (2011), p. 064001.

[152] Karl J Strnat and Reinhold MW Strnat. "Rare earth-cobalt permanent magnets". In: *J. Magn. Magn. Mater.* 100.1-3 (1991), pp. 38–56.

[153] JF Herbst and JJ Croat. "Neodymium-iron-boron permanent magnets". In: *J. Magn. Magn. Mater.* 100.1-3 (1991), pp. 57–78.

[154] JMD Coey. "New permanent magnets; manganese compounds". In: *J. Condens. Matter Phys.* 26.6 (2014), p. 064211.

[155] Vitalij K Pecharsky and Karl A Gschneidner Jr. "Giant magnetocaloric effect in $Gd_5(Si_2Ge_2)$". In: *Phys. Rev. Lett.* 78.23 (1997), p. 4494.

[156] O Gutfleisch, A Yan, and K-H Müller. "Large magnetocaloric effect in melt-spun $LaFe_{13-x}Si_x$". In: *J. Appl. Phys.* 97.10 (2005), p. 10M305.

[157] Oliver Gutfleisch et al. "Mastering hysteresis in magnetocaloric materials". In: *Philos. Trans. Royal Soc. A* 374.2074 (2016), p. 20150308.

[158] Franziska Scheibel et al. "Hysteresis design of magnetocaloric materials: From basic mechanisms to applications". In: *Energy Technol.* 6.8 (2018), pp. 1397–1428.

[159] Tino Gottschall et al. "Making a cool choice: The materials library of magnetic refrigeration". In: *Adv. Energy Mater.* 9.34 (2019), p. 1901322.

[160] D Sander et al. "The 2017 magnetism roadmap". In: *J. Phys. D Appl. Phys.* 50.36 (2017), p. 363001.

[161] Jeotikanta Mohapatra and Jia Ping Liu. "Rare-Earth-Free Permanent Magnets: The Past and Future". In: *Handbook of Magnetic Materials*. Vol. 27. Elsevier, 2018, pp. 1–57.

[162] MD KuzâMin et al. "Towards high-performance permanent magnets without rare earths". In: *J. Condens. Matter Phys.* 26.6 (2014), p. 064205.

[163]   Sankalp Kota, Maxim Sokol, and Michel W Barsoum. "A progress report on the MAB phases: atomically laminated, ternary transition metal borides". In: *Int. Mater. Rev.* (2019), pp. 1–30.

[164]   Michel W Barsoum. "The $M_{N+1}AX_N$ phases: A new class of solids: Thermodynamically stable nanolaminates". In: *Prog. Solid. State Ch.* 28.1-4 (2000), pp. 201–281.

[165]   Arni Sigurdur Ingason, Martin Dahlqvist, and Johanna Rosén. "Magnetic MAX phases from theory and experiments: a review". In: *J. Condens. Matter Phys.* 28.43 (2016), p. 433003.

[166]   Xiaoyan Tan et al. "Magnetocaloric effect in $AlFe_2B_2$: toward magnetic refrigerants from earth-abundant elements". In: *J. Am. Chem. Soc.* 135.25 (2013), pp. 9553–9557.

[167]   Johan Cedervall et al. "Magnetic structure of the magnetocaloric compound $AlFe_2B_2$". In: *J. Alloys Compd.* 664 (2016), pp. 784–791.

[168]   R Barua et al. "Anisotropic magnetocaloric response in $AlFe_2B_2$". In: *J. Alloys Compd.* 745 (2018), pp. 505–512.

[169]   Ping Chai et al. "Investigation of magnetic properties and electronic structure of layered-structure borides AlT_2B_2 (T= Fe, Mn, Cr) and $AlFe_{2-x}Mn_xB_2$". In: *J. Solid State Chem.* 224 (2015), pp. 52–61.

[170]   Krisztina Kádas et al. "AlM_2B_2 (M= Cr, Mn, Fe, Co, Ni): a group of nanolaminated materials". In: *J. Condens. Matter Phys.* 29.15 (2017), p. 155402.

[171]   A El Boukili et al. "Magnetocaloric and cooling properties of the intermetallic compound $AlFe_2B_2$ in an AMR cycle system". In: *Intermetallics* 104 (2019), pp. 84–89.

[172]   Liqin Ke, Bruce N Harmon, and Matthew J Kramer. "Electronic structure and magnetic properties in T_2AlB_2 (T= Fe, Mn, Cr, Co, and Ni) and their alloys". In: *Phys. Rev. B* 95.10 (2017), p. 104427.

[173]   Haiming Zhang et al. "Crystal structure of Cr_4AlB_4: A new MAB phase compound discovered in Cr-Al-B system". In: *J. Mater. Sci. Technol.* 35.4 (2019), pp. 530–534.

[174]   Mohammad Khazaei et al. "Novel MAB phases and insights into their exfoliation into 2D MBenes". In: *Nanoscale* 11.23 (2019), pp. 11305–11314.

[175]   Nanxi Miao et al. "Computational prediction of boron-based MAX phases and MXene derivatives". In: *Chem. Mater.* 32.16 (2020), pp. 6947–6957.

[176]   W Jeitschko. "Die Kristallstruktur von MoAlB". In: *Monatsh. Chem.* 97.5 (1966), pp. 1472–1476.

[177]   Wolfgang Jeitschko. "The crystal structure of Fe_2AlB_2". In: *Acta. Crystallogr. B. Struct. Sci.* 25.1 (1969), pp. 163–165.

[178]   W Jung and K Schweitzer. "Die Kristallstrukturen der ternären Boride $Al_2Ru_3B_2$ und Al3Ru4B2". In: *Z. Kristallogr. Cryst. Mater.* 174 (1986), pp. 109–110.

[179]   NF Chaban and IUB KUZ'MA. "Ternary systems Cr-Al-B and Mn-Al-B". In: *Akademiia Nauk SSSR, Izvestiia, Neorganicheskie Materialy* 9 (1973), pp. 1908–1911.

[180]   Martin Ade and Harald Hillebrecht. "Ternary borides Cr_2AlB_2, Cr_3AlB_4, and Cr_4AlB_6: The first members of the series $(CrB_2)nCrAl$ with n= 1, 2, 3 and a unifying concept for ternary borides as MAB-phases". In: *Inorg. Chem.* 54.13 (2015), pp. 6122–6135.

[181]   Lennart Häggström et al. "Mössbauer and X-ray studies of Fe_5PB_2". In: *J. Solid State Chem.* 13.1-2 (1975), pp. 84–91.

[182]   Sarah Hirt, Felix Hilfinger, and Harald Hillebrecht. "Synthesis and crystal structures of the new ternary borides $Fe_3Al_2B_2$ and $Ru_9Al_3B_8$ and the confirmation of $Ru_4Al_3B_2$ and $Ru_9Al_5B_{8-x}$(x≈2)". In: *Z. Kristallogr. Cryst. Mater.* 233.5 (2018), pp. 295–307.

[183]   Johan Cedervall et al. "Magnetostructural transition in Fe_5SiB_2 observed with neutron diffraction". In: *J. Solid State Chem.* 235 (2016), pp. 113–118.

[184]   Michael A McGuire and David S Parker. "Magnetic and structural properties of ferromagnetic Fe_5PB_2 and Fe_5SiB_2 and effects of Co and Mn substitutions". In: *J. Appl. Phys.* 118.16 (2015), p. 163903.

[185]   Mirosław Werwiński et al. "Magnetic properties of Fe_5SiB_2 and its alloys with P, S, and Co". In: *Phys. Rev. B* 93.17 (2016), p. 174412.

[186]   Tej N Lamichhane et al. "A study of the physical properties of single crystalline Fe_5B_2P". In: *J. Magn. Magn. Mater.* 401 (2016), pp. 525–531.

[187]   Daniel Hedlund et al. "Magnetic properties of the Fe_5SiB_2-Fe_5PB_2 system". In: *Phys. Rev. B* 96.9 (2017), p. 094433.

[188]   Ingo Opahle, Georg KH Madsen, and Ralf Drautz. "High throughput density functional investigations of the stability, electronic structure and thermoelectric properties of binary silicides". In: *Phys. Chem. Chem. Phys.* 14.47 (2012), pp. 16197–16202.

[189]   Ingo Opahle et al. "High-throughput study of the structural stability and thermoelectric properties of transition metal silicides". In: *New J. Phys.* 15.10 (2013), p. 105010.

[190]   Qiang Gao et al. "Designing rare-earth free permanent magnets in heusler alloys via interstitial doping". In: *Acta Mater.* 186 (2020), pp. 355–362.

[191] Dominik Ohmer et al. "High-throughput design of $211 - M_2AX$ compounds". In: *Phys. Rev. Materials* 3 (5 May 2019), p. 053803.

[192] Harish K Singh et al. "High-throughput screening of magnetic antiperovskites". In: *Chem. Mater.* 30.20 (2018), pp. 6983–6991.

[193] G Kresse and J Furthmüller. "Efficient iterative schemes for ab initio total-energy calculations using a plane-wave basis set". In: *Phys. Rev. B* 54.16 (1996), pp. 11169–11186.

[194] Georg Kresse and Daniel Joubert. "From ultrasoft pseudopotentials to the projector augmented-wave method". In: *Phys. Rev. B* 59.3 (1999), p. 1758.

[195] Klaus Koepernik and Helmut Eschrig. "Full-potential nonorthogonal local-orbital minimum-basis band-structure scheme". In: *Phys. Rev. B* 59.3 (1999), p. 1743.

[196] Joshua D Bocarsly et al. "A simple computational proxy for screening magnetocaloric compounds". In: *Chem. Mater.* 29.4 (2017), pp. 1613–1622.

[197] S Kirklin et al. "The Open Quantum Materials Database (OQMD): assessing the accuracy of DFT formation energies". In: *npj Comput. Mater.* 1.1 (2015), pp. 1–15.

[198] Mirosław Werwiński et al. "Magnetocrystalline anisotropy of Fe_5PB_2 and its alloys with Co and 5d elements: A combined first-principles and experimental study". In: *Phys. Rev. B* 98.21 (2018), p. 214431.

[199] Ivan A Zhuravlev, Vladimir P Antropov, and Kirill D Belashchenko. "Spin-fluctuation mechanism of anomalous temperature dependence of magnetocrystalline anisotropy in itinerant magnets". In: *Phys. Rev. Lett.* 115.21 (2015), p. 217201.

[200] PM Oppeneer. "Handbook of Magnetic Materials". In: *Vol. 13, Elsevier, Amsterdam* (2001).

[201] Xiao-Hong Li et al. "Elastic and acoustical properties of Cr_3AlB_4 under pressure". In: *J. Phys. Chem. Solids* 126 (2019), pp. 65–71.

[202] Yanchun Zhou et al. "Electrical conductive and damage-tolerant nanolaminated MAB phases Cr_2AlB_2, Cr_3AlB_4 and Cr_4AlB_6". In: *Mater. Res. Lett.* 5.6 (2017), pp. 440–448.

[203] Johan Cedervall et al. "Influence of Cobalt Substitution on the Magnetic Properties of Fe_5PB_2". In: *Inorg. Chem.* 57.2 (2018), pp. 777–784.

[204] Stig Rundqvist et al. "X-ray investigations of the ternary system Fe-P-B. Some features of the systems Cr-P-B, Mn-P-B, Co-P-B and Ni-P-B". In: *Acta Chem. Scand.* 16.1 (1962), pp. 1–19.

[205]   Cristina Bormio-Nunes et al. "Magnetization studies of binary and ternary Co-rich phases of the Co–Si–B system". In: *J. Alloys Compd.* 508.1 (2010), pp. 5–8.

[206]   HE Baurecht, H Boller, and H Nowotny. "Röntgenographische Untersuchunge in den Dreistoffen Cr-P-C, Cr-As-C und Cr-P-B". In: *Monatsh. Chem.* 102.2 (1971), pp. 373–384.

[207]   CN Guy and AA Uraz. "The chromium-boron system". In: *J. Less Common Met.* 48.2 (1976), pp. 199–203.

[208]   ZG Xie, DY Geng, and ZD Zhang. "Reversible room-temperature magnetocaloric effect in Mn_5PB_2". In: *Appl. Phys. Lett.* 97.20 (2010), p. 202504.

[209]   Xuelong Wang et al. "Oxysulfide LiAlSO: a lithium superionic conductor from first principles". In: *Phys. Rev. Lett.* 118.19 (2017), p. 195901.

[210]   Anubhav Jain et al. "The Materials Project: A materials genome approach to accelerating materials innovation". In: *APL Mater.* 1.1 (2013), p. 011002. ISSN: 2166532X.

[211]   Ingo Opahle et al. "Effect of N, C and B interstitials on the structural and magnetic properties of alloys with Cu_3Au-structure". In: *arXiv preprint arXiv:2001.00959* (2020).

[212]   D Potashnikov et al. "Magnetic ordering in the nano-laminar ternary Mn_2AlB_2 using neutron and X-ray diffraction". In: *J. Magn. Magn. Mater.* 471 (2019), pp. 468–474.

[213]   Johan Cedervall et al. "Magnetic and mechanical effects of Mn substitutions in $AlFe_2B_2$". In: *J. Magn. Magn. Mater.* 482 (2019), pp. 54–60.

[214]   Félix Mouhat and François-Xavier Coudert. "Necessary and sufficient elastic stability conditions in various crystal systems". In: *Phys. Rev. B* 90.22 (2014), p. 224104.

[215]   Yuelei Bai et al. "Phase stability and weak metallic bonding within ternary-layered borides CrAlB, Cr_2AlB_2, Cr_3AlB_4, and Cr_4AlB_6". In: *J. Am. Chem. Soc.* 102.6 (2019), pp. 3715–3727.

[216]   Uichiro Mizutani. "Hume-Rothery rules for structurally complex alloy phases". In: *MRS Bull.* 37.2 (2012), pp. 169–169.

[217]   Yiming Zhang et al. "The role of Hume-Rothery's rules play in the MAX phases formability". In: *Materialia* 12 (2020), p. 100810.

[218]   Stefan Maintz et al. "LOBSTER: A tool to extract chemical bonding from plane-wave based DFT". In: *J. Comput. Chem.* 37.11 (2016), pp. 1030–1035.

[219] Patrick Bruno. "Tight-binding approach to the orbital magnetic moment and magnetocrystalline anisotropy of transition-metal monolayers". In: *Phys. Rev. B* 39.1 (1989), p. 865.

[220] Bernard Hallemans, Patrick Wollants, and Jozef Roos. "Thermodynamic reassessment and calculation of the Fe-B phase diagram". In: *Z. Metallkd.* 85.10 (1994), pp. 676–682.

[221] Jyoti Thakur et al. "Enhancement of magnetic anisotropy of Fe_5PB_2 with W substitution: ab-initio study". In: *AIP Conf. Proc.* Vol. 2093. AIP Publishing LLC. 2019, p. 020012.

[222] Vladimir Antropov, Liqin Ke, and Daniel Åberg. "Constituents of magnetic anisotropy and a screening of spin–orbit coupling in solids". In: *Solid State Commun.* 194 (2014), pp. 35–38.

[223] Manuel Richter. "Band structure theory of magnetism in 3d-4f compounds". In: *J. Phys. D Appl. Phys.* 31.9 (1998), p. 1017.

[224] GHO Daalderop, PJ Kelly, and MFH Schuurmans. "Magnetocrystalline anisotropy and orbital moments in transition-metal compounds". In: *Phys. Rev. B* 44.21 (1991), p. 12054.

[225] Christina AC Garcia, Joshua D Bocarsly, and Ram Seshadri. "Computational screening of magnetocaloric alloys". In: *Phys. Rev. Materials* 4.2 (2020), p. 024402.

[226] Jon Ander Arregi et al. "Magnetization reversal and confinement effects across the metamagnetic phase transition in mesoscale FeRh structures". In: *J. Phys. D: Appl. Phys.* 51.10 (2018), p. 105001.

[227] Parul Arora, MK Chattopadhyay, and SB Roy. "Magnetocaloric effect in MnSi". In: *Appl. Phys. Lett.* 91.6 (2007), p. 062508.

[228] Minghui Yu, LH Lewis, and AR Moodenbaugh. "Large magnetic entropy change in the metallic antiperovskite Mn_3GaC". In: *J. Appl. Phys.* 93.12 (2003), pp. 10128–10130.

[229] Lucas T Alameda et al. "Topochemical deintercalation of Al from MoAlB: stepwise etching pathway, layered intergrowth structures, and two-dimensional MBene". In: *J. Am. Chem. Soc.* 140.28 (2018), pp. 8833–8840.

[230] Yi-Lun Hong et al. "Chemical vapor deposition of layered two-dimensional $MoSi_2N_4$ materials". In: *Science* 369.6504 (2020), pp. 670–674.

[231] Lei Wang et al. "Intercalated architecture of MA_2Z_4 family layered van der Waals materials with emerging topological, magnetic and superconducting properties". In: *Nat. Commun* 12 (2021), p. 2361.

[232] Lei Kang and Zheshuai Lin. "Second Harmonic Generation of $MoSi_2N_4$ Layer". In: *arXiv preprint arXiv:2009.06977* (2020).

[233] Si Li et al. "Valley-dependent properties of monolayer $MoSi_2N_4$, WSi_2N_4, and $MoSi_2As_4$". In: *Phys. Rev. B* 102.23 (2020), p. 235435.

[234] Chen Yang et al. "Valley pseudospin in monolayer $MoSi_2N_4$ and $MoSi_2As_4$". In: *Phys. Rev. B* 103.3 (2021), p. 035308.

[235] San-Dong Guo et al. "Intrinsic piezoelectricity in monolayer MSi_2N_4 (M= Mo, W, Cr, Ti, Zr and Hf)". In: *EPL (Europhysics Letters)* 132.5 (2020), p. 57002.

[236] Yunshan Zhao et al. "Thermal Transport in 2D Semiconductors—Considerations for Device Applications". In: *Adv. Funct. Mater* 30.8 (2020), p. 1903929.

[237] Yuxi Wang et al. "Thermal properties of two dimensional layered materials". In: *Adv. Funct. Mater* 27.19 (2017), p. 1604134.

[238] Xiao Wan et al. "Optimizing Thermal Transport in Graphene Nanoribbon Based on Phonon Resonance Hybridization". In: *Mater. Today Phys.* (2021), p. 100445.

[239] Shichen Deng et al. "Electric-field-induced modulation of thermal conductivity in poly (vinylidene fluoride)". In: *Nano Energy* 82 (2021), p. 105749.

[240] Han Meng et al. "Thermal conductivity of one-dimensional carbon-boron nitride van der Waals heterostructure: A molecular dynamics study". In: *Int. J. Heat Mass Transf.* 180 (2021), p. 121773.

[241] Eui-Hyeok Yang et al. *Synthesis, Modelling and Characterization of 2D Materials and their Heterostructures*. Elsevier, 2020.

[242] Chengru Wang et al. "Superior thermal conductivity in suspended bilayer hexagonal boron nitride". In: *Sci. Rep* 6.1 (2016), pp. 1–6.

[243] Zhe Luo et al. "Anisotropic in-plane thermal conductivity observed in few-layer black phosphorus". In: *Nat. Commun* 6.1 (2015), pp. 1–8.

[244] Rusen Yan et al. "Thermal conductivity of monolayer molybdenum disulfide obtained from temperature-dependent Raman spectroscopy". In: *ACS nano* 8.1 (2014), pp. 986–993.

[245] Alexander A Balandin et al. "Superior thermal conductivity of single-layer graphene". In: *Nano letters* 8.3 (2008), pp. 902–907.

[246] Houfu Song et al. "Two-dimensional materials for thermal management applications". In: *Joule* 2.3 (2018), pp. 442–463.

[247] Pei Huang et al. "Graphene film for thermal management: A review". In: *Nano Materials Science* 3.1 (2021), pp. 1–16.

[248] Ashwin Ramasubramaniam, Doron Naveh, and Elias Towe. "Tunable band gaps in bilayer transition-metal dichalcogenides". In: *Phys. Rev. B* 84.20 (2011), p. 205325.

[249] Sajedeh Manzeli et al. "2D transition metal dichalcogenides". In: *Nat. Rev. Mater.* 2.8 (2017), pp. 1–15.

[250] Yongqing Cai et al. "Lattice vibrational modes and phonon thermal conductivity of monolayer MoS 2". In: *Phys. Rev. B* 89.3 (2014), p. 035438.

[251] Jiebin Peng, Gang Zhang, and Baowen Li. "Thermal management in MoS_2 based integrated device using near-field radiation". In: *Appl. Phys. Lett* 107.13 (2015), p. 133108.

[252] Guangzhao Qin et al. "On the diversity in the thermal transport properties of graphene: a first-principles-benchmark study testing different exchange-correlation functionals". In: *Comput. Mater. Sci.* 151 (2018), pp. 153–159.

[253] Fengnian Xia et al. "Graphene Field-Effect Transistors with High On/Off Current Ratio and Large Transport Band Gap at Room Temperature". In: *Nano Letters* 10.2 (2010), pp. 715–718.

[254] Xue Liu et al. "High performance field-effect transistor based on multilayer tungsten disulfide". In: *ACS nano* 8.10 (2014), pp. 10396–10402.

[255] Wei Wu et al. "High mobility and high on/off ratio field-effect transistors based on chemical vapor deposited single-crystal MoS_2 grains". In: *Appl. Phys. Lett* 102.14 (2013), p. 142106.

[256] Ryan C Cooper et al. "Nonlinear elastic behavior of two-dimensional molybdenum disulfide". In: *Phys. Rev. B* 87.3 (2013), p. 035423.

[257] You Zhou et al. "Development of high-thermal-conductivity silicon nitride ceramics". In: *J. Asian Ceram. Soc.* 3.3 (2015), pp. 221–229.

[258] Bohayra Mortazavi et al. "Exceptional piezoelectricity, high thermal conductivity and stiffness and promising photocatalysis in two-dimensional $MoSi_2N_4$ family confirmed by first-principles". In: *Nano Energy* 82 (2021), p. 105716. ISSN: 2211-2855.

[259] Jihai Yu et al. "High intrinsic lattice thermal conductivity in monolayer MoSi2N4". In: *New Journal of Physics* 23.3 (Mar. 2021), p. 033005.

[260] Georg Kresse and Jürgen Hafner. "Ab initio molecular dynamics for liquid metals". In: *Phys. Rev. B* 47.1 (1993), p. 558.

[261] Hendrik J Monkhorst and James D Pack. "Special points for Brillouin-zone integrations". In: *Phys. Rev. B* 13.12 (1976), p. 5188.

[262] Xiaokun Gu, Baowen Li, and Ronggui Yang. "Layer thickness-dependent phonon properties and thermal conductivity of MoS_2". In: *J. Appl. Phys* 119.8 (2016), p. 085106.

[263] Han Xie, Ming Hu, and Hua Bao. "Thermal conductivity of silicene from first-principles". In: *Appl. Phys. Lett.* 104.13 (2014), p. 131906.

[264] Aamir Shafique and Young-Han Shin. "Strain engineering of phonon thermal transport properties in monolayer 2H-MoTe 2". In: *Phys. Chem. Chem. Phys.* 19.47 (2017), pp. 32072–32078.

[265] Huake Liu et al. "Disparate strain dependent thermal conductivity of two-dimensional penta-structures". In: *Nano letters* 16.6 (2016), pp. 3831–3842.

[266] Bo Peng et al. "Thermal conductivity of monolayer MoS_2, $MoSe_2$, and WS_2: interplay of mass effect, interatomic bonding and anharmonicity". In: *RSC Advances* 6.7 (2016), pp. 5767–5773.

[267] Liang-Feng Huang and Zhi Zeng. "Roles of Mass, Structure, and Bond Strength in the Phonon Properties and Lattice Anharmonicity of Single-Layer Mo and W Dichalcogenides". In: *J. Phys. Chem. C* 119.32 (2015), pp. 18779–18789.

[268] G.A. Slack. "Nonmetallic crystals with high thermal conductivity". In: *J. Phys. Chem. Solids* 34.2 (1973), pp. 321–335.

[269] Antonio Politano and Gennaro Chiarello. "Probing the Young's modulus and Poisson's ratio in graphene/metal interfaces and graphite: a comparative study". In: *Nano Res.* 8.6 (), pp. 1847–1856. (Visited on 10/16/2019).

[270] Ning Zhang et al. "Superior structural, elastic and electronic properties of 2D titanium nitride MXenes over carbide MXenes: a comprehensive first principles study". In: *2D Mater.* 5.4 (July 2018), p. 045004. ISSN: 2053-1583. (Visited on 06/28/2019).

[271] Alexander A Balandin. "Thermal properties of graphene and nanostructured carbon materials". In: *Nat. Mater.* 10.8 (2011), pp. 569–581.

[272] Delong Li et al. "Recent progress of two-dimensional thermoelectric materials". In: *Nanomicro Lett.* 12.1 (2020), pp. 1–40.

[273] Ssennoga Twaha et al. "A comprehensive review of thermoelectric technology: Materials, applications, modelling and performance improvement". In: *Renew. Sustain. Energy Rev.* 65 (2016), pp. 698–726.

[274] R Bistritzer and Allan H MacDonald. "Electronic cooling in graphene". In: *Phys. Rev. Lett* 102.20 (2009), p. 206410.

[275] Hangbo Qi et al. "Two-dimensional $Al_2I_2Se_2$: A promising anisotropic thermoelectric material". In: *J. Alloys Compd* 876 (2021), p. 160191.

[276] Alexander A Balandin and Denis L Nika. "Phononics in low-dimensional materials". In: *Mater. Today* 15.6 (2012), pp. 266–275.

[277] David G Cahill et al. "Nanoscale thermal transport. II. 2003–2012". In: *Appl. Phys. Rev.* 1.1 (2014), p. 011305.

[278] Baowen Li, Lei Wang, and Giulio Casati. "Thermal diode: Rectification of heat flux". In: *Phys. Rev. Lett* 93.18 (2004), p. 184301.

[279] Andre Konstantin Geim. "Graphene: status and prospects". In: *Science* 324.5934 (2009), pp. 1530–1534.

[280] Fredrik Schedin et al. "Detection of individual gas molecules adsorbed on graphene". In: *Nat. Mater.* 6.9 (2007), pp. 652–655.

[281] Likai Li et al. "Black phosphorus field-effect transistors". In: *Nat. Nanotechnol.* 9.5 (2014), p. 372.

[282] Changbin Nie et al. "Ultrafast growth of large-area monolayer MoS_2 film via gold foil assistant CVD for a highly sensitive photodetector". In: *Nanotechnology* 28.27 (2017), p. 275203.

[283] Renyuan Li et al. "MXene Ti_3C_2: an effective 2D light-to-heat conversion material". In: *ACS nano* 11.4 (2017), pp. 3752–3759.

[284] Kenji Watanabe, Takashi Taniguchi, and Hisao Kanda. "Direct-bandgap properties and evidence for ultraviolet lasing of hexagonal boron nitride single crystal". In: *Nat. Mater.* 3.6 (2004), pp. 404–409.

[285] Chen Shen et al. "Two-Dimensional Layered MSi_2N_4 (M = Mo, W) as Promising Thermal Management Materials: a comparative study". In: *Phys. Chem. Chem. Phys.* (2021).

[286] Sevil Sarikurt, Tuğbey Kocabaş, and Cem Sevik. "High-throughput computational screening of 2D materials for thermoelectrics". In: *J. Mater. Chem. A* 8.37 (2020), pp. 19674–19683.

[287] Zakaria Y Al Balushi et al. "Two-dimensional gallium nitride realized via graphene encapsulation". In: *Nat. Mater.* 15.11 (2016), pp. 1166–1171.

[288] Tae Hoon Seo et al. "Direct growth of GaN layer on carbon nanotube-graphene hybrid structure and its application for light emitting diodes". In: *Sci. Rep.* 5 (2015), p. 7747.

[289] Sten Haastrup et al. "The Computational 2D Materials Database: high-throughput modeling and discovery of atomically thin crystals". In: *2D Mater.* 5.4 (2018), p. 042002.

[290] Hasan Şahin et al. "Monolayer honeycomb structures of group-IV elements and III-V binary compounds: First-principles calculations". In: *Phys. Rev. B* 80.15 (2009), p. 155453.

[291] U Öpik and Maurice Henry Lecorney Pryce. "Studies of the Jahn-Teller effect. I. A survey of the static problem". In: *Proceedings of the Royal Society of London. Series A. Mathematical and Physical Sciences* 238.1215 (1957), pp. 425–447.

[292] Isaac B Bersuker, Natalia N Gorinchoi, and Victor Z Polinger. "On the origin of dynamic instability of molecular systems". In: *Theor. Chim. Acta* 66.3-4 (1984), pp. 161–172.

[293] IB Bersuker and BERSUKER IB. "Are activated complexes of chemical reactions experimentally observable ones?" In: *Nouv. J. Chim.* 4.3 (1980), pp. 159–168.

[294] Richard C Powell. *Symmetry, group theory, and the physical properties of crystals*. Vol. 172. Springer, 2010.

[295] Xavier Gonze and Changyol Lee. "Dynamical matrices, Born effective charges, dielectric permittivity tensors, and interatomic force constants from density-functional perturbation theory". In: *Phys. Rev. B* 55.16 (1997), p. 10355.

[296] L Lindsay, DA Broido, and Natalio Mingo. "Flexural phonons and thermal transport in graphene". In: *Phys. Rev. B* 82.11 (2010), p. 115427.

[297] Zhehao Sun et al. "Ultra-low thermal conductivity and high thermoelectric performance of two-dimensional triphosphides (InP_3, GaP_3, SbP_3 and SnP_3): A comprehensive first-principles study". In: *Nanoscale* (2020).

[298] Shiqiang Hao et al. "Computational prediction of high thermoelectric performance in hole doped layered GeSe". In: *Chem. Mater.* 28.9 (2016), pp. 3218–3226.

[299] Li-Dong Zhao et al. "SnSe: a remarkable new thermoelectric material". In: *Energy Environ. Sci.* 9.10 (2016), pp. 3044–3060.

[300] AV Petrov and EL Shtrum. "Heat conductivity and the chemical bond in ABX_2-type compounds". In: *Soviet Physics-Solid state* 4.6 (1962), pp. 1061–1065.

[301] Andreas Savin et al. "ELF: The electron localization function". In: *Angew. Chem* 36.17 (1997), pp. 1808–1832.

[302] Yu Xiao et al. "Origin of low thermal conductivity in SnSe". In: *Phys. Rev. B* 94.12 (2016), p. 125203.

[303] Wolfgang G Zeier et al. "Thinking like a chemist: intuition in thermoelectric materials". In: *Angew. Chem* 55.24 (2016), pp. 6826–6841.

[304] Manoj K Jana et al. "The Origin of Ultralow Thermal Conductivity in InTe: Lone-Pair-Induced Anharmonic Rattling". In: *Angew. Chem* 128.27 (2016), pp. 7923–7927.

[305] Michele D Nielsen, Vidvuds Ozolins, and Joseph P Heremans. "Lone pair electrons minimize lattice thermal conductivity". In: *Energy Environ. Sci.* 6.2 (2013), pp. 570–578.

[306] Eric J Skoug and Donald T Morelli. "Role of lone-pair electrons in producing minimum thermal conductivity in nitrogen-group chalcogenide compounds". In: *Phys. Rev. Lett.* 107.23 (2011), p. 235901.

[307] DT Morelli, V Jovovic, and JP Heremans. "Intrinsically minimal thermal conductivity in cubic I-V-VI semiconductors". In: *Phys. Rev. Lett* 101.3 (2008), p. 035901.

[308] Loay Elalfy, Denis Music, and Ming Hu. "Metavalent bonding induced abnormal phonon transport in diamondlike structures: Beyond conventional theory". In: *Phys. Rev. B* 103.7 (2021), p. 075203.

[309] Mohammed Al-Fahdi, Xiaoliang Zhang, and Ming Hu. "Phonon transport anomaly in metavalent bonded materials: contradictory to the conventional theory". In: *J. Mater. Sci.* 56.33 (2021), pp. 18534–18549.

[310] Andrei V Kovalevsky et al. "Designing strontium titanate-based thermoelectrics: insight into defect chemistry mechanisms". In: *J. Mater. Chem. A.* 5.8 (2017), pp. 3909–3922.

[311] David Michael Rowe. *Thermoelectrics handbook: macro to nano*. CRC press, 2018.

[312] David Michael Rowe. *Modules, systems, and applications in thermoelectrics*. Vol. 2. CRC press, 2012.

[313] Wei He et al. "Recent development and application of thermoelectric generator and cooler". In: *Appl. Energy* 143 (2015), pp. 1–25.

[314] Yinglu Tang et al. "Convergence of multi-valley bands as the electronic origin of high thermoelectric performance in $CoSb_3$ skutterudites". In: *Nat. Mater* 14.12 (2015), pp. 1223–1228.

[315] Ali Saramat et al. "Large thermoelectric figure of merit at high temperature in Czochralski-grown clathrate $Ba_8Ga_{16}Ge_{30}$". In: *J. Appl. Phys.* 99.2 (2006), p. 023708.

[316] Ruijuan Yan et al. "Effects of Doping Ni on the Microstructures and Thermoelectric Properties of Co-Excessive NbCoSn Half-Heusler Compounds". In: *ACS Appl. Mater. Interfaces* 13.29 (2021), pp. 34533–34542.

[317] Ning Wang et al. "High-Temperature Thermoelectric Monolayer Bi_2TeSe_2 with High Power Factor and Ultralow Thermal Conductivity". In: *ACS Appl. Energy Mater.* 5.2 (2022), pp. 2564–2572.

[318] Franck Gascoin et al. "Zintl phases as thermoelectric materials: tuned transport properties of the compounds $Ca_xYb_{1-x}Zn_2Sb_2$". In: *Adv. Funct. Mater.* 15.11 (2005), pp. 1860–1864.

[319] AV Kovalevsky et al. "Towards a high thermoelectric performance in rare-earth substituted $SrTiO_3$: effects provided by strongly-reducing sintering conditions". In: *Phys. Chem. Chem. Phys* 16.48 (2014), pp. 26946–26954.

[320] Jian He and Terry M Tritt. "Advances in thermoelectric materials research: Looking back and moving forward". In: *Science* 357.6358 (2017).

[321] Jian He, Yufei Liu, and Ryoji Funahashi. "Oxide thermoelectrics: The challenges, progress, and outlook". In: *J. Mater. Res.* 26.15 (2011), p. 1762.

[322] Turan Birol and Craig J Fennie. "Origin of giant spin-lattice coupling and the suppression of ferroelectricity in EuTiO$_3$ from first principles". In: *Phys. Rev. B* 88.9 (2013), p. 094103.

[323] T Kolodiazhnyi et al. "Evidence of Eu^{2+} 4f electrons in the valence band spectra of EuTiO$_3$ and EuZrO$_3$". In: *J. Appl. Phys.* 112.8 (2012), p. 083719.

[324] TR McGuire et al. "Magnetic structure of EuTiO$_3$". In: *J. Appl. Phys.* 37.3 (1966), pp. 981–982.

[325] Sascha Populoh et al. "Perovskite and related oxides for energy harvesting by thermoelectricity". In: *Perovskites and Related Mixed Oxides* (2016), pp. 189–210.

[326] L Sagarna et al. "Structure and thermoelectric properties of EuTi(O,N)$_3 \pm \delta$". In: *J. Appl. Phys.* 114.3 (2013), p. 033701.

[327] Xingxing Xiao et al. "Tailoring the structure and thermoelectric properties of BaTiO$_3$ via Eu^{2+} substitution". In: *Phys. Chem. Chem. Phys* 19.21 (2017), pp. 13469–13480.

[328] L Sagarna et al. "Electronic structure and thermoelectric properties of nanostructured EuTi$_{1-x}$Nb$_x$O$_{3-\delta}$ (x= 0.00; 0.02)". In: *Appl. Phys. Lett.* 101.3 (2012), p. 033908.

[329] Jin-Jian Zhou, Olle Hellman, and Marco Bernardi. "Electron-phonon scattering in the presence of soft modes and electron mobility in SrTiO$_3$ perovskite from first principles". In: *Phys. Rev. Lett* 121.22 (2018), p. 226603.

[330] Terumasa Tadano and Shinji Tsuneyuki. "First-principles lattice dynamics method for strongly anharmonic crystals". In: *J. Phys. Soc. Jpn* 87.4 (2018), p. 041015.

[331] Yusuke Oba et al. "First-principles study of phonon anharmonicity and negative thermal expansion in ScF$_3$". In: *Phys. Rev. Mat.* 3.3 (2019), p. 033601.

[332] John P Perdew et al. "Restoring the density-gradient expansion for exchange in solids and surfaces". In: *Phys. Rev. Lett* 100.13 (2008), p. 136406.

[333] Roman Wahl, Doris Vogtenhuber, and Georg Kresse. "SrTiO$_3$ and BaTiO$_3$ revisited using the projector augmented wave method: Performance of hybrid and semilocal functionals". In: *Phys. Rev. B* 78.10 (2008), p. 104116.

[334] Vladimir I Anisimov, Ferdi Aryasetiawan, and AI Lichtenstein. "First-principles calculations of the electronic structure and spectra of strongly correlated systems: the LDA+U method". In: *J. Condens. Matter Phys* 9.4 (1997), p. 767.

[335] SL Dudarev et al. "Electron-energy-loss spectra and the structural stability of nickel oxide: An LSDA+ U study". In: *Phys. Rev. B* 57.3 (1998), p. 1505.

[336] June Hyuk Lee et al. "A strong ferroelectric ferromagnet created by means of spin–lattice coupling". In: *Nature* 466.7309 (2010), pp. 954–958.

[337] Konstantin Z Rushchanskii, Nicola A Spaldin, and Marjana Ležaić. "First-principles prediction of oxygen octahedral rotations in perovskite-structure $EuTiO_3$". In: *Phys. Rev. B* 85.10 (2012), p. 104109.

[338] Chia-Ling Chien, S DeBenedetti, and F De S Barros. "Magnetic properties of $EuTiO_3$, Eu_2TiO_4, and $Eu_3Ti_2O_7$". In: *Phys. Rev. B* 10.9 (1974), p. 3913.

[339] Takuro Katsufuji and H Takagi. "Coupling between magnetism and dielectric properties in quantum paraelectric $EuTiO_3$". In: *Phys. Rev. B* 64.5 (2001), p. 054415.

[340] Keivan Esfarjani and Harold T Stokes. "Method to extract anharmonic force constants from first principles calculations". In: *Phys. Rev. B* 77.14 (2008), p. 144112.

[341] Trevor Hastie, Robert Tibshirani, and Jerome Friedman. *The elements of statistical learning: data mining, inference, and prediction*. Springer Science & Business Media, 2009.

[342] Yi Wang et al. "Density functional theory-based database development and CALPHAD automation". In: *JOM* 65.11 (2013), pp. 1533–1539.

[343] Shin-ichiro Tamura. "Isotope scattering of dispersive phonons in Ge". In: *Phys. Rev. B* 27.2 (1983), p. 858.

[344] Junichiro Shiomi, Keivan Esfarjani, and Gang Chen. "Thermal conductivity of half-Heusler compounds from first-principles calculations". In: *Phys. Rev. B* 84.10 (2011), p. 104302.

[345] PG Klemens. "The thermal conductivity of dielectric solids at low temperatures (theoretical)". In: *Proceedings of the Royal Society of London. Series A. Mathematical and Physical Sciences* 208.1092 (1951), pp. 108–133.

[346] Yinchang Zhao et al. "Quartic anharmonicity and anomalous thermal conductivity in cubic antiperovskites A_3BO (A= K, Rb; B= Br, Au)". In: *Phys. Rev. B* 101.18 (2020), p. 184303.

[347] PG Klemens. "Thermal conductivity and lattice vibrational modes". In: *Phys. Solid State*. Vol. 7. Elsevier, 1958, pp. 1–98.

[348] Keivan Esfarjani, Gang Chen, and Harold T Stokes. "Heat transport in silicon from first-principles calculations". In: *Phys. Rev. B* 84.8 (2011), p. 085204.

[349] Zhiting Tian et al. "Phonon conduction in PbSe, PbTe, and $PbTe_{1-x}Se_x$ from first-principles calculations". In: *Phys. Rev. B* 85.18 (2012), p. 184303.

[350] Yi Xia. "Revisiting lattice thermal transport in PbTe: The crucial role of quartic anharmonicity". In: *Appl. Phys. Lett.* 113.7 (2018), p. 073901.

[351] T He et al. "Superconductivity in the non-oxide perovskite MgCNi$_3$". In: *Nature* 411.6833 (2001), pp. 54–56.

[352] Roger H Mitchell. *Perovskites: modern and ancient*. Vol. 7. Almaz Press Thunder Bay, 2002.

[353] K KUNDU ASISH. *MAGNETIC PEROVSKITES: Synthesis, Structure and Physical Properties*. SPRINGER, 2017.

[354] T Okuda et al. "Large thermoelectric response of metallic perovskites: Sr 1- x La x TiO 3 (0<˜ x<˜ 0. 1)". In: *Phys. Rev. B* 63.11 (2001), p. 113104.

[355] Guichuan Xing et al. "Low-temperature solution-processed wavelength-tunable perovskites for lasing". In: *Nat. Mater.* 13.5 (2014), pp. 476–480.

[356] Mao-Hua Zhang et al. "Deciphering the phase transition-induced ultrahigh piezoresponse in (K, Na) NbO3-based piezoceramics". In: *Nat. Commun.* 13.1 (2022), pp. 1–10.

[357] Mingzhen Liu, Michael B Johnston, and Henry J Snaith. "Efficient planar heterojunction perovskite solar cells by vapour deposition". In: *Nature* 501.7467 (2013), pp. 395–398.

[358] Sergey V Krivovichev. "Minerals with antiperovskite structure: a review". In: *Z. fur Krist. - Cryst. Mater.* 223.1-2 (2008), pp. 109–113.

[359] Yonggang Wang et al. "Antiperovskites with exceptional functionalities". In: *Adv. Mater.* 32.7 (2020), p. 1905007.

[360] JY Lin and HD Yang. "MgCNi3: a conventional and yet puzzling superconductor". In: *Superconductivity Research at the Leading Edge* (2003), p. 111.

[361] Masatomo Uehara et al. "Superconducting properties of CdCNi3". In: *J. Phys. Soc. Jpn.* 76.3 (2007), p. 034714.

[362] G Kresse and J Furthmüller. "Efficiency of ab-initio total energy calculations for metals and semiconductors using a plane-wave basis set". In: *Comput. Mater. Sci.* 6.1 (1996), pp. 15–50.

[363] Paolo Giannozzi et al. "QUANTUM ESPRESSO: a modular and open-source software project for quantum simulations of materials". In: *J. Condens. Matter Phys.* 21.39 (2009), p. 395502.

[364] E Kucukbenli et al. "Projector augmented-wave and all-electron calculations across the periodic table: a comparison of structural and energetic properties". In: *arXiv preprint arXiv:1404.3015* (2014).

[365] MPAT Methfessel and AT Paxton. "High-precision sampling for Brillouin-zone integration in metals". In: *Phys. Rev. B* 40.6 (1989), p. 3616.

[366] Philip B Allen and Božidar Mitrović. "Theory of superconducting Tc". In: *Solid state physics* 37 (1983), pp. 1–92.

[367] A Togo and I Tanaka. "First principles phonon calculations in materials science". In: *Scr. Mater.* 108 (2015), pp. 1–5.

[368] Bosen Wang and Kenya Ohgushi. "Post-perovskite Transition in Anti-structure". In: *Sci. Rep.* 6.1 (2016), pp. 1–7.

[369] "Synthesis and characterization of Ge–Cr-based intermetallic compounds: $GeCr_3$, $GeCCr_3$, and $GeNCr_3$". In: ().

[370] Ertugrul Karaca et al. "Prediction of phonon-mediated superconductivity in new Ti-based M_2AX phases". In: *Sci. Rep.* 12.1 (2022), pp. 1–10.

[371] Jia-Xin Yin et al. "Giant and anisotropic many-body spin–orbit tunability in a strongly correlated kagome magnet". In: *Nature* 562.7725 (2018), pp. 91–95.

[372] LA Fenner, AA Dee, and AS Wills. "Non-collinearity and spin frustration in the itinerant kagome ferromagnet Fe_3Sn_2". In: *J. Condens. Matter Phys.* 21.45 (2009), p. 452202.

[373] Mamoru Mekata. "Kagome: The story of the basketweave lattice". In: *Phys. Today* 56.2 (2003), p. 12.

[374] H-M Guo and M Franz. "Topological insulator on the kagome lattice". In: *Phys. Rev. B* 80.11 (2009), p. 113102.

[375] Gang Xu et al. "Chern semimetal and the quantized anomalous Hall effect in $HgCr_2Se_4$". In: *Phys. Rev. Lett.* 107.18 (2011), p. 186806.

[376] Hua Chen, Qian Niu, and A. H. MacDonald. "Anomalous Hall Effect Arising from Noncollinear Antiferromagnetism". In: *Phys. Rev. Lett.* 112 (1 Jan. 2014), p. 017205.

[377] J. Kübler and C. Felser. "Non-collinear antiferromagnets and the anomalous Hall effect". In: *EPL (Europhysics Letters)* 108.6 (Dec. 2014), p. 67001.

[378] Evelyn Tang, Jia-Wei Mei, and Xiao-Gang Wen. "High-temperature fractional quantum Hall states". In: *Phys. Rev. Lett.* 106.23 (2011), p. 236802.

[379] Yi Zhou, Kazushi Kanoda, and Tai-Kai Ng. "Quantum spin liquid states". In: *Rev. Mod. Phys.* 89.2 (2017), p. 025003.

[380] Kenya Ohgushi, Shuichi Murakami, and Naoto Nagaosa. "Spin anisotropy and quantum Hall effect in the kagomé lattice: Chiral spin state based on a ferromagnet". In: *Phys. Rev. B* 62.10 (2000), R6065.

[381] Simeng Yan, David A Huse, and Steven R White. "Spin-liquid ground state of the S= 1/2 kagome Heisenberg antiferromagnet". In: *Science* 332.6034 (2011), pp. 1173–1176.

[382] Tian-Heng Han et al. "Fractionalized excitations in the spin-liquid state of a kagome-lattice antiferromagnet". In: *Nature* 492.7429 (2012), pp. 406–410.

[383] II Mazin et al. "Theoretical prediction of a strongly correlated Dirac metal". In: *Nat. Commun.* 5.1 (2014), pp. 1–7.

[384] R Chisnell et al. "Topological magnon bands in a kagome lattice ferromagnet". In: *Phys. Rev. Lett.* 115.14 (2015), p. 147201.

[385] Gang Xu, Biao Lian, and Shou-Cheng Zhang. "Intrinsic quantum anomalous hall effect in the kagome lattice $Cs_2LiMn_3F_{12}$". In: *Phys. Rev. Lett.* 115.18 (2015), p. 186802.

[386] W Zhu et al. "Interaction-driven spontaneous quantum Hall effect on a kagome lattice". In: *Phys. Rev. Lett.* 117.9 (2016), p. 096402.

[387] Charles L Kane and Eugene J Mele. "Quantum spin Hall effect in graphene". In: *Phys. Rev. Lett.* 95.22 (2005), p. 226801.

[388] B Andrei Bernevig, Claudia Felser, and Haim Beidenkopf. "Progress and prospects in magnetic topological materials". In: *Nature* 603.7899 (2022), pp. 41–51.

[389] Hubertus Giefers and Malcolm Nicol. "High pressure X-ray diffraction study of all Fe–Sn intermetallic compounds and one Fe–Sn solid solution". In: *J. Alloys Compd.* 422.1-2 (2006), pp. 132–144.

[390] Lennart Häggström, Tore Ericsson, and Roger Wäppling. "An investigation of CoSn using Mössbauer Spectroscopy". In: *Phys. Scr.* 11.2 (1975), p. 94.

[391] Mingu Kang et al. "Dirac fermions and flat bands in the ideal kagome metal FeSn". In: *Nat. Mater.* 19.2 (2020), pp. 163–169.

[392] Zhiyong Lin et al. "Flatbands and emergent ferromagnetic ordering in Fe_3Sn_2 kagome lattices". In: *Phys. Rev. Lett.* 121.9 (2018), p. 096401.

[393] Zheng-Zhe Lin and Xi Chen. "Tunable Massive Dirac Fermions in Ferromagnetic Fe_3Sn_2 Kagome Lattice". In: *Phys. Status Solidi-R* 14.5 (2020), p. 1900705.

[394] Zhiyong Lin et al. "Dirac fermions in antiferromagnetic FeSn kagome lattices with combined space inversion and time-reversal symmetry". In: *Phys. Rev. B* 102.15 (2020), p. 155103.

[395] Qi Wang et al. "Anomalous Hall effect in a ferromagnetic Fe_3Sn_2 single crystal with a geometrically frustrated Fe bilayer kagome lattice". In: *Phys. Rev. B* 94.7 (2016), p. 075135.

[396] Hiroaki Tanaka et al. "Three-dimensional electronic structure in ferromagnetic Fe_3Sn_2 with breathing kagome bilayers". In: *Phys. Rev. B* 101.16 (2020), p. 161114.

[397] Hang Li et al. "Large topological Hall effect in a geometrically frustrated kagome magnet Fe_3Sn_2". In: *Appl. Phys. Lett.* 114.19 (2019), p. 192408.

[398] T Kida et al. "The giant anomalous Hall effect in the ferromagnet Fe_3Sn_2—a frustrated kagome metal". In: *J. Condens. Matter Phys.* 23.11 (2011), p. 112205.

[399] Hang Li et al. "Large anomalous Hall effect in a hexagonal ferromagnetic Fe_5Sn_3 single crystal". In: *Phys. Rev. B* 101.14 (2020), p. 140409.

[400] H Zhang, CQ Xu, and Xianglin Ke. "Topological Nernst effect, anomalous Nernst effect, and anomalous thermal Hall effect in the Dirac semimetal Fe_3Sn_2". In: *Phys. Rev. B* 103.20 (2021), p. L201101.

[401] Brian C Sales et al. "Electronic, magnetic, and thermodynamic properties of the kagome layer compound FeSn". In: *Phys. Rev. Mater.* 3.11 (2019), p. 114203.

[402] Bahar Fayyazi et al. "Bulk combinatorial analysis for searching new rare-earth free permanent magnets: Reactive crucible melting applied to the Fe-Sn binary system". In: *Acta Mater.* 141 (2017), pp. 434–443.

[403] Bahar Fayyazi et al. "Experimental and computational analysis of binary Fe-Sn ferromagnetic compounds". In: *Acta Mater.* 180 (2019), pp. 126–140.

[404] D Tréheux and P Guiraldenq. "Etude des diagrammes d'equilibre binaires par la methode des couples de diffusion. Application au systeme fer-etain". In: *Scr. Mater.* 8.4 (1974), pp. 363–366.

[405] KC Hari Kumar, Patrick Wollants, and Lucas Delaey. "Thermodynamic evaluation of Fe-Sn phase diagram". In: *Calphad* 20.2 (1996), pp. 139–149.

[406] John P Perdew, Kieron Burke, and Matthias Ernzerhof. "Generalized gradient approximation made simple". In: *Phys. Rev. Lett.* 77.18 (1996), p. 3865.

[407] Stefano Baroni, Paolo Giannozzi, and Eyvaz Isaev. "Density-functional perturbation theory for quasi-harmonic calculations". In: *Rev. Mineral. Geochem.* 71.1 (2010), pp. 39–57.

[408] L Häggström et al. "Studies of the magnetic structure of FeSn using the Mössbauer Effect". In: *Physica Scripta* 11.1 (1975), p. 47.

[409] G Le Caër et al. "A Mossbauer study of $FeSn_2$". In: *J. Phys. F Met. Phys.* 15.8 (1985), p. 1813.

[410] KHJ v Buschow, PG Van Engen, and R Jongebreur. "Magneto-optical properties of metallic ferromagnetic materials". In: *J. Magn. Magn. Mater.* 38.1 (1983), pp. 1–22.

[411] JF CannOn. "Effect of high pressure on the structures of AB3-type layered compounds." In: *High Pressure Science and Technology III (C. Homan, RK MacCrone & E. Whalley, eds.). Mater. Res. Soc., Symp*. Vol. 22. 1984, pp. 113–116.

[412] Mirko Doberšek, Ivan Kosovinc, and Konrad Schubert. "Metallographie und Konstitution der Fe-Ecke des Systems Fe–C–Sn". In: *Arch. Eisenhuttenwes.* 55.6 (1984), pp. 263–266.

[413] K Kanematsu. "Stability of Crystal Structure of (Fe, V)$_3$M and (Fe, Ni)$_3$M (M= Si, Ge, Sn) and Its Analysis Based on Rigid Band Model". In: *Trans. Jpn. Inst. Met.* 27.4 (1986), pp. 225–232.

[414] Hisao Yamamoto. "Mössbauer effect measurement of intermetallic compounds in iron-tin system: Fe$_5$Sn$_3$ and FeSn". In: *J. Phys. Soc. Jpn.* 21.6 (1966), pp. 1058–1062.

[415] B Malaman et al. "Structure cristalline du stannure de fer Fe3Sn2". In: *Acta Crystallogr. B* 32.5 (1976), pp. 1348–1351.

[416] AM Van der Kraan and KHJ Buschow. "The 57Fe Mössbauer isomer shift in intermetallic compounds of iron". In: *Physica B+C* 138.1-2 (1986), pp. 55–62.

[417] VV Pavlyuk et al. "Interaction of the components in the Fe-Sn-Sb system". In: *Pol. J. Chem.* 71.1 (1997), pp. 11–15.

[418] JC Waerenborgh et al. "Crystal structure, 57Fe Mössbauer spectroscopy and magnetization of U$_x$Fe$_6$Sn$_6$ ($0 < x < 0.6$)". In: *Intermetallics* 13.5 (2005), pp. 490–496.

[419] Arkady S Mikhaylushkin et al. "High-pressure structural behavior of large-void CoSn-type intermetallics: Experiments and first-principles calculations". In: *Phys. Rev. B* 77.1 (2008), p. 014102.

[420] Dasannacharya BA and Roy AP. "Neutron Diffraction Study of Antiferro-magnetism in FeSn$_2$". In: *J. Phys. Soc. Jpn.* 17.1 (1962), pp. 247–248.

[421] EE Havinga, H Damsma, and P Hokkeling. "Compounds and pseudo-binary alloys with the CuAl$_2$ (C16)-type structure I. Preparation and X-ray results". In: *J. Less-common Met.* 27.2 (1972), pp. 169–186.

[422] Marc Armbrüster et al. "Crystal structures of iron distannide, FeSn$_2$, and cobalt distannide, CoSn$_2$". In: *Z Krist-New Cryst. St,* 222.2 (2007), pp. 83–84.

[423] Marc Armbrüster et al. "Chemical bonding in compounds of the CuAl$_2$ family: MnSn$_2$, FeSn$_2$ and CoSn$_2$". In: *Eur. J. Chem.* 16.34 (2010), pp. 10357–10365.

[424] B.N. Brockhouse, H.E. Abou-Helal, and E.D. Hallman. "Lattice vibrations in iron at 296 K". In: *Solid State Commun.* 5.4 (1967), pp. 211–216.

[425] D.C. Wallace, P.H. Sidles, and G.C. Danielson. "Specific heat of high purity iron by a pulse heating method". In: *J. Appl. Phys.* 31.1 (1960), pp. 168–176.

[426] Bo Sundman, Bo Jansson, and Jan-Olof Andersson. "The thermo-calc databank system". In: *Calphad* 9.2 (1985), pp. 153–190.

[427] Ling Fan et al. "DFT Calculations and Thermodynamic Re-Assessment of the Fe-Y Binary System". In: *J. Phase Equilib. Diff.* 42.3 (2021), pp. 348–362.

[428] Chen Shen et al. "Thermodynamic Reassessment of the Au-In Binary System Supported with First-Principles Calculations". In: *J. Phase Equilib. Diff.* 42.4 (2021), pp. 479–488.

[429] CA Edwards and A Preece. "A Study of the Constitution of the Iron-Tin Alloys". In: *J. Iron Steel Inst. London* 124 (1931), pp. 41–69.

[430] M Arita et al. "MEASUREMENTS OF ACTIVITY, SOLUBILITY, AND DIFFUSIVITY IN α AND Γ IRON-TIN ALLOYS BETWEEN 1183 AND 1680 K". In: *Int. J. Mater. Res.* 12.30 (1981), pp. 244–250.

[431] Hiroaki Okamoto, TB Massalski, et al. "Binary alloy phase diagrams". In: *ASM International, Materials Park, OH, USA* (1990), p. 12.

[432] T Yamamoto, T Takashima, and K Nishida. "INTER-DIFFUSION IN THE ALPHA-SOLID SOLUTION OF THE Fe-Sn SYSTEM". In: *J. Jpn. Inst. Met.* 45.10 (1981), pp. 985–990.

[433] C Jannin, A Michel, and P Lecocq. "Magnetism and Properties of Different Phases in the Fe-Sn System". In: *Comptes Redus Hebomadaires Seances Acad. Sci* 257 (1963), pp. 1906–1907.

[434] KC Mills and ET Turkdogan. "Liquid miscibility gap in iron-tin system". In: *Trans. Metall. Soc. AIME.* 230.5 (1964), p. 1202.

[435] Ortrud Kubaschewski. *Iron-Binary phase diagrams*. Springer Science & Business Media, 2013.

[436] E Isaac and G Tammann. "On the alloys of iron with tin and gold". In: *Z Anorg Chem* 53 (1907), p. 281.

[437] AN Fedorenko and VG Brovkin. "Vapor pressure of tin and thermodynamic properties of the tin–iron system". In: *Sb. Nauchn. Tr.–Gos. Proektn. Nauchno-Issled. Inst. Gipronikel* 3 (1977), pp. 83–89.

[438] D Treheux, D Duc, and P Guiraldenq. "Determination of the Solubility Limits of Sn in the Alpha and Gamma Phases of Fe". In: *Mem. Sci. Rev. Met.* 71.5 (1974), pp. 289–293.

[439] M Singh and S Bhan. "Contribution to the Fe-Sn system". In: *J. Mater. Sci. Lett.* 5.7 (1986), pp. 733–735.

[440] Shinya Nunoue and Eiichi KATO. "Mass Spectrometric Determination of the Miscibility Gap in the Liquid Fe-Sn System and the Activities of This System at 1550 °C and 1600°C". In: *Tetsu-to-Hagané* 73.7 (1987), pp. 868–875.

[441] Yu-Chih Huang, Wojciech Gierlotka, and Sinn-Wen Chen. "Sn–Bi–Fe thermodynamic modeling and Sn–Bi/Fe interfacial reactions". In: *Intermetallics* 18.5 (2010), pp. 984–991.

[442]   R Luck and B Predel. "The Enthalpy of Mixing of Liquid Iron–Tin Alloys De-
        termined by Means of a New High-Temperature Calorimeter". In: *Z. Metallkd.*
        76.10 (1985), pp. 684–686.

[443]   GI Batalin, VS Sudavtsova, and VP Kurach. "Thermodynamic Properties of
        Liquid Fe–Sn Alloys". In: *Izv. Akad. Nauk SSSR, Met.* 4 (1984), pp. 50–51.

Chen Shen

Materials Modeling, Ph.D.

Alarich-Weiss-Str. 8, 64287, Darmstadt Germany

 (+49) 17645954117 | ✉ chenshen@tmm.tu-darmstadt.de | 🎓 Google Scholar (Chen SHEN (沈忱))

EDUCATION

Technische Universität Darmstadt *Darmstadt, Germany*

- Supervisor: Prof. Dr. Hongbin Zhang *10. 2018 - 12. 2022*
- Ph.D. Dissertation: Designing Functional Materials Driven by Lattice Degree of Freedom

Technische Universität Darmstadt *Darmstadt, Germany*

- Supervisor: Prof. Dr. Hongbin Zhang *05. 2015 - 06. 2018*
- Master Thesis: Thermodynamic Assessment of the Magnetic Materials System Supported with First-principles Calculations

Central South University *Changsha, China*

- Supervisor: Prof. Dr. Wenmi Chen *08. 2010 - 09. 2014*
- Bachelor Thesis: Experimental study on flocculants screening test for bauxite washing sludge sedimentation and separation

RESEARCH INTERESTS

During my Ph.D., an integrated computational paradigm combining the high throughput (HTP) density functional theory (DFT), machine learning (ML), and CALculation of PHAse Diagram (CALPHAD) methods was established to design the functional materials, especially energy materials, including permanent magnets, magnetocaloric materials, superconductors, thermoelectric materials, thermal management materials, and low-dimensional catalytic material. The work focuses on studying the role of the lattice in various interactions, calculating and predicting the properties resulting from the corresponding couplings. In addition, in cooperation with other experimental groups, research has also been carried out in phase diagram optimization, high-temperature and high-pressure ceramics, ferroelectrics, negative thermal expansion materials, and optical electronics.

HTP DFT	HTP DFT is mainly engaged in designing functional materials and systematically studying the mechanism behind some critical physical phenomena and properties, such as magnetism, mechanics, anharmonicity, and superconductivity.
CALPHAD	Combining DFT, the CALPHAD method is used to construct a thermodynamic database, which can be addressed to guide the experimental synthesis of novel functional materials in stable and metastable states.
ML	Atomistic models with DFT accuracy can be constructed by developing machine learning interatomic potentials (MLIP) combining HTP calculations and ML.

PROJECT EXPERIENCE

ERC Advanced Grant COOL INNOV *Europe*

MAIN PARTICIPANT OF THE PROJECT *05. 2019 - 05. 2022*

- In this project, we aim to reconstruct three-dimensional microstructures, evaluate corresponding magnetic hysteresis, and implement a deep generative learning algorithm to optimize the magnetic hysteresis in the latent space of microstructures. In this way, the last microstructure ↔ property link can be established.

Fulbright-Cottrell *Germany*

PARTICIPANT OF THE PROJECT *05. 2019 - 01. 2023*

- The aim of this project is to develop a new integrated paradigm to incorporate high throughput DFT calculations, machine learning, and CALPHAD phase diagram, to bridge the gap to multi-scale simulations and to experiments with mutual validation.

NOVAMAG: NOVel, critical materials free, high Anisotropy phases for permanent MAGnets, by desin

Germany

PARTICIPANT OF THE PROJECT

08. 2018 - 09. 2019

- We participated in this project by contributing to the thermodynamic modeling of phase diagrams. First-principles calculations were carried out to obtain essential parameters, such as mean magnetic moments and Curie temperature, to construct CALPHAD modeling of the magnetic Gibbs energy. The atomic order-disorder transition was considered using the standard cluster variation method. To account for the interplay between chemical and magnetic degrees of freedom, first-principles calculations were performed to investigate the interaction between magnetism and spatial ordering, and the resulting relations were implemented into the CALPHAD modeling. Efficient screening of RE-free uniaxial materials and magnetic characterization could be achieved. Fe-Sn was used as a prototype system.

Hessian Competence Center for High-Performance Computing (HKHLR)

Germany

PRINCIPAL INVESTIGATOR

2020/2021/2022

- High Throughput Screening for Novel ternary chalcogenides and binary transition metal nitrides. (Project:00694, 21.1 Mio. core-h)
- Study for external electric field tuned thermal transport properties of two-dimensional materials based on the high throughput density functional theory and machine learning. (Project:01218, 23.3 Mio. core-h)
- High-throughput discovery of MAB and Mbene superconductors. (Project:20160, 17.5 Mio. core-h)

Phadwiki.com

China

FOUNDER

08. 2020 - present

- Initiated and established the first comprehensive platform for non-profit computing simulation learning exchange in China. Invite many doctors and postdocs in the field of simulation to share knowledge and advanced computing experience, aiming to create a large-scale computing simulation ecological environment suitable for scientific research workers to learn and exchange.

PUBLICATIONS

(Co†-)First-author & Corresponding author*

2023	H. Wang, Y. Jiao, B. Wu, D. Wang*, Y Hu, F Liang, **C. Shen***, A Knauer, D Ren*, H. Wang*, P. A. Aken, H. Zhang, M. Grätzel, Z. Sofer, P. Schaaf, Exfoliated 2D Layered and Nonlayered Metal Phosphorous Trichalcogenides Nanosheets as Promising Electrocatalysts for CO2 Reduction. *Angew. Chem.*, 2023.	*Angew. Chem.*
2023	S. Lin, **C. Shen***, H. Zhang, Electric-field-tunable thermal conductivity in anti-ferroelectric materials. *Mater. Today Phys.*, 2023.	*Mater. Today Phys.*
2023	**C. Shen**, M. Dai, F. Liang, W. Xie, A. Weidenkaff, T. Tadano*, H. Zhang*, Thermal transport properties of EuTiO$_3$: A comparative theoretical and experimental investigation. *Mater. Today Phys.*, in press.	*Mater. Today Phys.*
2023	R. Yan†, **C. Shen**†, R. Eilhardt, T. Luo, R. Xie, W. Xie*, M. Widenmeyer, S. Yoon, H. Zhang, A. Weidenkaff, Beneficial contribution of interstitial Cu disorder to electron and phonon transport properties in ZrNiSn half-heusler thermoelectric materials. *Mater. Today Phys.*, in press.	*Mater. Today Phys.*
2023	**C. Shen**†, I. Samathrakis†, K. Hu, HK. Singh, N. Fortunato, H. Liu, O. Gutfleisch, H. Zhang*, Thermodynamical and topological properties of metastable Fe$_3$Sn. *Npj Comput. Mater.*, 8, 248.	*Npj Comput. Mater.*
2022	D. Wei, E Zhou, X. Zheng, **C. Shen***, H. Zhang, H. Wang*, Z. Qin*, G. Qin*, Electric-controlled thermal transistor based on Janus monolayer MoSSe. *Npj Comput. Mater.*, 8 (1), 260.	*Npj Comput. Mater.*
2022	MH. Zhang†, **C. Shen**†, CH. Zhao†, M. Dai, FZ. Yao, B. Wu*, J. Ma, H. Nan, D. Wang, Q. Yuan, L. Silva, L. Fulanović, A. Schökel, P. Liu, HB. Zhang, JF. Li, N. Zhang*, K. Wang*, J. Rödel, M. Hinterstein, Deciphering the phase transition-induced ultrahigh piezoresponse in (K,Na)NbO$_3$-based piezoceramics. *Nat. Commun.*, 2022, 13, 3434.	*Nat. Commun.*
2022	**C. Shen**, N. Hadaeghi, HK. Singh, T. Long, L. Fan, G. Qin, H. Zhang*, Two-dimensional bucking structure induces the ultra-low thermal conductivity: A comparative study of the group GaX (X = N, P, As). *J. Mater. Chem. C*, 2022, 10, 1436.	*J. Mater. Chem. C*
2022	**C. Shen**, L. Wang, D. Wei, Y. Zhang, G. Qin*, X. Chen*, H. Zhang*, Novel Two-Dimensional Layered M$_2$SiN$_4$ (M = Mo, W): New Promising Thermal Management Materials. *Phys. Chem. Chem. Phys.*, 2022, 24, 3086.	*Phys. Chem. Chem. Phys*
2022	D. Wei, E Zhou, X. Zheng, **C. Shen***, H. Zhang, H. Wang*, Z. Qin*, G. Qin*, Electric-controlled thermal transistor based on Janus monolayer MoSSe. *Npj Comput. Mater.*, 2022, 8, 1.	*Npj Comput. Mater.*

2022	L. Yu, Y. Zhan, D. Wei, **C. Shen***, HB. Zhang, ZZ. Qin*, GZ Qin*, Multifunctional two-dimensional graphene-like boron nitride allotrope of g-B_3N_5: A competitor to g-BN? *J. Alloys Compd.*, 2022, 921, 165913.	*J. Alloys Compd.*
2022	B. Li, Y. Yang, H. Qi, Z. Sun, F. Yang, K. Huang, Z. Chen, B. He, X. Xiao, **C. Shen***, N. Wang*, Monolayer $Sc_2I_2S_2$: An Excellent n-Type Thermoelectric Material with Significant Anisotropy. *ACS Appl. Energy Mater.*, 2022, 6, 7230.	*ACS Appl. Energy Mater.*
2022	H. Qi, Z. Sun, **C. Shen***, C. Zheng, Z. Wang, X. Wang, M. Zhang, N. Wang*, High thermoelectric performance of monolayer $Al_2X_2Se_2$ (X=Cl, Br, I) with strong anisotropy in lattice thermal conductivity. *ACS Appl. Energy Mater.*, 2022, 5, 7371.	*ACS Appl. Energy Mater.*
2022	Z. Chang, K. Liu, Z. Sun, K. Yuan, S. Cheng, Y. Gao, X. Zhang*, **C. Shen***, H. Zhang, N. Wang*, D. Tang*, First-principles investigation of the significant anisotropy and ultrahigh thermoelectric efficiency of a novel two-dimensional $Ga_2I_2S_2$ at room temperature. *Int. J. Extrem. Manuf.*, 2022, 4, 025001.	*Int. J. Extrem. Manuf.*
2022	Q. Fan, J. Yang, H. Qi, L. Yu, G. Qin, Z. Sun, **C. Shen***, N. Wang*, Anisotropic thermal and electrical transport properties induced high thermoelectric performance in an $Ir_2Cl_2O_2$ monolayer. *Phys. Chem. Chem. Phys.*, 2022, 24, 11268.	*Phys. Chem. Chem. Phys.*
2022	S. Cheng, Y. He, Z. Chang, Z. Sun, X. Zhang, D. Tang, GK. Li, N. Wang*, **C. Shen***, B. Jiang*, Structural, elastic, phononic, optical and electronic properties investigation of two-dimensional XIS (X=Al, Ga, In) for photocatalytic water splitting. *Int. J. Hydrog. Energy*, 2022, 47, 41640.	*Int. J. Hydrog. Energy*
2021	**C. Shen**, Q. Gao, NM. Fortunato, HK. Singh, I. Opahle, O. Gutfleisch, H. Zhang*, Designing of magnetic MAB phases for energy applications. *J. Mater. Chem. A*, 2021, 9, 8805.	*J. Mater. Chem. A*
2021	**C. Shen**, K. Hu, L. Fan, H Zhang*, Thermodynamic Reassessment of the Au-In Binary System Supported with First-Principles Calculations. *J. Phase Equilibria Diffus.*, 2021, 42, 479.	*J. Phase Equilibria Diffus.*
2021	B. Li, Y. Yang, Z. Sun, H. Qi, Z. Xiong, K. Wu, H. Li, K. Sun, X. Xiao, **C Shen***, N. Wang*, First-Principles Investigation on the Significant Anisotropic Thermoelectric Transport Performance of a Hf_2Cl_4 Monolayer. *J. Phys. Chem. C*, 2021, 126, 525.	*J. Phys. Chem. C*
2021	H. Qi, Z. Sun, N. Wang*, G. Qin, H. Zhang, **C. Shen***, Two-dimensional $Al_2I_2Se_2$: A promising anisotropic thermoelectric materials. *J. Alloys Compd.*, 2021, 876, 160191.	*J. Alloys Compd.*
2021	Y. Xiao, L. Tang, W. Zhang*, **C. Shen***, Theoretical insights into the selective and activity of CuAu catalyst for O_2 and CO_2 electroreduction. *Comput. Mater. Sci.*, 2021, 192, 110402.	*Comput. Mater. Sci.*
2021	L. Fan, **C. Shen***, K. Hu, H. Liu, H. Zhang, DFT Calculations and Thermodynamic Re-Assessment of the Fe-Y Binary System. *J. Phase Equilib. Diffus.*, 2021, 42, 348.	*J. Phase Equilib. Diffus.*
2021	Y. Xiao*, **C. Shen***, T. Long, Theoretical Establishment and Screening of an Efficient Catalyst for N_2 Electroreduction on Two-Dimensional Transition-Metal Borides (MBenes). *Chem. Mater.*, 2021, 33, 4023.	*Chem. Mater.*
2021	Y. Zhang, **C. Shen***, T. Long, H. Zhang*, Thermal conductivity of h-BN monolayers using machine learning interatomic potential. *J. Phys.: Condens. Matter*, 2021, 33, 105903.	*J. Phys.: Condens. Matter*

Co-author

2023	Y. Xiao*, **C. Shen**, W. Zhang, M. Zhang, H. Zhang, T. Shao, Z Xiong, Y. Ding, S. Hao, L. Liu, Y. Chen, J. Li*, Electrocatalytic Biomass Upgrading of Furfural using Transition-Metal Borides via Density Functional Theory Investigation. *Small*, 2205876.	*Small*
2023	A. Rodriguez, C. Lin, H. Yang, M. Al-Fahdi, **C. Shen**, K. Choudhary, Y. Zhao, J. Hu, B. Cao, H. Zhang, M. Hu*, Million-Scale Atomic Data Integrated Single Deep Neural Network for Predicting Complete Phonon Properties of Heusler Crystals Spanning the Periodic Table. *Npj Comput. Mater.*, 9 (1), 20.	*Npj Comput. Mater.*
2022	KC. Zhang*, **C. Shen**, H. Zhang, YF Li, Y Liu, Effect of quartic anharmonicity on the carrier transport of cubic halide perovskites $CsSnI_3$ and $CsPbI_3$. *Phys. Rev. B*, 2022, 106, 235202.	*Phys. Rev. B*

2022	A. Rodriguez, C. Lin, H. Yang, M. Al-Fahdi, **C. Shen**, K. Choudhary, Y. Zhao, J. Hu, B. Cao, H. Zhang, M. Hu*, Million-Scale Atomic Data Integrated Single Deep Neural Network for Predicting Complete Phonon Properties of Heusler Crystals Spanning the Periodic Table. *Npj Comput. Mater.*, 2022, accepted.	*Npj Comput. Mater.*
2022	HK. Singh, A. Sehrawat, **C. Shen**, I. Samathrakis, I. Opahle, H. Zhang, R. Xie*, High-throughput screening of Half-antiperovskites with a stacked kagome lattice. *Acta Mater.*, 2022, 242, 118474.	*Acta Mater.*
2022	I. Samathrakis, N. Fortunato, HK. Singh, **C. Shen**, H. Zhang*, Tunable anomalous hall and nernst effects in MM'X compounds. *J. Phys.: Condens. Matter*, 2022, 51, 025703.	*J. Phys.: Condens. Matter*
2022	A. Reitz, P. Hanna, **C. Shen**, HK. Singh, K. Jayanthi, N. Kubitzaf, A Navrotsky, H. Zhang, U. Wiedwald, C. S. Birkel*, Cr_3GeN: A new nitride with orthorhombic antiperovskite structure. *Chem. Mater*, 2022, 34, 10304.	*Chem. Mater.*
2022	J. Sinclair, J. P. Siebert, M. Juelsholt, **C. Shen**, H. Zhang, and C. S. Birkel*, Facile sol gel-based synthesis of the phosphorus-containing MAX Phase V_2PC. *Inorg. Mater.*, 2022, 61, 16976.	*Inorg. Mater.*
2022	L. Yu, J. Xu, **C. Shen**, E. Zhou, J. Wu, H. Zhang, X. Zheng, H. Wang, G. Qin*, Realizing ultra-low thermal conductivity by the strong synergy of asymmetric geometry and electronic structure in boron nitride and arsenide. *Rare Met.*, 2022, 42, 210.	*Rare Met.*
2022	T. Long, Y. Zhang, NM. Fortunato, **C. Shen**, M Dai, H. Zhang*, Inverse design of crystal structures for multicomponent systems. *Acta Mater.*, 2022, 231, 117898.	*Acta Mater.*
2022	Y. Xiao*, **C. Shen**, Z. Xiong, J. Li*, W. Zhang, A strategy to address the challenge of electrochemical CO_2 and N_2 coupling to synthesis urea on two-dimensional metal borides (MBenes) by computational screening. *Mater. Today Phys.*, 2022, 26, 100726.	*Mater. Today Phys.*
2022	Y. Xiao, **C. Shen**, W. Zhang*, Screening and prediction of metal-doped α-borophene monolayer for nitric oxide elimination. *Mater. Today Chem.*, 2022, 25, 100958.	*Mater. Today Chem.*
2022	Z. Xiong, Y. Xiao*, **C. Shen**, Screening of the Transition Metal Single Atom Anchored on α-Borophene Catalysts as a Feasible Strategy for Electrosynthesis of Urea. *Chem. Mater.*, 2022, 34, 9402.	*Chem. Mater.*
2022	N. Wang, **C. Shen**, Z. Sun, B. Li, H. Xiao*, X. Zu, H. Zhang, Z. Yin, L. Qiao*, Thermal Transport and Mechanical Properties of Layered Oxychalcogenides LaCuOX (X = S, Se, and Te). *ACS Appl. Energy Mater.*, 2022, 5, 6943.	*ACS Appl. Energy Mater.*
2022	E. Zhou, J. Wu, **C. Shen**, H. Zhang, G. Qin*, The stable behavior of low thermal conductivity in 1T-sandwich structure with different components. *J. Appl. Phys.*, 2022, 131, 185702.	*J. Appl. Phys.*
2022	HK. Singh, I. Samathrakis, **C. Shen**, H. Zhang*, Giant anomalous Hall and anomalous Nernst conductivities in antiperovskites and their tunability via magnetic fields. *Phys. Rev. Materials*, 2022, 6, 045402.	*Phys. Rev. Materials*
2022	L. Yu, Y. Tian, X. Zheng, H. Wang, **C. Shen**, G Qin*, Abnormal enhancement of thermal conductivity by planar structure: A comparative study of graphene-like materials. *Int. J. Therm. Sci.*, 2022, 174, 107438.	*Int. J. Therm. Sci.*
2022	F. Duan, **C. Shen**, H. Zhang, G Qin*, Hydrodynamically enhanced thermal transport due to strong interlayer interactions: A case study of strained bilayer graphene. *Phys. Rev. B*, 2022, 105, 125406.	*Phys. Rev. B*
2022	N. Wang, **C. Shen**, Z. Sun, H. Xiao*, H. Zhang, Z. Yin, L. Qiao*, High-Temperature Thermoelectric Monolayer Bi_2TeSe_2 with High Power Factor and Ultralow Thermal Conductivity. *ACS Appl. Energy Mater.*, 2022, 5, 2564.	*ACS Appl. Energy Mater.,*
2021	Y. Xiao*, **C. Shen**, N. Hadaeghi, Transition-Metal Borides (MBenes) as New High-Efficiency Catalysts for Nitric Oxide Electroreduction to Ammonia by a High-Throughput Approach. *Small*, 2021, 17, 2100776.	*Small*
2021	N. Wang, H. Gong, Z. Sun, **C. Shen**, B. Li, H. Xiao*, X. Zu, D. Tang, Z. Yin, X. Wu, H. Zhang, L. Qiao*, Boosting Thermoelectric Performance of 2D Transition-Metal Dichalcogenides by Complex Cluster Substitution: The Role of Octahedral Au6 Clusters. *ACS Appl. Energy Mater.*, 2021, 4, 12163.	*ACS Appl. Energy Mater.*
2021	R. Yan, R. Xie, W. Xie*, **C. Shen**, W. Li, B. Balke, S. Yoon, H. Zhang, A. Weidenkaff, Effects of Doping Ni on the Microstructures and Thermoelectric Properties of Co-Excessive NbCoSn Half-Heusler Compounds. *ACS Appl. Mater. Interfaces*, 2021, 13, 34533.	*ACS Appl. Mater. Interfaces*

2021	Y. Xiao*, **C. Shen**, N. Hadaeghi, Quantum Mechanical Screening of 2D MBenes for the Electroreduction of CO_2 to C1 Hydrocarbon Fuels. *J. Phys. Chem. Lett.*, 2021, 12, 6370.	*J. Phys. Chem. Lett.*
2021	HK. Singh*, I. Samathrakis, NM. Fortunato, J. Zemen, **C. Shen**, O. Gutfleisch, H. Zhang*, Multifunctional antiperovskites driven by strong magnetostructural coupling. *Npj Comput. Mater.*, 2021, 7, 98.	*Npj Comput. Mater.*
2021	T. Long, NM. Fortunato, I. Opahle, Y. Zhang, I. Samathrakis, **C. Shen**, O. Gutfleisch, H. Zhang*, Constrained crystals deep convolutional generative adversarial network for the inverse design of crystal structures. *Npj Comput Mater*, 2021, 7, 66.	*Npj Comput. Mater.*
2021	Y. Xiao*, **C. Shen**, Predicted Electrocatalyst Properties on Metal insulator $MoTe_2$ for hydrogen evolution reaction and oxygen reduction reaction application in fuel cells. *Energy Fuels*, 2021, 35, 9, 8275.	*Energy Fuels*
2021	KC. Zhang*, L. Cheng, **C. Shen**, Y. Li, Y. Liu, Y. Zhu, Thickness-dependent anisotropic transport of phonons and charges in few-layered $PdSe_2$. *Phys. Chem. Chem. Phys.*, 2021, 23, 18869.	*Phys. Chem. Chem. Phys.*
2021	X. Wang, W. Feng, **C. Shen**, Z. Sun, H. Qi, M. Yang, Y. Liu, Y. Wu, X. Wu*, The verification of thermoelectric performance obtained by high-throughput calculations: the case of GeS_2 monolayer from first-principles calculations. *Front. Mater.*, 2021, 8, 709757.	*Front. Mater.*
2021	K. Hu, S. Dong, **C. Shen**, H. Liu*, H. Peng, G. Cai, ZP. Jin, Measurement of phase equilibria in Ti-Co-Ge ternary system. *J. Alloys Compd.*, 2021, 793, 653-661.	*J. Alloys Compd.*

CONFERENCES & RESEARCH VISITS

Deutsche Physikalische Gesellschaft (DPG)   *Regensburg*, *Germany*
                                                                                        09. 2022

Talk: Self-consistent phonon calculations of lattice dynamical properties

Psi-k 2022   *Lausanne, Switzerland*
                                                                                        08. 2022

Poster: Self-consistent phonon calculations of lattice dynamical properties in cubic $EuTiO_3$ comparing with experimental results

2022 CAMD Summer School   *Copenhagen*, *Denmark*
                                                                                        08. 2022

Poster: Designing Functional Materials Driven by Lattice Degree of Freedom

Virtual Materials Design   *Karlsruhe*, *Germany*
                                                                                        07. 2022

Poster: High-throughput design of magnetic materials

1st China-Germany Meeting on 2D Materials   *Mainz, Germany*
                                                                                        04. 2022

Poster: Designing 2D thermoelectric and thermal management materials

APS March Meeting   *Online*, *US*
                                                                                        03. 2021

Talk: Designing of magnetic MAB phases for energy applications

Vist Prof. Zhanpeng Jin's Group   *Changsha*, *China*
                                                                                        11. 2018-02.2019

Invited to visit Prof. Jin's group, guided the students in DFT calculations

Deutsche Physikalische Gesellschaft (DPG)   *Dresden*, *Germany*
                                                                                        03. 2018

Poster：Thermodynamic Assessment of the Magnetic Materials System supported with First-Principles Calculations

TEACHING EXPERIENCE

CALPHAD Lab   *TU Darmstadt*

LECTURER   *Winter Semester 2020/2021/2022*

- Instruct undergraduates to use related software for thermodynamic calculations and phase diagram optimization.

Quantum Materials Design   *TU Darmstadt*

TEACHING ASSISTANT   *Summer Semester 2020/2021*

- Assist professors in writing course design and teaching plans and guide students to finish related projects.

Master Thesis   *TU Darmstadt*

SUPERVISOR   *2019 - 2021*

- Supervise eight graduate students to complete the graduation project calculation and thesis writing. And helped two Chinese postgraduates to achieve the design and writing of CSC proposals.

SCHOLARSHIPS & AWARDS

- TOP STARS Award 2019 （TATA Steel Challenge Award）
- TUDa Scholarship for the international student （2018）
- *Roll student* of Central South University （2014）
- Student Leadership of Central South University （2 times）
- Scholarship of Central South University （3 times）

SKILLS & INTERESTS

- **Language:** Chinese (native), English (fluent), German (fluent)
- **Computer:** Proficient in programming with Python; using Photoshop and Illustrator
- **Interests:** Soccer, badminton